Thermally Deformable Mirrors : a new Adaptive Optics scheme for Advanced Gravitational Wave Interferometers

Marie Kasprzack

LAL 14-176
Septembre 2014

Universite Paris Sud 11

Ecole doctorale Particules, noyaux, cosmos (ed 517)

laboratoire de l'accelerateur lineaire

THÈSE

présentée pour obtenir le grade de

DOCTEUR EN SCIENCES PHYSIQUES

de l'université Paris XI

Spécialité: Physique

par

Marie Kasprzack

Thermally Deformable Mirrors: a new Adaptive Optics scheme for Advanced Gravitational Wave Interferometers

Soutenue le 26 septembre 2014 devant la Commission d'Examen

MM.	A. Stocchi	Président
	R. Adhikari	Rapporteur
	F. Druon	Rapporteur
	J. Gascon	Examinateur
	J.Y. Vinet	Examinateur
	F. Cavalier	Directeur de thèse
	R. Day	Directeur de thèse

Ed eccolo ora qui, uguale e sconosciuto,

quel profumo, nel mondo, umido
e raggiante: e io qui, perso nell'atto
sempre riuscito e inutile, umile

e squisito, di sciogliere l'intatto
senso nelle sue mille immagini...

P.P. Pasolini

Acknowledgements

This thesis work results from the conjoint efforts of two groups of the Virgo collaboration, the VIRGO group at LAL and the Optics group from EGO, and has been performed partly in France and partly in Italy. This partnership was a supplementary challenge to the scientific goals of the thesis and I would like to thank all the people that made this great experience possible.

First of all, I would like to thank the director of the LAL, Achille Stocchi, for welcome me in his lab and for being the president of my thesis committee. Thank you to the Director Ferrini, for welcome me at EGO site. For their rewarding and patient review of my work, thank you to Frédéric Druon and to Rana Adhikari, that also accepts to cross the ocean to come to the defense. Thank you to Jules Gascon and Jean-Yves Vinet for examining my work.

I would like to warmly thank my two thesis supervisors, Fabien Cavalier et Richard Day, for their trust and their support all along these years. Thank you for giving me the opportunity to work on a such exciting subject, and for having always being present and supportive. It was a great honor to work with you, to learn from you and share your enthusiasm for the world of gravitational wave detectors. In very different manners you have taught me how to perform a good work, with always giving me the liberty to try by myself. Now that you have shown me the way, I will try to follow your paths...

Thanks to Julien Marque for the work with him in Cascina and his precious advices. Many thanks to all the people in the Optics group for the wonderful work time with them : Eric Genin, Benjamin Canuel, Antonino Chiummo, Gabriel Pillant and Andrea Magazzu. I would like to thank in particular Gabriele Vajente for his inestimable help in debugging simulations and setups and for the time he took to patiently share his knowledge about detectors, locking and Gaussian beams.

The experimental work is always the result of patient team effort. I would like to thanks Daniel Sentenac for his helpful contribution to the first experiments in the Optics lab in Cascina. Many thanks to Adam Kutynia for all the time he dedicated to the design and realization of the second prototype. A lot of work presented in this thesis would not have been possible without him. Thanks to Alberto Gennai for his help for the driver control.

I would like to thank all the people in Cascina for their warm welcome and for sharing their passion: Matteo, Bas, Paolo, Severine, Henrich, Maddalena, and so many people I am sorry to not mention. You made these years a very rich human experience.

I would also like to thank Patrice Hello for his help in mastering the Bessel functions and other Hermite polynomials. Many thanks to the members of the VIRGO Group at LAL for integrating me in their team for the last year of thesis: Marie-Anne, Florent, Samuel, Nicolas. In particular, thanks to Nicolas Leroy for being always available and his great help in the experiments. Many thanks to the people from the CALVA Hall: Dominique, Vincent and Ivan.

Good luck to Annalisa for the end of her thesis, it was nice to share with you the adventure of thermal systems.

Ces remerciements ne seraient pas complets sans quelques mots pour mes parents, ainsi que Anne et Stanislas. Merci pour leur affection et leur présence sans faille à mes côtés.

Contents

Introduction

The gravitational waves are predicted by the Einstein's theory of General Relativity. However, they have not been directly observed so far, despite they have been tracked for fifty years with different instruments. The main reason is that the interaction of the gravitational waves with the matter is very weak. Therefore, detecting their effect on matter among the noise sources inherent to any instrument is a challenge. The advanced gravitational wave interferometers, currently in development worldwide, are to the most promising instruments for a first detection. To reach their target sensitivity, they will use high power lasers. Unfortunately, they will also be very sensitive to thermal effects occurring in the optical components that will decrease the quality of the laser beam fundamental Gaussian mode. In particular, the matching of the main beam into the interferometer will suffer from these defects, leading to power losses and noise coupling and thus potentially affecting the detector sensitivity. It will be then crucial to correct any optical aberration at the input of the interferometer.

The aim of this thesis is to propose a new system of adaptive optics especially dedicated for Advanced Gravitational Interferometers, that is based on a new actuation device: the Thermally Deformable Mirror (TDM). To meet the stringent requirements of the noise and optical compatibility, the device is based on the thermal actuation: a high quality optical substrate is in contact with a set of resistors which power can be tuned individually. The absorption of the power in the substrate generates a temperature gradient and therefore locally changes the value of the refractive index. A laser beam that is going through the substrate and is reflected by its back side will experience a phase variation that modifies its wavefront. By accurately choosing the power values of the resistors, the TDM will be able to correct the wavefront aberrations of the incident laser beam.

In Chapter 1, the main features of the gravitational waves, described as a consequence of the General Relativity, are explained. One of the Advanced Gravitational Wave Detectors, Advanced Virgo, is described with a brief summary of the main noise sources. The thermal effects at different stages of the interferometer are also presented.

In Chapter 2, a review of the existing adaptive optics corrective devices is proposed, together with a study of their compatibility for a gravitational detector environment. In particular, an analysis of the thermal actuated systems is performed in order to determine the compliance with our requirements. After the need of a new system is established, we start the description of the TDM with a deep study of the actuation properties in Chapter 3. The thermal and opto-mechanical features of several substrates are compared to determine the best material choice. In Chapter 4 the system design is proposed from the description of the aberrations encountered in an optical system. In particular, the spatial frequency required for the set of actuators is justified. Afterwards, two prototypes are characterized in Chapter 5. A deep analysis of the features of each prototype through its ability to generate the aberrations studied is the previous chapter is performed.

In the last two chapters, we study the implementation of the devices in an adaptive optics system for improvement of the mode matching. First, in Chapter 6 we analyze the suppression of high order modes with the combined actuation of two TDMs. We then simulate a control scheme in different configurations. We deduce important features for the experimental corrective setup that is presented in Chapter 7. With this system, we are able to experimentally demonstrate the ability of the TDMs to improve the matching into a cavity.

Chapter 1

Interferometric Detection of the Gravitational Waves

At the beginning of the 20^{th} century, Einstein introduced his Theory of General Relativity [1] which connects the matter and the space-time: the distribution of mass energy induces the space-time curvature and the space-time curvature determines the motion of the matter. The Gravitational Waves (GWs) can be described as perturbations of the space-time metric propagating at the speed of light, produced by the acceleration of bodies. The emission of GWs is particularly important in the case of binary systems, for example binary system of neutron stars. Up to now, the existence of GWs has be confirmed trough indirect observations. The first detection by kilometric interferometers is expected within the next years and will open a new way in astronomical observations.

In this introduction chapter, the basics of the GW generation and their main characteristics are first briefly described. Then, the principle of their interferometric detection is explained and the main features of Advanced Virgo are summarized.

1.1 General Relativity and Gravitational waves

In General Relativity [2, 3], the infinitesimal space-time interval ds between two infinitely close points is given by, using the Einstein summation convention:

$$ds^2 = g_{\mu\nu} dx^\mu dx^\nu \tag{1.1}$$

where dx is the infinitesimal coordinate change. The metric tensor $g_{\mu\nu}$ defines the metric of the space time.

The relation between the energy matter distribution and the metric is then given by the Einstein equation :

$$\mathbf{R}_{\mu\nu} - \frac{1}{2} g_{\mu\nu} R + \Lambda g_{\mu\nu} = \frac{8\pi G}{c^4} \mathbf{T}_{\mu\nu} \tag{1.2}$$

with $\mathbf{R}_{\mu\nu}$ the Ricci tensor describing the space curvature, R the curvature, Λ the Cosmological Constant, $\mathbf{T}_{\mu\nu}$ the stress-energy tensor describing the matter distribution, G the Newton universal gravitation constant and c the speed of light in vacuum. When the space time curvature is small, the metric $g_{\mu\nu}$ can be linearly approximated through:

$$g_{\mu\nu} = \eta_{\mu\nu} + h_{\mu\nu} \tag{1.3}$$

with $\eta_{\mu\nu}$ the metric describing the Minkowski space-time and $h_{\mu\nu}$ a small perturbation, $|h_{\mu\nu}| \ll 1$. The perturbation propagates as a tensor wave leading to write (using Lorenz gauge) Eq.1.2 as :

$$\underbrace{\Box \overline{h}_{\mu\nu}}_{\text{propagation term}} = -\frac{16\pi G}{c^4} \underbrace{(T_{\mu\nu} - \frac{1}{2} g_{\mu\nu} T^k_k)}_{\text{source term}} \tag{1.4}$$

with the d'Alembertian $\Box$ being:

$$\Box = \nabla^2 - \frac{1}{c^2} \frac{\partial^2}{\partial t^2} \tag{1.5}$$

and

$$\overline{h}_{\mu\nu} = h_{\mu\nu} - \frac{1}{2} h \ \eta_{\mu\nu}, \ h = \eta^{\mu\nu} h_{\mu\nu} \tag{1.6}$$

In the absence of a source term, the solution is a propagating wave called Gravitational Wave (GW) which takes the general form of a plane wave:

$$h_{\mu\nu} = \begin{pmatrix} 0 & 0 & 0 & 0 \\ 0 & h_+ & h_\times & 0 \\ 0 & h_\times & -h_+ & 0 \\ 0 & 0 & 0 & 0 \end{pmatrix} e^{-i(\omega t - kz)} \tag{1.7}$$

with h_+ and $h_\times$ the scalar amplitudes of the two states of polarization of the wave and the matrix representing the effect of a GW on the space dimensions. As usual k is the wavevector, ω the angular frequency and t the time.

In the Transverse Traceless (TT) gauge, a GW modifies the distance between free objects placed with an effect rotated of $\pi/2$ between the h_+ and $h_\times$ polarizations. An example is to consider a circle of free masses with a diameter L_0 as in Fig.1.1 crossed in the perpendicular direction by a GW. The circle will successively contract and expand by δL in the x and y directions for the h_+ polarization.

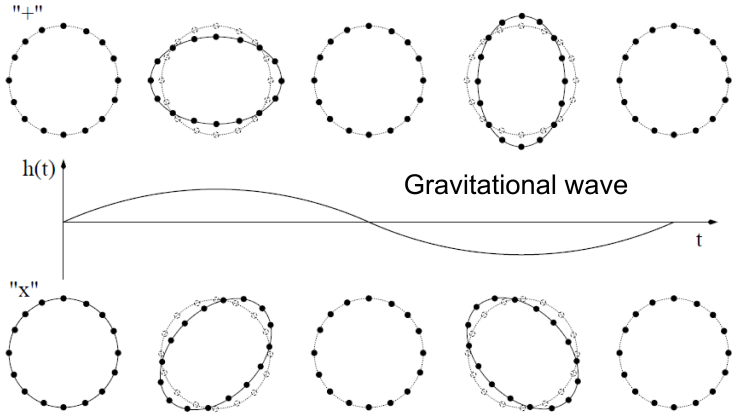

FIGURE 1.1: Effect of a GW over a circle of free fall masses

We can show that the effect is directly proportional to the GW amplitude. Let's consider two objects infinitely close in $A(x, y, z) = (0,0,0)$ and $B(x_B, y_B, z_B)$ in the TT coordinates system, in which objects do not move. The distance between these objects is:

$$L^2 = g_{\mu\nu}(x^\mu_B - x^\mu_A)(x^\nu_B - x^\nu_A) = (\delta_{ij} + h^{TT}_{ij})x^i_B x^j_B \tag{1.8}$$

With $L_0 = \delta_{ij}x^i_B x^j_B$ and $x^i_B = L_0 n^i$ with $\vec{n}$ the unit spatial vector between A and B, we can rewrite:

$$L = (L_0^2(\delta_{ij} + h^{TT}_{ij}n^i n^j))^{1/2} \tag{1.9}$$

$$L = L_0(1 + h^{TT}_{ij}n^i n^j)^{1/2} \tag{1.10}$$

$$L \simeq L_0(1 + \frac{1}{2}h^{TT}_{ij}n^i n^j) \tag{1.11}$$

We define $\delta L = L - L_0$ and we have:

$$\frac{\delta L}{L_0} = \frac{h}{2} \tag{1.12}$$

The relative change in the distances between free masses is directly proportional to the amplitude of the GWs.

1.2 Gravitational wave sources

The gravitational luminosity $\mathcal{L}$ of a source is given by:

$$\mathcal{L} = \frac{G}{5c^5}\left\langle \dddot{Q}_{ij}\ \dddot{Q}^{ij} \right\rangle \tag{1.13}$$

with Q_{ij} the quadrupole momentum of the source:

$$Q_{ij}(t) = \int_{source} \rho(t, \vec{x})(x^i x^j - \frac{1}{3}\vec{x} \cdot \vec{x}\delta^{ij})\mathrm{d}\vec{x} \tag{1.14}$$

As an order of magnitude,

$$Q \sim \epsilon \ M \ R^2 \tag{1.15}$$

with M the object mass, R its typical size and ϵ the asymmetry factor. The typical time scale is $\tau = \frac{R}{v}$, leading to:

$$\dddot{Q} \sim \epsilon \ \frac{M}{\tau^3} \ R^2 \tag{1.16}$$

By rewriting Eq.1.13 one can show that a source of GWs has to be relativist, compact and asymmetric:

$$\mathcal{L} \simeq \frac{c^5}{G} \ \epsilon^2 \ \left(\frac{R_s}{R}\right)^2 \ \left(\frac{v}{c}\right)^6 \tag{1.17}$$

with ϵ the source asymmetry, R the source extension, v its velocity and R_s the corresponding Schwarzshild radius. R_s/R represents the source compacity. According to Eq. 1.13, the luminosity $\mathcal{L}$ becomes significant (about $c^5/G \simeq 5 \cdot 10^{53}$ W), if all other terms are close to unity. It means that the source has to be asymmetric, compact and relativistic. We will see that even when these conditions are fulfilled, the generated GWs have very small amplitude when arriving on Earth.

1.3 Sources

According to the previous criterion, some astrophysical objects are privileged sources for GW emission. For example, the compacity and the term v/c are close to unity for stars collapsing to a neutron star or to a black hole: the collapsing stars are likely important sources of GWs if their asymmetry is sufficient or for binary systems involving compact objects. In this section, we will review some of the main astrophysical sources.

1.3.1 Compact Binary Coalescence

The coalescence of an astrophysical object (black hole or neutron star) binary system is the consequence of the energy loss of the system by emission of GW. The corresponding GW signal, called *chirp*, is characterized by a distinct wave form: an increase of amplitude and frequency over the time up to the final collapse. The research of such signals is made with a template bank and can be triggered by electromagnetic observations.
The Binary Neutron Star (BNS) *range* is a standard figure of merit to express the sensitivity of a GW interferometric detector. By definition, it corresponds to the volume-

and orientation-averaged distance at which a compact binary coalescence consisting of two 1.4 $M_\odot$ neutron stars (where $M_\odot$ = 1 solar mass) gives a matched filter signal-to-noise ratio of 8 in a single detector. Another often quoted number is the BNS *horizon*: the distance at which an optimally oriented and located BNS system would be observed with a signal to noise ratio of 8. The horizon is a factor of 2.26 larger than the range [4]. A typical amplitude of these sources is $h = 10^{-21}$ for a BNS range about 100 Mpc. At their final sensitivity, the detectors should be able to detect 0.4 to 200 BNS per year.

1.3.2 "Burst" sources

The transient sources are defined as GW emitters of "brief" duration from sub-second to weeks. For these sources, the GW wavefront is not well known and the GWs will be identified by excess power events in the strain data. A lot of different sources can produce short signals, such as protoneutron star convection, protoneutron rotational instabilities, oscillations in the neutron stars, accretion disk instabilities and eccentric black hole binaries. The observation of the GW emission from neutron stars will hopefully help to study their structure, that nowadays is poorly understood. A typical transient source are the explosions of a star into a supernova leading to a neutron star. The GW generated with the typical amplitude are detectable only in our Galaxy, leading to a low expected detection rate with one supernova every thirty years. The expected burst range at the final sensitivity of the detectors is about 100 Mpc supposing an emission about 10^{-2} $M_\odot c^2$.

1.3.3 Pulsars

Pulsars are neutron stars emitting a periodic radio pulse. The GW emission will occur if the pulsar is not symmetrical with respect to its rotation axis. The frequency of the GW signal will be the double of its rotation frequency, leading to quasi-monochromatic signal which can be integrated over time in order to increase the signal to noise ratio. The estimated amplitudes are about $h \sim 10^{-26}$ for known pulsars.

1.4 Proof of existence

Up to now, we have only indirect evidence of the GW existence, notably thanks to the work of the physicists Hulse and Taylor in 1974. They observed the modifications of the optical period of the double pulsar PSR B1913+16 and found that the energy loss of the

system is compatible with the energy loss via GW predicted by the General Relativity. Hulse and Taylor won the Physics Nobel prize in 1993.

1.5 Ground base observation

The very weak amplitude of the GWs makes their detection particularly delicate. Fortunately, the detectors are sensitive to the amplitude of the GWs and not to their intensity, as is the case for example for the sensors of the electromagnetic waves. The signal emitted by the sources then only decreases with the inverse of the distance. Therefore, an improvement of a factor 10 in the sensitivity of the detectors will increase the volume of observable sources by a factor 1000.
Since the 60's [5], several instruments have been constructed in the attempt to detect GWs. The most sophisticated are the giant laser interferometers, which are currently five around the world. Virgo, and its upgrade version Advanced Virgo, is one of them and is presented thereafter.

As previously seen, a GW of amplitude h is changing by δL the distance L between free masses according to:

$$\frac{\delta L}{L} = \frac{h}{2} \tag{1.18}$$

in the ideal case of a gravitational wave perpendicular to the plan of these masses. It is known that an efficient way to detect the small length variations δL is to use an interferometer. The principle is to compare the phase shift acquired by correlated beams of wavelength λ following different paths by studying the recombined field after the propagation. The interference in the recombined beam depends on the phase shift $\delta\phi$ occurring from a difference of δL in the optical path length with:

$$\delta\phi = \frac{2\pi}{\lambda}\delta L \tag{1.19}$$

Based on this simple principle, the interferometer technique is developed in different designs and is widely used in a lot of applications. One of the most simple interferometers is the Michelson interferometer, invented by Michelson and Morlay at the end of the 19^{th} century [6]. With this instrument they performed the famous experiment that led to prove the non-existence of ether by showing the invariance of the speed of light with respect to the Earth motion (Physics Nobel price 1887).
Nowadays, the Michelson interferometer promises to be the key for the first detection of the GWs and for the start of the GW astronomy. We will see what the features of the instrument adapted to these new challenges are.

1.6 Optical configuration of the interferometric instruments

Notation An optical field propagating in space described by the spatial coordinates $\vec{r} = x\vec{u_x} + y\vec{u_y} + z\vec{u_z}$ can be written at the instant t:

$$\psi(r,t) = \psi_0 e^{-i(\vec{k}.\vec{r}-\omega t)} \tag{1.20}$$

with $\vec{k}$ the wave vector,

$$|\vec{k}|^2 = n\frac{2\pi}{\lambda} = n\frac{\omega}{c} = k_x^2 + k_y^2 + k_z^2 \tag{1.21}$$

where λ is the wavelength, ω is the pulsation. The propagation along the z axis from the plane z_1 to z_2 is written:

$$\psi(z_2) = \psi(z_1)e^{-ik(z_2-z_1)} \tag{1.22}$$

The interaction of an incident optical field ψ_i with a reflecting surface is described using the following convention:

$$\psi_r = ir\psi_i \tag{1.23}$$

$$\psi_t = t\psi_i \tag{1.24}$$

with ψ_r the reflected field and ψ_t the transmitted field. The reflecting coefficient r and the transmission coefficient t of the surface follow the energy conservation law:

$$r^2 + t^2 + \mathcal{L} = 1 \tag{1.25}$$

with $\mathcal{L}$ the losses produced by scattering or absorption.

1.6.1 The Michelson Interferometer

As shown in Fig.1.2, an input laser field ψ_{in} is injected in the interferometer where it is divided in two fields of half-power by a beam splitter. Each of them is sent into a so-called *arm* where it is reflected back by an end mirror. At the plane of the beam splitter, the two fields are then recombined and sent to the output port. According to the fields in Fig.1.2, we can write [7]:

$$\psi_1 = ir_{BS}\psi_{in} \qquad \psi_3 = t_{BS}\psi_{in} \tag{1.26}$$

$$\psi_2 = -r_Y r_{BS} e^{-2ikL_Y}\psi_{in} \qquad \psi_4 = -ir_X t_{BS} e^{-2ikL_X}\psi_{in} \tag{1.27}$$

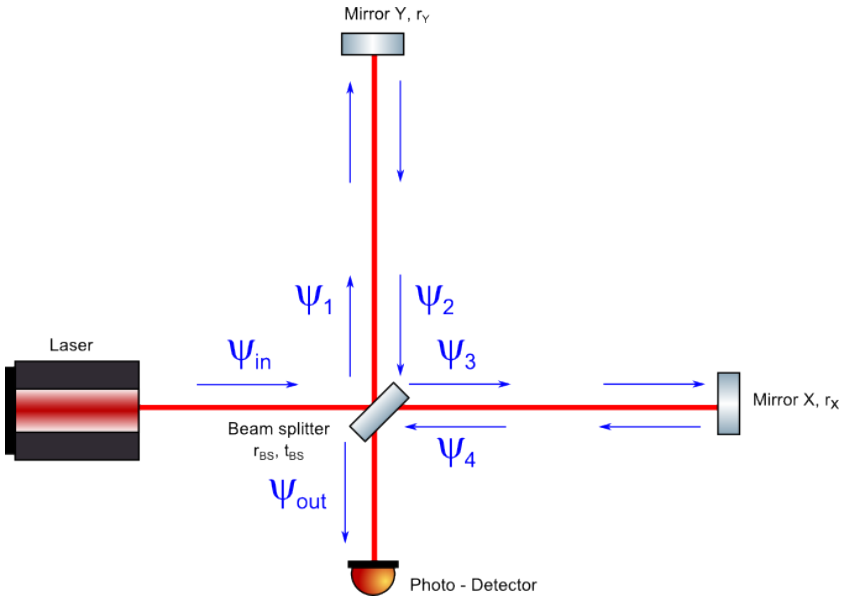

FIGURE 1.2: Scheme of the Michelson interferometer. The field propagation is indicated by the blue arrows.

The field at the output of the detector is then:

$$\psi_{out} = t_{BS}\psi_2 + ir_{BS}\psi_4 \tag{1.28}$$

$$\psi_{out} = -r_{BS}t_{BS}(r_X e^{-2ikL_X} + r_Y e^{-2ikL_Y})\psi_{in} \tag{1.29}$$

We can consider that the beam splitter is perfectly dividing the input power $P_{in}|\psi_{in}|^2$ into equal parts without losses:

$$r_{BS} = t_{BS} = \frac{1}{\sqrt{2}} \tag{1.30}$$

A photodetector at the output port will then provide the power:

$$P_{out} = |\psi_{out}|^2 = \frac{1}{4}({r_X}^2 + {r_Y}^2)(1 + C\cos(2k\Delta L_0))P_{in} \tag{1.31}$$

From Eq.1.31 it appears that the output power is modulated by the optical path length difference between the arms $\Delta L_0 = L_X - L_Y$. It also depends on the end mirror reflectivities and the contrast C is defined by:

$$C = \frac{P_{out_{max}} - P_{out_{min}}}{P_{out_{max}} + P_{out_{min}}} = \frac{2r_X r_Y}{{r_X}^2 + {r_Y}^2} \tag{1.32}$$

The contrast is equal to 1 ($P_{out_{min}} = 0$, $P_{out_{max}} = P_{in}$) when the interferometer has mirrors with equal reflectivity and has no losses. The output port is called the asymmetrical port: it can only see the optical path differences between the arms. The common field is rejected towards the input, that is called the symmetrical port.

When a gravitational wave of amplitude h is passing through the interferometer, the optical path length between the arms varies (see Eq1.18) and according to Eq.1.19, the phase is:

$$\begin{aligned}\phi &= 2k\left[\left(L_X + \frac{\delta L_X}{2}\right) - \left(L_Y - \frac{\delta L_Y}{2}\right)\right] \\ \phi &= 2k\Delta L_0 + 2k\left(\frac{\delta L_X + \delta L_Y}{2}\right) \\ \phi &= \phi_0 + \phi_{GW}\end{aligned} \tag{1.33}$$

Reporting this in Eq.1.31, the power at the output port can be rewritten when the dephasing from the gravitational wave is weak ($\phi_{GW} = 2k\delta L << 1$):

$$P_{out} = \frac{P_{in}}{4}({r_X}^2 + {r_Y}^2)\left(1 + C\left[\cos(\phi_0) - \sin(\phi_0)\phi_{GW}\right]\right) \tag{1.34}$$

The power variation induced by the gravitational wave:

$$\delta P_{out} = \frac{P_{in}}{4}\left({r_X}^2 + {r_Y}^2\right) C\sin(\phi_0)\phi_{GW} \tag{1.35}$$

is maximal when $r_X \simeq r_Y \simeq 1$

$$\delta P_{out} = \frac{P_{in}}{2} C\sin(\phi_0)\phi_{GW} \tag{1.36}$$

1.6.2 Sensitivity of the interferometer

The minimal amplitude h of a gravitational wave that an instrument is able to detect is the *sensitivity* of this detector. This is given over a certain frequency range, in which we are interested in the spectral content of the gravitational wave signal. The sensitivity is then the amplitude spectral density expressed in $1/\sqrt{Hz}$ and is written $\tilde{h}(f)$. The sensitivity of the detector is inherently limited by the quantum noise: the Standard Quantum Limit (SQL) is the sum of the *shot noise* and *radiation pressure noise*, and is the lowest achievable noise.

1.6.2.1 Shot noise

Over the detection frequency range, the sensitivity is equally limited by the fundamental noise related to the discreteness of the photons: the shot noise [**?**]. For a photo-detector with a perfect quantum efficiency, the probability distribution of the photon observation is Poissonian. The detected power during a brief measurement time T can be written:

$$P_{out} = N\frac{h_p\nu}{T} \tag{1.37}$$

with N the average number of photons reaching the detector, h_p the Planck constant and ν the frequency of the laser. The uncertainty on the power detected during a brief measurement time T is:

$$\sigma_P = \sigma_N \frac{h_p \nu}{T} \tag{1.38}$$

Combining these equations with $\sigma_N = \sqrt{N}$, we find:

$$\sigma_P = \sqrt{\frac{2 h_p \nu P_{out}}{T}} \tag{1.39}$$

The amplitude spectral density of the shot noise is then, with Eq. 1.31, and considering only the positive frequencies:

$$\delta\tilde{n}_{shot} = \sqrt{h_p \nu (1 + C\cos(\phi_0)) P_{in}} \tag{1.40}$$

We can only detect a gravitational wave signal which is higher than the shot noise level. From Eq. 1.36, we have then:

$$\delta P_{out} > \delta\tilde{n}_{shot} \tag{1.41}$$

that implies:

$$\frac{P_{in}}{2} C \sin(\phi_0) \frac{2\pi L \tilde{h}}{\lambda} > \sqrt{h_p \nu (1 + C\cos(\phi_0)) P_{in}} \tag{1.42}$$

The smallest signal we can detect is the sensitivity of the Michelson interferometer:

$$\tilde{h}_{shot} = \frac{\sqrt{\lambda}}{2\pi} \frac{1}{L} \sqrt{\frac{h_p c}{2 P_{in}}} \frac{\sqrt{1 + C\cos(\phi_0)}}{C\sin(\phi_0)} \tag{1.43}$$

The best sensitivity is obtained for $C = 1$ and $\phi_0 = 2\pi q$ with q an integer. The difference between the arms is a multiple of the wavelength. This condition is called the *dark fringe* condition: the power exiting the interferometer is equal to zero. We get:

$$\tilde{h}_{shot} = \frac{\sqrt{\lambda}}{2\pi} \frac{1}{L} \sqrt{\frac{h_p c}{2 P_{in}}} \tag{1.44}$$

In practice the contrast is different from 1, due to the asymmetries in the end mirror reflectivities. Then, the optimal sensitivity is then given by:

$$\tilde{h}_{shot} = \frac{\sqrt{\lambda}}{2\pi} \frac{1}{L} \sqrt{\frac{h_p c}{2 P_{in}}} \frac{1}{\sqrt{1 - \sqrt{1 - C^2}}} \tag{1.45}$$

From Eq. 1.44, we can infer that the sensitivity increases with the arm length increase and the power increase. We aim to detect gravitational waves with a typical amplitude

of $|h| = 10^{-22}$. With a laser of 1064 nm at 100 W and an arm length of 1 m, the sensitivity is: $\tilde{h} = 10^{-18}\ 1/\sqrt{Hz}$. According to Eq. 1.44, the solution is to increase the power of the laser and to increase the length of the arms.

1.6.2.2 Radiation pressure

However, when the laser power increases the interferometer becomes sensitive to the radiation pressure noise: the impact of the photons on the mirrors induces a mirror displacement. This noise depends on $1/f^2$ of the motion frequency f. The radiation pressure noise is given by:

$$\tilde{h}_{rad}(f) = \frac{1}{mf^2L}\sqrt{\frac{\tilde{h}P_{in}}{2\pi^3 c\lambda}} \tag{1.46}$$

with m the mass of the mirror. This noise is expected to dominate the sensitivity at low frequencies. The effects of the radiation pressure fluctuations can be reduced by increasing the mass of the mirrors, or by decreasing the laser power at the expense of degrading sensitivity at higher frequencies [8].
Fortunately, the performance of the Michelson can be improved by optically folding the arms: we will use the so-called the *Fabry-Perot* cavities.

1.6.3 The Fabry-Perot cavity

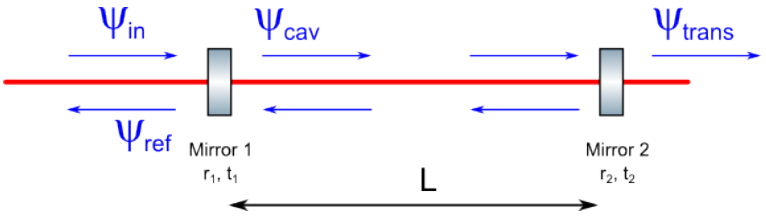

FIGURE 1.3: A Fabry-Perot cavity of length L.

A Fabry-Perot cavity is composed of 2 mirrors M1 and M2 with the respective reflectivity and transmission coefficients r_1, r_2, t_1 and t_2. We can write the fields propagating through the cavity (see Fig1.3):

$$\psi_{cav} = t_1\ \psi_{in} - r_1 r_2 e^{-2ikL}\ \psi_{cav} \tag{1.47}$$

$$\psi_{ref} = ir_1\ \psi_{in} + it_1 r_2 e^{-2ikL}\ \psi_{cav} \tag{1.48}$$

$$\psi_{trans} = t_2 e^{-ikL}\ \psi_{cav} \tag{1.49}$$

With $P_{in} = |\psi_{in}|^2$, we can infer from Eq.1.47 that the power stored inside the cavity is:

$$P_{cav} = |\psi_{cav}|^2 = \frac{t_1^2}{|1 + r_1 r_2 e^{-2ikL}|^2} P_{in} \tag{1.50}$$

The stored power in the cavity is maximal when $e^{-2ikL} = -1$. This is the resonance condition, defining the gain of the cavity:

$$G_{cav} = \frac{t_1^2}{(1 - r_1 r_2)^2} \tag{1.51}$$

A small change in cavity length will affect the power stored inside the cavity:

$$P_{cav} = \frac{G_{cav}}{1 + [\frac{2\sqrt{r_1 r_2}}{1 - r_1 r_2} \sin(\frac{2\pi\delta L}{\lambda})]^2} P_{in} \tag{1.52}$$

The power stored inside the cavity is at its half value when:

$$\sin(\frac{2\pi\delta L}{\lambda}) = \frac{1 - r_1 r_2}{2\sqrt{r_1 r_2}} \tag{1.53}$$

It means that the Full Width at Half Maximum (FWHM) of the Airy peak of the cavity is:

$$\delta L_{FWHM} = \frac{\lambda}{4\mathcal{F}} \tag{1.54}$$

with $\mathcal{F}$ the finesse of the cavity (see Fig. 1.4).

$$\mathcal{F} = \frac{\pi\sqrt{r_1 r_2}}{1 - r_1 r_2} \tag{1.55}$$

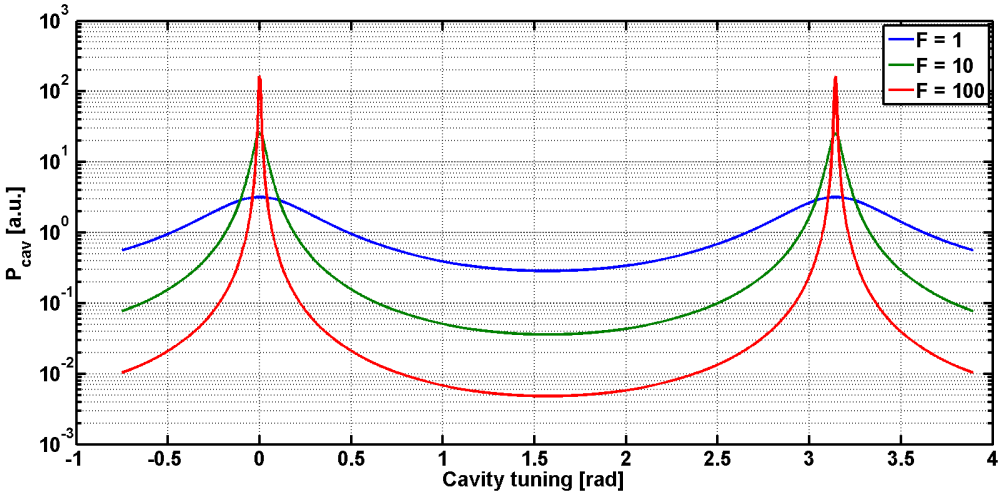

FIGURE 1.4: Resonances of the fundamental in Fabry-Perot cavities exhibiting different finesses. The FWHM of the Airy peak decreases with the finesse increase.

We have then the following equation for the power of the cavity:

$$P_{cav} = \frac{G_{cav}}{1 + [\frac{2\mathcal{F}}{\pi}\sin(\frac{2\pi\delta L}{\lambda})]^2} P_1 \tag{1.56}$$

The field reflected by the cavity is (from Eq.1.48):

$$\psi_{ref} = i\frac{r_1 + r_2(t_1^2 + r_1^2)e^{-2ikL}}{1 + r_1 r_2 e^{-2ikL}}\psi_1 \tag{1.57}$$

Around the resonance, the phase of the reflected field is:

$$\phi_{FP} = \frac{4\pi}{\lambda}\frac{2\mathcal{F}}{\pi}\delta L \tag{1.58}$$

The dephasing is amplified with respect to a single mirror by a factor $\frac{2\mathcal{F}}{\pi}$. To compute the sensitivity, we now have to take into account the frequency response of the cavity, the Fabry-Perot cavity being a low-pass filter as we will see in the next section.

1.6.4 Frequency response of a Fabry-Perot cavity

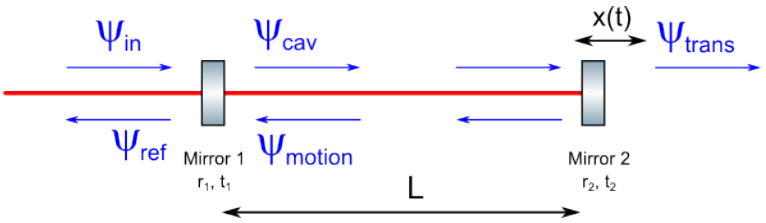

FIGURE 1.5: A Fabry-Perot cavity with a motion of the end mirror

If we consider a sinusoidal motion of the end mirror with (see Fig. 1.5):

$$x(t) = x_0 \cos(\omega_s t) \tag{1.59}$$

we have [9] with ψ_{cav} the field inside the cavity before the end mirror:

$$\psi_{motion} = ir_2 e^{-2ikx(t)}\psi_{cav} \tag{1.60}$$

Supposing that the motion amplitude is very small, we have at the first order:

$$\psi_{motion} = ir_2(1 - 2ikx_0 cos\omega_s t)\psi_{cav} \tag{1.61}$$

$$\psi_{motion} = ir_2\psi_{cav} + \frac{2\pi}{\lambda}x_0 r_2(e^{i\omega_s t} + e^{-i\omega_s t})\psi_{cav} \tag{1.62}$$

We observe that the motion is creating two sidebands at the frequencies $\pm f_s$. In the same way, a gravitational wave will create two sidebands at audio frequencies. At the sideband frequency and when the cavity is resonant for $e^{-2ikL} = -1$:

$$\psi_{motion}(\omega_s) = kx_0 r_2 \frac{1}{1 - r_1 r_2 e^{2i\frac{\omega_s}{c}L}} \psi_{cav}(0) \tag{1.63}$$

And we obtain the field reflected by the cavity at the first order in $\omega_s L$:

$$\psi_{ref}(\omega_s) = -\frac{2\pi r_2}{\lambda} x_0 \frac{G_{cav}}{1 + i\frac{f_s}{\frac{c}{4L\mathcal{F}}}} \psi_{in} \tag{1.64}$$

with the pole of the cavity $f_c = \frac{c}{4L\mathcal{F}}$.

1.6.5 Impact on a Michelson interferometer

The Fabry-Perot cavity is equivalent to a mirror with a complex reflectivity:

$$r_{FP} = \rho_{FP} e^{i\phi_{FP}} \quad \text{with} \quad \begin{cases} \rho_{FP} &= |\frac{r_1 - (r_1^2 + t_1^2) r_2}{1 - r_1 r_2}| \\ \phi_{FP} &= \frac{4\pi}{\lambda} \frac{2\mathcal{F}}{\pi} \delta L \end{cases} \tag{1.65}$$

It means that replacing the arms of the Michelson interferometer with Fabry-Perot cavities is equivalent to have a Michelson interferometer with complex reflecting coefficients (see Fig. 1.6). We can rewrite the output power of a Michelson (Eq.1.31) with this new reflectivity:

$$P_{out} = \frac{1}{4}(r_{FP_X}^2 + r_{FP_Y}^2)(1 + C\cos(\Delta\phi_{FP}))P_{in} \tag{1.66}$$

with the contrast:

$$C = \frac{2 r_{FP_X} r_{FP_Y}}{r_{FP_X}^2 + r_{FP_Y}^2} \tag{1.67}$$

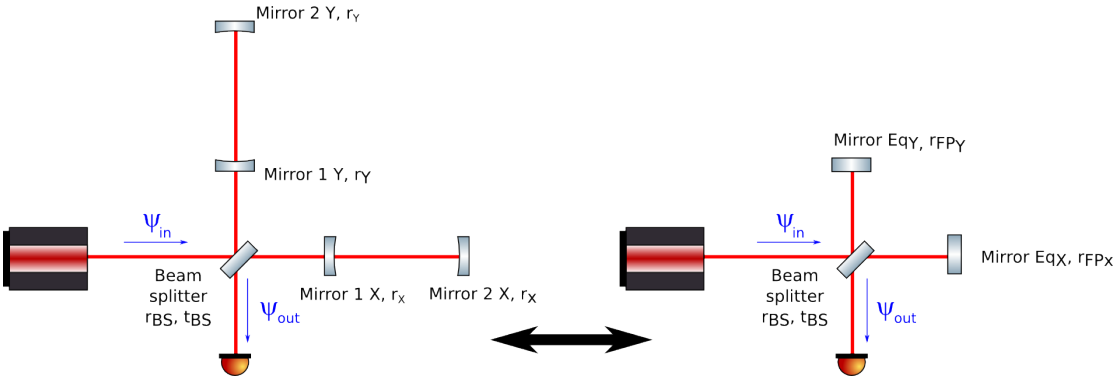

FIGURE 1.6: The interferometer with Fabry-Perot cavities is equivalent to a Michelson interferometer with complex reflecting coefficients

We can now deduced the response of the detector with respect to a gravitational wave:

$$\delta\tilde{P}_{out}(f) = \frac{P_0}{2} C sin(\phi_0) \delta\tilde{\phi}(f) \tag{1.68}$$

$$\delta\tilde{P}_{out}(f) = \frac{P_0}{2} C sin(\phi_0) \frac{4\pi}{\lambda} \frac{2\mathcal{F}}{\pi} \frac{L\tilde{h}}{1 + i(\frac{f}{f_{cav}})} \tag{1.69}$$

By comparison with the shot noise, we can show that the sensitivity is given by:

$$\tilde{h}(f) = \tilde{h}_{Mich} \frac{\pi}{2\mathcal{F}} (1 + i\frac{f}{f_{cav}}) \tag{1.70}$$

The sensitivity is then increased by a factor $2\mathcal{F}/\pi$, but is also filtered by the poles of the cavities.

Moreover, there is still room for improvement. We have seen that when the interferometer is set on the dark fringe no power is exiting from the detection port. All the power is reflected back to the input of the interferometer and is lost. In order to increase the power inside the interferometer, we can re-inject it by placing a mirror in front of the input port as shown in Fig. 1.7

1.6.6 Power Recycling (PR)

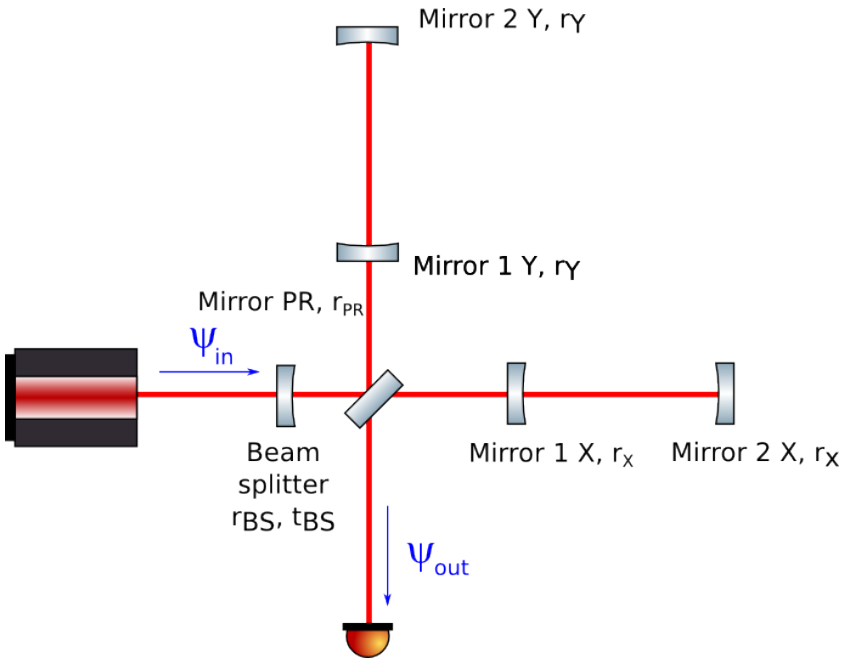

FIGURE 1.7: The Power Recycling (PR) configuration of the interferometer

In this Power Recycling (PR) configuration, the maximal recycling gain is given at resonance by:

$$G_R = \frac{t_R^2}{(1 - r_R \rho_{FP})^2} \tag{1.71}$$

We can then rewrite the sensitivity directly from Eq.1.70:

$$\tilde{h}(f) = \frac{1}{G_R} \tilde{h}_{Mich} \frac{\pi}{2\mathcal{F}} (1 + i \frac{f}{f_{cav}}) \tag{1.72}$$

The main effect of the power recycling mirror is to increase the power by the recycling gain, and thus to increase the sensitivity. The power recycling mirror is only seen by the fields common to the two arms, that are exciting the interferometer through the symmetric port. The differential signals, like the audio-sidebands created by a gravitational wave, are coming out the detector through the antisymmetric port. Then the power recycling mirror has no effect on the audio-sidebands.

1.6.7 Signal Recycling (SR)

By placing a mirror Signal Recycling (SR) before the output of the interferometer, we will affect the audio sidebands (hopefully from the gravitational waves) and we will be able to shape the frequency response of the detector. This will allow to increase the sensitivity in a particular frequency range, to improve the efficiency of the detection for specific signals.

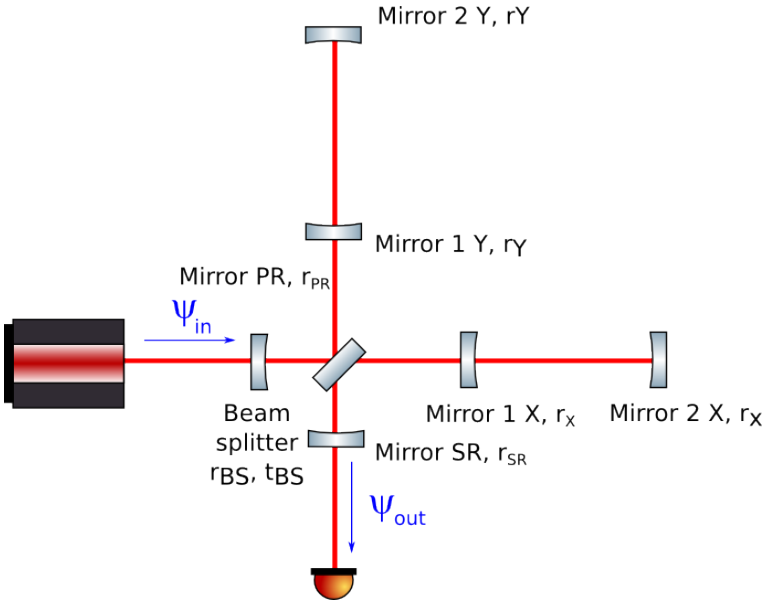

FIGURE 1.8: The Signal Recycling (SR) configuration

The full response of the dual recycled interferometer for the sidebands is then:

$$\psi_{out}(\omega_s) = -\frac{2t_S t_R}{1 - r_R R}\frac{t_i^2 r_e}{1 - r_i r_e}\frac{e^{i\phi}}{1 - r_s r_F P(\omega_s) e^{2i\phi}} \tag{1.73}$$

$$\frac{e^{-i\frac{\omega_s}{c}L}}{1 - r_i r_e e^{-2i\frac{\omega_s}{c}L}}\frac{2\pi}{\lambda} x_0 \psi_{in} \tag{1.74}$$

We have the complex coefficients:

$$r_{FP}(\omega_s) = \frac{r_i - r_e(1-L)e^{-2i\frac{\omega_s}{c}L}}{1 - r_i r_e e^{-2i\frac{\omega_s}{c}L}} \tag{1.75}$$

$$R = \frac{r_i - r_e(1-L)}{1 - r_i r_e} \tag{1.76}$$

The dephasing of the SR cavity will shape the detector response as presented in Fig. 1.9 [9].

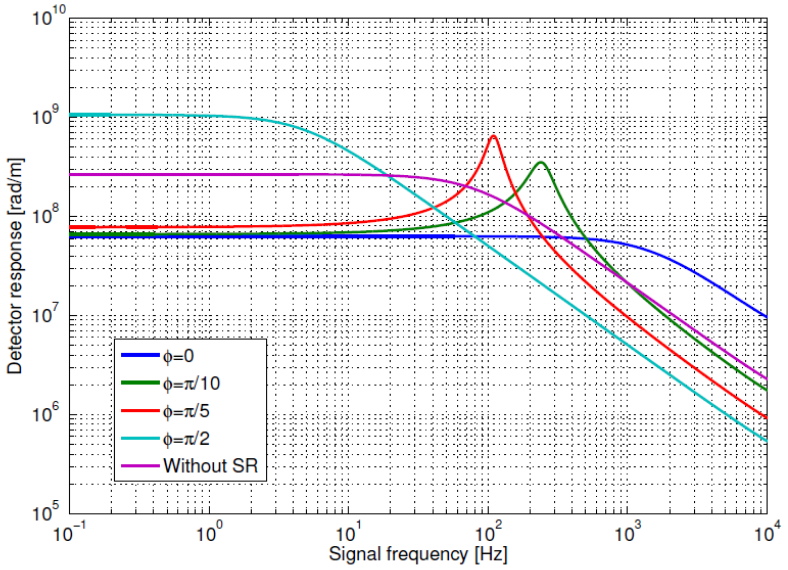

FIGURE 1.9: Response of a dual recycled detector to differential displacement as a function of the signal frequency for different positions of the Signal Recycling mirror [9].

1.6.8 Stability of the Recycling Cavitys (RCs)

The arm cavities are *stable*, that means that the resonance position of the fundamental mode is well separated from the high order modes through the different *Gouy phases* (see Appendix A) they have accumulated along the laser beam propagation. To have stable RCs, it would be necessary to have kilometer long cavities as well. Therefore the RCs in

Advanced Virgo have been chosen to be *marginally stable* for space reason and simplicity of the system (no additional focusing elements). However it means that the resonance position of any high order mode is close to the resonance position of the fundamental mode. If for any reason, some power of the fundamental mode is coupled to a high order mode, this mode can become resonant in the cavity. This is why the Advanced Virgo interferometer will be very sensitive to the optical defects that can occur inside the RCs for one side, and for the other side to the defects contained in the input laser beam at the level of the injection. Therefore, the subject of this thesis is motivated amongst others, as it will be explained in Section 1.9, by the necessity to provide a corrective system ensuring that the beam is properly matched into the interferometer.

1.6.9 Optical configurations among the network

In order to have an efficient worldwide detection network, three Advanced Interferometers are currently in construction or commissioning:

- the Advanced Virgo Interferometer, located in Cascina, near Pisa (Italy) is a three-kilometer long Michelson interferometer with a dual recycling configuration (see Fig. 1.10). The construction will be achieved in 2015 and the first data acquisition campaigns, called *Science Runs*, are expected to start in 2016.
- the LIGO Livingston Observatory, located near Baton Rouge (LA) in the United-States, is a four-kilometer long Michelson interferometer with a dual recycling configuration. Unlike Advanced Virgo, the recycling cavities have been chosen stable and the instrument will be less sensitive to the optical defects. The construction is already done and the first locks of the full interferometer have been achieved. The first Science Runs are expected for the next year (2015).
- the Handford LIGO Observatory, located in the state of Washington, in United States, exhibits the same configuration as the Livingston Interferometer, but its planning is shifted of few months forward.

LIGO will probably install a complementary detector in India, starting in 2018, with the first runs planned in 2020. Another detector, KAGRA, is currently in construction in Japan. It will benefit from different environmental conditions, being built underground, and from different technologies with notably cryogenic systems. This network of detectors will allow to reach good localization capabilities and sky coverage [4].

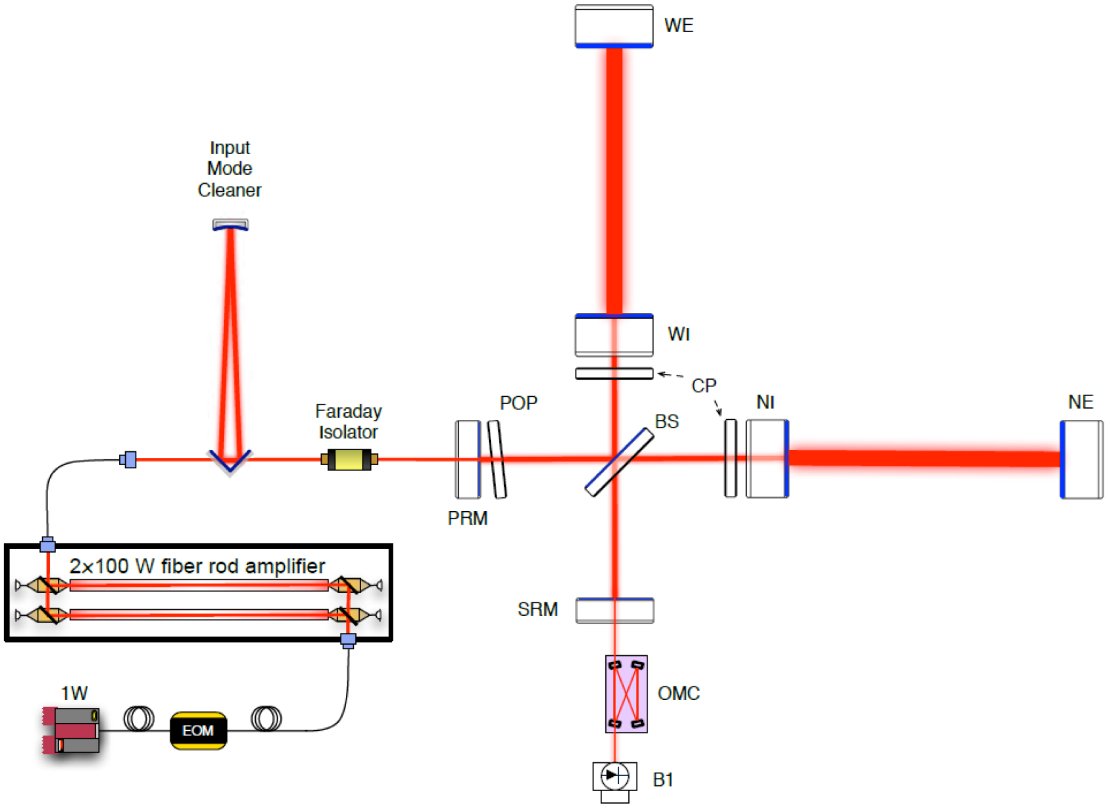

FIGURE 1.10: Simplified layout of Advanced Virgo: main optical elements

1.7 Description of some subsystems

Simply building an interferometer in dual recycling configuration as previously exposed does not ensure to reach the expected sensitivity. Indeed the detection of a gravitational wave is a fight against the noise sources, coming from the environment of the detector and from the detector itself. Among the environmental noise sources, we can distinguish the Newtonian noise, associated with gravity gradient variations; the seismic noise and the electromagnetic noise, from the natural or human activity. The technical noise sources in the interferometer are the scattered light and the control noise. In addition to the shot noise, when all the technical noises are under control, the main noise sources are the seismic noise and the thermal noise. Different subsystems are ensuring that the interferometer is kept under control and that the impact of the noise sources is minimal.

1.7.1 Prestabilized laser

The continuous wave high power laser system will deliver about 175 W in the fundamental mode (TEM_{00}) at the stage of the injection. The frequency will be prestabilized

on a reference cavity and it will be controlled in amplitude. The beam jitter and the beam geometry will be cleaned by two short mode cleaner cavities.

1.7.2 Injection

After the laser beam has been produced by the pre-stabilization system, the injection ensures that it is properly adapted in size, position and power and has the required noise properties (frequency stabilization, power stabilization and beam jitter control) [10] to be sent to the interferometer. The general scheme of the injection is given in Fig. 1.11. The main elements of this subsystem are:

- the Electro-Optical Modulator that provides the five modulation frequencies for the interferometer control
- the Faraday isolator to isolate the laser from the light reflected back from the interferometer
- the Input Power Control that provides the required power during the lock acquisition
- the Input Mode Cleaner (IMC). This is a triangular cavity (144-m long) ensuring the purity of the fundamental mode TEM_{00} by filtering the incident beam. It also reduces the amplitude and pointing fluctuations of the beam
- the reference cavity, that is a smaller triangular cavity ($\sim$ 30 cm), used to stabilize the laser frequency at the begin of the lock acquisition
- the Mode Matching Telescope (MMT) ensures the position and size of the beam are adapted to the interferometer. It will greatly help in reducing the mismatch due to the focus aberration (beam divergence).

1.7.3 Suspensions

1.7.3.1 Seismic noise

The seismic motion of the ground affects the test mass position through:

$$\tilde{x} \simeq \alpha/\nu^2 \tag{1.77}$$

with the coefficient α depending on the site. For Cascina, α is about 10^{-7} m.$\sqrt{Hz^3}$. To have a good sensitivity, the seismic noise has to be attenuated by at least 10 orders of

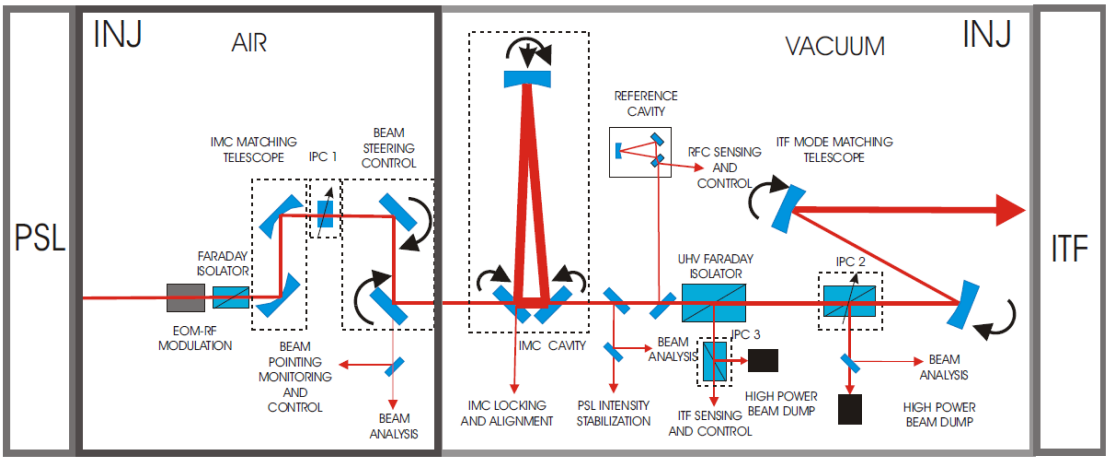

FIGURE 1.11: Scheme of the main elements of the injection subsystem

magnitude. All test masses, as well as some benches of the injection and the detection, are then suspended to Superattenuators (see Fig. 1.12). Based on an inverted pendulum with three legs, a superattenuator provides an attenuation at low frequencies (> 1 Hz), leading to have a "free fall" test mass above its eigen resonant frequency. This will dump the seismic noises. The pendulum chain has a height of 8 m and provides the required attenuation starting from about 4 Hz. However, the Earth curvature makes the pendulum non parallel to each other (3.10^{-4} rad for the 3 km long cavities). Therefore, the vertical motions of the suspensions necessarily couple to the horizontal motions, and have to be attenuated as well. This is the role of the seismic filter chain: the suspensions are made of several stages of passive and active filters, that are acting like oscillators.

1.7.3.2 Thermal noise

Thermal noise occurs at different level in the suspensions: in mirror substrate and coating and in the suspension wires. It adds an a random motion to the test masses. We can distinguish:

- the thermal noise in the pendular motion of the test mass and the suspensions, that has a resonant frequency at 0.6 Hz and that is limiting the sensitivity between 3 and 50 Hz. It can be minimize by adequately choosing the suspension wire material (for example silica) with a quality factor as the high as possible.
- the mirror thermal noise, limiting the sensitivity between 50 and 200 Hz.
- the vibration modes of the suspension wires, called violin modes, have some resonant frequencies around 300 Hz.

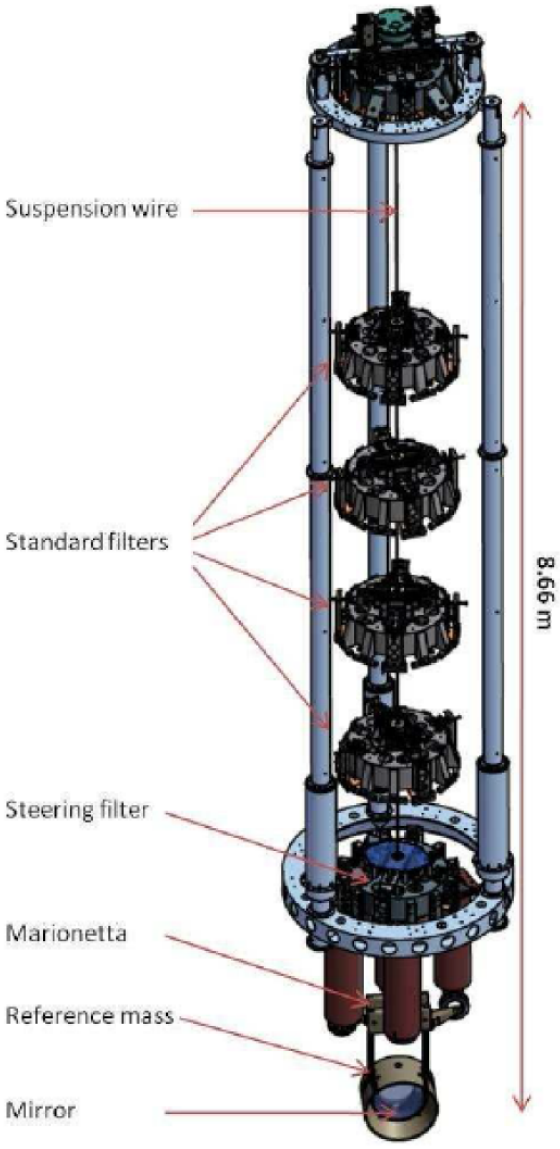

FIGURE 1.12: The Virgo superattenuator: the mechanical filter chain adopted to attenuate seismic vibration in the detection band, the three-leg inverted pendulum, the filters and the payload that contains the test mass are well visible.

1.7.4 Vacuum system

The whole system is placed under vacuum, to avoid the phase noise due to variations of the air refraction index. The vacuum system is divided in two parts: the tubes and the towers. The vacuum in the tubes has a very high quality ($2.5\ 10^{-9}$ mbar), ensured by various vacuum pumps. A serial of baffles, to trap the diffused light and reduce the phase noise is installed all along the tubes. The ten towers contained the superattenuators and the vacuum quality is lower to afford the presence of electronics. The link between the towers and the tubes is made via cryotraps, that retains the residual contaminants (notably water) inside the towers.

1.7.5 Control of the interferometer

The control of the positions (longitudinal and angular) of the test masses and the bench is made possible thanks to the information delivered by the Radio-Frequency (RF) on the laser beam. Five modulation frequencies will be needed in AdV, three for the interferometer control, one for the IMC cavity control and one to facilitate the lock acquisition of the interferometer.

1.7.6 Detection

The aim of the detection system is to extract the gravitational wave signal from the signal going out the interferometer through the anti-symmetric port, that is composed of the dark fringe and the auxiliary beams. The High Order Modess (HOMs) contained in the dark fringe are filtered by a so-called Output Mode Cleaner (OMC) to minimize the contrast defect and maximize the detector sensitivity.

1.7.7 Mirrors

The main substrates are the four test masses (Input Test Masss (ITMs), End Test Masss (ETMs)), and the Power and Signal Recycling. The other substrates in the main cavities are the beam splitter, the IMC end mirror and the compensating plates for the TCS.

The mirrors are 35 cm diameter fused silica substrates with 20 cm thickness and a flatness better than 0.5 nm Root Mean Square (RMS). The maximum substrate absorption is of 3 ppm/cm and the maximum coating absorption is 2 ppm. The Radius of Curvature (RoC) of the input test masses is of 1420 m and the RoC of the end test masses is 1683 m. The recycling mirrors have about 1430 m of curvature. The RoC after polishing will not be better than $\pm$ 10 m while the optical simulations show that $\pm$ 2 m are needed for the ITM and ITM and $\pm$ 8 m for the RC mirrors. This already shows that complementary systems will be needed to reach the specifications.

1.7.8 Thermal Compensation System (TCS)

This is the aim of the TCS subsystem, that will sense and correct the aberrations in the core optics. The main corrective devices are presented in Chapter 2.

Science Run	Start	End	Objectives or Changes after the run
VSR1	05/2007	10/2007	Scattered light mitigation TCS installation Mirror magnets strength reduction Start of the Virgo + installation
VSR2	07/2009	01/2010	
VSR3	07/2010	10/2010	High Finesse Fabry Perot cavities Monolithic suspensions Decreased performances due to large ROC asymmetry of the end mirrors
VSR4	06/2011	09/2011	Better performances thanks to thermal compensation system

TABLE 1.1: Science runs of Virgo and Virgo+ with some noteworthy steps concerning the thermal compensation systems

1.8 From Virgo to Advanced Virgo

The first Virgo Science Run (VSR) started on May 18^{th} 2007 and the last science run (VSR4) ended September 3^{rd} 2011. Table 1.1 gives some highlights on the main steps towards the final sensitivity.

During the commissioning, some problems concerning the optical aberrations has been faced in the arm cavities and the use of the thermal compensation systems greatly improved the performance of the interferometer (see Chapter 2). No gravitational wave was detected neither in Virgo or LIGO but the results extracted from the data analysis of the Science runs have allowed to set upper limits on astrophysical models. With the reached sensitivity, the number of observable sources was a few per year in the best optimistic case. In order to increase the volume of observable sources by a factor 1000, the sensitivity has to be increased by a factor 10: this is the advanced generation of detectors. The optical configuration of Advanced Virgo, with respect to Virgo +, is:

- addition of a signal recycling cavity: the Advanced Interferometer will be dual recycled to be able to shape the sensitivity curve for astrophysical sources
- the beam size on the test masses is enlarged to reduce the thermal noise in the mid-frequency range
- the cavity finesse is increased: from $\mathcal{F} = 150$ (Virgo +) to $\mathcal{F} = 443$
- the power at the input of the injection is increased by a factor 5: the power entering the interferometer is 125 W after the IMC
- the radiation pressure becomes a limit in the arm cavities at low frequencies

- the losses will reach 100 W around the mirrors and will create diffused light despite the better coatings. New baffles will be installed to reduce the phase noise.

Then the design sensitivity curve of Advanced Virgo is presented in Fig. 1.13.

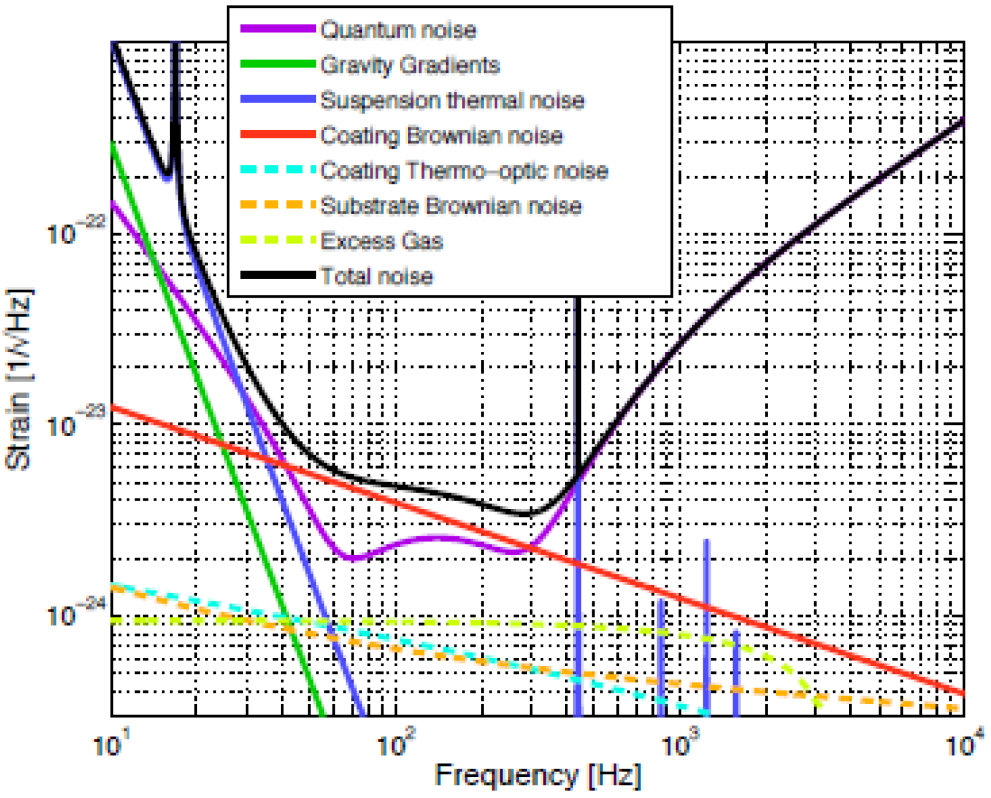

FIGURE 1.13: Contribution of the noise sources to the design sensitivity of Advanced Virgo

1.9 Need of adaptive optics for the mode matching correction

Since the laser power will dramatically increase in the next generation of detectors, the thermal effects, that are present in many optical components, will occur in different parts of the interferometers. The induced wavefront distortions will have an impact in the main cavities, but also on some subsystems. If not compensated, they can be the source of a noise that limits the performance of those detectors [11]. With the stringent requirements on detector sensitivity, their correction in real time is one of the main challenges for the next years.

First, the deformations generated by the thermal effects in the mirrors are presented. This is particularly important for us, since our corrective device is based on a thermal actuation (see Chapter 3). Then, we review the main consequences of the thermal effects in Advanced Virgo and we highlight the need of a adaptive optics mode matching correction system in some strategic places of the detector.

1.9.1 Basics of thermal effects

The thermal effects happen when a laser beam at high power is in interaction with an optical element. A small amount of the laser power is absorbed by the coating and/or by the substrate if it is going through it, and leads to the appareance of a temperature gradient in the component. The analytical study of the temperature field in both mirror substrate and coating heated by a laser beam has been conducted by P. Hello and J.-Y. Vinet [12, 13]. In the typical case of the Virgo main cavity configuration, the theoretical increase of temperature is 7 K for an absorption of 1 W in the coating (i.e. few ppm) and is 2 K for an absorption of 1 W in the Fused Silica (FS) substrate.

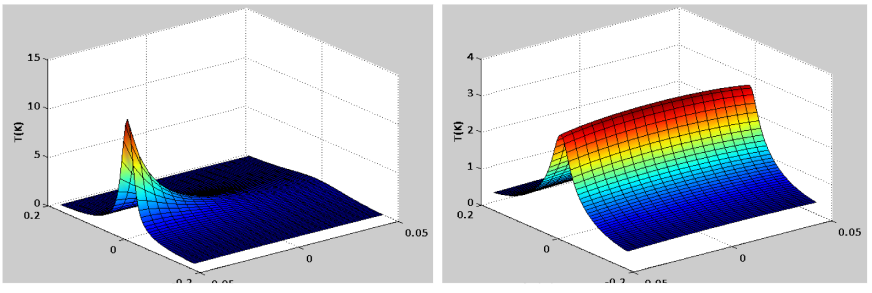

FIGURE 1.14: Analytical temperature field generated by a laser beam of 21.5 mm radius heating a FS cylindrical substrate of 0.2 m radius and 0.1 m thickness for 1 W absorbed (a) in the coating and (b) in the substrate.

Thermal Loss Mechanism	**Relative strength in Silica**
Thermal lensing	1
Thermal expansion	0.06

TABLE 1.2: Relative strengths of thermal deformation in fused silica being normalized with respect to the thermal lensing effect

Considering a laser beam going through a substrate of thickness d, the initial optical path is given by:

$$S_0 = nd \tag{1.78}$$

The increase of temperature ΔT along the beam direction will induce a change in the optical path [14, 15]:

$$\Delta S_0 = n\Delta d + d\Delta n = \Delta S_{TL} + \Delta S_{TE} \tag{1.79}$$

The first effect is the *thermal lensing* effect: the local variation of the refraction index n with respect to the temperature T generates an increase of the optical path difference:

$$\Delta S_{TL} = \int_0^d \Delta n dz = \frac{dn}{dT} \int_0^d \Delta T dz \tag{1.80}$$

with $\frac{dn}{dT}$ the thermooptic coefficient, that is constant over a given temperature range.

The second effect is the *thermal expansion* of the substrate along the optical axis through the thermo-elastic deformation:

$$\Delta S_{TE} = \alpha(1+\nu)n \int_0^d \Delta T dz \tag{1.81}$$

with α the thermal expansion coefficient and with ν the Poisson coefficient. In the previous equations, we neglect the stress tensor and stress optical coefficients relative to the beam polarization.

The Optical Path Length (OPL) along the beam direction is then given by the formula [15]:

$$OPL = S_0 + \Delta S_{TL} + \Delta S_{TE} \tag{1.82}$$

$$OPL = \int_d (\Delta T[\frac{dn}{dT} + \alpha(1+\nu)n] + n)dz \tag{1.83}$$

The relative magnitude of these effects for the FS substrate is given in Table 1.2: in this case the thermal lensing is the dominant mechanism.

For the Advanced Virgo Fabry-Perot cavities, with 125 W input power and a arm cavity of finesse 443, the optical path increase due to substrate and coating thermal lensing in a test mass is about 0.8 μm, corresponding to a focal length of 5 km. The thermo-elastic deformation of the faces will be about 50 nm [10].

The main part of these thermal effects is axis-symmetric but the thermal effects can lead to non uniform optical path distortions due to asymmetry in the heating pattern and absorption inhomogeneities in the substrate and/or coating. This will produce high spatial frequency wavefront deformations in the laser beam [16] that are not easily predictable. These effects can also change over time.

1.9.2 Thermal effects in the ITF

1.9.2.1 In the arm cavities

When a beam circulates in a Fabry-Perot cavity, a small part will be absorbed in the coatings generating a temperature gradient inside the substrate. This will slightly change the RoC by thermal expansion. The mode of the cavity will then be modified. In the example of the Advanced Virgo arms, where there will be much more power circulating with respect to Virgo (from 20 kW to 700 kW), this effect becomes relevant: the cavity will become less concentric and the spot size on the mirrors will decrease.

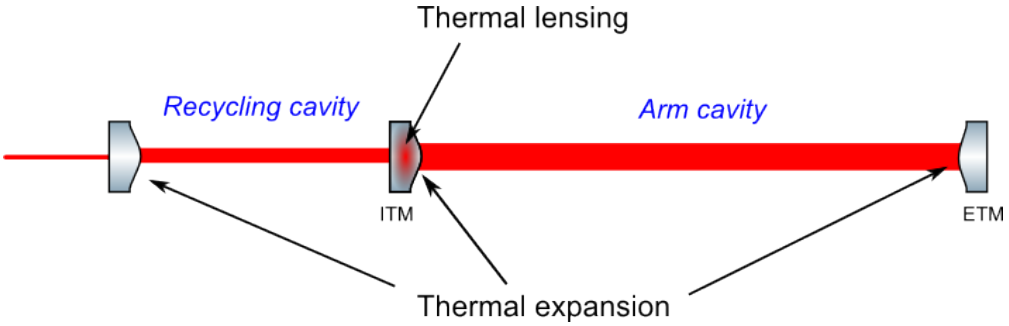

FIGURE 1.15: Thermal expansion in an Advanced Virgo arm due to absorption in the input and end test masses as well as in the recycling cavity. The effect has been dramatically amplified in the picture. Thermal lensing is experienced by the beam inside the recycling cavity.

An immediate consequence is that the input beam will no longer match the cavity mode. This mismatching will generate power coupling to the HOMs that might become resonant in the cavity and lead to power losses. The stability of the arm cavities will help to limiy this effect. If the thermal expansion is different in the two arms, the contrast defect will increase on the dark fringe. As a consequence, the requirement for Advanced Virgo is to keep the RoC value of the test masses at $\pm$ 2 m with respect to the design, and the

asymmetry between mirrors lower than 5 m.
Moreover, the amplitude of the thermal lensing in the ITMs will increase by more than one order of magnitude with respect to Virgo. This effect is not seen by the arm cavities, thanks to the coating position, but will affect the recycling cavities (see Fig.1.15).

1.9.2.2 In the recycling cavities

The recycling cavities are affected by both the thermal expansion and thermal lensing. The latter changes the cavity mode, leading to decrease the matching of the fundamental mode from the injection with the interferometer. As previously seen, the recycling cavities of Advanced Virgo are not stable. It means that the position of the high orders modes is very close to the resonance in the recycling cavities. So, when thermal deformation occurs, the distortions in the fundamental mode lead to appareance of high order modes that can potentially become resonant and thus produce power losses.
For the carrier, it is not a problem: being resonant in the arms, the stability of the arm cavities is transposed to the recycling cavities. However, there is mismatch created between the arm cavity mode and the output mode cleaner mode. Moreover, the mode-healing effect can influence the transfer of the GW audio sidebands to the SRC output.

But the RF sidebands used for the control are rejected by the arm cavities. Thermal deformations decrease the recycling cavity gain and finally decrease the sideband power. The recycling gain above 50% for the sidebands is required in order to afford a good control of the interferometer. Optical simulations [10] have shown that the total distortions have then to be lower than 2 nm RMS for both common and differential optical path length distortions (see Fig.1.16). An adaptive optics system, with a high order mode correction capability, is necessary to reach these specifications.

Thermal effects have then a huge impact on the main cavities of the interferometer, through the fundamental phenomena discussed before: the thermal lensing and the thermal expansion. To keep them under control, some systems have been especially developed. They are briefly presented in Chapter 2.

1.9.3 Matching sensitive systems

Actually, it is not only the core optics of the Fabry–Perot cavities of gravitational wave detectors that require adaptive optics corrections. Indeed, performance of some parts of the detector are critically linked to the matching efficiency and, besides being sensitive

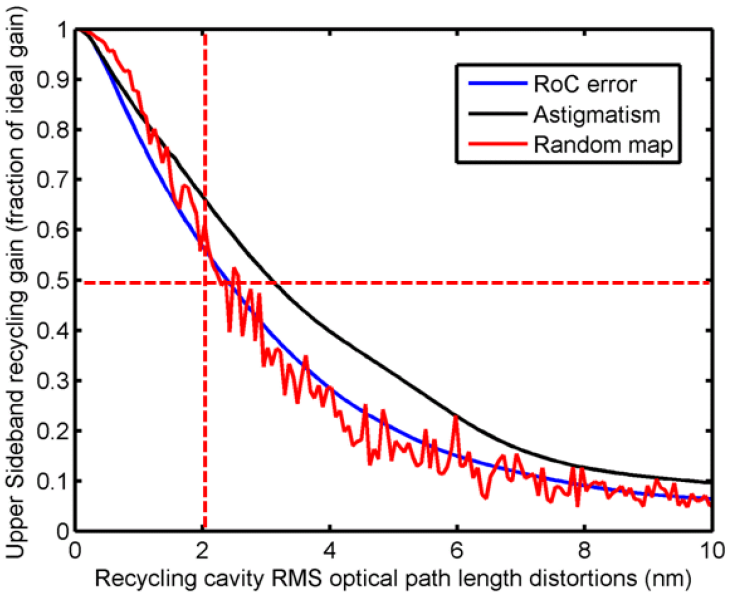

FIGURE 1.16: Recycling gain of a RF sideband as a function of the optical defects amplitude in the recycling cavity. The curves shows the dependence of recycling gain on three types of distortions: RoC, astigmatism and general polishing errors. In order to ensure a good control of the cavities, the gain has to be at least 50% of the ideal gain, which corresponds to aberration amplitude below 2 nm RMS [10].

to the "cold" defects, these systems will also likely suffer from thermal effects. For them an adaptive optics system is also required, to be able to maintain permanently a optimal matching into the various cavities.

We identified three systems for which the control of the matching is fundamental: at the stage of the beam injection into the interferometer, into the Output Mode Cleaner at the detection stage and generally for matching into squeezing systems.

1.9.3.1 At the injection

Important thermal effects have been already observed in Virgo in the injection system. In Advanced Virgo the power will increase by almost a factor 5 and will reach 125 W at the interferometer input. The thermal effects are then expected to occur in the different stages, in particular in the Faraday isolators and at the output of the IMC. Thermal effects in the last system will affect the laser beam coupling onto the interferometer, leading to loss of power coupled into the interferometer and then to a direct loss in the detector sensitivity for frequencies above 100 Hz. According to [11], the typical power losses due to nonperfectly matched cavities, including the mode matching into the interferometer was typically more than 15% in Initial Virgo. With an adequate correction, the power stored in the arms would have been increased by 10%, corresponding to an

improvement of about 3% in the BNS range (see Section 1.1). Considering 1 ppm of absorption in the IMC with 180 W of input power, it has been estimated that the mismatch will reach 10 % when the coupling efficiency is required to be higher than 99% at the input of the interferometer [10]. Fortunately, the main part of the mismatch will be composed of defocus, that will be managed by the Mode Matching Telescope (MMT) with optics position remotely controlled by translation stages. But the astigmatism produced by the IMC output mirror and the subsequent high order modes will still need to be corrected to reach the required coupling into the interferometer.

1.9.3.2 At the detection

As seen previously, the goal of the OMC is to extract the dark fringe beam from the output signal of the interferometer. The dark fringe signal will be read in DC, so the OMC has to filter the high order modes from the carrier but also from the RF sidebands. The high order modes and the sideband fields do not contribute to the signal but increase the shot noise [17, 18] through the contrast defect. The light back-scattered by the cavity should be low to avoid to add any phase noise to the sensitivity [19]. A matching equal or better than 99% [10] has then to be ensured with the OMC, mostly controlled by a MMT. However, as for the injection, it is not able to correct for high order modes, especially astigmatism, that is foreseen to be the main power contributor to the dark fringe [20]. The high order mode content is likely to be time varying with the thermal effects occurring in the main cavities.

1.9.3.3 Squeezing

Assuming the thermal effects and all technical noises are under control, the main limiting noise source of the interferometer is the quantum noise (see Section 1.6.2). In order to improve the overall detector sensitivity and to go beyond the SQL, it is foreseen to employs squeezed light. The Geo600 and LIGO collaborations have already observed an improvement up to 3 dB by injecting squeezed light into the dark port of the interferometers [**?**]. This corresponds to an improvement of a factor 2 for h amplitude and a factor 8 for the detection rate.

However the squeezing efficiency depends strongly on the mismatching losses between the various cavities that are on the squeezed light path [21]. For example, in Advanced Virgo, the optical losses are expected to be about 24% overall the squeezing system (see Fig.1.17 (a) [22]). This will limit the squeezing to 6 dB in the best case scenario. With a system providing an optimal coupling into the interferometer and into the OMC

for example, the losses could be reduced to about 11%. The mismatch correction will improve the squeezing by additional 2 dB (see Fig. 1.17 (b)).

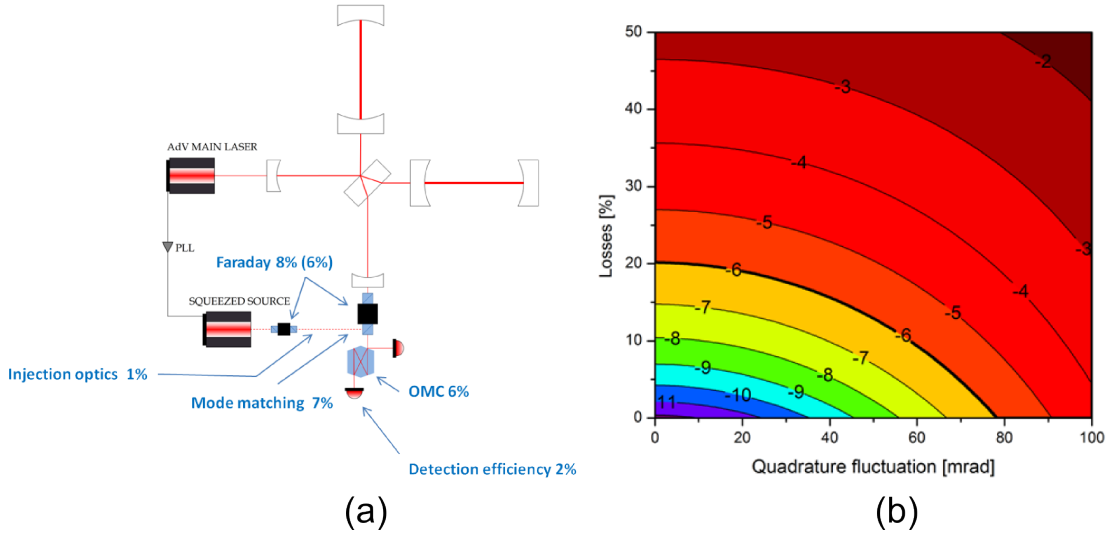

FIGURE 1.17: [22] (a) Estimated losses in the different parts of a squeezing system for Advanced Virgo . (b) The achievable squeezing factor depends both on the optical losses an on the phase jitter noise. If the beam jitter fluctuations are kept around 20 mrad, a reduction of the mismatch from 24% to 11% will improve the squeezing by 2 dB.

1.10 Conclusion

In Advanced Virgo, the whole interferometer will be very sensitive to all defects that may be present in the cavities due to static or thermal effects with the increase of laser power. The crucial importance of compensation for axis-symmetric and non-axisymmetrics defects has been enhanced since the Marginally Stable Recycling Cavities (MSRC) solution has been adopted. In order to reach the design sensitivity, the optical path length distortions have to be corrected in many points of the interferometer, in the arm cavities and in the recycling cavities, with the help of compensating systems that are briefly presented in Chapter 2.

Moreover, the statics or time varying optical defects will also have a great impact on some specific subsystems, in particular through the matching into various cavities. An appropriate system, with the capability to correct high order mode aberrations in real time, will therefore provide a great help in risk mitigation to reach the Advanced Virgo sensitivity.

The goal of this thesis is to propose an adaptive optics system for mode matching correction that can be used in the different systems of the gravitational wave detectors. In particular, we will focus on the requirements for the matching into the interferometer at the injection stage. The work is centered on the design and proof-of-principle tests of such a mode matching correction system.

Chapter 2

Adaptive Optics Systems for Mode Matching

We saw in Chapter 1 how crucial it will be to maintain a high matching in the resonant cavities of Advanced Virgo. In particular the matching into the main cavities at the last stages of the injection, as well as into the detection filter cavities will be determinant to reach the target sensitivity. Ensuring the matching into the filter cavities of a squeezing system is also necessary to meet the requirements. In order to perform such matching, we need a corrective device compatible with the various constraints on vacuum, noise coupling and high optical quality for integration in the GW interferometer environment. Furthermore, the matching must be kept under control even with time varying aberrations, as it is the case with the thermal aberrations in the interferometer.

Since the beginning of the studies on interferometric GW detectors, thermal aberrations are foreseen to be a source of problems and the idea to passively or actively compensate them was present very early [12]. In the last years, different systems have emerged to face troubles in the detectors and new prototypes are under development in anticipation of the next generations. After a review of the GW interferometer environmental constraints, we present some commercially available adaptive optics technologies. We determine what limits their integration into the interferometer environment. Then we focus on the existing systems for the GW detectors. Finally, given that a full adaptive optics system for the mode matching is still missing, we show how the device we propose is able to reach our stringent requirements, benefiting from being at the crossroad of the adaptive optics devices and GW device families.

2.1 General description of an adaptive optics system

Along its propagation through an optical system, a light beam interacts with several optical components or media that can introduce static or time varying aberrations in addition to the expected transformations. The term *aberration* is here understood in the large meaning of any deviation from an ideal Gaussian beam. The signal at the output can therefore suffer from distortions or information losses. To correct the defects accumulated through the propagation, a system of adaptive optics is composed of three elements: a sensor to detect the aberrations, a signal processor to compute the correction and a corrective device placed along the beam path to apply the correction (see Fig.2.1). Unlike a static or a passive compensation, the system is able to respond to situation changes by controlled adjustments of the correction (feed-back).

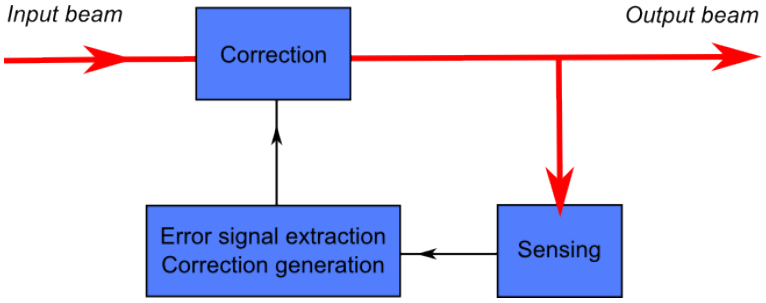

FIGURE 2.1: General scheme of an adaptive optics system: the beam aberrations are detected by a sensor that generates an error signal which is processed to compute the actuation. The correction is then applied by the corrective device.

The adaptive optics technique was established during the 20^{th} century to improve the quality of the images received by the ground-based telescopes. The principle is to correct in "real time", that means with a high frequency rate, the phase deformations introduced by the atmosphere in order to retrieve the diffraction limit of the optical instruments. More generally, an adaptive optics system has to correct in real time any deformation that appears in an optical system and that reduces its performance. Some authors draw a distinction between adaptive optics, active optics and active compensation, according to criteria of time-scale, degrees of freedom, amplitude, design... Here *adaptive optics* will be the generic term embracing all these techniques.

The simplicity of the adaptive optics systems, as well as the improvements along with decreasing prices of the technologies, are ensuring them a large success. Recently adaptive optics have found a large range of new applications in ophthalmology [23] [24], microscopy [25], astronomy [26] and laser fields [27] [28]. This diversity leads today to a lot of different corrective devices, which size varies from the micrometer to the meter scale, and as many sensing and control techniques. Design specifications are highly

dependent on the application, so we will focus our study to the systems potentially compatible with our requirements.

2.2 The control of aberrations in optical cavities

In the context of the GW interferometers, the optical aberrations are coming from both static and dynamic defects of the optics along the beam path. The statics defects may be due to the surface defects, from polishing or coating, to the substrate inhomogeneities or to misalignments (distortions from the lenses, clipping). Some optical benches and optics are suspended and beam misalignment or position changes with respect to the optical elements may create dynamic defects. Power fluctuations will also modify the thermal effects. Several adaptive optics systems will then be necessary to ensure that the beam mode is preserved all along its propagation through the system and is well adapted to the resonant cavities. For example, in a simple cavity system, the preservation of the fundamental mode can be made in two complementary directions : correction of the incident beam aberrations before it is entering the cavity and correction of the defects of the cavity itself. These are respectively referred as *mode matching* and *in situ* corrections (see Fig.2.2).

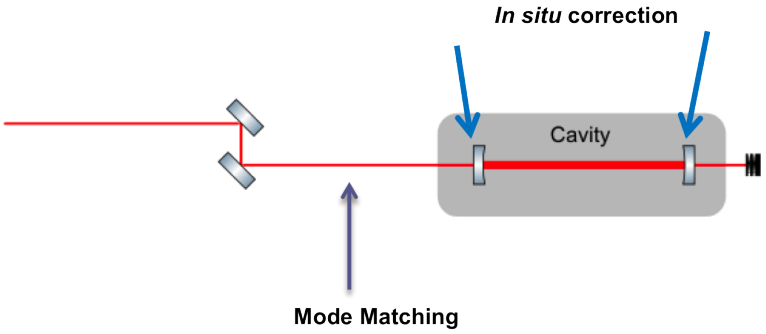

FIGURE 2.2: Adaptive optics can act at two stages for a simple resonant cavity: adaptation of the beam to the cavity through the mode matching and *in situ* correction of the mirror defects

2.2.1 In-situ corrections

The aim of the *in-situ* corrections is to correct statics or thermal defects occurring inside the cavity. For example, surface defects of the mirrors can convert the fundamental mode into high order modes, increasing the round-trip losses and the scattered light [29]. At high power, these defects together with substrate inhomogeneities may also become sources of non-Gaussian repartition of the heat inside the substrates, leading to "hot

spots". With an appropriate correction, the power losses may be reduced and the stored power inside the cavity may increase.

Furthermore, as discussed before in Chapter 1, the thermal lensing changes the cavity geometry. It can be an important source of mismatch, changing the fundamental resonant mode properties and then reducing the overlap integral (Eq. 2.1) with the incident beam. A correction that recovers the original mirror RoC and compensate the eventual asymmetries will help in maintaining a cavity geometry close to the initial one even at high power. Some systems presented thereafter are dedicated to *in-situ* corrections in the main cavities.

2.2.2 Mode Matching

The *mode matching* correction consists in the correction of the beam *before* its injection into the cavity that is supposed to be perfect. The aim is to ensure that the maximum of power is coupled into the cavity set to the resonance of its fundamental mode. The beam has to match the amplitude and phase distributions of the resonant mode of the cavity: the waist size and waist position have to be adapted to the cavity geometry. Moreover the high order modes introduced by the static or thermal aberrations have to be canceled or reduced. The mode matching η is defined as the overlap integral of the complex field ψ_i of the incident beam with the complex field ψ_0 of the fundamental mode of the cavity.

$$\eta = \left(\frac{|\int \psi_i \psi_0^* dS|^2}{\int |\psi_i|^2 dS \int |\psi_0|^2 dS} \right)^2 \tag{2.1}$$

The power stored in a cavity at the resonance P_{cav} can then be rewritten [30] (see Eq. 1.50) :

$$P_{cav} = G'_{cav} P_i \tag{2.2}$$

with P_i the input power and G'_{cav} the gain of the cavity:

$$G'_{cav} = \eta \frac{1 - \mathcal{L}_i - r_i^2}{(1 - r_e r_i)^2} \tag{2.3}$$

where r_i, r_e are respectively the reflection coefficients of the input and end mirrors, $\mathcal{L}_i$ the energy loss due to absorption and scattering in the input mirror and G_{cav} is the cavity gain.

Coupling to high order modes The interaction with a cavity will lead to split of the input field ψ_i into the fundamental mode for one side and the high order mode content

in the other side. Indeed, while the fundamental mode resonates in the cavity, the aberrations, including misalignment, gain an additional phase shift, called *Gouy phase*, making them rejected by the cavity [31]. This can be understood through the projection of ψ_i into the mode basis generated from ψ_0. In Appendix A the demonstration of the coupling to specific modes is given for different examples of misalignments.
We can then simply write this separation in two parts as:

$$P_i = P_0 + P_a \quad \text{with} \quad \begin{cases} P_0 &= \eta P_i \\ P_a &= (1-\eta) P_i \end{cases} \tag{2.4}$$

with P_i is the power of the fundamental mode at the input of the cavity and P_a the power of the aberrations that will be reflected. It is straightforward that measuring P_a in the absence of internal losses will give the amplitude of the mismatching at the input of the cavity. Moreover the accurate determination of the mode content reflected by the cavity will directly inform on the aberration nature.

The aim of our system will be to improve the matching of an incident beam into the cavity, using an error signal from the cavity itself. A corrective device, a sensing method and a control scheme are then needed to create a complete adaptive optics system. In order to find a corrective device that is suitable for an integration in a Advanced Gravitational Wave Detector environment, we now review the requirements.

2.3 Requirements for a Mode Matching system

The control of noise sources in a gravitational wave detector environment, as previously demonstrated in Chapter 1 is a particularly sensitive subject. Before integrating a new device on any bench of the interferometer, one has to be sure that is not introducing noise at any level: diffused light, acoustic noise, electronic noise,... So the adaptive system, especially the corrective device that will be in the laser beam path, has to be compliant with very high requirements on optical quality and on system integration. For example, an adaptive system placed on the suspended injection bench in Advanced Virgo:

- has to be able to sustain high power laser (up to 100 W)
- must be polished and coated with a high precision, compatible with the surface quality requirements of the other passive optical components present in the beam path:
  - the surface roughness has to be lower than 0.1 nm

  - the flatness better than $\lambda/20$

- has to be high vacuum compatible (10^{-6} mbar)
- must not be a source of noise (electronic, magnetic, mechanical...)
- can act over long time scales. The actuation frequency is not a key criterion as the thermally induced aberrations are slowly varying ($\sim$ 10 mHz).

The requirements for the detection bench would be similar, with in both cases the constraint to ensure a matching better than 99%.

2.4 Corrective devices commercially available

The two main families of standard corrective devices are the Deformable Mirrors and the Spatial Light Modulators. The Spatial Light Modulators are used for high resolution phase correction with technologies that allows to reach a spatial resolution even better than few hundreds of nm [32] with an amplitude of actuation about λ. The residual defects are then very thin. However the inherent low damage threshold (few Watts) made them unsuitable devices for our high continuous power application.

2.4.1 Deformable mirrors

The deformable mirrors can be classified in two types: segmented mirrors and continuous shape mirrors. The segmented mirrors are often used for large scale mirrors, to reach a good optical quality and to reduce the weight of the system. At the opposite side of the scale, the Micro Electro Mechanical mirrors achieve a very high spatial resolution. But the segmented mirrors are unsuitable for our application: the mirror edges may generate diffraction effects. Furthermore, the Micro Electro Mechanical mirrors are not adapted to high power laser beams (damage threshold around few Watts). Different technologies are today commercially available for the continuous shape mirrors. They can be briefly described as following:

Stack mirrors The Piezoelectric Deformable Mirrors or Stack Array Mirrors were widely used technologies in adaptive optics. A thin reflective plate (Fig.2.3) is deformed by contact with piezoelectric actuators. Piezoelectric actuators are composed of a stack of piezoelectric disks for which their thickness varies according to electric field applied. This technology is today less employed due to some defects: high voltage required for common correction, high inter-actuator spaces and hysteresis effects. The

damage threshold could be high but the mirror is producing 1/f noise that will introduce mechanical vibrations on a suspended bench.

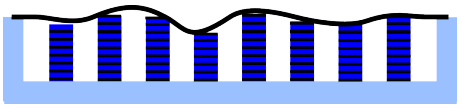

FIGURE 2.3: Schematic section of a stack mirror: the piezoelectric actuators (black and blue stripes) are mechanically deforming the reflective plate (in black).

Mono-morph and bi-morph mirrors Based on the same effect as the Piezoelectric Deformable Mirrors, bi-morph mirrors (Fig.2.4) are constituted of two piezoelectric plates bonded together between two glass plates. Thanks to the opposition of polarization between plates, the application of an electrical field allows to have a differential effect: when a one-plate contract, the other expands. Mono-morph mirrors are a particular configuration of bi-morph mirrors with one piezoelectric plate and thus offer simplicity of conception. They really worth consideration as the optical substrate is made from glass material and then can be polished to reach a high optical quality. They can also be used for high power laser beams. Unfortunately they present the same drawbacks as the Piezoelectric Deformable Mirrors: hysteresis and 1/f noise [33].

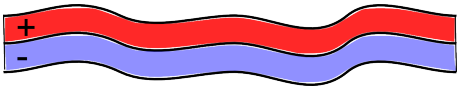

FIGURE 2.4: Schematic section of a bimorph mirror: the positive polarization is represented in red and the negative polarization is in blue. The laser beam can be reflected on one side or the other depending on the coating position.

Electrostatic mirrors A membrane (Fig.2.5) in conductive material is spread over an array of electrodes. The membrane is constrained at the edges and is deformed by application of an electric field. These mirrors have high amplitudes of deformation but are poorly linear. The optical quality of the surface is quite low in absence of tension, with presence of visible defects in commercial devices [34]. Although this type of mirror can sustain a 500 W laser beam, with special coatings to increase the damage threshold, thermal distortions are compromising its operation and it has to be used with few Watts of laser charge [35].

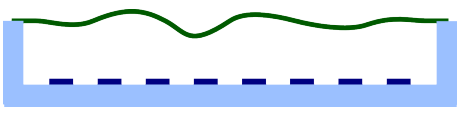

FIGURE 2.5: Schematic section of an electrostatic mirror: the conductive membrane (in green) is deformed by the action of the array of electrodes (in blue).

Electromagnetically actuated mirrors The voice-coil technology (Fig.2.6) is made of permanent magnets that are bonded to a thin optical membrane. When a current circulates into the coils, the plate is deformed thanks to the motion of magnets placed in front of them due to the Lorentz force. They perform with a high dynamic range of actuation and a high linearity. However the presence of electromagnetic fields could interfere with the suspended bench environment. To limit the risk of noise coupling, such a device is preferably not used in a GW interferometer, or has to be extensively tested before. Moreover, the membrane generally achieves a optical quality over our specifications in terms of surface RMS and reflectivity.

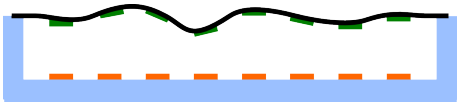

FIGURE 2.6: Schematic section of an electromagnetic mirror: the membrane (in black) is deformed by the action of the coils (in orange) on the magnets (in green).

Technology features	Requirements	Piezoelectric mirror	Mono and bimorph mirrors	Electrostatic mirror	Electromagnetic mirror
Laser operation (CW)	CW power > 100W (120 W/cm²)	Up to 1kW possible	Up to 1kW	Low damage threshold	Low damage threshold
Noise	Noise and coupling compatible with AGWD requirements	1/f noise	1/f noise	Possible noise from the power supply instabilities	Static electromagnetic fields
Vacuum compatible	< 10-6 mbar	No vacuum compatible*	No vacuum compatible*	No vacuum compatible*	No vacuum compatible*
Surface quality	Very high polished surface Roughness: rms < 0.1 nm Flatness: Peak to Valley< λ=20	Possible glass substrate: possible polishing and coating	Glass substrate: possible polishing and coating	No polishing Visible defects	Membrane: no surface better than 10 nm rms
* in the usual configuration provided by the companies					

TABLE 2.1: Features of some deformable mirrors with respect to our specifications for the integration in a Advanced GW detector

2.4.2 Device study conclusion

The features of the different deformable mirrors are summarized in Table 2.1. It appears that the current limits of the technologies are not providing any device fully compatible with the requirements mentioned at the beginning of the chapter, in terms of optical quality, noise requirements and high power sustainability. Furthermore, the critical point is the vacuum compatibility, as the standard devices are generally not foreseen for in-vacuum applications. Most of the scientific experiments are using the adaptive optics system outside their vacuum system [27, 28, 36, 37] and therefore can use standard mirror technologies. When it is necessary to put the system under vacuum, specific devices are developed. For example the deformable mirror designed for the Laser Mega-Joule laser facility looks very interesting (ILAO^{TM} (Intense Laser Adaptive Optics) Deformable Mirror): although the mirror substrate is a dielectric membrane, the device is vacuum compatible and claims a very good optical surface quality (better than 10 nm rms in active flat). It is low power consuming as it maintains the shape statically when the correction is constant. However, the membrane is deformed by a mechanical actuation that is excluded for the suspended benches due to the vibrations it may introduce.

2.5 Corrective devices for gravitational wave detectors

The thermal effects in the Advanced gravitational interferometers have been extensively studied before the construction of GEO600, Virgo and LIGO [12, 13, 38]. The most recent theoretical overview is available in [16]. These issues have given rise to a new family of adaptive optics correction systems based on thermal actuation. First conceptual proposals and proof of principle experiments were made between 2000 and 2004 [39–42]. They targeted the uniformity of the temperature distribution in the optics by different means. Ring heaters [43, 44], external pump beams [45, 46] and radiative heaters [47] were the first corrective systems tested and implemented in the interferometer gravitational wave detectors. The selected solutions for the Advanced Virgo baseline are briefly described in Section 2.5.1, together with a short analysis of their (un)compatibility for an integration in a mode matching system. Their position in the interferometer is presented in Fig.2.7.

The experience gathered with core optics thermal effects gave birth then to a second family of adaptive optics systems aimed at optimizing the beam coupling into Fabry-Perot cavities. The first real adaptive optics system was proposed in [48, 49]. Another system using a segmented heater [50] was presented later on for its implementation in Advanced LIGO. Both systems are described in Section 2.5.2.

The new concept of Thermally Deformable Mirror (TDM) with proof of principle was proposed in [11]. It is a complementary device to the injection mode matching optics. It can further improve the matching of the fundamental mode of the laser beam into the interferometer. This technology is more efficient than [50] since the correction is directly applied in the laser beam path. This solution is described in Section 2.6.

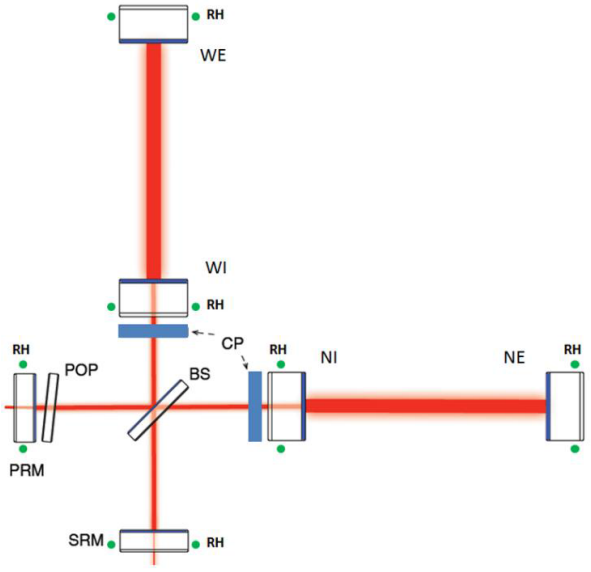

FIGURE 2.7: [10] Position of some thermal corrective device in Advanced Virgo: Ring Heaters (RHs) are placed around the test masses and the PR and SR. Two Compensating Plates (CPs) are put in the recycling cavities. The position of the double axicon scanning lasers are not indicated.

2.5.1 In situ corrective devices

We have seen that the control of the RoC of the test masses is necessary to increase the precision of the curvature obtained after polishing and to control the thermal lensing and expansion. The two first devices presented thereafter are based on the thermal expansion of the substrate under the exposure to heat radiation. They both have one degree of freedom.

2.5.1.1 The Ring Heater

The principle of the ring heater is to benefit from the power emitted by a circular heater placed around the substrate. In order to couple the maximum of power into the substrate, a reflective shield can be added around the heater.

Control of the RoC in the cavities In Advanced Virgo, a ring heater [10] will be placed around each of the suspended mirrors. The ring heater provides a negative RoC correction with power increase over the test masses in both arms and in the recycling cavities. It will be used to reach the nominal values of the RoCs, to equalize the two arms and to control the thermal lensing in the mirrors due to the absorption of the main laser.

FIGURE 2.8: Scheme of the ring heater position around a test mass. The ring heater is composed of two emitting elements inside a circular shield. In the zoom picture, the annular element of the prototype is made of glass and is surrounded by a gold coated copper shield. Pictures are from the Advanced Virgo TCS group

.

Description The device is composed of 2 emitting elements. Each one is made of an electrical wire wound around an insulated circle. They are both placed inside a IR reflecting shield (see Fig.2.8). The DC current passing through the wire is heating the device by Joule effect. The test mass is then heated radiatively: the heater creates a thermal gradient inside the mirror. The thermal expansion decreases the RoC of the front surface [43] in the arm cavities. The thermal lensing compensates the laser beam thermal lensing in the recycling cavities. By tuning the current in the wire, the RoC can be adjusted to the required value.

At the time of the writing, the final design of the ring heater is not yet determined: the annular part will be made of glass or aluminum, circular or rectangular, and the wires will be in manganine, nichrome or phosphorus bronze. It has to be surrounded by a gold coated shield to reflected the maximum power into the test mass. The ring heater will operate at high temperatures ($100 - 200°C$). It will be positioned at 18 cm with a precision of few millimeters from the High Reflective (HR) face of the mirror in order

to have the maximal dynamic range (- 1.6 m/W). This is enough to reach the range specifications and the required precision is easily achieved.

Suitability for a Mode Matching use This solution is non-invasive: the device is heating the mirror radiatively, minimizing the noise sources and the impact on the test masses. It can be switched off without any damage on the experiment.

The dynamic range is high but the correction is limited to the RoC compensation. It is relatively high power consuming with respect to a central heating actuation system. Being suspended around the test mass, the device provides a correction pattern that is not perfectly uniform due to the mechanical contact to maintain the emitting elements inside the shield [51]. Above all, it is not appropriate for our application: the suspension is needless for a mode matching device, that do not have to behave as a free mass, and is not suitable for small optical components.

2.5.1.2 Central Heating Radius of Curvature Correction (CHRoCC)

The CHRoCC was developed and used in Virgo+ [47]. It provides a positive RoC correction with power increase by heating the high reflectivity side of a test mass. The main difference in principle with the ring heater is that the heat is projected on the central part of the mirror.

Control of the RoC in the main cavities In Advanced Virgo, it is planned to install a CHRoCC on the end mirror of the 144 m Input Mode Cleaner with the objective of having a fine adjustment of the RoC in order to avoid high order mode resonances. It could also be used in the main cavities to increase and equalize the RoCs of their end mirrors. Like for the Input Mode Cleaner, if these cavities are close to degeneracy, it could also help to optically move these RoC values far from the resonance of high order modes.

Description The CHRoCC is composed of a ceramic heater placed at the focus of an ellipsoidal reflector, which the second focus is close to the high reflectivity surface of the end mirror (see Fig.2.9). The maximum working temperature of the heater is 1200° C, that corresponds to 15 W absorbed by the substrate. At the middle range, it corresponds to a RoC change of 325 m. This system has already given very good results in Virgo+, allowing to equalize the RoCs of the arms and to remove the degeneracy for the optical modes of 5^{th} order.

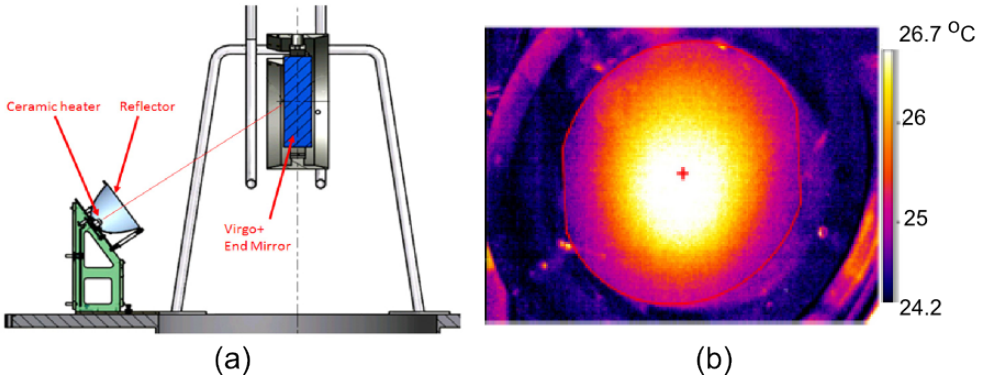

FIGURE 2.9: (a) Schematic representation of the CHRoCC in front of one Virgo+ end mirror. (b) Thermal image of the end mirror heated by the CHRoCC at 500° C. [47]

Suitability for Mode Matching Like the ring heater, this solution is non invasive and limited to the RoC correction. The projection makes the heating pattern slightly astigmatic, that increases the RMS of the mirror surface. The dynamic range is very high and the power consumption is low with respect to lateral heating systems [52]. The space needed for the projection makes this device unsuitable for small systems, that is a major inconvenient for a mode matching use.

In Chapter 1, we have seen that the control of the high order modes defects is crucial, in particular in the recycling cavities. In the following, the systems have a higher degree of actuation. The two first systems, based on the projection of a CO_2 laser source, will be implemented in Advanced Virgo. The third system, called *CHRAC*, is still under development.

2.5.1.3 CO_2 lasers devices

To perform the control of the optical defects in the recycling cavities independently from the main cavity corrections, the proposed solution is to insert a compensating plate in each of the recycling cavities, near to the input test masses of the long Fabry-Perot cavities (ITMs) [10]. The objective is to modify the transmitted optical path length by heating the compensating plate with the appropriate pattern. The compensative plates will then be the target substrate for a CO_2 laser: a double axicon will correct the symmetric part and a scanning system will be in charge of the asymmetric or high-frequency defects.

Description The double axicon system is a central heating system projecting two circular independent heat patterns, that can be power modulated. A scheme of the setup is presented in Fig.2.10. The double axicon system increases the flexibility of the axis-symmetric correction with respect to a simple axicon. The theoretical results after

correction exhibit a residual RMS of 0.4 nm leading to 6 ppm losses. The needed power for the $C0_2$ laser is about 18 W.

With the scanning system using galvanometer actuators, the HR surface of the test mass is scanned with a pick-off of the CO_2 laser beam modulated in power by an acousto-optic modulator (see Fig. 2.10 (b)). The scanning spot diameter is 1 cm. Thus, the correction of the residual distortions is performed on a central square surface of 16×16 cm^2. Its allows to have an active surface larger than the interferometer beam waist (5 cm) to reach the RMS specifications. Simulations show that the residual optical path length RMS is reduced by a factor 20 for spatial correction below the frequency of 40 m^{-1}, that meets the requirements for Advanced Virgo.

Suitability for a Mode Matching use Whereas the double axicon is limited to a very specific pattern of correction, the scanning system allows a very flexible correction of the high order mode aberrations at low power. But the projection systems needed to apply the correction on the optical substrate are again requiring an important space and are therefore not suitable for a mode matching device. Furthermore, the CO_2 scanning system can make some high frequency phase noise due to the scanning.

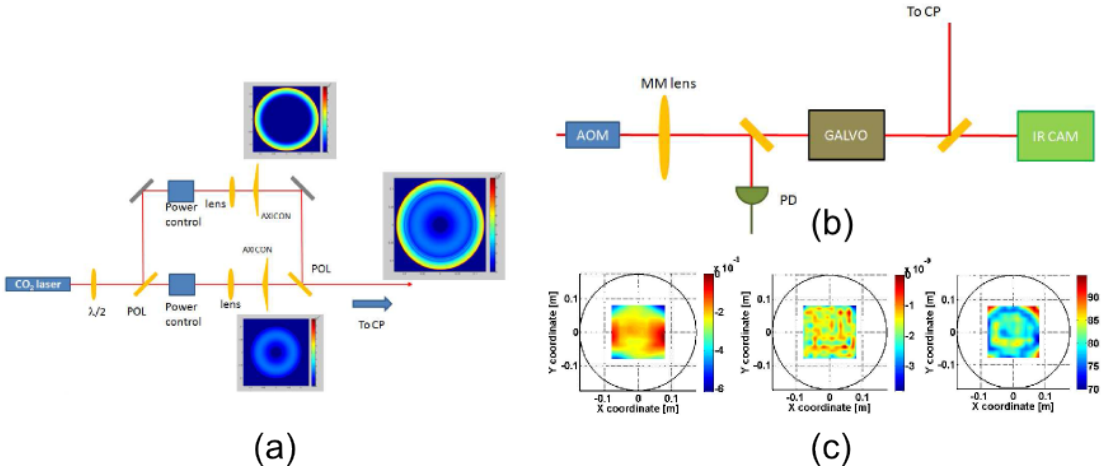

FIGURE 2.10: (a) Scheme of the double axicon setup: a CO_2 laser beam is divided in two beams orthogonally polarized. Each beam is shaped individually with an axicon lens. The heat pattern is then created by recombination and sent to the compensating plate. (b) Scheme of the scanning system setup. The power after the AOM is monitoring by the photodiode (c) Example of high spatial frequency correction: in left image, possible optical path length at 25 W before correction. In the center, residual path length after correction. At right, correction heating pattern performed by the scanning system.

2.5.1.4 Central Heating for Aberration Correction (CHRAC)

The CHRAC has been proposed [53] for high order mode correction in the main cavities of the Advanced and future generations of the interferometers to reduce the scattered light. In particular, the principle has been developed to help in reaching the surface polishing specification for the Laguerre-Gauss cavities. The experimental demonstration of its performance is still under study to confirm the theoretical expectations. Thence their characteristics are unknown at the time of the writing of this document.

Description Composed of an array of Alumina ceramic heaters mounted outside of the mirror payload vacuum tower, the thermal heat pattern can be projected on the HR surface of a mirror through a ZnSe lens to modify the shape: the correction is made by the thermal expansion of the mirror substrate (see Fig 2.11). The power emitted by each heater is individually controlled.

Suitability for a Mode Matching use The main advantage of this device is, like the scanning pattern, its capacity to correct high order mode aberrations. The implementation requires a projection system, limiting the use of this device to large systems.

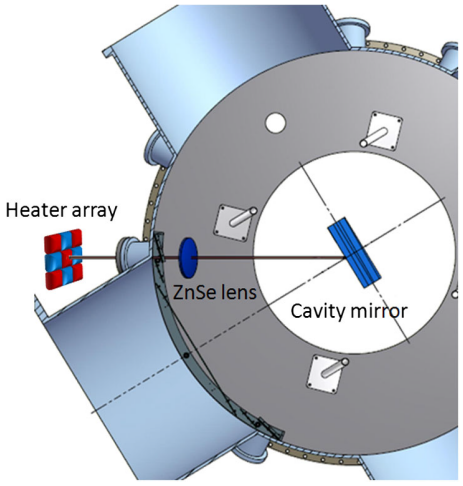

FIGURE 2.11: Scheme of the CHRAC implementation for a suspended test mass. The heater array is located outside the vacuum tower. The pattern is projected via a ZnSe lens onto the HR surface of the test mass.

2.5.2 Mode Matching devices

All devices presented in the previous section are based on the projection of a heat pattern, requiring a large space for implementation and being unsuitable for the mode matching on the one hand. On the other hand, the actuation is based on the thermal expansion of the HR side of the test masses, expect for the $C0_2$ devices. The actuation range is then smaller than the one expected from a thermal lensing actuation for the fused silica substrate (see Table 1.2), that is currently mainly used in the detectors. A device for the mode matching calls for large amplitudes of actuation and high order modes correction. Two systems especially studied for the mode matching are presented in the following section.

2.5.2.1 First Adaptive Optics system for GW interferometers

In [48] an adaptive optics system was proposed to ensure a suitable beam matching with a mode cleaner, correcting the expected thermally induced aberrations in the next generation of high power interferometers as well as the high temporal frequency beam jitter noise.

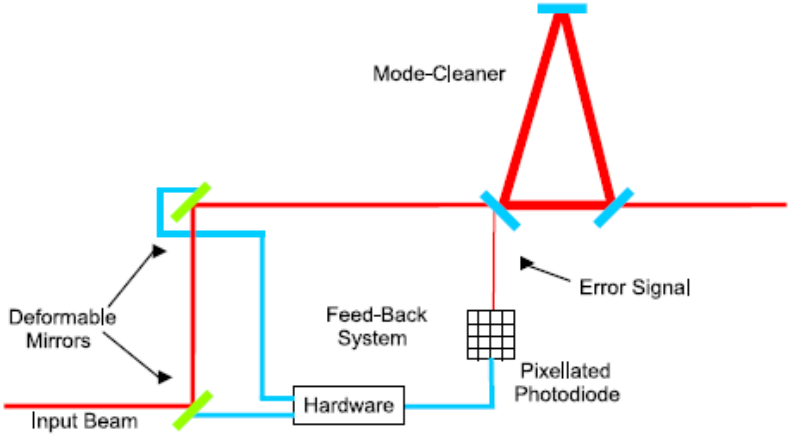

FIGURE 2.12: Theoretical scheme of the elements for the correction of the matching into the Input Mode Cleaner in the [48] proposal.

Description This adaptive optics system is composed of two deformable mirrors placed beforehand an Input Mode Cleaner cavity. The sensing, done with a pixellated photodiode, is based on the Ward technique [54](see Appendix A) to detect the high order modes, taking the advantage of the filtering behavior of the triangular cavity.
A proof of principle of this experiment has been realized in a quite different configuration [49] : a single deformable mirror was placed at the end of one of the arms of a small Michelson interferometer. The interference pattern at the antisymmetric port

was used to recover the high order mode composition. The actuation for the deformable mirror was then computed in terms of Zernike decomposition and applied in one arm of the Michelson. This experiment has been pursued with the successive use of two commercially available mirrors: a membrane mirror and a piezoelectric mirror.

Analysis of the Mode Matching use The efficient detection scheme uses directly the mismatching information, that is the modes rejected by the cavity, to compensate the high order modes. However, the actuation part is not compatible with an integration in the gravitational wave detectors. As we have seen previously in Section 2.4, the proposed mirrors are not suitable for an use in Advanced Virgo. None of them is vacuum compatible. The first one is not able to sustain high power due to the membrane properties. The second one is piezo-actuated. Even if the noise measurements are promising, noise disturbances are expected when integrated in a suspended bench as explained in Section 2.4. But the use of standard devices allows to perform the correction up to high time frequencies (up 50-60 Hz), that could not be achieved by thermal actuation.

2.5.2.2 The LIGO Quadrant Ring Heater

The principle of the Quadrant Ring Heater [55] is based a ring heater design, with the heater split in four independent sections. Therefore the device can reduce by transmission the divergence of a beam that is going through its substrate as well as compensate the astigmatism of this beam in two directions. The heat transfer is made by conduction, the actuators being in thermal contact with the substrate. This made it unsuitable for a use with the suspended test masses of the interferometer: it is then reserved for cavity matching applications.

Description The substrate is heated by four independently controlled heaters in thermal contact with its barrel (see Fig 2.13 (a)). The conduction ensures a high power coupling into the substrate while the use in transmission benefits from the thermal lensing and increases the correction efficiency with respect to the thermal expansion provided in reflection. Therefore this device exhibits a high dynamic range from minus infinity to -10 m, that corresponds to a RoC of 4.5 m, assuming that the mirror acts like a plano-lens. The maximum power required is 2.4 W per actuator, with a working temperature of 200°.

Analysis of the Mode Matching use The Quadrant Ring Heater is completely dedicated to a mode matching correction and has made the experimental demonstration

of its ability for compensating an astigmatic thermal lensing. The order of correction is increased with respect to the ring heater (see Fig. 2.13 (b) and (c)) but is lower than for a scanning system. This device has a high dynamic range and the substrate can be chosen and prepared accordingly to meet the optical quality requirements mentioned at the beginning of the chapter. The experimental tests exhibited a cross-coupling between the position and the beam size when an astigmatic correction is performed but this effect could be compensated by additional steering mirrors. Complementary tests to determine the behavior under vacuum will enhance the promising results of this device.

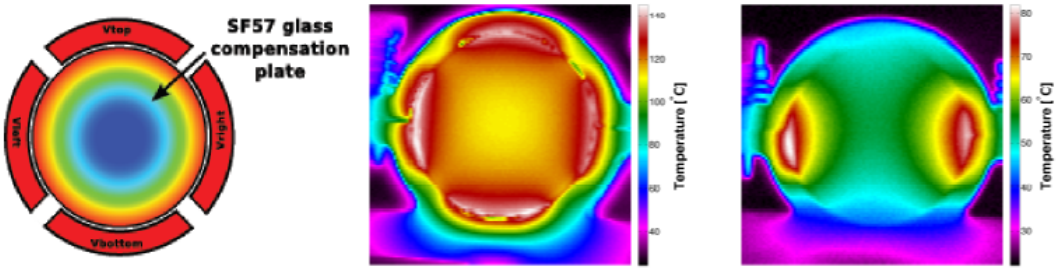

FIGURE 2.13: [55] (a) Scheme of the Quadrant Ring Heater (b) Experimental thermal image of a symmetric actuation (c) Experimental thermal image of an astigmatic actuation.

2.5.3 Conclusion on the devices for the gravitational wave detectors

With respect to commercial devices, the advantages of thermal systems are considerable: standard vacuum compatible substrates can be deformed without mechanical actuation by local temperature changes. They can benefit from a high optical quality, with an adequate choice of the substrates, polishings and coatings. Some of these systems are already included in the next generation designs, especially the devices dedicated to *in situ* corrections inside the main cavities. Concerning the mode matching, the most suitable device presented here, the Quadrant Ring Heater, is unfortunately not able to correct aberration modes higher than astigmatism (see Table 2.2). The techniques offering higher degrees of actuation (Scanning system and CHRAC) will not be effective in small optical systems where available space is reduced. The adaptive optics system of [49] does not offer a solution to the problem of the correction device compatibility to GW environment.

It appears from this study that ideally we would like to have a thermally actuating device able to correct high order modes, based on the technologies of thermal compensation systems, which have been proved to be efficient and compatible with our noise requirements for one hand, and in the other hand to integrate the design of a standard deformable mirror, which has a high resolution correction and is an efficient way to correct beam phase. Based on all this knowledge, we are now able to propose this

innovative device together with a complete adaptive optics system dedicated to mode matching in highly sensitive environment.

Device	Heat transfer	d.o.f.*	Correction order
Ring Heater	Radiation	1	RoC
CHRoCC	Radiation	1	RoC
Quadrant Ring Heater	Conduction	4	RoC Astigmatism
Double Axicon	Radiation	2	RoC
Scanning laser	Radiation	16	High order modes
CHRAC	Radiation	9	High order modes
Adaptive optics system in the [49] proposal	none	2 ×19	High order modes Beam jitter

TABLE 2.2: Summary of the device main features (* degree of freedom in the current prototypes)

2.6 A new adaptive optics system

The proposed solution is a Thermally Deformable Mirror (TDM) that consists in a standard mirror with an array of resistors in contact with its rear side. Each resistor can be individually tuned to modify locally the temperature of the substrate. By this way the optical path length of the beam in the substrate is locally changed by thermal lensing. The laser beam is going through the substrate thanks to the anti reflective coating in the front side and is reflected on the backside. With this technology, a relevant choice of the mirror allows to meet the very high requirements on the optical quality.

The cavity matching improvement will be performed with two TDMs placed in front the cavity into which the matching has to be increased. They will be controlled thanks to the detection of the high order modes reflected by the cavity. An example is given in Fig.2.14 with the experimental proof-of-principle setup of Chapter 7. A proposition for the integration of the mode matching system in the suspended injection bench of Advanced Virgo is indicated in Fig. 2.15, where the needed space has been anticipated in the design. They can be placed just before the input Mode Matching Telescope (MMT) that controls the beam position of the beam and the beam size for its injection into the interferometer. This means that the tip and tilt defects will be corrected independently from the TDMs. Therefore, it is not necessary for the TDM to take care of these low order aberrations: we will not study the possibility to correct neither the tip/tilt or the focus with the TDMs.

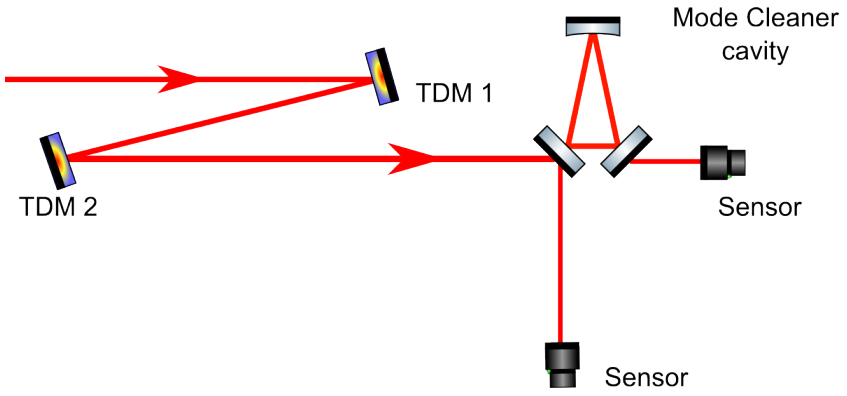

FIGURE 2.14: Proof-of-principle setup: two TDMs are correcting the matching into a mode cleaner cavity. The sensing is made through the study of the transmission and reflection port outputs.

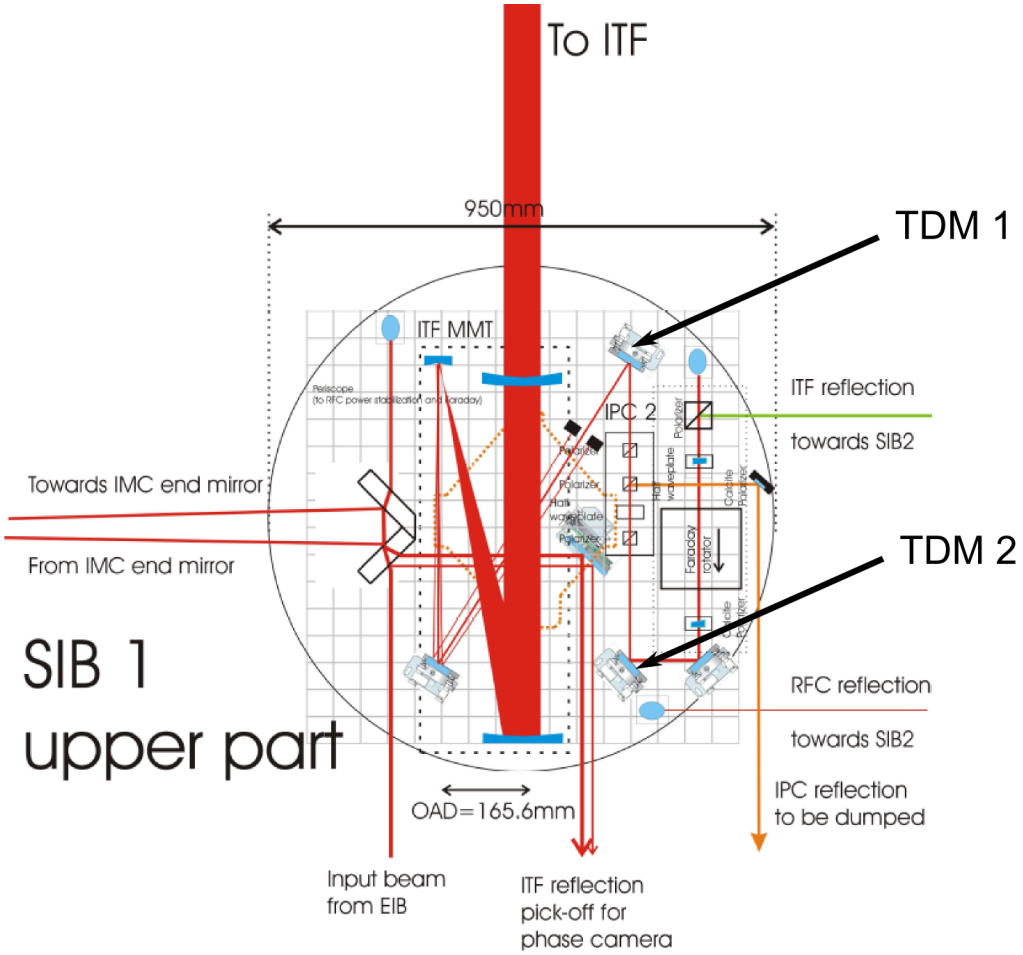

FIGURE 2.15: Proposal for the position of the TDMs in the suspended injection bench of Advanced Virgo [10]. They are placed at the end of the Injection subsystem, just before the Mode Matching Telescope.

The thermal properties of the actuation are extensively studied in the next chapter. The device features are the subject of Chapter 4 where we propose a design analysis. Afterwards, the experimental demonstration of the performance is realized in Chapter 5. The optimal position of the devices in the setup as well as the actuation scheme are investigating in Chapter 6. Finally the experimental improvement of the mode matching is discussed in Chapter 7.

Chapter 3

Thermally Deformable Mirror Principle

The Thermally Deformable Mirror (TDM) is based on the control of the thermal lensing inside an optical substrate. It is designed to correct high order mode aberrations in order to ensure a very good matching of the laser beam onto an optical setup and in particular to ensure a matching higher than 99 % for the injection of Advanced Virgo.

In this chapter, we study the theoretical behavior of the TDM and how it defines and limits the features of the device. First of all, the temperature field generated by the actuation is determined. The study is focused on the spatial behavior, as the temporal response is not a critical parameter for our purpose and is measured in Chapter 5. We see how the mirror can be modeled by a spatial filter.
Afterwards, we review the influence of the substrate material on the spatial frequency and the amplitude of the actuation. We will be able to define the best glass properties required for the realization of a prototype.

3.1 Principle of Actuation

As seen in Chapter 1, the optical path length experienced by a laser beam through a substrate depends on its temperature. In order to control accurately the phase of the beam, the TDM is a mirror in thermal contact with a body whose emitted power can be tuned. It can be a resistor as proposed in [11], which is locally dissipating heat in the substrate. The active area is then composed of an array of resistors to control the optical path length with a relatively high spatial frequency. The mirror is used with

the Anti Reflective (AR) coating on the front surface, in order to allow the beam to propagate through the substrate and to be reflected back by the High Reflective (HR) after propagation (see Fig.3.1). The dephasing $\phi(x, y)$ of a beam (wavelength λ) due to the round-trip propagation in the substrate (thickness d) is (see Eq. 1.82 in Chapter 1):

$$\phi(x, y) = \frac{4\pi}{\lambda}(OPD + nd) \tag{3.1}$$

with the Optical Path Difference (OPD) due to the temperature increase:

$$OPD = \left[\frac{dn}{dT} + \alpha(1+\nu)(n-1)\right] \int_{z=0}^{d} \Delta T(x, y, z)dz \tag{3.2}$$

with $\frac{dn}{dT}$ the coefficient of variation of the refraction index n with respect to the temperature T, α the coefficient of thermal expansion, ν the Poisson coefficient and ΔT the temperature elevation in the substrate.

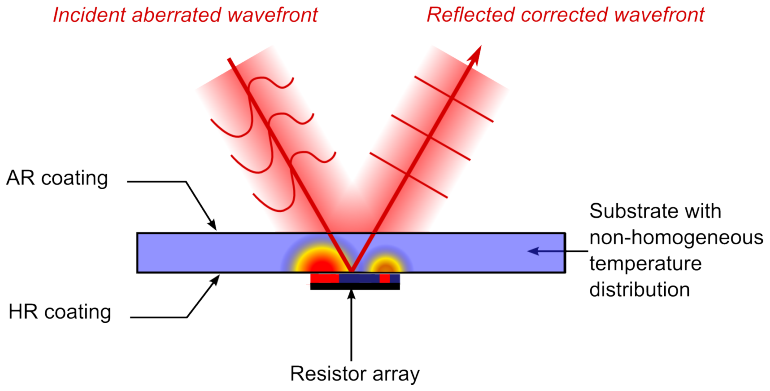

FIGURE 3.1: Schematic representation of the TDM principle: the wavefront of a laser beam is modified by reflection on the back side of a substrate for which its temperature is tuned by an array of resistors.

3.2 Temperature field in a substrate

We consider a perfectly homogeneous cylindric substrate placed under vacuum. The heat transfer is made by conduction from the resistor to the mirror without losses. The heat is absorbed in the coating and there is no internal heat generation inside the substrate. The mirror is evacuating the heat only by radiation from all its sides (see Fig.3.2). We want to understand what the shape of the deformation with respect to an incoming field of power is.

The general heat equation is:

$$\rho C_p \frac{\partial T}{\partial t}(r, z, t) - \kappa \Delta T(r, z, t) = 0 \tag{3.3}$$

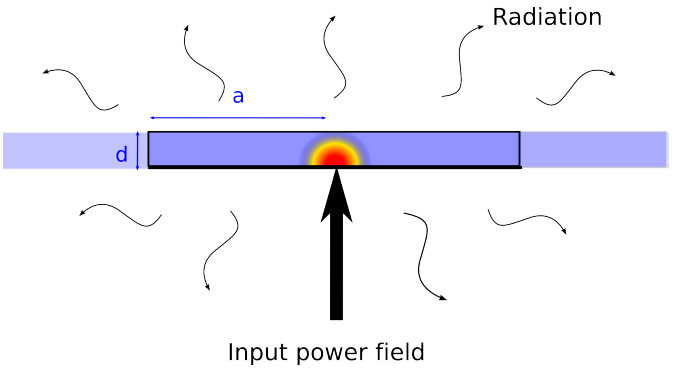

FIGURE 3.2: An input power field is applied on the back side of the TDM of thickness d under vacuum and is absorbed in the HR coating. The heat transfer is made by thermal conduction into the substrate. Then the heat is evacuated by radiation. To solve the heat equation in the spatial frequency domain, the radius a is considered close to the infinite.

with ρ the density of the substrate, C_p its heat capacity and κ its thermal conductivity. In the steady-state, it simplifies to the Laplacian of the temperature distribution:

$$\Delta T(r,z) = 0 \tag{3.4}$$

The heat flux F radiated by the surfaces can be linearized in the hypothesis of small increases of temperature T_{max} with respect to the external temperature T_e [56]:

$$\frac{T_{max} - T_e}{T_e} \ll 1 \tag{3.5}$$

and we have:

$$F = 4\sigma\varepsilon T_e^3 \delta T \tag{3.6}$$

with σ the Stefan-Boltzmann constant, ε the emissivity of the substrate and δT the variation of temperature with respect to the external temperature ($\delta T = T - T_e$).
The boundary conditions are, with $P(r)$ the absorbed power distribution and z_0 the center of the substrate:

$$-\kappa \left.\frac{\partial T}{\partial z}\right|_{z=z_0-d/2} = P(r) - \sigma\varepsilon T_e^3 \delta T(r, z_0 - d/2) \tag{3.7}$$

$$-\kappa \left.\frac{\partial T}{\partial z}\right|_{z=z_0+d/2} = \sigma\varepsilon T_e^3 \delta T(r, z_0 + d/2) \tag{3.8}$$

$$-\kappa \left.\frac{\partial T}{\partial r}\right|_{r=a} = \sigma\varepsilon T_e^3 \delta T(a, z) \tag{3.9}$$

3.2.1 Solution in the Gaussian case with $z_0 = 0$

When the mirror is heated by an incident laser beam, i.e. when the incident power distribution has a Gaussian shape, the analytical solution is presented in [56]. We give here the main results of this study.
A solution to the steady state equation (Eq. 3.4) can be written as a Dini series:

$$T(r,z) = \sum_m [A_m e^{k_m z} + B_m e^{-k_m z}] J_0(k_m r) \tag{3.10}$$

with J_0 the Bessel function of the first kind of order 0. The coefficients A_m and B_m are given by the boundary conditions (Eq. 3.7 and 3.8):

$$A_m = \frac{\varepsilon p_m a}{\kappa} e^{-3\zeta_m d/2a} \frac{\zeta_m - \tau}{(\zeta_m + \tau)^2 - (\zeta_m - \tau)^2 e^{-2\zeta_m d/a}} \tag{3.11}$$

$$B_m = \frac{\varepsilon p_m a}{\kappa} e^{-\zeta_m d/2a} \frac{\zeta_m + \tau}{(\zeta_m + \tau)^2 - (\zeta_m - \tau)^2 e^{-2\zeta_m d/a}} \tag{3.12}$$

with the input power $P(r)$ written as a Dini series:

$$P(r) = \sum_m p_m J_0(\zeta_m \frac{r}{a}) \tag{3.13}$$

and ζ_m are the solutions to Eq. 3.9 with $k_m = \zeta_m / a$ and $\tau = 4\sigma\varepsilon T_e^3 a/\kappa$. The temperature distribution is then:

$$T(r,z) = \sum_m \frac{p_m a}{\kappa} e^{-\zeta_m d/2a} \frac{(\zeta_m - \tau) e^{-\zeta_m (d-z)/a} + (\zeta_m + \tau) e^{-\zeta_m z/a}}{(\zeta_m + \tau)^2 - (\zeta_m - \tau)^2 e^{-2\zeta_m d/a}} J_0(\zeta_m \frac{r}{a}) \tag{3.14}$$

In the case of a gaussian incident beam of power P and waist w, the intensity distribution is:

$$I(r) = \frac{2P}{\pi w^2} e^{-2r^2/w^2} \tag{3.15}$$

and the p_m coefficients of the Dini distribution are, if the mirror is much larger than the beam waist [57]:

$$p_m \simeq \frac{P}{\pi a^2} \frac{\zeta_m^2}{(\zeta_m^2 + \tau^2) J_0(\zeta_m)^2} \exp(-\frac{1}{8} \zeta_m^2 \frac{w^2}{a^2}) \tag{3.16}$$

3.2.2 General axis-symmetric case: solution in the spatial frequency domain

By solving the heat equation in the spatial frequency domain, the TDM can be modeled by a spatial filter whose the transfer function can be found analytically. Again we consider that the system is axis-symmetric with $T(r,z)$ the temperature distribution

inside the mirror. The two-dimensional Fourier Transform of an axis-symmetric function $f(r)$ is:

$$\mathcal{F}(u) = FT[f(r)] \tag{3.17}$$

$$\mathcal{F}(u) = \iint_{-\infty}^{+\infty} f(\mathbf{r}) e^{-2i\pi \mathbf{u}\cdot\mathbf{r}} \mathrm{d}\mathbf{r} \tag{3.18}$$

with $\mathbf{r}$ the vector of the spatial coordinates and $\mathbf{u}$ the vector of the spatial frequencies. Working with the polar coordinates (r, θ), we choose the origin of θ such as $\mathbf{u}\cdot\mathbf{r} = ur\sin\theta$. This leads to, with the sin parity:

$$\mathcal{F}(u) = \iint_{-\infty}^{+\infty} f(r) r e^{-2i\pi ur\sin\theta} \mathrm{d}r\mathrm{d}\theta \tag{3.19}$$

$$\mathcal{F}(u) = 2\int_{-\infty}^{+\infty} f(r) r \underbrace{\int_{0}^{\pi} \cos\left(2\pi ur\sin\theta\right)\mathrm{d}\theta}_{\pi J_0(2\pi ur)} \mathrm{d}r \tag{3.20}$$

where we recognize the J_0 the Bessel function of the first kind of order 0. The two dimensional Fourier transform of a circular symmetry function is then the Hankel Transform (HT) $\mathcal{H}_0(u)$ of order 0.

$$\mathcal{F}(u) = 2\pi \int_{0}^{+\infty} f(r) r J_0(2\pi ur) \mathrm{d}r \tag{3.21}$$

$$\mathcal{F}(u) = \mathcal{H}_0(u) = HT[f(r)] \tag{3.22}$$

Writing Eq. 3.4 in the spatial frequency domain, we have:

$$HT[\Delta T(r,z)] = -u^2\Theta(u,z) + \frac{\partial^2\Theta}{\partial z^2}(u,z) = 0 \tag{3.23}$$

with $\Theta(u,z) = HT[T(r,z)]$, the temperature distribution in the spatial frequency domain.

The problem can be simplified supposing a mirror with infinite dimensions in the radial direction, due to the small size of the actuator with respect to the mirror diameter. The boundary conditions are then only Eq. 3.7 and Eq. 3.8, that we can rewrite, with

$z_0 = d/2$:

$$-\left.\frac{\partial\Theta(u,z)}{\partial z}\right|_{z=0} = \frac{1}{\kappa}\mathcal{P}_{in}(u) - u_0\Theta(u,0) \tag{3.24}$$

$$-\left.\frac{\partial\Theta(u,z)}{\partial z}\right|_{z=d} = u_0\Theta(u,d) \tag{3.25}$$

$\mathcal{P}_{in}(u)$ is the input power distribution and we define the fundamental spatial frequency u_0:

$$u_0 = \frac{4\sigma\varepsilon T_e^3}{\kappa} \tag{3.26}$$

We find the general solution:

$$\Theta(u,z) = A(u)e^{-uz} + B(u)e^{uz} \tag{3.27}$$

Eq. 3.24 and Eq. 3.25 lead respectively to:

$$A(u)\left[u+u_0\right] = \frac{\mathcal{P}_{in}}{\kappa} - B(u)\left[u-u_0\right] \tag{3.28}$$

$$B(u) = \left[\frac{u-u_0}{u+u_0}\right]A(u)e^{-2ud} \tag{3.29}$$

Combining both solutions, we obtain:

$$A(u) = \frac{\mathcal{P}_{in}(u)}{\kappa\left[u+u_0\right]\left(1+\left[\frac{u-u_0}{u+u_0}\right]^2 e^{-2ud}\right)} \tag{3.30}$$

$$B(u) = \frac{\mathcal{P}_{in}(u)}{\kappa\left[u+u_0\right]\left(1+\left[\frac{u-u_0}{u+u_0}\right]^2 e^{-2ud}\right)}\left[\frac{u-u_0}{u+u_0}\right]e^{-2ud} \tag{3.31}$$

and the general solution is written from Eq. 3.27:

$$\Theta(u,z) = \frac{\mathcal{P}_{in}(u)}{\kappa\left[u+u_0\right]\left(1+\left[\frac{u-u_0}{u+u_0}\right]^2 e^{-2ud}\right)}\left[e^{-uz} + \left[\frac{u-u_0}{u+u_0}\right]e^{-2ud}e^{uz}\right] \tag{3.32}$$

3.2.3 Transfer function of the actuation

We now know the temperature distribution inside the substrate as a function of the power applied at the back face. The temperature gradient experienced by a beam is given by the integration of the temperature distribution over the thickness d of the substrate. We define the temperature transfer function $H(u)$ of the mirror by the ratio

of the substrate temperature distribution and the input power distribution:

$$H(u) = \frac{\int_0^d \Theta(u,z)\mathrm{d}z}{\mathcal{P}_{in}(u)} \tag{3.33}$$

$$H(u) = \frac{\left(1-e^{-ud}\right)}{\kappa u\left[u+u_0\right]} \frac{\left(1+\left[\frac{u-u_0}{u+u_0}\right]e^{-ud}\right)}{\left(1+\left[\frac{u-u_0}{u+u_0}\right]^2 e^{-2ud}\right)} \tag{3.34}$$

This filter has not a "standard" shape (see Fig.3.3). However, it can be approximated by a band-pass filter (BP) of order 2 in series with low-pass filter (LP) of order 1 whose equations are:

$$H(u) \simeq \frac{d}{\kappa} BP(u).LP(u) \tag{3.35}$$

$$BP(u) = \frac{ud}{u^2+ud+u_{c_1}} \qquad u_{c_1} = u_0 \tag{3.36}$$

$$LP(u) = \frac{u_{c_2}^2(u+u_{c_2})}{u^2+u_{c_2}u+u_{c_2}^2} \qquad u_{c_2} = \frac{1}{d} \tag{3.37}$$

with u_{c_1} and u_{c_2} the cut-off frequencies of the filters. They respectively depend on u_0, that means on the thermal conductivity κ and the emissivity ϵ of the substrate, and of the thickness d. For a FS substrate, u_0 is about 4 m^{-1} and $1/d$ is 100 m^{-1} for a thickness $d = 10$ mm.

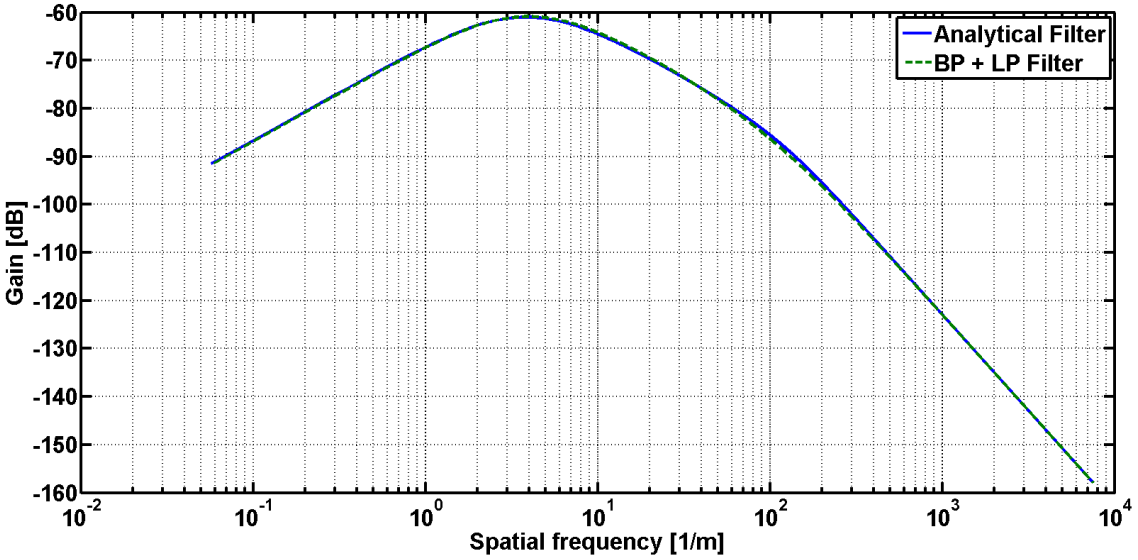

FIGURE 3.3: H(u): Transfer function of the a Fused Silica substrate ($u_0 \simeq 4\ \mathrm{m}^{-1}$) with a thickness of 1 cm ($1/d = 100\ \mathrm{m}^{-1}$)

In the approximation of low spatial frequencies ($u \to 0$) the filter becomes:

$$H \simeq \frac{ud}{\kappa u_0^2} \tag{3.38}$$

And in the approximation of the high spatial frequencies, ($u \to \infty$) the filter becomes:

$$H \simeq \frac{1}{\kappa u^2} \tag{3.39}$$

This transfer function completely characterizes the TDM as a spatial filter of 2^{nd} order for the input power field. We can extract a rough indication on the substrate behavior. The high spatial frequencies will be attenuated in $1/u^2$ while the low frequencies will be reduced by ud. An increase of the thickness will increase the gain only at low frequencies, so the response will have an higher amplitude but will also have a larger width (see Fig.3.4). An increase of the thermal conductivity, lowering the fundamental spatial frequency u_0, will lead to a decrease in the impulse response amplitude at all frequencies (see Fig.3.5). If u_0 is greater than $1/d$, the filter is equivalent to a band-pass (see Fig.3.5, $u_0 \simeq 400$ m^{-1}).

An ideal substrate would preserve as much as possible the high frequencies, in order to have a good resolution in the actuation, and would provide a high amplitude of actuation for all frequencies as well. It means that a low thermal conductivity, that gives a high u_0, would be preferable. This could be understand instinctively: a low thermal conductivity will limit the temperature homogenization all over the substrate. For the thickness, a trade-off between the amplitude and the resolution has to be found. Indeed, a larger thickness will give a higher amplitude response by integration but will smooth the spatial frequencies. In the case of a correction over several tens of millimeter square, as it is standard for laser beam corrections, the spatial frequencies above 100 m^{-1} are the most relevant. For these high frequencies, it appears from Fig.3.4 and Fig.3.5 that the influence of the thickness will be relatively low whereas the variations of u_0 will dramatically impact the TDM response.

3.2.4 Impulse response in the spatial domain

In the spatial domain, the inverse Hankel transform of the transfer function $H(u)$ gives the impulse response shape of the actuation, whose important parameters are the amplitude and the Half Width Half Maximum (HWHM). Unfortunately, performing an analytical inversion of the exact transfer function (Eq. 3.34) or of the approximations (Eq. 3.35) is not possible due to divergence of the expressions for r = 0.

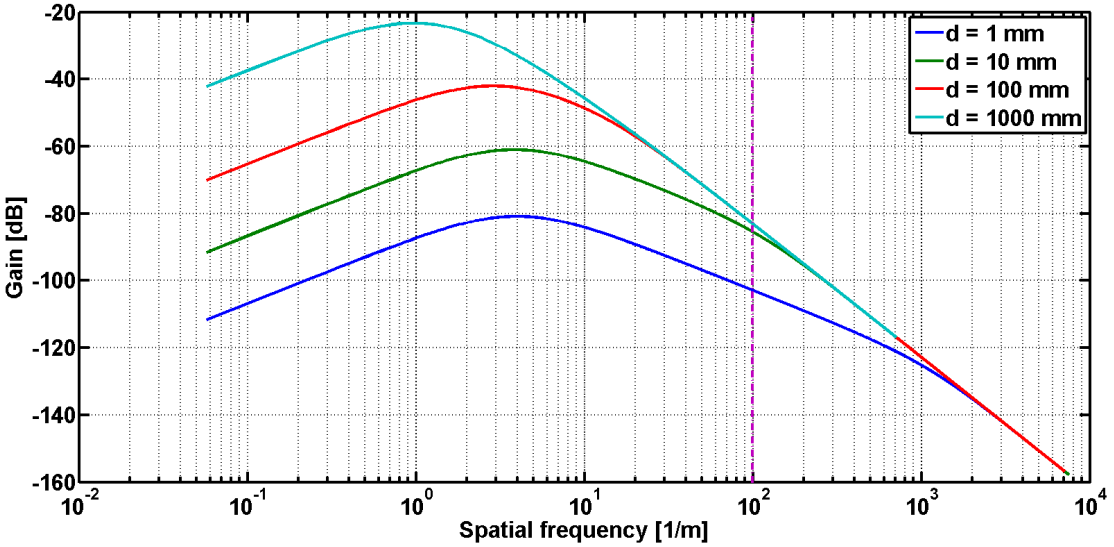

FIGURE 3.4: H(u): Transfer function of the a Fused Silica substrate ($u_0 \simeq 4$ m^{-1}) with a thickness d varying from 1 mm to 10 cm. Above 100 m^{-1} and for thicknesses greater than 1 cm, the influence of d on the response becomes very low.

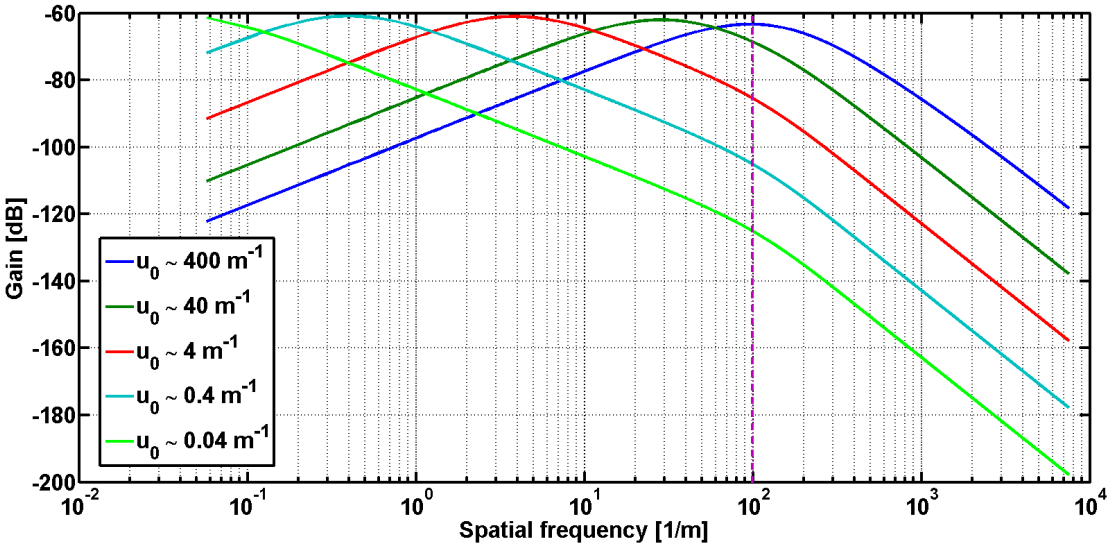

FIGURE 3.5: H(u): Transfer function of a 1 cm thickness substrate with the fundamental spatial frequency u_0 varying from 40 m^{-1} to 0.04 m^{-1}. An increase of u_0 by a factor 10 decreases the response amplitude in the high frequencies of about 20 dB.

The effect of the filter on some input power distributions $\mathcal{P}_{in}(u)$ is obtained numerically by multiplying them in the spatial frequency domain with the transfer function $H(u)$ (or by a convolution with the impulse response $h(r)$ in the spatial coordinates).

$$G(u) = \mathcal{P}_{in}(u).H(u) \tag{3.40}$$

The responses have a width that decreases with the decrease of the actuator size. For an actuator smaller than 500 μm, the response is equivalent to the impulse response. The

normalized results are presented in Fig.3.6 with $g(r)$ the response in the spatial coordinates. The fundamental spatial frequency u_0 will dominate the response of the substrate.

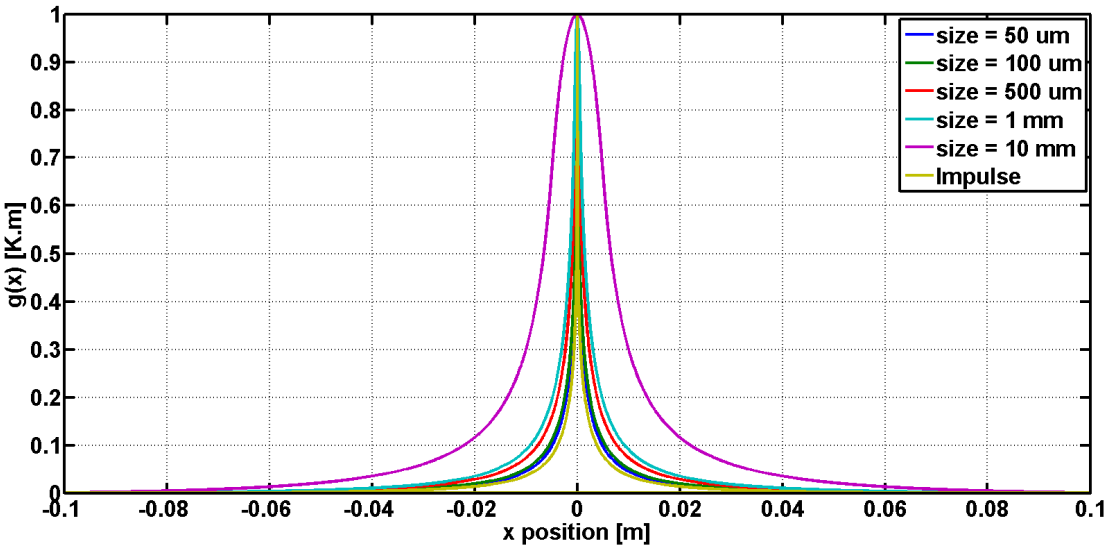

FIGURE 3.6: Actuation responses $g(r)$ for different actuator sizes, with a constant input power $P_{in} = 0.1$ W. The simulation is made for a 1 cm thickness substrate with the fundamental spatial frequency $u_0 \simeq 4$ m^{-1}.

$G(u)$ has the dimension of a temperature field integrated over the mirror thickness, in [K.m]. Then, in order to compute the OPD induced by the TDM, we can simply multiply the filter by the opto-mechanical parameters of the substrate according to Eq. 3.2:

$$G_{OPD}(u) = \left[\frac{dn}{dT} + \alpha(1+\nu)(n-1)\right] G(u) \tag{3.41}$$

in the limit of small amplitudes, where $\frac{dn}{dT}$ is constant.

However, our model is not completely accurate, as we neglected the lateral dimension of the substrate. A numerical model will help in computation of the simulation with finite radial dimensions. We will start by studying $g(r)$, that is the response of the TDM $G(u)$ in spatial coordinates. Then we will focus on the optical properties of the substrate to determine $g_{OPD}(r)$.

3.3 Characterization of the substrate parameters

A model of the previous situations has been set up with a Finite Element Analysis (FEA) software (*Comsol*). In this chapter, we take as a reference configuration the following model: a square actuator of 1x1mm^2 is in contact with a plate of Fused Silica (FS)

substrate of 50.8 mm diameter (2") and 10 mm thickness. The coupled power into the substrate is 100 mW. This is illustrated in Fig.3.7).

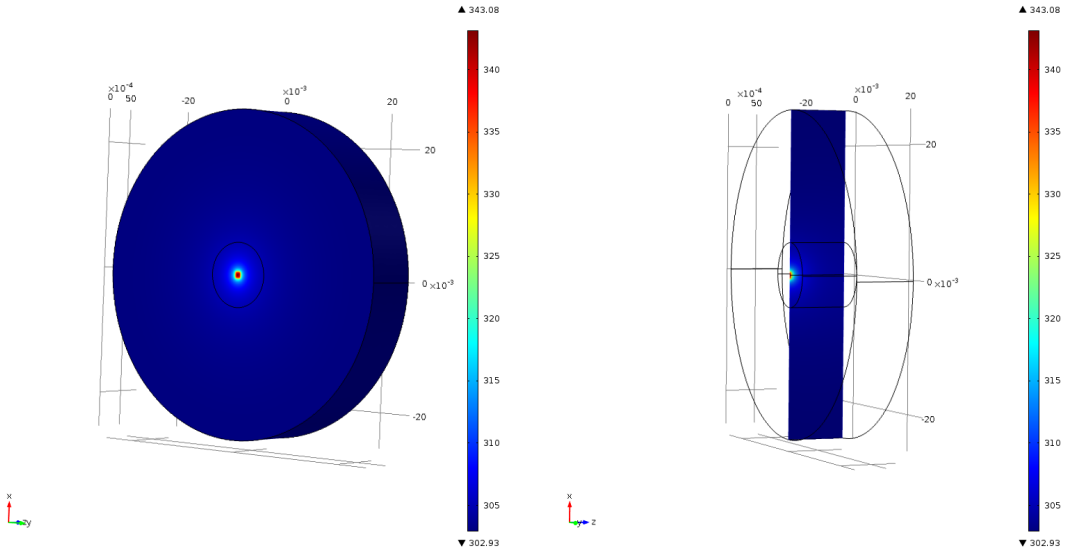

(A) (B)

FIGURE 3.7: FEA simulation of a square input of 1mm^2 with 0.1 W absorbed in the substrate: (A) View of the power input side of the mirror (B) View of a central slice. The substrate material is made of fused silica (FS)

3.3.1 Approximation of the impulse response

The simulation is made for several power distribution inputs with square shape. For a very small surface of actuation, we expect to have the mirror response dominated by the thermal properties of the substrate and to be equivalent to the impulse response. Due to the resolution of our model, the size of the smallest tested actuation is limited to 50x50 μm^2. Larger inputs with 100x100 μm^2, 500x500 μm^2 and 1x1 mm^2 surfaces have also been tested.
Unlike the analytical model and as as shown in Fig.3.8, the response shapes are superimposed. This global shape is due to the heat radiation by the barrel of the substrate that dominates the low spatial frequencies. For example, if we increase by a factor 2 the radius of the substrate, the response for an actuator of 1 mm is enlarged (see Fig.3.9)

The HWHM of the actuation is linearly dependent to the logarithm of actuator size: for an increase of a factor 10 in the actuator side, the HWHM increases by more than a factor 3. Near to the actuation in $r = 0$, the response amplitude increases with the decrease of the actuator size, due to the power density increase. The largest input leads to the largest output width and the smallest amplitude (see Fig.3.10). For 50x50 μm^2 surface, the TDM response has a HWHM of 0.5 mm. For the 1x1 mm^2 input, the response is 2.3 mm width.

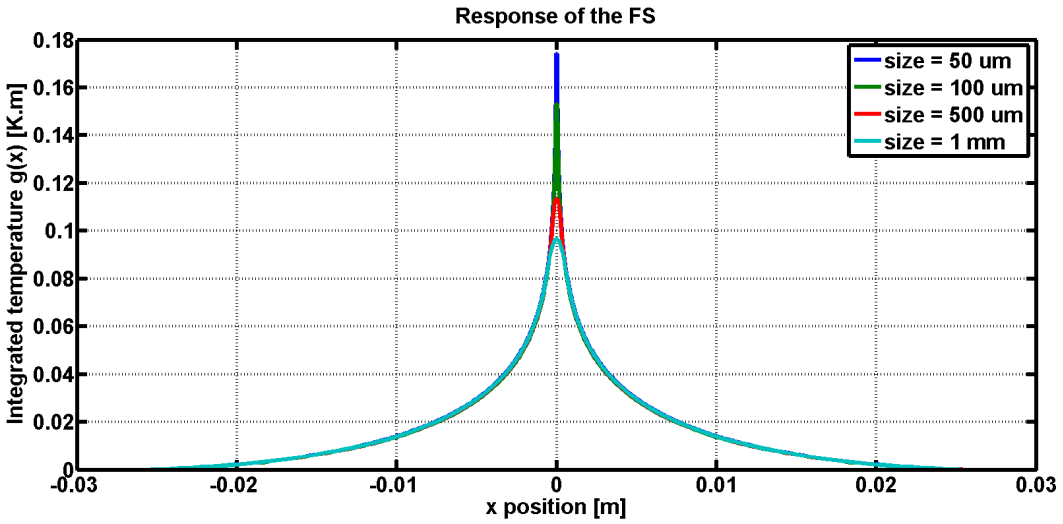

FIGURE 3.8: Response of the fused silica substrate for different sizes of square actuators coupling 0.1 W into the substrate, the other parameters being fixed.

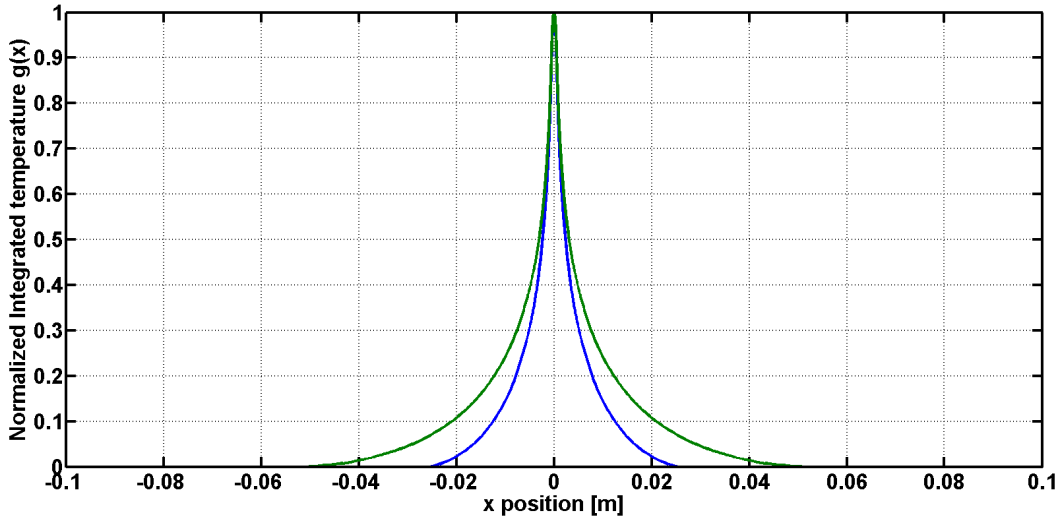

FIGURE 3.9: Comparison of the normalized responses of the FS substrate to 1mm actuator for a substrate of 2"diameter (blue) and 4" diameter (green).

3.3.2 Linearity with the temperature

An hypothesis of the analytical model developed in the previous paragraph is the small increase of temperature. To determine the limit of the model, we check the domain of linearity with the FEA simulation (see Fig.5.12). The linearity of the analytical model is valid up to a few Watts for a FS substrate. At 1 W, it corresponds to a temperature increase of 280 K inside the substrate. This figure is not realistic as we are above the maximum temperature allowed for the coatings. We will now continue our study with a 1x1mm^2 resistor at 0.1 W: it corresponds to a difference of $\delta T = 40$ K and a maximum integrated temperature $g_{max} = 0.04$ K.m.

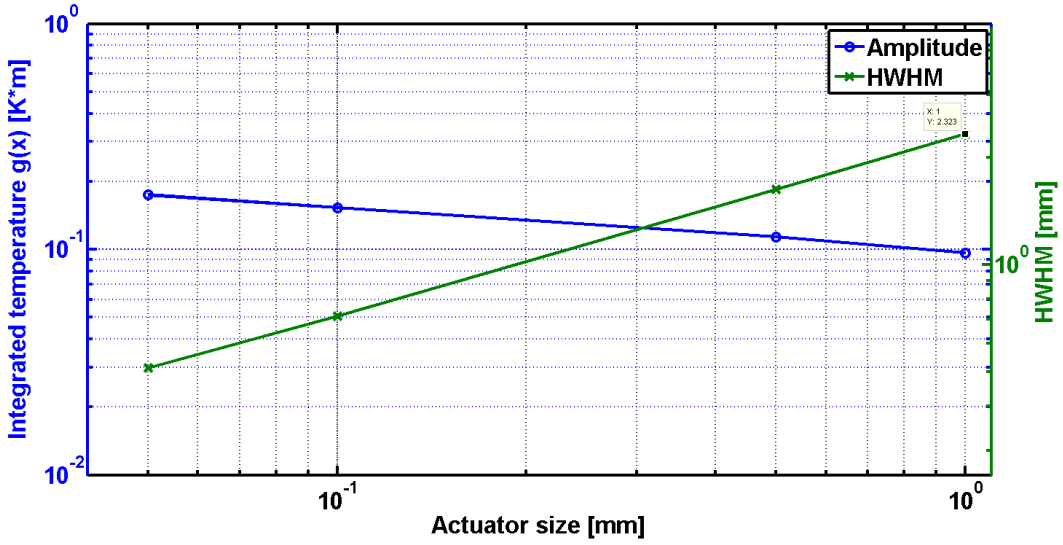

FIGURE 3.10: Variation of the response parameters as a function of the actuator size for the fused silica substrate and 0.1 W absorbed by the substrate, the other parameters being fixed.

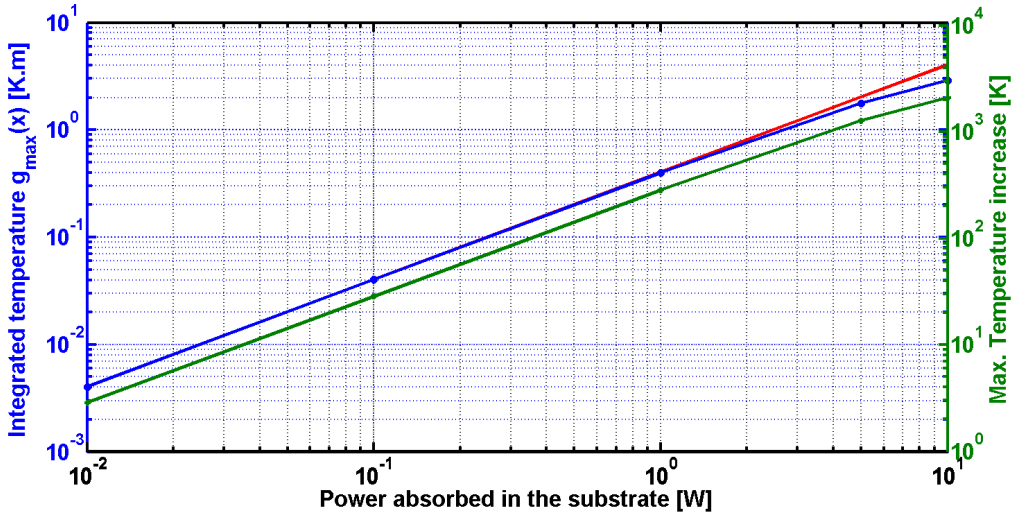

FIGURE 3.11: Amplitude of the substrate response g_{max} as a function of the input power for the FS computed with the FEA simulation (in blue). The maximum temperature difference inside the substrate δT is represented in green. In red is given the linear behavior for sake of reference

Material		Thermal			Optical		Mechanical
	Density	Thermal conductivity	Heat capacity	Thermal expansion	Refraction index	$\frac{\partial n}{\partial T}$	Poisson ratio
	ρ kg.m^{-3}	κ W.m^{-1}.K^{-1}	C_p J.kg^{-1}.K^{-1}	α 10^{-6} K^{-1}	n	10^{-6} K^{-1}	ν
BK7	2510	1.114	858	7.1	1.5	2.4	0.206
FS	2202	1.38	745	0.55	1.47	8.7	0.17
SF57	5510	0.62	360	9.2	1.8	6.8	0.248
Zerodur	2530	1.46	820	0	1.54	14.3	0.243
CaF_2	3180	9.71	854	18.85	1.43	-10	0.26
Sapphire	3980	40	764	9.03	1.75	13.1	0.02

TABLE 3.1: Material table from Handbooks. The emissivity of all substrates is fixed at 0.9, emissivity of the Fused Silica, as we have seen that the emissivity has a very low impact on the substrate response.

3.3.3 Material study

We compare some common substrates that are suitable for polishing and coating according to the optical requirements for Advanced Virgo [11]: the Crown Borosilicate (BK7), Fused Silica (FS), SF57, Zerodur, CaF_2 and Sapphire. Their properties are summarized in Table 3.1. The aim of this study is to find the material with the best features: high amplitude of response and small increase of temperature with respect to the input power, small width of the optical path length to reach an high precision.

3.3.3.1 Temperature field in different substrates

According to the model previously developed in the first part of this chapter, the temperature distribution in a substrate depends on the thermal conductivity and the emissivity of this substrate through u_0 (see Eq. 3.34). We observe the response temperature distribution for the different substrates. The geometrical parameters are fixed: the substrate plate is 10 mm thick and has a diameter of 2". The resistor is a square of 1 mm size, coupling 0.1 W in the substrate.

The simulated responses are summarized in Fig.3.12. The maximum temperature integral is obtained for the SF57 with $g_{max} = 96.5\ 10^{-3}$ K.m, whereas the minimum temperature integral is obtained for the Sapphire with $g_{max} = 1.6\ 10^{-3}$ K.m, leading to almost a factor 50 between the 2 temperature fields. This is related to the thermal conductivity κ of the material: when κ varies from 0.1 to 1000 W.m^{-1}.K^{-1}, the amplitude of the temperature decreases by almost 4 orders of magnitude. The emissivity has a much lower effect: the relative variation is lower than 2 % between substrates for the emissivity variation from 0 to 1.
The important parameter in the fundamental spatial frequency u_0 is then the thermal

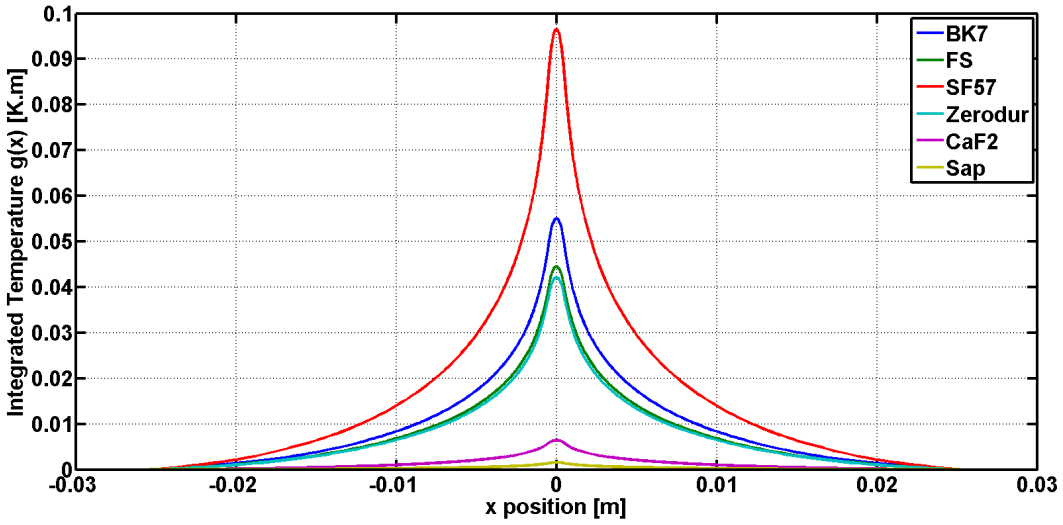

FIGURE 3.12: FEA simulation of the temperature increase in different substrates for an input power of 0.1 W generated by a resistor of 1mm^2, absorbed in a plate of 2" diameter and 10 mm thickness

conductivity κ. Though we retrieve the behavior expected from the analytical simulations in Section 3.2.3: the thermal conductivity has a great impact on the substrate response $g(r)$, whose amplitude is higher for substrates with a low thermal conductivity. They would then be chosen in priority. However, the optical properties are determining the final amplitude of the actuation.

3.3.3.2 Influence of the optical parameters

Amplitude of the response in different substrates From the temperature integration over the thickness, we compute the OPD in the substrates according to Eq. 3.2, where all thermal effects defined in Chapter 1 are included in the computation. Indeed, while the thermo-elastic effect can be neglected for the FS and the Zerodur, it becomes relevant for the BK7, CaF2 and SF57 material. The relative strengths of the thermal effects for each substrate are summarized in Table 3.2.
The substrate response depends on the following optical and mechanical parameters: the refraction index n, $\frac{\partial n}{\partial T}$, the thermal expansion coefficient α and the Poisson ratio ν. In order to have the maximum OPD increase for a given temperature increase in the substrate, i.e. for a given κ, we would like to have a high $\frac{\partial n}{\partial T}$ for the thermal lens part, as well as a high α and ν for the thermo-mechanical part.

The largest OPD is obtained with the SF57 (see Table 3.3 and Fig.3.13). Even if their optical and mechanical parameters are among the higher values, the Sapphire and the CaF_2 exhibit the smallest OPD of the substrate set. They will not be the preferred

Material	Thermal lens $\frac{\partial n}{\partial T}$ 10^{-6} K^{-1}	Thermo-Elastic $\alpha(n-1)(\nu+1)$ 10^{-6} K^{-1}	Ratio
BK7	2.40	4.28	1.78
FS	8.70	0.29	0.03
SF57	6.80	6.85	1.01
Zerodur	14.3	0	0
CaF_2	-10	10.2	1.02
Sapphire	13.1	6.91	0.53

TABLE 3.2: Relative strength of the thermal effects with respect to the thermal lensing (in K^{-1}, results from FEA simulations).

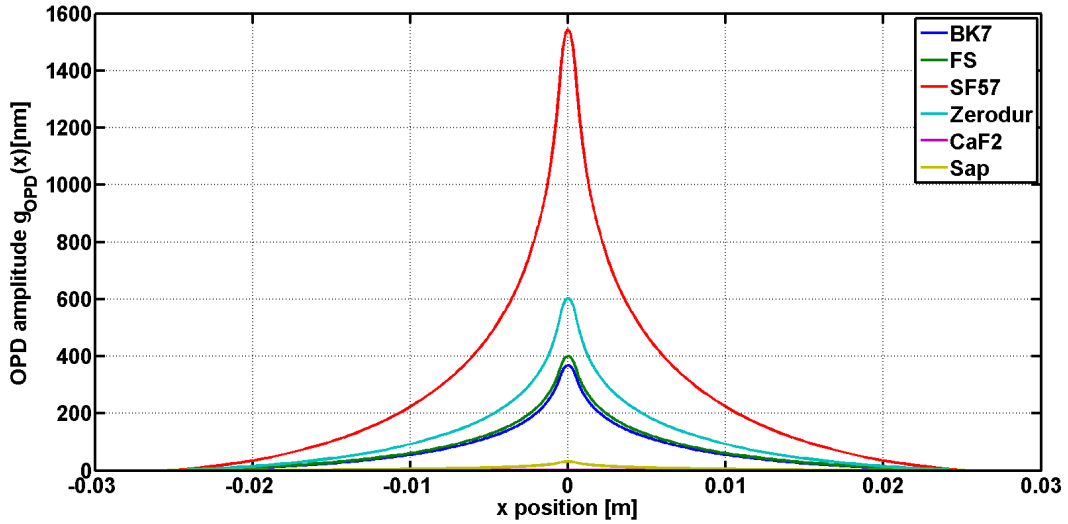

FIGURE 3.13: FEA simulation of the OPD increase in different substrates for an input power of 0.1 W generated by a resistor of 1mm^2, absorbed in a plate of 2" diameter and 10 mm thickness

choice for our device.

A discriminant parameter between the remaining elements is the working temperature. For a given input power, we are looking for the material that gives the maximum OPD for the minimum ΔT, in order to keep the material at a reasonable temperature and to ensure to stay in the linear domain. The Zerodur has an actuation range twice lower than the SF57, both in amplitude and temperature. For a given power, the SF57 is then a more efficient material, but the temperature increase should be accurately controlled. For safety reasons, the Zerodur might be an appropriate solution, along with the FS and the BK7 substrates that are a good trade-off with a reasonable increase of temperature with respect to the SF57 (see Fig.3.14). Furthermore, the FS would be preferred to the BK7 according to this criteria.

Resolution of the response in different substrates The width of the OPD (HWHM) will determine the maximum achievable spatial resolution of the correction. Following

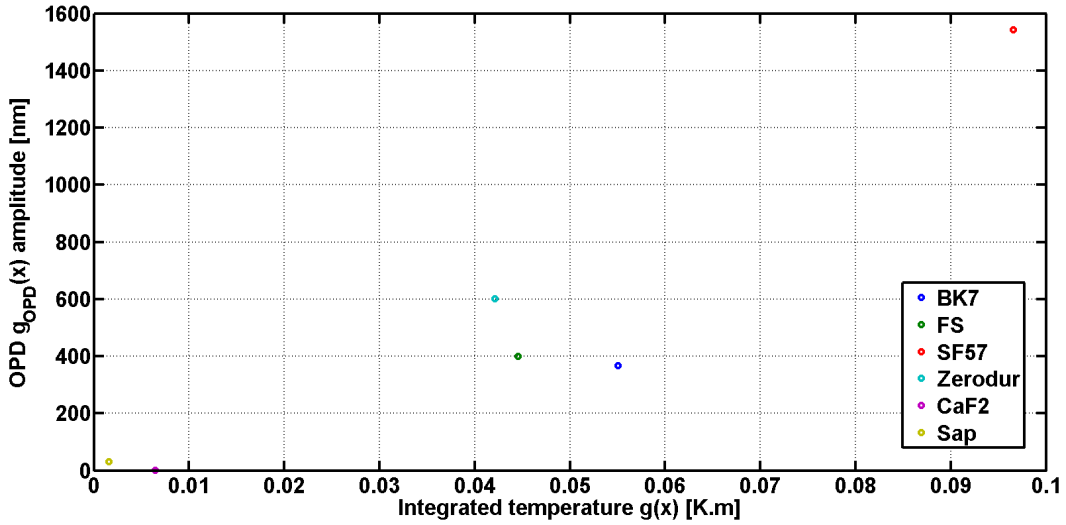

FIGURE 3.14: Comparison of the OPD amplitude inside the different substrates as a function of the amplitude of the integrated temperature g_{max}. The SF57 exhibits the largest response both in amplitude and temperature.

Material	ΔT (K)	OPD Amplitude (nm)	OPD HWHM (mm)
BK7	52.5	368	2.39
FS	43.1	400	2.41
SF57	91.2	1543	2.32
Zerodur	40.9	603	2.41
CaF_2	9.0	1.4	2.48
Sapphire	4.6	31	2.49

TABLE 3.3: Material behaviors for a $1mm^2$ resistor dissipating 0.1 W input power in the 10 mm thick substrate.

the study from [11], we can compute the width of the OPD for different κ, the other parameters being fixed (see Fig.3.15). We can observe that the increase of the HWHM is correlated to the temperature increase of the substrate, i.e. to the parameter κ. The smallest width is obtained with the SF57, followed by the BK7, the FS and the Zerodur. The results are given in Table 3.3. However, the relative variation of the HWHM between the substrates is lower than 5%. We can then consider that the HWHM is mainly determined by the actuation and that is not a key criteria in the choice of the substrate.

3.3.4 Influence of the thickness

Once the substrate material is defined, the substrate geometry still needs to be determined. If the radial dimension of the mirror can be neglected, as it is much greater than the actuator size, the thickness has an impact on both the amplitude and the width of the response as shown before in the filter approximation (see Eq. 3.35 in Section 3.2.3). Computing the OPD for different thicknesses of the FS substrate with the FEA

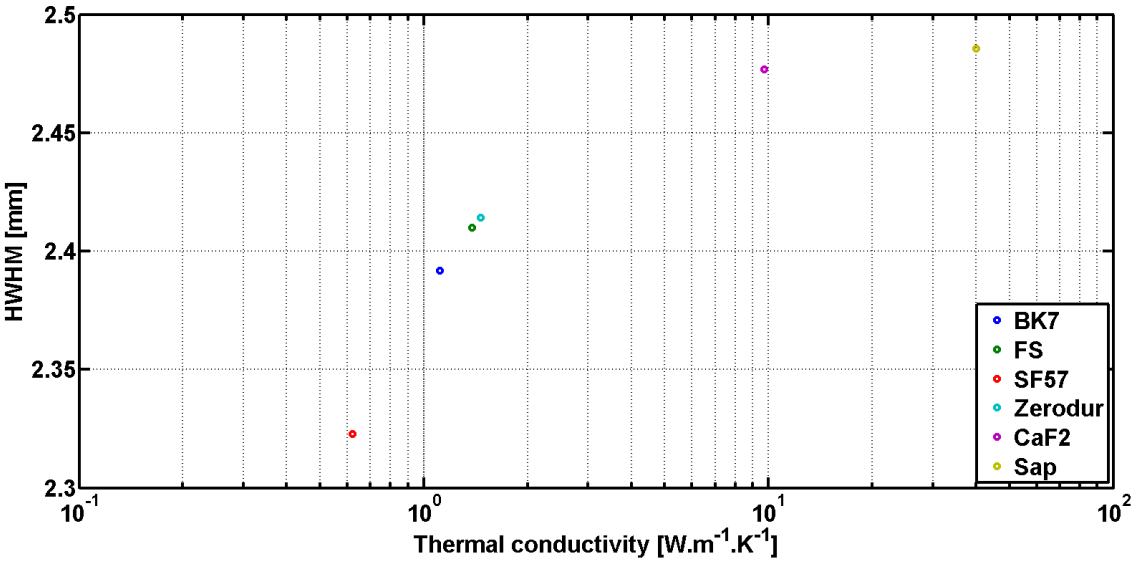

FIGURE 3.15: Influence of the thermal conductivity κ on the HWHM of the OPD response.

.

simulation, we obtain that the larger the thickness, the larger the amplitude. The gain of about 10 nm for a thickness increase of a factor 2, that corresponds to a relative variation of about 2.5 %. The influence on the HWHM is also negligible (less than 5 % of variation). We then retrieve that the thickness has a very weak influence on the behavior of the substrate response at high frequencies.

3.4 Conclusion

We have shown that an infinite radial dimension optical substrate that dissipates heat radiatively is a linear spatial filter for an axis-symmetric input power distribution absorbed at one of its faces. The parameters of the filter are the fundamental spatial frequency u_0, characteristic of the substrate through the thermal conductivity, and the thickness of the substrate. The high spatial frequencies are attenuated as $1/u^2$. The FEA simulations have shown that the HWHM of the response highly depends on the actuator size and is relatively independent of the substrate thickness or of the thermal substrate properties. The global shape of the temperature distribution is given by the heat radiation. The most important parameter determining the amplitude of actuation is the thermal conductivity, weighted by the optical parameters of the substrate.

For the prototypes studied in Chapter 5, some commons materials like the BK7 or the FS substrate with standard dimensions will be relatively efficient materials. In the case of the FS material, the simulated response to an actuator of 1mm^2 with 0.1 W absorbed

power with a plate of 2" diameter for 10 mm thickness is a shape of 4.8 mm width with an amplitude of 400 nm.

Chapter 4

Thermally Deformable Mirror Design

In Chapter 3 we have defined the parameters of the spatial response of the system to the input power delivered by one actuator located at the center of the mirror. The response parameters are determined by the geometry of the system and by the substrate thermal and optical properties. This Optical Path Difference (OPD) over the substrate generated by one actuator i is called the *influence function* $I_i(r, \theta)$ of the system with i indicating the actuator number.

We now examine the interaction of a set of actuators. We establish the design requirements in order to perform an efficient matching correction with the TDM. We express them in terms of actuator density over the active area and propose a configuration for the prototypes.

4.1 Correction of a wavefront

The *influence matrix* $M(x, y)$ that contains the K influence functions of the K actuators represents the device actuation capability. They can be known by analytical simulations as in the previous chapter, or by experimental calibration of the TDM as we will do in Chapter 5. The analytical influence fonction $I_i(x, y)$ is given by:

$$I_i(x, y) = I_i(r, \theta) = g^i_{OPD}(r, \theta) \tag{4.1}$$

with $g^i_{OPD}(r, \theta)$ the phase deformation produced by the actuator i over the TDM substrate. When it is sampled with equal dimensions n_s in both dimensions of the Cartesian plan, I_i is a matrix of $n_s \times n_s$ points (see Fig.4.1), but it is often equivalently stored as a

vector of $n_s^2 \times 1$ dimensions. The influence matrix is then a three dimensional $n_s \times n_s \times K$

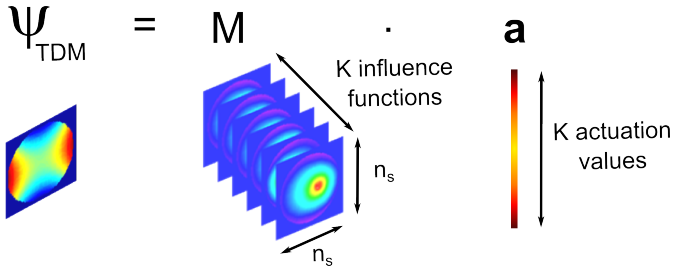

FIGURE 4.1: Construction of ϕ_{TDM} the wavefront deformation generated by the TDM from the interaction matrix M and the actuation vector $\mathbf{a}$.

matrix. The equivalent two dimensional representation is the $n_s^2 \times K$ matrix:

$$M_{2D} = \begin{bmatrix} I_1(1) & \cdots & I_i(1) & \cdots & I_K(1) \\ \vdots & \cdots & \vdots & \cdots & \vdots \\ I_1(j) & \cdots & I_i(j) & \cdots & I_K(j) \\ \vdots & \cdots & \vdots & \cdots & \vdots \\ I_1(n_s^2) & \cdots & I_i(n_s^2) & \cdots & I_K(n_s^2) \end{bmatrix} \tag{4.2}$$

The phase deformation can be described by a linear superposition of the influence functions of the mirror through the interaction matrix:

$$\phi_{TDM} = M \cdot \mathbf{a} = \sum_{i=1}^{K} I_i(x,y) a_i \tag{4.3}$$

with $\mathbf{a} = (a_1, \cdots, a_i, \cdots, a_K)$ the actuation vector driving the K actuators (see Fig.4.1).

Correcting an aberrated wavefront amounts to produce the opposite phase deformation with the active device. To fit the incident wavefront ϕ_i, the deformable mirror has to generate a phase deformation ϕ_{TDM} that minimizes the wavefront error ϕ_e:

$$\phi_e = \phi_i - \gamma \phi_{TDM} \tag{4.4}$$

with the angle of incidence θ_i of the wavefront is given through $\gamma = 2\cos(\theta_i)$. We consider that the correction is performed under normal incidence and that the factor 2 is included in the TDM phase deformation, leading to $\gamma = 1$.

The deformation every actuator has to create is calculated in order to tune individually the power coupled into the substrate. For the moment, we suppose that any wavefront deformation produced by the device is a linear combination of the influence functions. This will be checked experimentally in Chapter 5. Thus, finding the best values of actuation that will produce a known wavefront deformation, in sense of the least-square

algorithm, is a basic problem in adaptive optics [58–60]. The general least-square solution is the actuation vector $\mathbf{a}$ that minimizes the error ϵ:

$$\epsilon = \|\phi_e\|_2^2 = \sum_{k=1}^{n_s}\sum_{l=1}^{n_s}(\phi_i(k,l) - \phi_{TDM}(k,l))^2 \tag{4.5}$$

That is, with Eq. 4.3:

$$\epsilon = \frac{1}{n_s^e}\sum_{k=1}^{n_s}\sum_{l=1}^{n_s}(\phi_i(k,l) - M(k,l)\cdot\mathbf{a})^2 \tag{4.6}$$

We obtain analytically, minimizing ϵ:

$$\mathbf{a} = (M^t M)^{-1} M^t \phi_i \tag{4.7}$$

The inversion of the influence matrix can lead to ill-conditioned problem. It will be discussed in Chapter 5.

The quality of the correction can be evaluated through the characteristics of the wavefront error ϕ_e, that would be ideally flat. The mean value of the correction that is equivalent to a flat phase shift of the wavefront, or piston, is not relevant since it is not seen by the correction system. So, the root mean square of ϕ_e is a good figure of merit of the correction:

$$\sigma_e = \sqrt{\epsilon} \tag{4.8}$$

for a wavefront sampled in $n_s \times n_s$ points.
The spectral content of the wavefront error gives information on the residual pattern that will remain in the corrected wavefront. We define the spectra of the correction through the 2-dimensional Fourier transform of ϕ_e:

$$\mathcal{S}_e = \mathcal{F}[\phi_e(x,y)] \tag{4.9}$$

4.2 Key features of the correction

In addition to its dependence on the influence function parameters, the TDM performance will depend on the number and density of actuators. We can intuitively say that the higher the density, the better the reproduction of the incident wavefront will be.

4.2.1 Spatial transfer function of the TDM

Following the work of [61] and [62], a deformable mirror can be considered as a high-pass step filter for the wavefront aberrations, whose the frequency threshold is the inverse of twice the actuator spacing or *pitch* δ (see Fig.4.2). This simplified approach allows to have a rule of thumb of the mirror behavior: the low spatial frequencies will be compensated by the TDM whereas it will not be able to correct frequencies higher than the inverse of twice the actuator spacing.

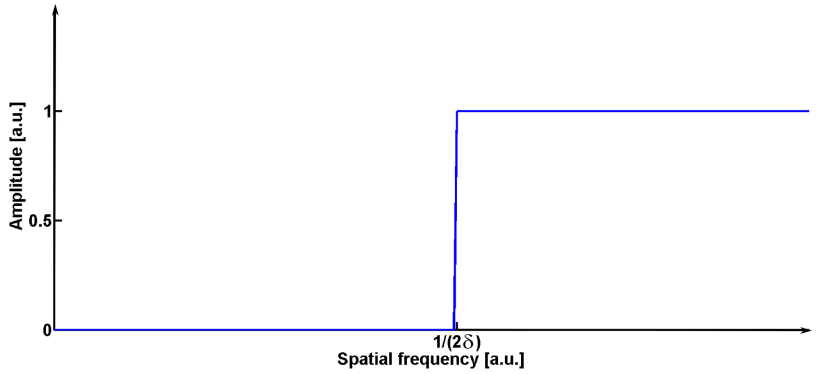

FIGURE 4.2: Ideal high-pass step filter of a deformable mirror with actuators spaced by the distance δ. The ideal wavefront correction leads to a null transfer function below the threshold frequency $1/(2\delta)$.

Nevertheless, an exact expression can be found for the mirror transfer function [61]. Applying the Fourier transform to Eq. 4.4, the exact transfer function of the mirror characterized by the interaction matrix M is:

$$H_{TDM} = \frac{\mathcal{F}[\phi_e]}{\mathcal{F}[\phi_i]} = \left[1 - \frac{\mathcal{F}[M \cdot \mathbf{a}]}{\mathcal{F}[\phi_i]}\right] \tag{4.10}$$

It clearly appears from Eq. 4.10 that the transfer function depends on the incident wavefront ϕ_i. The analysis of the TDM has then to be made with respect to a given input. In the following, the performance of the deformable mirror is expressed relatively to some standard aberrations, related to the basis of the Zernike polynomials (see Section 4.3). But first, a simple model in one dimension will show the relative importance of the design parameters.

We consider a regularly deformed wavefront, like a sinusoid, of fixed spatial frequency f_{WF}. The actuators are a 1 D representation of the influence functions previously computed from the Finite Element Analysis (FEA) model. They are spaced by an initial distance $\delta = \delta_0$: the mirror design frequency is then $f_m = 1/\delta_0$. The amplitude of actuation is computed by the least-square approach of Section 4.1.

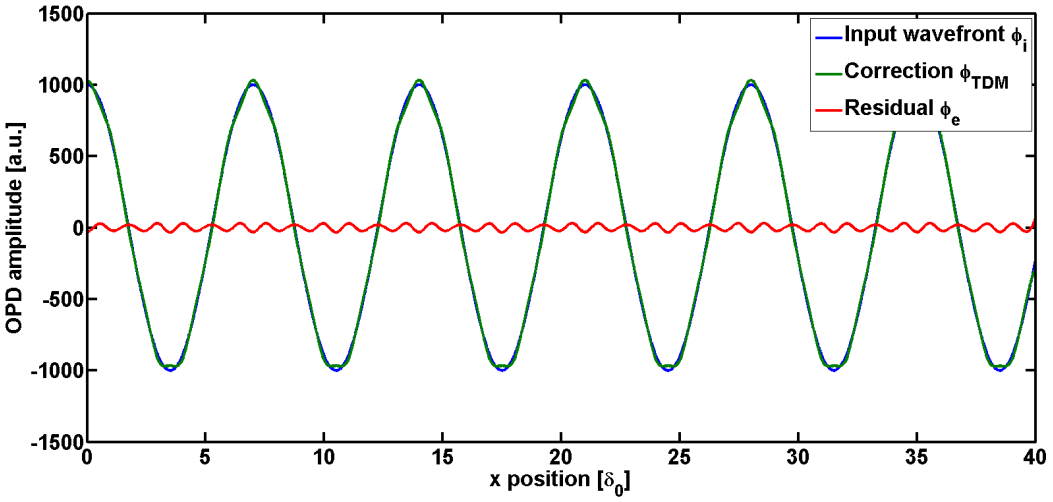

FIGURE 4.3: Illustration of the foot print produced by the TDM correction: the residual (or output) wavefront in red contains a new frequency $f_p = 1/\delta_0$

4.2.2 Illustration of the footprint

First, we choose $\delta_0 = 1/(7f_{WF})$, such as to have the ideal cut-off frequency of the TDM $f_c = 1/(2\delta_0)$ higher than f_{WF}. The incident wavefront, the correction generated by the actuators and the residual wavefront are represented in Fig.4.3. The correction of the input frequency is performed properly: the RMS of the wavefront σ_e is reduced by a factor 40. However, we notice the appearance of a new sinusoid line, whose period is δ_0, that was initially not in the spectrum. It is clearly related to the actuator pattern and is called the *footprint* of the actuators. Consequently the TDM will inject in the corrected wavefront high spatial frequencies at $f_p = 1/\delta_0$, that is above its ideal correction frequency capability f_c.

4.2.3 Effect of the density

To highlight the impact of the actuator density on the correction efficiency, the pitch δ is made varying from 0.01 δ_0 to 10 δ_0. With respect to the input wavefront frequency, the cut-off frequency of the ideal equivalent high-pass step filter would be $f_c = 2/(7\delta_0)$ that is a pitch of 3.5 δ_0.

The RMS σ_e of the residual wavefront increases with the increase of the pitch up to reach the value of the input wavefront RMS when the correction becomes completely inefficient after 5 δ_0 (see Fig.4.4a). Up to the ideal f_c, the correction ratio is better than 0.8. However, one can expect to reduce the incident wavefront RMS by a factor 10 for example to obtain a satisfactory correction. In this case, the minimum inter-actuator distance required will be about 1.5 δ_0.

The observation of the spectrum $\mathcal{S}_e$ gives information about the dominant frequency. As

expected, it corresponds to the footprint f_p and is shifted towards the high-frequencies when the pitch decreases (see Fig.4.4b). Above the ideal cut-off frequency f_c, the spectrum is dominated by the frequency of the input wavefront f_{WF}, meaning that the input wavefront is no more corrected.

According to these graphs, we can say that the TDM can perform a correction up to δ of about 3 δ_0 with $\sigma_e \simeq 0.6\ \sigma_i$. That corresponds to an inter-actuator distance close the one given by the rule of thumb. The density of actuators confirms to have a huge impact on the TDM performance.

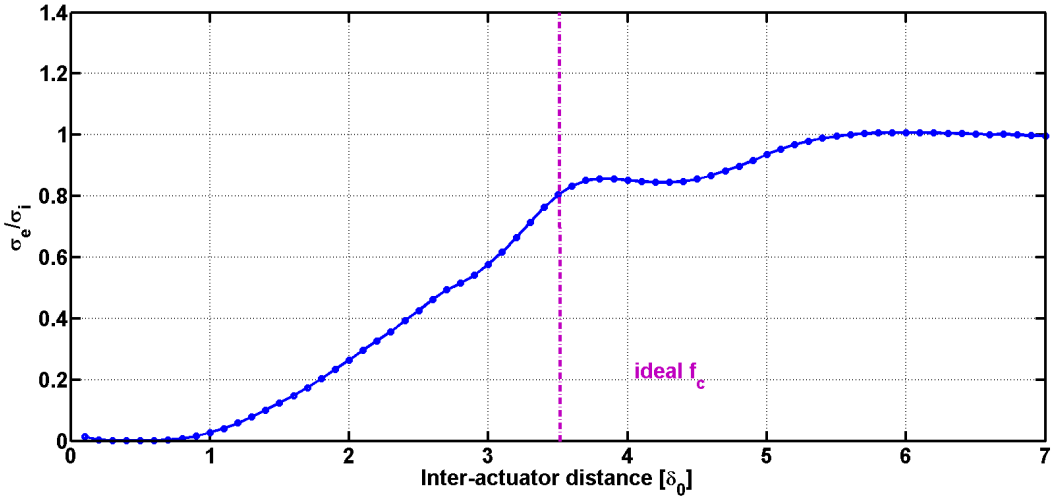

(A) Ratio of the residual wavefront RMS on the input wavefront RMS as a function of the inter-actuator period. The RMS of the residual wavefront σ_e increases with the decrease of the density. The first point is due to a numerical problem.

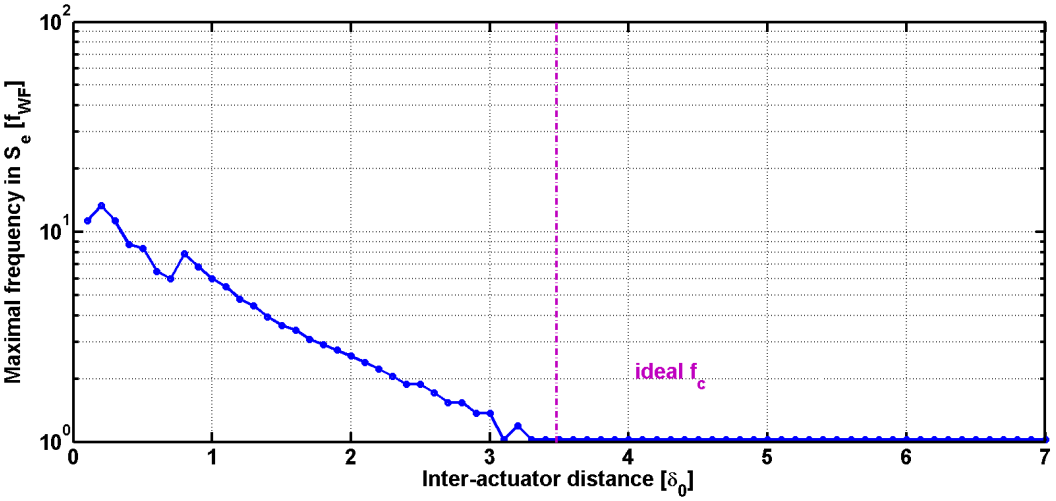

(B) Dominant frequency in the spectra $\mathcal{S}_e$ of the residual wavefront as a function of the inter-actuator period: above the ideal cut-off frequency, the spectra is dominated by the input wavefront frequency f_{WF}.

FIGURE 4.4: Study of the inter-actuation distance impact on the correction

4.2.4 Effect of the coupling

For a given actuator density, the correction will be affected by the size and shape of the influence functions. This can be evaluated by the *actuator coupling*, that is the deformation produced at the site of an actuator by its neighbor actuator. It can be defined through the equation (autocorrelation or overlap integral, see Fig.4.5b):

$$R = (I(x) * I(-x))(\delta) = \int_{-\infty}^{\infty} I(x)I(x-\delta)\mathrm{d}x \tag{4.11}$$

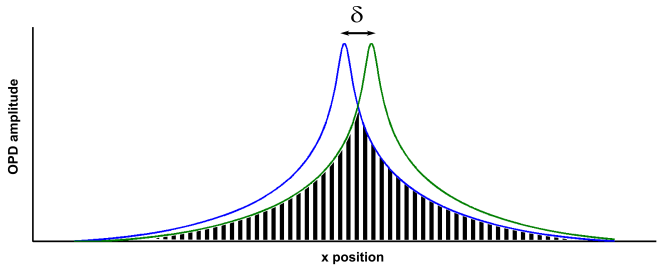

(A) Representation of the inter-actuator coupling by the hatched area for two actuators separated by a pitch δ.

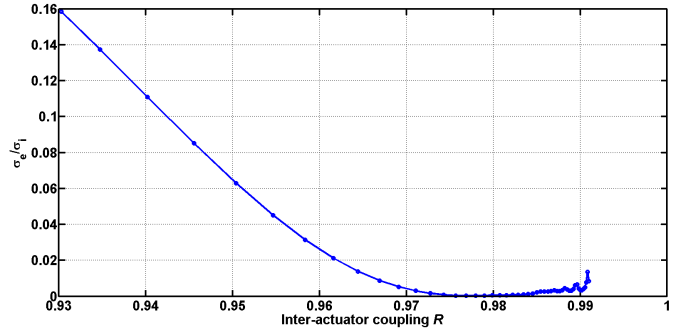

(B) Evolution of the correction ratio σ_i/σ_e as a function of the inter-actuator coupling R. The best configuration is obtained when the coupling is about 0.98. The actuator pitch is $\delta = \delta_0$ and the input wavefront frequency is $f_{WF} = 1/(7\delta_0)$.

Here the amount of coupling is determined by the size of the resistors, filtered by the thermal response of the mirror. The reference coupling R_0 is equal to 0.97 and corresponds to an actuator of 1 mm side. For a coupling varying of 5%, the correction ratio σ_e/σ_i decreases by 16%. The actuator size is varying from a factor 100. The best correction ratio is obtained for a coupling of about 0.98. The coupling will always have the tendency to be high in the TDM, due to the intrinsic width of the thermal actuation.

4.2.5 Lateral shift of the wavefront

The last effect is the lateral position of the wavefront with respect to the actuators. Back to the initial configuration with the coupling R_0, the actuator pitch δ_0 and the input wavefront frequency $f_{WF} = 1/(7\delta_0)$, the input wavefront is laterally shifted by

from 0 to δ_0. The relative variation of σ_e is lower 3%. In this case, the relative position has then a very small impact on the correction performance. But it could have in case of non asymmetric aberrations and a device with privileged correction directions.

4.2.6 Conclusion

We have estimated the relative influence of some parameters on σ_e and $\mathcal{S}_e$ in a naive model: the density of actuators f_m is extremely decisive for the quality of the correction performed by the mirror, especially for the amplitude of the output wavefront. It also determines the value of the footprint frequency. It has then to be carefully choose to meet the system performance requirements. The lateral position of the incoming wavefront with respect to the actuators has a low impact on the correction in this model. The actuator size, that is affecting the coupling which will be relatively high, has to be carefully chosen. Now we have a better understanding of the some key parameters and we can perform the analysis in two dimensions for realistic incoming wavefront.

4.3 Optical system aberrations

4.3.1 Aberrations defined in the Zernike polynomial basis

Here we call *high order aberration* any difference between the wavefront of a laser beam and the corresponding ideal laser beam having the same curvature and divergence. That means that the divergence correction as well as the tip/tilts are not taken into account into the evaluation of the corrective device performance. Furthermore, this allows us to work at the beam waist as a reference position. In this plane, any aberration can be completely expressed by a unique decomposition in a given orthogonal basis.

In the context of an optical system that has a finite aperture dimension under homogeneous illumination, like a telescope or more generally any imaging optical system, an analysis of the aberrations with a basis of orthogonal polynomials, for example the Zernike polynomials, is a very useful tool for the wavefront description. In the other hand however, for a Gaussian beam whose the intensity is no more uniform, more suitable bases to describe the beam composition are the Hermite-Gauss basis in the Cartesian coordinates or the Laguerre-Gauss basis in cylindrical coordinates. The Zernike inform about the phase content whereas the Hermite-Gauss describe a complex field. The relation between the Hermite-Gauss mode description and the Zernike description is therefore not straightforward.

Then, we will try to overcome this difficulty by studying a laser beam with the assumption of small amplitude aberrations occurring in a given plane for a perfect Gaussian beam amplitude. To work with the Zernike polynomials, we will see how we can restrain the study pupil area as a function of the beam waist w_0. The impact on the Hermite-Gauss composition will be studied in Chapter 6.

The Zernike polynomials define a complete orthogonal basis over the unit circle. They are frequently used to describe the aberrations of an optical system, since the first polynomials directly correspond to the fundamental aberrations (see Table 4.1). A wavefront can be expressed in terms of Zernike polynomials according to [7]:

$$\phi(r,\theta) = \sum_{n,m} c_{nm} Z_n^m(r,\theta) \tag{4.12}$$

where c_{nm} are the expansion coefficients, n, m are integers with $n \geq |m|$ and with $n-|m|$ even. The polar coordinates (r,θ) are restricted to $0 \leq r \leq 1$. The Zernike polynomials are:

$$Z_n^m(r,\theta) = R_n^{|m|}(r) \begin{cases} N_n^m \sin(m\theta) & \text{for } m < 0 \\ -N_n^m \cos(m\theta) & \text{for } m \geq 0 \end{cases} \tag{4.13}$$

where $\sin(m\theta)$ and $\cos(m\theta)$ are the azimuthal functions and the radial functions $R_n^{|m|}$ are:

$$R_n^{|m|} = \sum_{s=0}^{(n-|m|)/2} (-1)^s \frac{(n-s)!}{s!(\frac{n+|m|}{2}-s)!(\frac{n-|m|}{2}-s)!} r^{n-2s} \tag{4.14}$$

The N_n^m normalization factor is chosen in order to have:

$$\int_{r=0}^{1}\int_{\theta=0}^{2\pi} Z_n^m(r,\theta)^2 r \mathrm{d}r\mathrm{d}\theta = 1 \quad \text{that is} \qquad N_n^m = \sqrt{\frac{(2-\delta_{m,0})(n+1)}{\pi}} \tag{4.15}$$

It means that the RMS of the wavefront can be easily accessed through the decomposition:

$$\mathrm{RMS}(\phi) = \sqrt{\sum_{n,m} c_{n,m}^2} \tag{4.16}$$

The first Zernike polynomials are reported in Table 4.1, where we use the single index classification of the ANSI standard with the index j:

$$j = \frac{n(n+2)+m}{2} \tag{4.17}$$

The order of the polynomials corresponds to the constant values of n. The spatial representation of the Zernike polynomials is given in Appendix B.

order	j	m	n	Z_n^m	Optical Name
0	0	0	0	1	Piston
1	1	-1	1	$r\cos(\theta)$	Tilt
	2	1	1	$r\sin(\theta)$	Tilt
2	3	-2	2	$r^2\cos(2\theta)$	Astigmatism
	4	0	2	$2r^2-1$	Focus/Field curvature
	5	2	2	$r^2\sin(2\theta)$	Astigmatism
3	6	-3	3	$r^3\cos(3\theta)$	Trefoil
	7	-1	3	$(3r^3-2r)\cos(\theta)$	Coma
	8	1	3	$(3r^3-2r)\sin(\theta)$	Coma
	9	3	3	$r^3\sin(3\theta)$	Trefoil
4	10	-4	4	$r^4\cos(4\theta)$	Quadrifoil
	11	-2	4	$(4r^4-3r^2)\cos(2\theta)$	2^{nd} order astigmatism
	12	0	4	$6r^4-6r^2+1$	Spherical aberration
	13	2	4	$(4r^4-3r^2)\sin(2\theta)$	2^{nd} order astigmatism
	14	4	4	$r^4\sin(4\theta)$	Quadrifoil
5	15	-5	5	$r^5\cos(5\theta)$	Pentafoil
	16	-3	5	$(5r^5-4r^3)\cos(3\theta)$	2nd order trefoil
	17	-1	5	$(10r^5-12r^3+3r)\cos(\theta)$	2nd order coma
	18	1	5	$(10r^5-12r^3+3r)\sin(\theta)$	2nd order coma
	19	3	5	$(5r^5-4r^3)\sin(3\theta)$	2nd order trefoil
	20	5	5	$r^5\cos(5\theta)$	Pentafoil

TABLE 4.1: Zernike polynomials table

4.3.2 Size of the aperture pupil

According to the standard methods used in adaptive optics the mirror performance is evaluated through the Zernike description. As the polynomials are defined over the unit circle, we need to define the aperture pupil of our system. The radius of this active area required to correct the aberrations properly can be inferred by the amount of beam power we would like to control. The Gaussian power distribution of a laser beam at the waist w_0 is expressed over a radius a as a function of the total power P_0:

$$P(a) = \int_{r=0}^{a}\int_{\theta=0}^{2\pi} I(r,\theta) r \mathrm{d}r\mathrm{d}\theta \tag{4.18}$$

$$P(a) = 2\pi\ I_0 \int_{r=0}^{a} r e^{-2\frac{r^2}{w_0^2}}\mathrm{d}r \tag{4.19}$$

$$P(a) = P_0\left(1-e^{-2\frac{a^2}{w_0^2}}\right) \qquad P_0 = \frac{1}{2}\pi w_0^2 I_0 \tag{4.20}$$

with I_0 the maximum intensity at the beam center with coordinates (0,0). The pupil radius r_p is then defined by:

$$r_p = w_0\sqrt{-\frac{1}{2}\ln\left(1-\frac{P}{P_0}\right)} \tag{4.21}$$

For a correction that acts on at least 99% of the power and at maximum 99.9% of the power, we have a reasonable radius of the the aperture pupil r_p:

$$0.99 \leq P_{corr} \leq 0.999 \tag{4.22}$$

$$1.52\ w_0 \leq r_p \leq 1.86\ w_0 \tag{4.23}$$

In the case of a 2.6 mm beam waist, the active area is within the interval of 4 and 4.8 mm radius. The minimum power $P_{min} = 0.99$ will be used in the following to give the minimum requirements on the actuation spatial frequency and amplitude.

Prototypes Now, we anticipate the prototypes described in the Chapter 5. They have respectively an active area of 9 mm and 10.6 mm diameter and are then within the specifications for the power correction. However, in the Zernike description, the high spatial frequencies are located at the circumference [63, 64]. This implies to have an aperture pupil smaller than the active area to benefit from extra-actuators at the edge of the pupil. The actuators being about 1×1 mm^2, we restrict the aperture pupil to respectively 7 mm and 8.2 mm diameter. In the following of this chapter, focused on the Zernike description, we will use this radius to compute the efficiency of correction and to design the TDMs. In Chapters 6 and 7 focused on the mode matching, the description will be different and the aperture pupil will not be relevant any more.

The Hermite-Gaussian TEM_{mn} modes have a spatial expansion that depends on their indexes n, m. In order to correct the beam up to the order $n + m = 5$, the pupil radius might be increased by a factor $\sqrt{\max(n, m)} = \sqrt{5}$. Here, we expect to have mainly a Gaussian beam with a small amount of high order modes, such as the beam dimension is dominated by the fundamental mode.

4.3.3 Spatial frequency requirements

4.3.3.1 Characteristic spatial frequency

For each order, the Zernike can be characterized by their spatial frequency. The spectrum of the Zernike polynomials depends on the Bessel functions of the first kind [65]:

$$\mathcal{F}[Z_n^m(r,\theta)] = \frac{J_{n+1}(2\pi k)}{\pi k} \begin{cases} i^m(-1)^{\frac{n-m}{2}} \sin(m\eta) & \text{for } m < 0 \\ i^m(-1)^{\frac{n-m}{2}} \cos(m\eta) & \text{for } m \geq 0 \end{cases} \tag{4.24}$$

Each Zernike polynomial depends on the azimuthal spatial frequency η (through $\cos(m\eta)$ or $\sin(m\eta)$) and on the radial spatial frequency k by $\frac{J_{n+1}(2\pi k)}{\pi k}$. For each Zernike order

	Prototype 1	P_{min}		Prototype 2	P_{max}	
	$\mathbf{r_p = 1.35w_0}$	$\mathbf{r_p = 1.52w_0}$		$\mathbf{r_p = 1.58w_0}$	$\mathbf{r_p = 1.86w_0}$	
Order	[mm]	[mm]	$[w_0]$	[mm]	[mm]	$[w_0]$
2	3.0	3.4	(1.3)	3.6	4.2	(1.6)
3	2.3	2.6	(0.99)	2.7	3.2	(1.2)
4	1.8	2.1	(0.8)	2.2	2.5	(0.98)
5	1.6	**1.8**	(0.67)	1.8	2.1	(0.82)

TABLE 4.2: Maximum actuator pitch δ^n_{max} requirements as a function of the Zernike order n. The distance are given in mm for the first and second prototypes with a waist $w_0 = 2.6$ mm and are also indicated as a multiple of the waist for the limits in the pupil.

n, the dominant spatial frequency k_0 corresponds to the maximum of $\frac{J_{n+1}(2\pi k)}{\pi k}$ (see Fig.4.6): it is the minimum spatial frequency a corrective device must achieve to have a chance to correct properly the order n. According to the ideal high-pass step filter, the maximum actuator pitch δ^n_{max} required is then at the order n:

$$f^n_{min} = 2k_0 \quad \Leftrightarrow \quad \delta^n_{max} = \frac{1}{2k_0}$$

The results are given in Table 4.2 for the different pupil radius encountered in this chapter. In order to correct the Zernike up to the order $n = 5$, the pitch has to be at maximum of 1.6 mm in the case of the smallest pupil. However, this is just a rough indication of the spatial density of the degree of actuation required and gives the lower limit on our model. We are now able to refine our design.

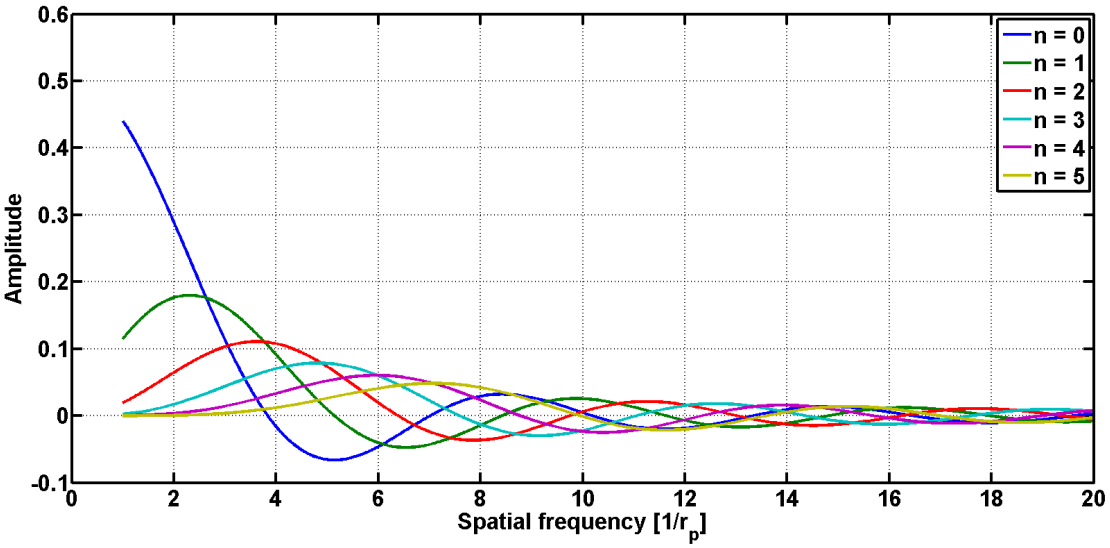

FIGURE 4.6: Spectrum of the Zernike over the unit circle for the different orders n: amplitude of the $\frac{J_{n+1}(2\pi k)}{\pi k}$ as a function of the spatial frequency $1/r$.

4.3.3.2 Maximal effective spatial frequency

When looking at the Zernike polynomials, it should be noted that the spatial frequency content is quite different between the polynomials of a same order: the characteristic spatial frequency does not provide information about the effective maximal frequency the Zernike contained in each mode.

This can be found by solving the radial expressions Z_n^m. For example, if we consider the polynomials of the 3^{rd} order, we have:

$$Z_3^{-1} = (3r^3 - 2r)\cos(\theta) = 0 \tag{4.25}$$

$$Z_3^{-3} = r^3 \cos(3\theta) = 0 \tag{4.26}$$

For those polynomials that have zeros along their radial dimension (other than 0), we retain the zero closest to the perimeter, that gives the highest spatial frequency. We are also only interested in the positive solutions since the polynomials are identical by symmetry. For example, from the roots of Eq. 4.25 $r_0 = \{0; \pm\sqrt{2/3}\}$, we focus on $r_0 = \sqrt{2/3}$. The maximum pitch $\delta_{max}^{n,m}$ is then given by the distance to the perimeter divided by 2 (high-pass step filter rule):

$$\delta_{max}^{n,m} = r_p(1 - r_0)/2 \tag{4.27}$$

For the polynomials that do not have zeros other than 0, for example Eq. 4.26, the dominant spatial frequency is given by the frequency $\theta_0 = 1/n$ of the azimuthal term (sine or cosine) at the circumference. The pitch is given by:

$$\delta_{max}^{n,m} = \pi r_p \theta_0 \tag{4.28}$$

In Table 4.3 we compute $\delta_{max}^{n,m}$ for the different pupil sizes. We can see that when the order of the polynomial increases, the zero position is going closer to the edges. This greatly changes the requirements, since in the maximum pitch between actuators has to be 0.1 mm to correct the maximum spatial frequency of the highest Zernike polynomial.

We are now able to give the spatial resolution requirements for our device with the minimum spatial frequency, from the characteristic Zernike frequency, and the maximum spatial frequency, from the highest frequency of the Zernike. The value of maximum spatial frequency gives very stringent constraints, that will be difficult to implement. Fortunately, these high frequencies are located at the circumference of the pupil. With the weighting of the Gaussian beam in the matching computation, they will likely not

		Prototype 1	P_{min}		Prototype 2	P_{max}	
		$\mathbf{r_p = 1.35w_0}$	$\mathbf{r_p = 1.52w_0}$		$\mathbf{r_p = 1.58w_0}$	$\mathbf{r_p = 1.86w_0}$	
Polynomial	Zeros	[mm]	[mm]	[w_0]	[mm]	[mm]	[w_0]
3	$\theta_0 = 1/4$	2.8	3.1	(*1.2*)	3.2	3.8	(*1.5*)
4	$r_0 = \sqrt{2}/2$	0.5	0.6	(*0.2*)	0.6	0.7	(*0.3*)
5	$\theta_0 = 1/4$	2.8	3.1	(*1.2*)	3.2	3.8	(*1.5*)
6	$\theta_0 = 1/6$	1.8	2.1	(*0.8*)	2.2	2.5	(*1.0*)
7	$r_0 = \sqrt{2}/3$	0.3	0.4	(*0.1*)	0.4	0.4	(*0.2*)
8	$r_0 = \sqrt{2}/3$	0.3	0.4	(*0.1*)	0.4	0.4	(*0.2*)
9	$\theta_0 = 1/6$	1.8	2.1	(*0.8*)	2.2	2.5	(*1.0*)
10	$\theta_0 = 1/8$	1.4	1.6	(*0.6*)	1.6	1.9	(*0.7*)
11	$r_0 = \sqrt{3}/2$	0.2	0.3	(*0.1*)	0.3	0.3	(*0.1*)
12	$r_0 = \sqrt{(3+\sqrt{3}/2)}$	0.2	0.2	(*0.1*)	0.2	0.3	(*0.1*)
13	$r_0 = \sqrt{3}/2$	0.2	0.3	(*0.1*)	0.3	0.3	(*0.1*)
14	$\theta_0 = 1/8$	1.4	1.6	(*0.6*)	1.6	1.9	(*0.7*)
15	$\theta_0 = 1/10$	**1.1**	1.2	(*0.5*)	1.3	1.5	(*0.6*)
16	$r_0 = 2/\sqrt{5}$	**0.2**	0.2	(*0.1*)	0.2	0.3	(*0.1*)
17	$r_0 = \sqrt{(6+\sqrt{6})/10}$	**0.1**	0.2	(*0.1*)	0.2	0.2	(*0.1*)
18	$r_0 = \sqrt{(6+\sqrt{6})/10}$	**0.1**	0.2	(*0.1*)	0.2	0.2	(*0.1*)
19	$r_0 = 2/\sqrt{5}$	**0.2**	0.2	(*0.1*)	0.2	0.3	(*0.1*)
20	$\theta_0 = 1/10$	**1.1**	1.2	(*0.5*)	1.3	1.5	(*0.6*)

TABLE 4.3: Maximal actuator pitch $\delta^{n,m}_{max}$ requirements for correction according to the zero position for each Zernike polynomial. The distance are given in mm for the first and second prototypes with a waist $w_0 = 2.6$ mm and are also indicated as a multiple of the waist for the limits in the pupil.

be dominant and the characteristic frequencies will have more importance as we will see in Section 4.4.1.

4.3.4 Amplitude requirements

We have seen in Chapter 1 that the expected power mismatch in Advanced Virgo is about 10%, mainly composed of focus. If we assume that the mismatch in a given plane is carried only by one type of aberration, we can compute the corresponding Zernike amplitude. We suppose that the phase aberration $\phi(r,\theta)$ is only contained in the aperture pupil:

$$\phi_{r_p}(r,\theta) = \begin{cases} Z^m_n(r,\theta) & \text{for } r \leq r_p \\ 0 & \text{for } r > r_p \end{cases} \tag{4.29}$$

and we compare the aberrated beam ϕ with the fundamental beam ϕ_0 resonant in the cavity at the waist plane (z = 0):

$$\phi_{w_0} = E_0 e^{-\frac{r^2}{w_0^2}} \tag{4.30}$$

$$\phi_{r_p,w_0} = \phi_{w_0} e^{-2i\frac{\pi}{\lambda}\phi_{r_p}(r,\theta)} \tag{4.31}$$

We remind here the power mismatch formula:

$$\eta^2_{r_p,w_0} = \left(\frac{|\int \phi_{r_p,w_0} \phi^*_{w_0} dS|^2}{\int |\phi_{r_p,w_0}|^2 dS \int |\phi_{w_0}|^2 dS} \right)^2 \tag{4.32}$$

that is:

$$\eta^2_{r_p,w_0} = \left(\frac{\left| \int_{r=0}^{\infty} \int_{\theta=0}^{2\pi} E_0 \exp\left(-\frac{r^2}{w_0^2} - 2i\frac{\pi}{\lambda}\phi_{r_p}(r,\theta)\right) r dr d\theta \right|^2}{\int_{r=0}^{\infty} \int_{\theta=0}^{2\pi} \left| E_0 \exp\left(-\frac{r^2}{w_0^2} - 2i\frac{\pi}{\lambda}\phi_{r_p}(r,\theta)\right)\right|^2 r dr d\theta \cdot \int_{r=0}^{\infty} \int_{\theta=0}^{2\pi} \left| E_0 \exp\left(-\frac{r^2}{w_0^2}\right)\right|^2 r dr d\theta} \right)^2 \tag{4.33}$$

With beam with a waist w'_0 different from w_0, if we choose a new $r'_p = r_p \frac{w'_0}{w_0}$ then it is straightforward that the mismatch is scaled invariant:

$$\eta^2_{r'_p,w'_0} = \eta^2_{r_p,w_0} = \eta^2_\alpha \qquad \text{for} \quad \frac{r'_p}{w'_0} = \frac{r_p}{w_0} = \alpha, \quad \alpha \in \mathcal{R}^*$$

It means that the amplitude is independent of the pupil radius and the beam waist if the ratio is preserved. The computed values are presented in Table 4.4 for a different ratio α, corresponding to the different active areas computed from Eq.4.22. The table can be used to specify any system with the same α where we want to maintain a matching better than 99%.

To correct a mismatch from 10% to better than 1% in power, we will need a device that is able to perform a correction of 600 nm PtV or 85 nm RMS in amplitude. However, we expect to have a mismatch mainly dominated by the focus term. It will likely be enough to have a design able to correct 5% of mismatching, so we can divided the amplitude requirements by 2.

4.4 Design analysis

From the simple computation above based on the Zernike polynomial properties, we are able to roughly determine the spatial frequency and amplitude requirements for a corrective device.

Now an accurate analysis can be performed using the influence function of the TDM in a systematic way. In the following, we study the effect of the actuator density and coupling to evaluate the theoretical performance of the prototypes. We implement a Matlab model that computes the actuation provided by the prototypes from the least-square minimization in each case presented thereafter and returns the residual mismatching.

	Prototype 1	P_{min}	Prototype 2	P_{max}
Index	$\mathbf{r_p = 1.35w_0}$	$\mathbf{r_p = 1.52w_0}$	$\mathbf{r_p = 1.58w_0}$	$\mathbf{r_p = 1.86w_0}$
3	278	346	384	535
	57	71	78	109
5	277	346	384	533
	57	71	78	109
6	332	444	514	841
	59	79	91	149
7	203	213	216	224
	36	38	38	40
8	203	213	216	224
	36	38	38	40
9	332	444	514	841
	59	79	91	149
10	365	521	625	1206
	59	83	99	192
11	249	279	293	336
	40	44	46	53
13	246	279	292	333
	40	44	46	53
14	369	522	628	1216
	59	82	99	192
15	396	584	727	1747
	57	85	105	252
16	291	346	373	473
	42	50	54	68
17	226	236	237	235
	33	34	34	34
18	226	236	237	235
	33	34	34	34
19	291	346	373	473
	42	50	54	68
20	396	**584**	727	1747
	57	**85**	105	252

TABLE 4.4: Amplitude (in nm) of the Zernike polynomials that are producing 10% of mismatch in power in a determined plane (no propagation). For each Zernike refered by the index j, the PtV is giving in the first row and the RMS in the second row (gray color), both in nm. The maximum peak-to-valley (PtV) is about 1.7 μm and the maximum RMS is about 260 nm.

Reference design In order to correct the Zernike aberrations up to the order 5, we need a minimum spatial frequency of actuation of 1.8 mm over the active pupil (see Table 4.2). According to the thermal simulations, the HWHM of actuation for a 1mm side actuator is about 2 mm, slightly depending on the substrate. We propose to study as a reference design 1 mm size actuators coupling power into a FS substrate. This design is a realistic objective for the building of the prototypes. A simple pattern for the TDM is to arrange the square actuators in square design. This gives for example the design of Fig.4.7. Other solutions may an hexagonal or a concentric pattern [24].

4.4.1 Correction characteristics with the reference design

4.4.1.1 Density study with 1 mm actuator size

For the aperture pupils corresponding to P_{min} and P_{max} with $w_0 = 2.6$ mm ($r_p^{min} = 1.52\ w_0 = 4$ mm and $r_p^{max} = 1.86\ w_0 = 4.4$ mm), we let the pitch varying from 1 mm to 2 mm for an actuator size of 1 mm. It is equivalent to the gap between actuators varying from 0 to 1 mm. In order to have actuators at the circumference of the pupil, the number of actuators varies to 10^2 to 7^2 actuators. This is presented in Fig.4.7. We study the correction in the case of the largest amplitudes (corresponding to P_{max}).

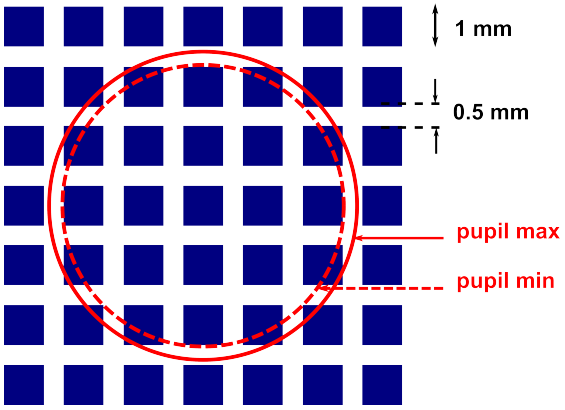

FIGURE 4.7: Example of the design for the gap of 0.5 mm with an actuator of 1x1 mm^2. There are 7^2 actuators. The aperture pupils corresponding to P_{min} and P_{max} are represented.

The correction efficiency is evaluated through the residual mismatch for the two pupil sizes (see Fig.4.8 and 4.9). We can see that the residual mismatch is lower than 1% for all Zernike if the gap is lower than 0.6 mm for the smallest aperture pupil. It is even lower than 0.1% for a gap maintained below 0.1 mm. For the largest aperture pupil, the results are very similar: the gap has also to be below 0.6 mm to maintain a mismatch lower than 1 %. This gives the requirements for an actuator size of 1mm.

4.4.1.2 Coupling study

As expected from the simulations with the simple model, there is an optimal trade-off between the size of the actuator and the gap to obtain the lowest mismatch. We make the actuator size varying from 50 μm to 1.5 mm and the gap varying from 0 to 1mm, and we compute the residual mismatch for each Zernike polynomial in each case. We retain the maximum mismatch over all Zernike. The results are presented in Fig.4.10 for $r_p = 4.0$ mm and in Fig.4.11 for $r_p = 4.4$ mm. We can see that the case where the constraints on the gap are the lowest ones is for a 1.5 mm actuator.

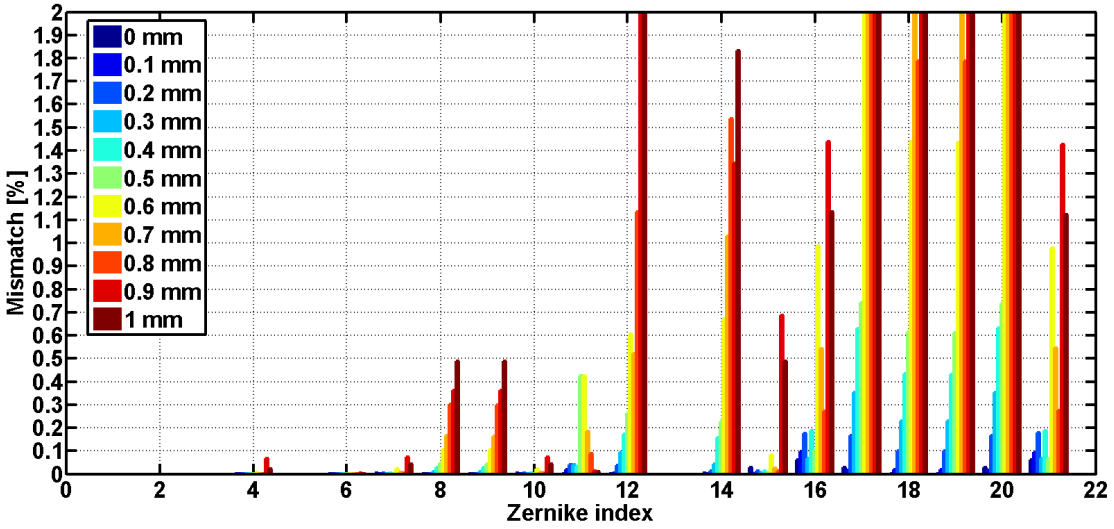

FIGURE 4.8: Pupil size $r_p^{main} = 4.0$ mm: Residual mismatch after the theoretical correction of the Zernike modes: the gap between actuators varies from 0 to 1 mm. The aperture pupil is 4 mm radius, corresponding to r_p^{min}. The actuators are 1 mm size with a FS substrate. The number of actuators varies from 9^2 to 5^2 in a square pattern.

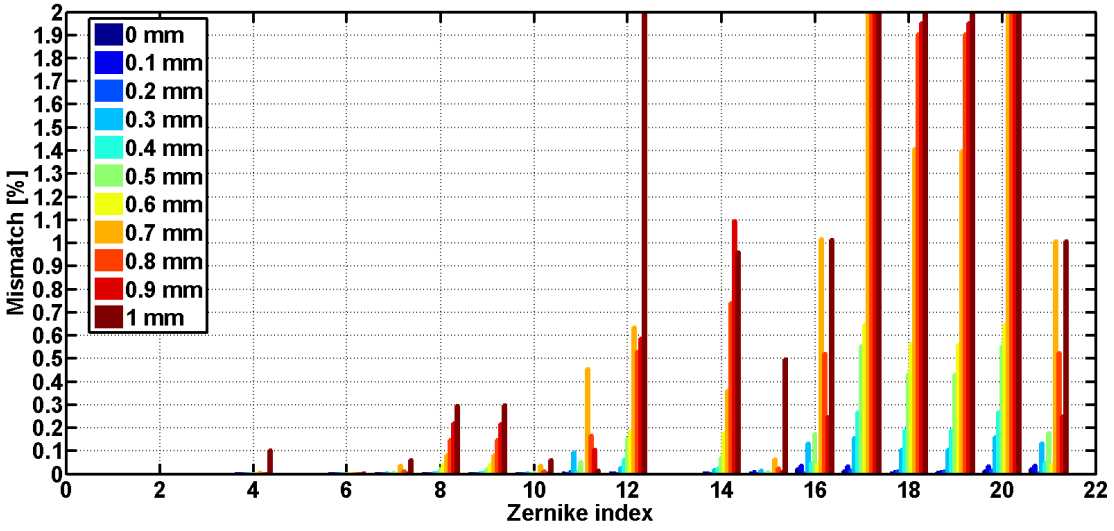

FIGURE 4.9: Pupil size $r_p^{max} = 4.4$ mm: Residual mismatch after the theoretical correction of the Zernike modes: the gap between actuators varies from 0 to 1 mm. The aperture pupil is 4.4 mm radius, corresponding to r_p^{max}. The actuators are 1 mm size with a FS substrate. The number of actuators varies from 10^2 to 5^2 in a square pattern.

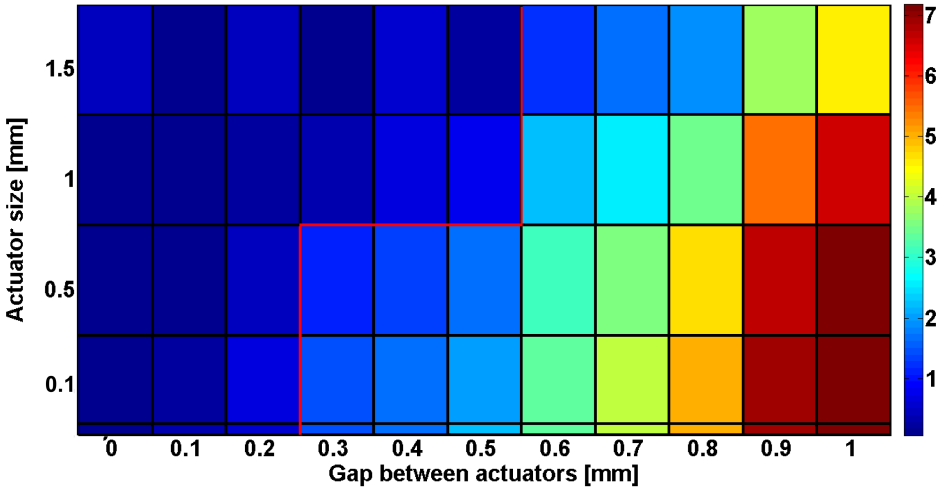

FIGURE 4.10: Pupil size $r_p^{min} = 4.0$ mm. Maximum residual mismatch after correction as a function of the actuator size and gap. The limits are marked by separation lines: mismatch equal or lower than 1% (red line). For an actuator of 1 mm, the maximum gap has to be 0.5 mm. For a gap of 0.5 mm, the best actuator size is 1.5 mm

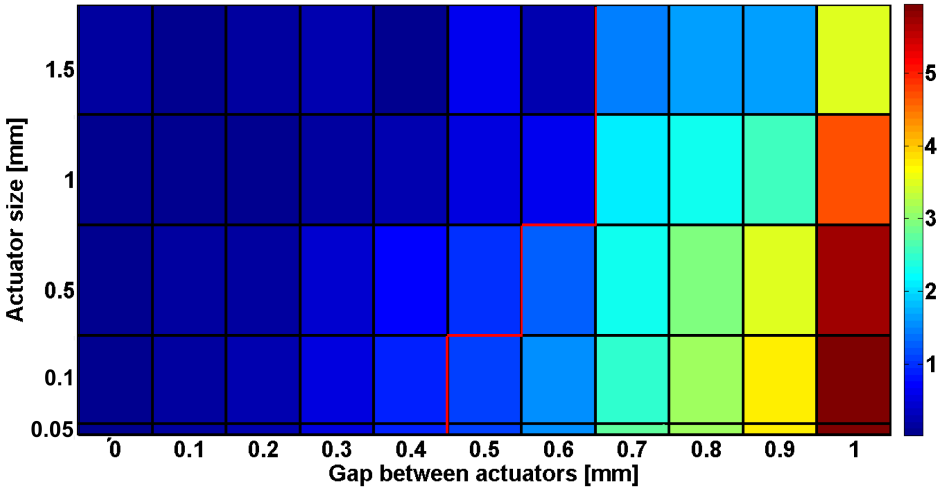

FIGURE 4.11: Pupil size $r_p^{max} = 4.4$ mm: Maximum residual mismatch after correction as a function of the actuator size and gap. The limits are marked by separation lines: mismatch equal or lower than 1% (red line). For an actuator of 1 mm, the maximum gap has to be 0.6 mm.

In conclusion of the study, we can say that for a size of 1 mm, the gap has to be maintain up to 0.5 mm. It corresponds to a spatial frequency of the actuation about 1.6 mm, that is in agreement with the characteristic spatial frequency of the Zernike computed in Section 4.3.3.

4.4.2 Prototypes for experimental demonstration

Design The prototypes that will be studied in the next chapter are build according to the design presented in Fig.4.12. The first prototype (respectively the second prototype) has the following features:

- the array is composed of a set of 61 actuators
- the size of the actuators is 0.9 × 0.9 mm^2 (respectively 1 × 1 mm^2)
- the gap between the actuators is 0.1 mm (respectively 0.2 mm)
- the active pupil area is a disk of 7 mm diameter (respectively 8.2 mm)

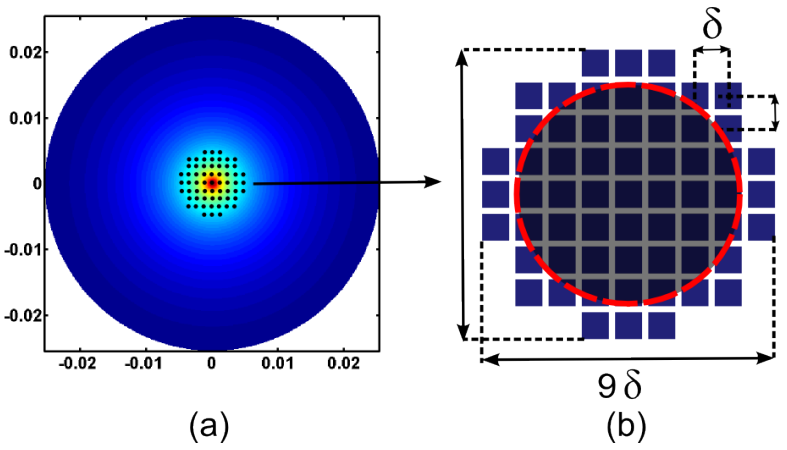

FIGURE 4.12: Prototype design for the TDM matrice array (a) actuator pattern with a FS substrate (2" diameter and 10 mm thickness) seen from the side of the actuators. The position of the actuators is indicated by the black holes (b) Zoom on the 61 actuators with the actuator pitch δ.

Expected performance We found that both designs allow to perform the required correction (see Fig.4.13), with a residual mismatch much lower than 1%. In the case of the first prototype, the worst correction is obtained for the mode 16 and 19. For the second prototype, the higher residual values are also for the mode 15 and 20. All these modes are from the order 5, that correspond to the highest spatial frequencies. But according to Table 4.3, we would have expect to have the worst correction for the mode 17, that contains the highest spatial frequency. By looking at the residual shapes (see Fig.4.15), we can see that the correction is dominated by the residual at the circumference of the pupil. For the other modes, the footprint of the actuators is clearly visible, demonstrating that we are at the limit of the correction.
It should be noticed that the actuation limits have not been set for this study.

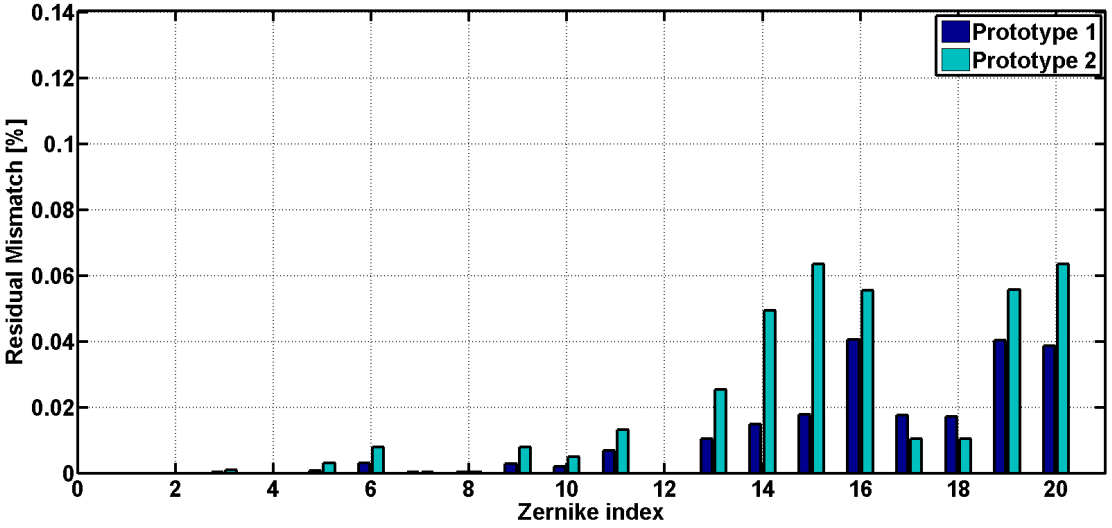

FIGURE 4.13: Theoretical residual mismatch for the Zernike modes after the correction has been performed for the two prototypes.

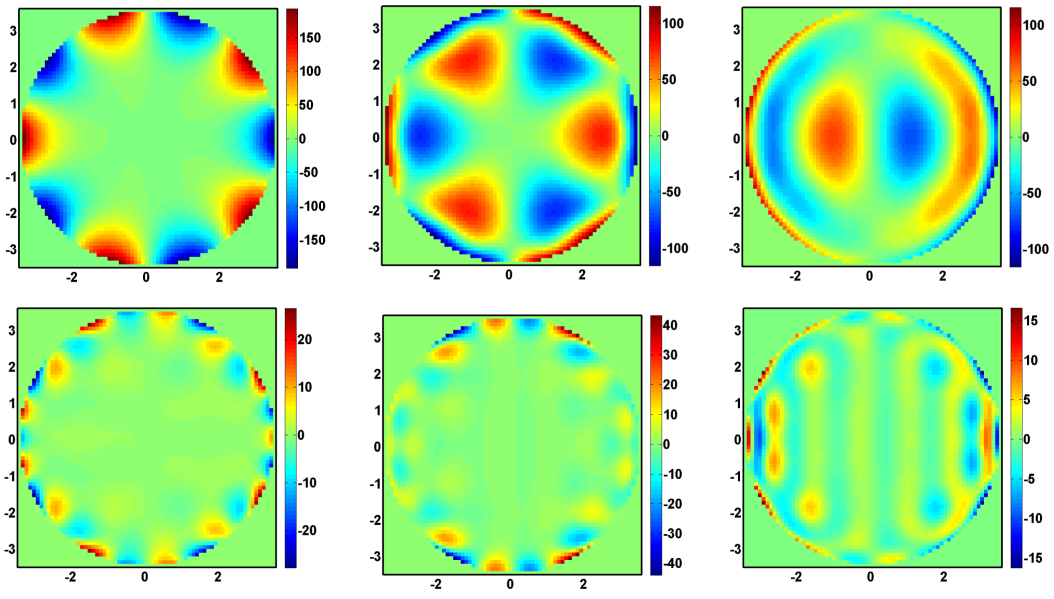

FIGURE 4.14: Simulation of the correction of the 5 order by the first prototype: the upper figures are the modes to be corrected and the lower figures are the residual shapes after correction: (a) Mode 15 (b) Mode 16 (c) Mode 17. Axis are in mm and the colorscale is in nm.

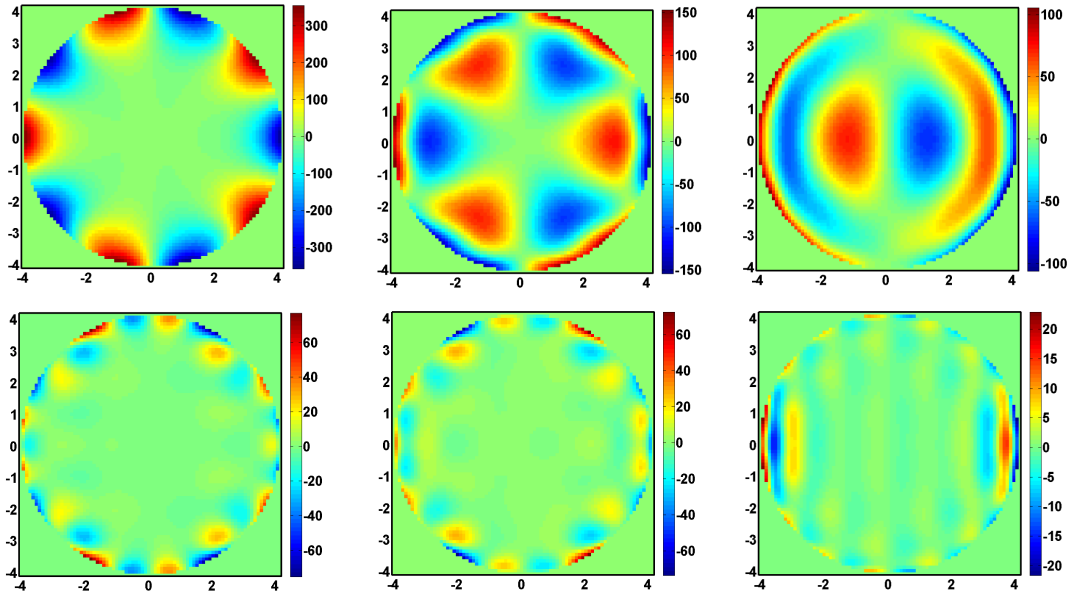

FIGURE 4.15: Simulation of the correction of the 5 order by the second prototype: the upper figures are the modes to be corrected and the lower figures are the residual shapes after correction: (a) Mode 15 (b) Mode 16 (c) Mode 17. Axis are in mm and the colorscale is in nm.

4.5 Conclusion

In this chapter, we have studied the main characteristics of the TDM. We have demonstrated that the size of the actuators and the distance between them are determinant for the quality of the correction.

We have proposed an active area to control at least 99% of the power of a Gaussian beam. The performance of the correction has been expressed in terms of Zernike polynomials. We infer from their properties that the spatial requirements are between 1.8 and 0.2 mm. To correct 10% of mismatching, the required amplitude has been found to be at least 580 nm PtV or 85 nm RMS. The gap and the dimension of the actuators have to be carefully chosen to optimize the correction ability. Furthermore, anticipating the experimental prototypes, we have demonstrated that their design allow to perform a correction that fulfills the Advanced Virgo needs.

Chapter 5

Thermally Deformable Mirror Experimental Performance

After the choice of the substrate and the determination of the geometry by the simulations, an experimental setup has been designed to test the performance of two TDM prototypes that have been successively realized. First, these prototypes and their main characteristics are presented in this chapter. Then we test the fundamental properties of the TDMs and determine the characteristics of their influence functions. Afterwards, we study the generation of Zernike polynomials by the TDMs in order to be finally able to deduce the mismatching correction they can perform.

5.1 Prototype description

All tests presented here are realized with two prototypes of the TDM designed to correct the aberrations of a 2.6 mm radius beam. The array of resistors can be put in contact with any kind of mirror substrate. Here we use a commercial fused silica with a 2" (50.8 mm) diameter, and 9.53 mm thick mirror with dielectric coatings. The mirror has a wedge of 3^o to separate any possible secondary reflections from the main probe beam. The first surface is coated with an AR coating, and the array of resistors is acting on the surface with a HR coating for 1064 nm. An interaction layer, like a glue or thermal paste, provides good contact between the resistors and the HR surface of the substrate.

5.1.1 First prototype

The actuators, made of resistive layers of 18 μm copper in contact with insulating layers of polyimide (Dupont Pyralux AP), are printed onto a multilayer flex circuit. The materials are designed to be used at a high temperature and could be manufactured to guarantee no outgassing of the circuit board under vacuum. This technology allows a high density of resistors: the actuation pattern is composed of 61 actuators of 0.9 mm x 0.9 mm each. The resistors are separated by a dead space of 100 μm (see Fig.5.1). They have a mean value of 400 Ω, with a standard deviation of 100 Ω for the whole sample (For example one of the tested array exhibits: R_{min} = 330 Ω, R_{max} = 850 Ω).
However, it should be noted that this prototype is relatively fragile: being at the limit of resolution of the layer deposition process, the technology leads to have a high dispersion in the quality of the resistors. It results in the heterogeneous values of resistors, whose some of them are easily burned.

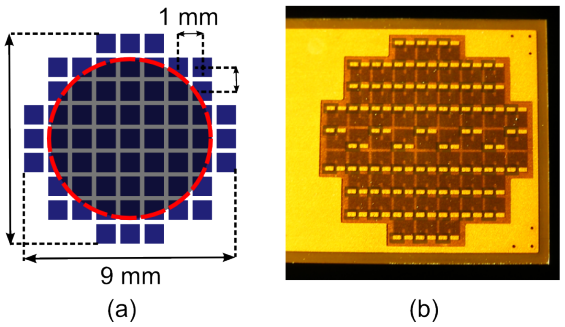

FIGURE 5.1: First prototype: (a) Scheme of the prototype array with the 61 resistors in blue and the pupil of observation defined by the area enclosed by the red circle. The resistors are separated by a dead space of 100 μm. (b) Picture of the prototype array

Temperature distribution To determine the distribution shape of the temperature dissipated by the resistors of the TDM array, we observed directly the TDM array in the focal plane of a ZnSe lens with a thermal camera (Fig 5.2 (a)). The temperature emission is not uniform: it looks horseshoe-shaped. It is easily explained by the structure of the resistor as made clear from Fig.5.2 (b). In the complete array, the orientation of the shapes is alternated according to the design of Fig.5.1 (b). No coupling between the resistors is apparent through this measurement. Moreover, we verified that the temperature increase is linearly dependent on the electric power increase.

5.1.2 Second prototype

The first tests have demonstrated the weakness of the conductive layer technology for our application. Due to the fragility of the matrix, it was difficult to obtain a bench of

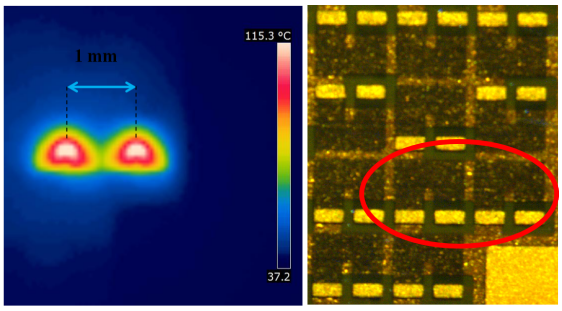

FIGURE 5.2: First prototype: (a) IR picture of two resistors (both of 310 Ω) switched on at 10 mA. The particular shape is easily recognized from (b) where these resistors are shown by the red circle. The temperature scale is not significant as the camera has not been calibrated

resistors all working together. A second type of resistor array has then been ordered and designed in order to have more reliability on the actuator quality. This time, the resistors are of surface-mount devices (Surface Mount Device (SMD)). They are coming from two suppliers (see specifications in Appendix C) and are 1 x 0.5 mm^2. Two resistors of 1 kΩ are set up in parallel to make a 1x1 mm actuator. According to the specifications, the resistors are able to sustain high temperatures up to 70^o C. Afterwards, their resistor value starts to decrease. This would lead to non linear effects, that could be compensated by a closed-loop control. The main advantage of having standard devices is the reliability on their physical properties (their characteristics are well documented). The actuators have a measured mean value of 500 Ω, with a standard deviation less than 2%, and this for any copy of this prototype. Furthermore, the actuators are able to sustain larger inputs (the power rating is about 140 mW).

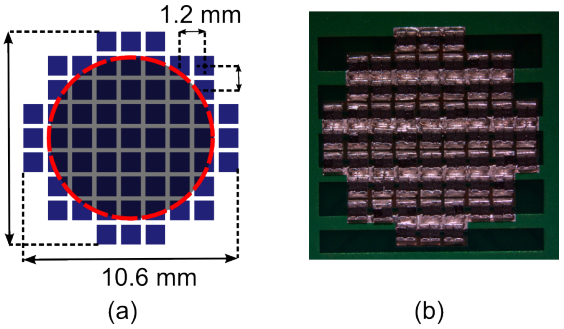

FIGURE 5.3: (Color online) (a) Scheme of the prototype array with the 61 resistors in blue and the pupil of observation defined by the area enclosed by the red circle. The actuators are separated by a dead space of 200 μm. (b) Picture of the prototype array with a microscope

Temperature distribution With the new structure of the actuators, the thermal shape is evidently very different from the first prototype one. In Fig.5.4 (a) we can see one actuator switched on, with the two hot spots corresponding to the center of the

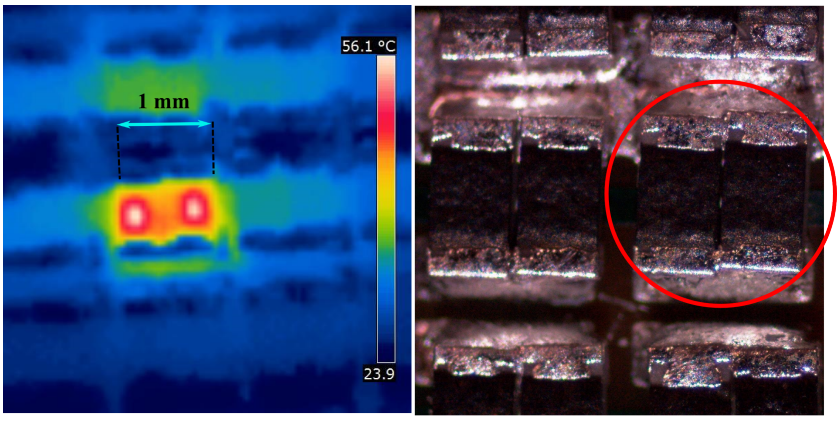

FIGURE 5.4: Second prototype: (a) IR picture of *one* actuator (500 Ω) switched on at 0.2 mW. The double construction is clearly seen. The temperature scale is not significant as the camera has not been calibrated. In (b) one actuator made of two resistors is seen with a microscope and indicated by the red circle.

resistors in parallel. We observe a heat coupling with the neighbor resistors through the solder path. This has an impact on the barycenter position of the influence functions as we will see in Section 5.3.2.1. The emission area of one actuator, determined by the thick film resistive area of the two resistors is about 0.6 x 1 mm^2.

5.1.3 Mounts

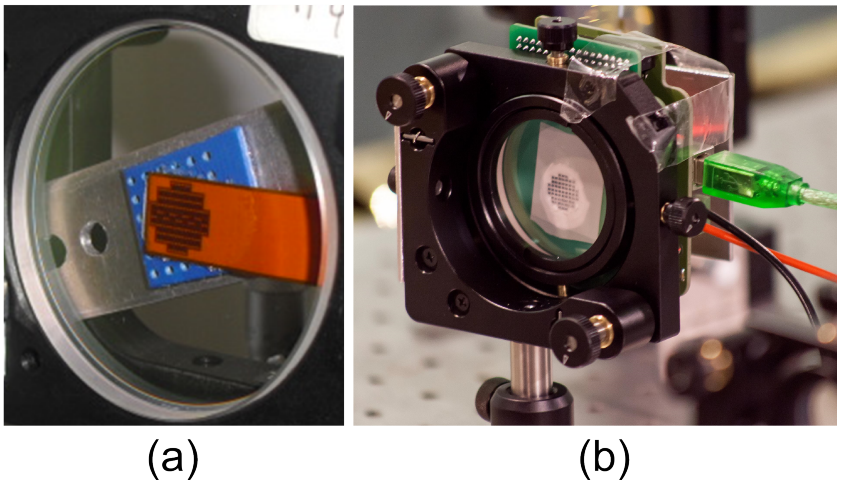

FIGURE 5.5: (a) Example of the first prototype mount (b) Example of the second prototype mount [Credit: Sylvain Crouzier, Paris-Sud University]

The mirrors are installed in 2" standard optical mounts. Additional components provide an adequate pressure in the center of the arrays in order to ensure that they are in good thermal contact with the back side (HR side) of the substrates (see Fig.5.5).

Moreover, thermal layers inserted between the resistor array and the substrate favor an homogeneous contact. They are made of thermal paste, thermal tape or glue.

5.2 Description of the setup

The setup shown in Fig.5.6 has been used to characterize the prototypes one after the other. The tests are made in air. The TDM reflects the laser beam from a Nd:YAG NPRO laser (λ = 1064 nm). A beam expander that generates a 2.6 mm radius beam ensures complete coverage of the TDM active surface. The phase modifications are imaged using a two-lens telescope and measured with a wavefront sensor from Phasics (see Section 5.2 below). This instrument has a maximum precision of 3 nm RMS. The tests were made with a 7 mm diameter pupil for the first prototype and 8.2 mm for the second prototype: the working aperture is inside the mirror actuation space (see Fig.5.1 and 5.3) to benefit from the actuation on the pupil periphery as recommended in [63, 64] and in Chapter 3.
For the Zernike characterization, the acquisition rate has been chosen to be 1 frame/s, as the time response of the system is a few seconds (see Section 5.3.4). A computer processes the data with a MATLAB program to determine the required current to be applied on the resistors according to the algorithm presented in Section 5.4.

For the first prototype, a set of 61 Digital Analog Converters (DACs) controls the currents sent to the array of resistors. Each resistor is individually delivered to a specific current value. This configuration allows to work with the tools developed for the actuation software in Virgo. For the characterization tests, the DACs have a working range limited to 8 mA.

For the second prototype, the setup was slightly different for what concerns the control part. A printed board with a "special" chip (see reference in Appendix C) is receiving the actuation order from the computer via a USB2.0 connection and is driving the actuators with the Pulse Width Modulation (PWM) method. The PWM consists in applying current pulses of different lengths with a rate that will on average give the required signal. With the large time constants (see Section 5.3.4) of our device, this will have no impact on the resistor actuation. The driver is able to accept 30 V in input, but we limit the input voltage to 10 V to respect the actuator range for which we have a precision of 12 bits (4096). P_{max} is then 0.25 W. The driving printed board being directly connected to the resistor array printed board (see Fig.5.7) allows to have a light (portable) device control.

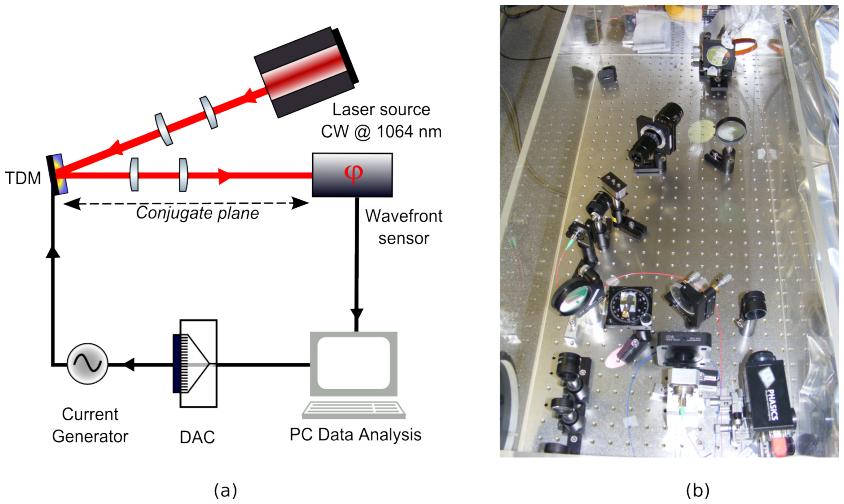

FIGURE 5.6: (a) Schematic of the adaptive optical setup of TDM characterization. The CW laser beam is directly sent to the TDM and the phase deformations occurring in the pupil area are analyzed by a wavefront sensor. The control scheme represented here is the one of the first prototype: the DACs are driving the current sent to the resistors. (b) View of the characterization setup in the laboratory.

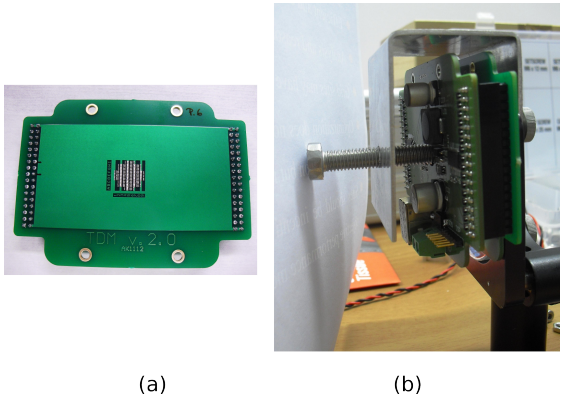

FIGURE 5.7: (a) View of the second prototype resistor array (b) Side view of the second prototype mount: the resistor array board and the control board are directly fitting together

Measuring the wavefront In order to measure the phase deformations that our device is introducing in the wavefront, we use a wavefront sensor that is based on the lateral shearing interferometer principle (Phasics) [66] : with an appropriate chessboard phase and intensity mask the incident wavefront is decomposed in four replicas that are propagating in four directions slightly tilted compared to the optical axis. The resulting interference pattern allows to recover the phase information for each point of the intersection by a spectral filtering of its Fourier transform spectrum. This reconstruction is made by the internal software of the wavefront sensor. Then, the phase maps are recorded in order to be processed by a MATLAB code we have developed. Before starting to use the system, we take a reference wavefront when no current is applied on the actuators. Then, all measurements are made with respect to this reference. When

using the TDM the tilt and focus contributions are subtracted numerically from the measured wavefront. For the first prototype, the RoC that was typically subtracted is of the order of 100 m to 50 m over the 7 mm pupil. The tilt subtracted was about 5 μrad. For the second prototype, the RoC that was typically subtracted is of the order of 4.4 m over the 8.2 mm pupil. All the measurements are mean over few seconds of data to lower the impact of environment (mainly air temperature fluctuations).

5.3 Actuator properties

5.3.1 Amplitude of response

Calibration Each actuator driven with a constant current produces a phase deformation: it is the individual spatial response of the actuator and may therefore be considered as the actuator influence function. In Fig.5.8 we show examples of these influence functions for three different actuators of the first prototype and of the second prototype.

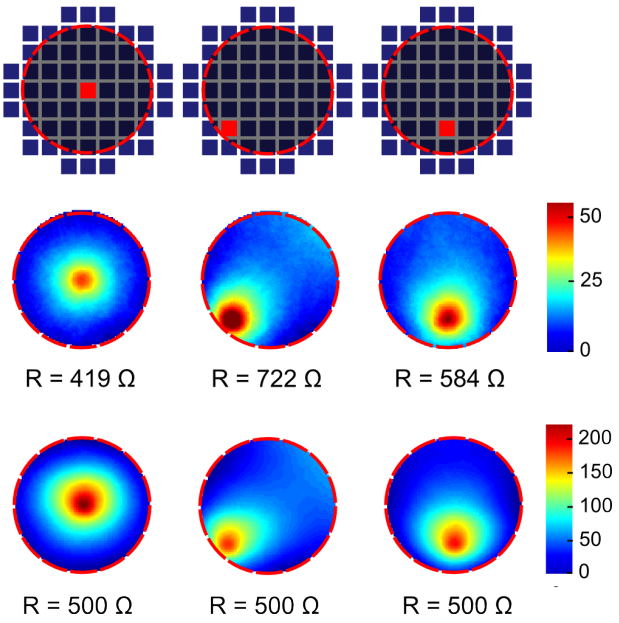

FIGURE 5.8: Three experimental influence functions of the TDM (colorscale in nm) with the resistor values and their corresponding position in the prototype array in red (a) First prototype with a driving at 5 mA (b) Second prototype with 0.195 W dissipated in each resistor (20 mA equivalent)

The first one is drived with 8 mA in each resistor. Due to the high heterogeneity in the resistor values, the amplitude of the influence functions are highly different from one resistor to its neighbors. For the second prototype, the resistor values are identical and for the same three actuator positions, the difference in amplitude is much smaller. The resistors are switched on at 0.195 W, that correspond to a driving current of 20 mA.

As the system is linear with the input power (see Section 5.3.3), we retrieve the factor 5 in the amplitudes of the central influence functions between the two prototypes. In Fig.5.9, we can observe the differences in actuation between the two prototypes. Despite the resistor uniformity, there is a factor 2 in the amplitudes of the second prototype. It comes from the measurement method (some responses are clipped by the working aperture) and from the pressure of the resistor array on the mirror surface.
In order to extract the maximum information from the influence functions, we will use the central actuator to measure some remarkable properties in the next sections.

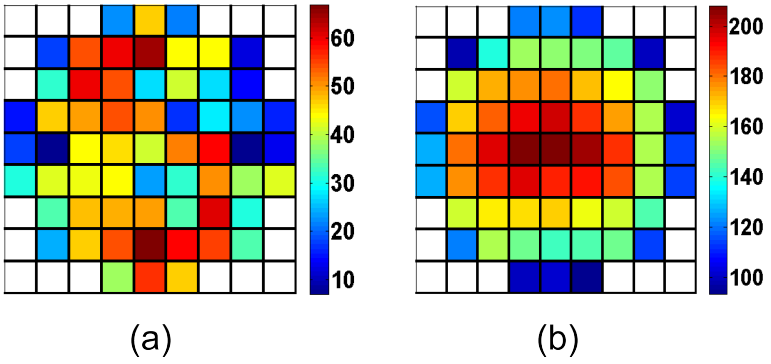

FIGURE 5.9: Schematic maps of the amplitude of the influence functions according to the actuator positions (a) First prototype with a driving at 8 mA (b) Second prototype with 0.195 W dissipated in each resistor (20 mA equivalent)

In Fig.5.10 we compare the profile of the central actuator influence functions with the simulations by FEA.

First prototype We see that the amplitude of the response is roughly equivalent for a simulated absorbed power of 16.5 mW. The total calculated dissipated power of the actuator is 27 mW. We may therefore conclude that approximately 61% of the total power dissipated by the resistor is absorbed by the substrate; the remaining 39% are presumably dissipated by convection on the backside of the heater array. The amplitude of deformation of the TDM at the maximum of the actuation command may be considered as the *stroke* of the actuator. In this case the stroke is 41 nm peak to valley (PtV) for R = 419 Ω .

Second prototype We find that the power coupling is about 0.16 for the second prototype, that corresponds to 30 mW absorbed in the substrate. The low coupling probably comes from the shape of the resistor and the difficulty to have a uniform contact between the resistor and the mirror. Furthermore, the heat could be dissipated by the edges, contrary to the first layer prototype as seen in Fig.5.4. However, as the power dissipated by the SMD resistor is much higher than the one dissipated by the

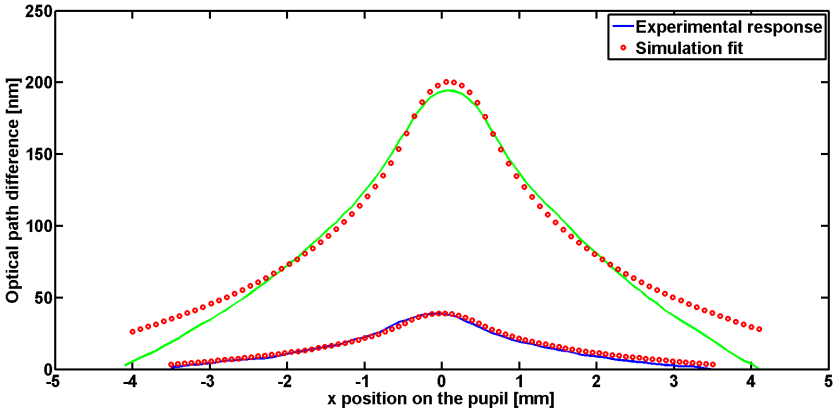

FIGURE 5.10: Comparison of the first and second prototypes influence function profiles of the central actuator to the FEA simulation. First prototype (in blue): the central actuator is dissipating 27 mW. Simulation of a 0.9 × 0.9 mm^2 actuator. Second prototype (in green): the central actuator is dissipating 200 mW. Simulation of 1 × 1 mm^2 actuator

layer resistor, the effective amplitude of the influence function is higher. The stroke of the second prototype is about 194 nm (R = 500 Ω).

Actuator shape We also see in Fig.5.10 that the experimental profiles are wider than the simulated. It could be due to the fact that the heat dissipation phenomena is not only the radiation as simulated: the convection and the conduction are also contributing to the heat evacuation. Performing the test in air slightly changes the shape at the edges of the TDM [11] by convection. Furthermore, we can suppose that there is also heat conduction from the TDM to the metallic optical mount. All these effects are not taken into account into the FEA simulation.

5.3.2 Coupling

5.3.2.1 Overlap between actuators: inter-actuator coupling

Due to the difference in actuator size and position between the two prototypes, the overlap of two neighbor actuation is slightly different. For the central actuator i, we define the experimental inter-actuator coupling σ over its actuation area A as the ratio of the deformation produced by the neighbor actuator j over the deformation produced by the actuator i :

$$R_{exp} = \frac{\int_A OPD_j \mathrm{d}A}{\int_A OPD_i \mathrm{d}A} \tag{5.1}$$

For the first prototype, the measured inter-actuator coupling with the neighbors is about 0.56. For the second prototype, it is about 0.62. From the simulations of the previous

chapter, we expected a higher coupling of about 0.97, but if we consider the actuation only inside the pupil, we retrieve the same results.

5.3.2.2 Power dissipation: influence on actuator position

For the second prototype, the computation of the barycenters shows that the position is not homogeneous in the vertical directions whereas the horizontal positions are regularly spaced (see Fig.5.11). The vertical positions are linked to the solder path positions: the barycenters of the actuators are closer in the direction of the solder line, that indicates some cross-coupling effect through the solder. It confirms that the heat coupling observed with the thermal camera (see Fig.5.4) has an effective influence on the actuation.

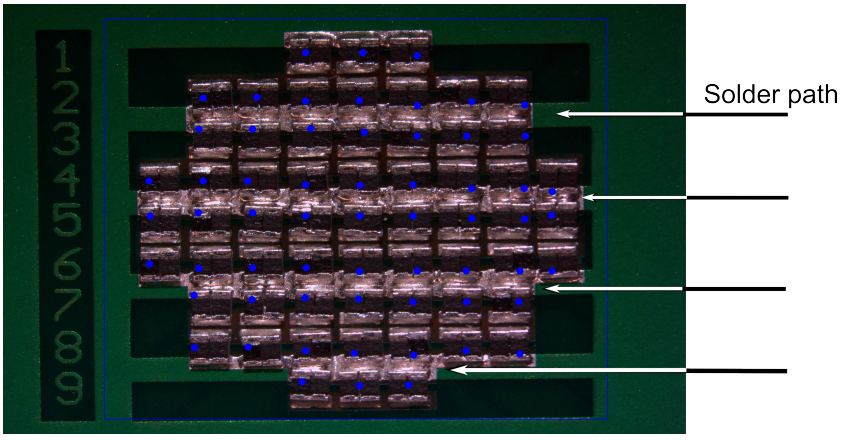

FIGURE 5.11: Second prototype: the actuation barycenters are extracted from the wavefront measurements and projected into a picture of the resistor array. They are indicated by a blue point. A correlation between the barycenter position and the solder lines can be inferred that indicates a cross-coupling effect through the heat dissipation by the solder. The actuation is therefore affected by the inter-resistor heat coupling.

5.3.3 Linearity

A fundamental requirement for a deformable mirror is that the actuator response to a command is linear. The RMS of the phase deformation is measured while increasing the current injected into the central actuator of the first prototype. In Fig.5.12 we see the resulting RMS as a function of dissipated power calculated from the current. We observe that for low powers we are limited by the precision of the wavefront sensor, but for higher powers we can state that the response of the actuator is proportional to the power (square of the injected current). The final influence functions are then normalized by the input power.

We checked experimentally that the wavefront response to the TDM correction is linear: the effect of switching on two actuators is equal to the superposition of the effect of the

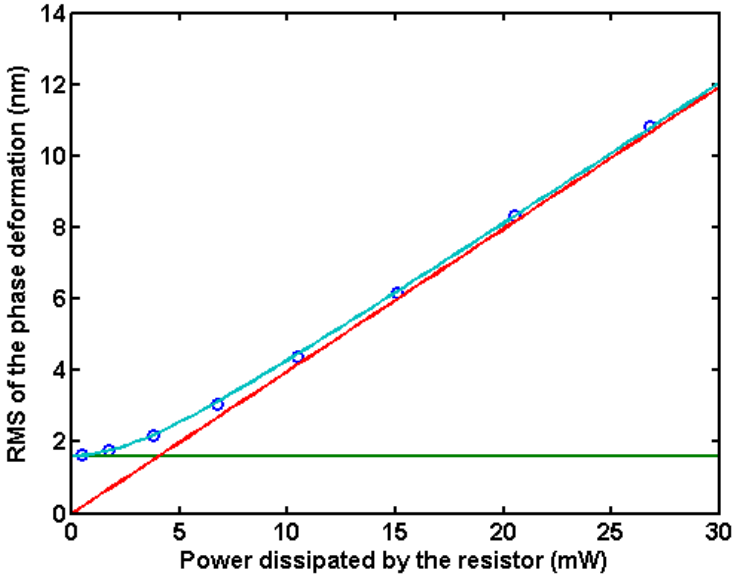

FIGURE 5.12: RMS of the phase deformation as a function of power dissipated by the central resistor in the substrate. The dots are the experimental measurement values. The blue line corresponds to the best fit of the experimental data. The slope is indicated by the red line and the offset by the green line: it corresponds to the noise level of the wavefront sensor, that is lowered by average of experimental data.

single actuators. Furthermore, some early tests have demonstrated that the absorption of the substrate was not modified by the temperature increase [67].

5.3.4 Time of response

Behavior of the mirror for one actuator The temporal behavior of the actuator may be characterized by measuring the evolution of the phase deformation after switching on the current to a few milliamperes. The experimental measurements show that the response can be modeled as a second-order system (sum of two exponentials). It has been observed that the time constants depend greatly on the thermal contact between the heater array and the mirror substrate. The use of thermal paste yields time constants of $\tau_1 \simeq 2$s and $\tau_2 \simeq 0.2$ s, which is about three times faster than when using glue as the thermal contact We can infer that there is a slow time constant for the heating of the whole mirror to reach the steady-state and a faster time constant driven by the local deformation. The measured time constants indicate that the actuation system should be driven at frequencies lower than 0.15 Hz. Furthermore, no hysteresis was found through the measurement campaign.

Behavior of the mirror for all the actuators In case of all the actuators switched together, the two time constants have larger values (see Fig.5.13 and 5.14). In this case it takes about one minute for the TDM to reach the steady-state.

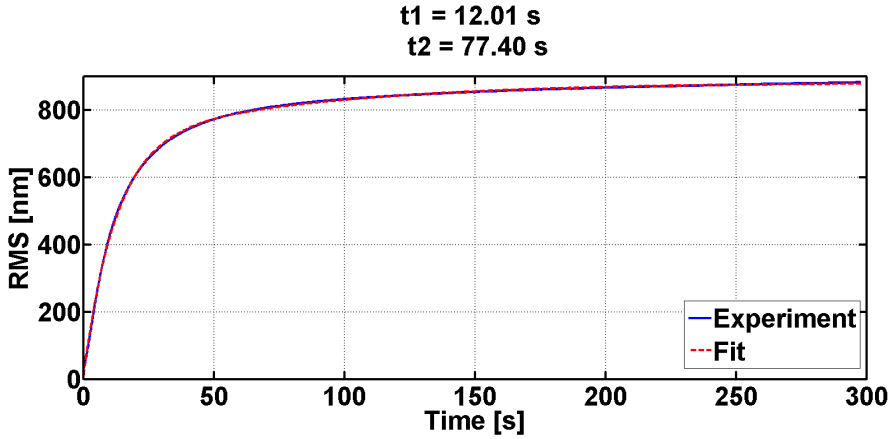

FIGURE 5.13: Establishment of the steady-state of the correction when all the actuators are switched on at the same time. The values of the two time constants are about 12 s for the fast time constant and more than 1 min for the slow time constant.

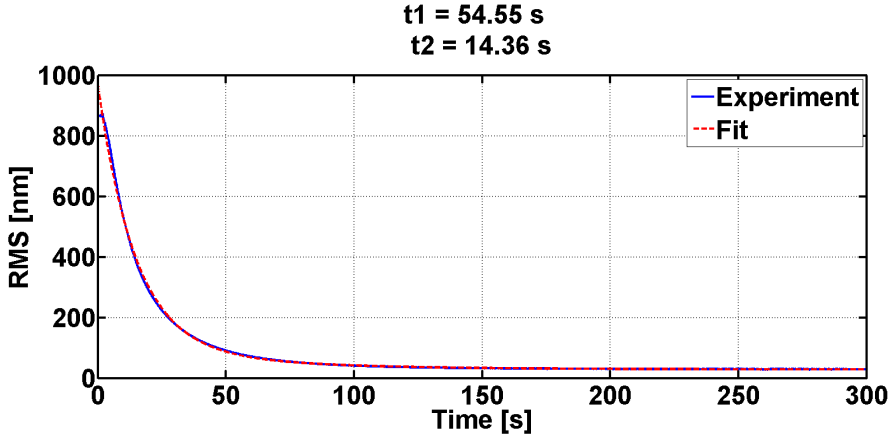

FIGURE 5.14: Back to the initial state with all the actuators are switched off at the same time. The values of the two time constants are about 14 s for the fast time constant and slightly less than 1 min for the slow time constant.

Moreover, the stability of the power supply is important to meet the noise requirements for Advanced Virgo [11].

5.4 Control algorithm

Now that the main features of the TDM have been established, we need to control the set of actuators to obtain the required wavefront correction. The first step is the *calibration* of each prototype, that is performed as follow: a reference wavefront is registered. One actuator is switched on and the mean actuation over few seconds is registered. The

actuator is switched off. A new reference is taken. The influence function is the actuation minus the mean of the two references. Thus the actuators are switched on one after the other and the influence functions are registered. The influence functions can be represented one by one in the interaction matrix M, obtained from the calibration of the 61 actuators: this is the *Zonal* description, limited by the sampling of the phase measurement. The *Modal* description expresses the TDM actuation in terms of Zernike modes (or any other basis over the circular pupil, like the TDM eigenmodes). The accuracy will be limited by the number of Zernike modes used for the projection. In order to reduce the numerical complexity of the algorithm that computes the correction, the influence matrix and the measured wavefronts are decomposed into Zernike modes. Another advantage of the modal control is the possibility to remove the Zernike modes we do not want to take into account in the correction by simply putting the corresponding coefficient to 0. Indeed the piston, tilt and curvature modes are not relevant for the performance of the TDM (as explained in Chapter 1). The measured wavefronts are then expressed by:

$$\phi = \sum_{i=1}^{n} \alpha_i Z_i \tag{5.2}$$

where α_i is the coefficient of the Zernike mode i. n is the number of Zernike modes used in the decomposition.

As seen before in Chapter 4, the computation of the actuation values requires to "inverse" the $m \times n$ influence matrix M, with m the number of actuators and n the number of Zernike modes used in the modal description. M likely being a non-square matrix, its inversion is not straightforward.

5.4.1 Least Square Algorithm (LSQ)

The Least Square Algorithm (LSQ) approach yields a non bounded vector that can have positive or negative values. The TDM is a one-directional actuation system, since we can only heat the substrate. This issue can be addressed operating with a constant added to each command. The so called *bias operation* consists of putting the actuators at the middle of their dynamic range and to make them fit a simple shape (piston or focus) before the calibration of the system. But both these methods are not taking into account the physical actuation limits of the device: the LSQ solution (see Chapter 4) might still give solutions out of the actuation range. These commands will be clipped resulting in inaccuracies or even instabilities or losses of control in the system when the actuators start to saturate.

5.4.2 Singular Value Decomposition

A well-known technique is to use the diagonalized form of the matrix via a diagonalization technique for a non square matrices, the *Singular Value Decomposition*. We suppose that the phase is described with a number of Zernike modes larger than the number of actuators: $n > m$. The $m \times n$ matrix can be decomposed in three sub-matrices:

$$M = U \cdot \Sigma \cdot W^T \tag{5.3}$$

- Σ is the $m \times n$ diagonal matrix of eigenvalues (or singular values) λ_i. The n λ_i are unique and the other values of the matrix are zeros.
- U is the $m \times m$ matrix of *eigenvectors* (or *left singular vectors*). Being a basis of the m-vector space, it is an orthogonal unitary matrix with $U \cdot U^T = I_m$. The eigenvectors are not unique.
- W^T is the $n \times n$ matrix of *eigenmodes* (or *right singular vectors*). Basis of the n-vector space, it is an orthogonal unitary matrix with $V \cdot V^T = I_n$. The w vectors are not unique and the vectors w_i with $i > n$ have no contribution in the recomposition of the matrix M.

The pseudo-inverse of M can now be computed from the reversible matrix Σ:

$$M^+ = W \cdot \Sigma^+ \cdot U^T \tag{5.4}$$

that verifies:

$$M^+ \cdot M = I_n \tag{5.5}$$

The vector $\mathbf{a}$ of actuation values to corrected the incident wavefront ϕ_i is then obtained by:

$$M \cdot \mathbf{a} \simeq \phi_i \tag{5.6}$$

that is

$$\mathbf{a} \simeq M^+ \cdot \phi_i \tag{5.7}$$

The eigenmodes, defined on the active pupil, are orthogonal and give information about the mirror capabilities. The corresponding eigenvalues λ_i are sort along the diagonal of Σ in a decreasing order (see Fig.5.15). The TDM will be efficiently described by the first eigenmodes of the decomposition (high eigenvalues). The first eigenmodes contain low spatial frequencies and are very close to the Zernike polynomials whereas we see the typical pattern of the actuators position in the chessboard structure in the last eigenmodes (see Fig.5.16). The last eigenmodes (low eigenvalues) have then a minor

importance in the recomposition of the matrix M. They are close or inside the measure noise and can be filtered (= set to 0) without impacting the TDM description. This will be an important point for the actuation determination.

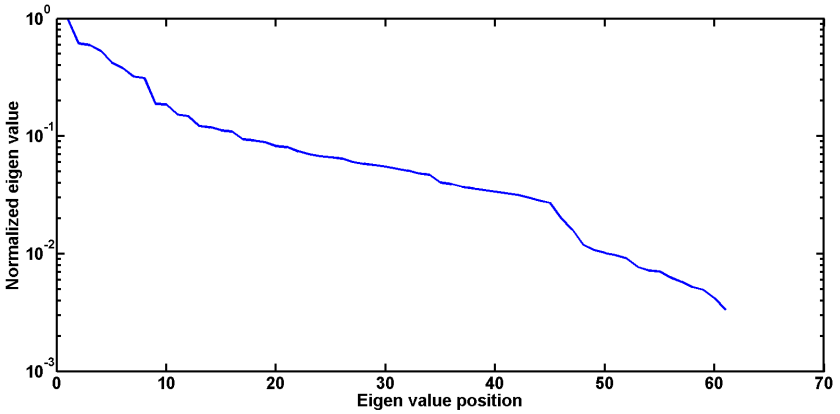

FIGURE 5.15: Representation of the 61 eigenvalues λ_i as a function of their index in Σ. The SVD has been made on the interaction matrix M obtained from the experimental calibration of the second prototype

The precision in the phase description is determined by the sampling of the experimental measurement and by the accuracy on the Zernike decomposition used to project the zonal interaction matrix in the basis of the Zernike modes. However, we have seen that some eigenmodes are not really significant in the description. When we reverse the matrix, the high index values will be dominant and they will increase the actuation required for a very low effect on the correction. We need then to filter the values at an appropriate point, in order to keep a good precision in the actuation. Moreover, the precision of the description has an impact on the actuation range of the system response. To illustrate this point, we implement a small simulation. We compute the actuation required to generate three Zernike modes with increasing spatial frequencies. The interaction matrix is the one obtained experimentally from a calibration of the second prototype and is described with the first 15 Zernike orders. As a function of the applied filter value, the actuation range increases. For example, the range of actuation is increased by a factor 5 for the mode Z_4^4. But a great increase of power will provide a small improvement in the precision. The difficulty is then to set the filter value to the appropriate point.

However, the LSQ and SVD are good solutions when the computing time can limit the performance of the system, the pseudo-inverse of M being computed once before the control loop starts the correction.

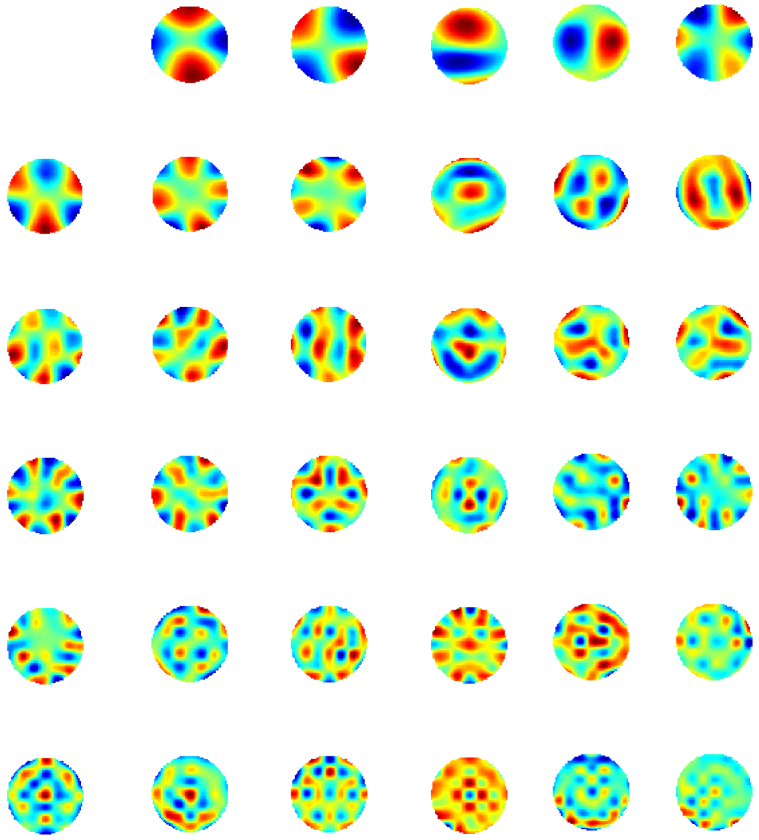

FIGURE 5.16: First 35 eigenmodes w_i in the decreasing order of the λ_i values. The SVD has been made on the interaction matrix M obtained from the experimental calibration of the second prototype

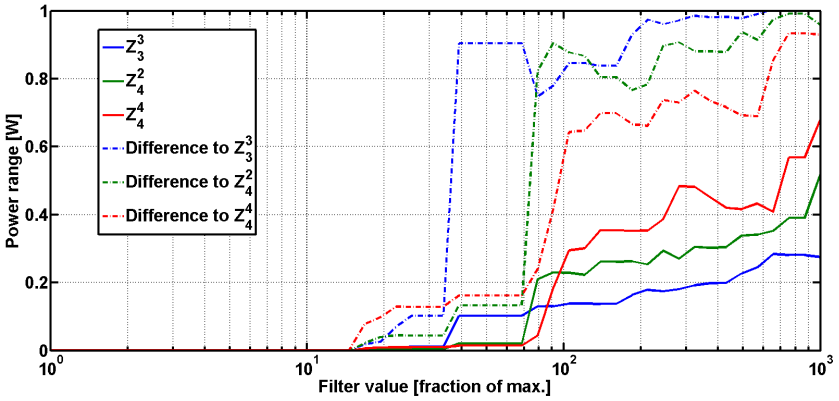

FIGURE 5.17: Maximum amplitude of actuation as a function of the value of the maximum eigenvalue (simulation).

5.4.3 Improved Least Square Algorithm

In order to improve the control of our system and to efficiently exploit the entire dynamic range, we decided to use an algorithm [68] that allows us to choose lower bounds l and upper bounds u for the command values a:

$$l_i \leq a_i \leq u_i \quad with\, i = 1...61 \tag{5.8}$$

where i indexes all the resistors. The optimal solution is still considered the one that minimizes the error of Eq. 4.5. Its gradient must be zero at the optimal point, except for those a_i that are at the boundary: for those the corresponding gradient component must be such that the decreasing direction points beyond the limit, or in other words to improve the error it would be necessary to relax one of the constraints of Eq. (5.8).
These kinds of search algorithms are typically much more computationally demanding than the simple least-square solution, taking about one third of a second for a standard PC. This is not an issue in our application, since the time available for the computation is long enough.

5.4.4 Closed-loop control

The constrained minimization algorithm can be used to find the best estimate of the correction commands needed to reproduce a target wavefront. If all influence functions were perfectly known, one single computation would be enough to find the optimal correction. To make the system more robust against uncertainties in the measured influence function or changes in the system response, we implemented an iterative, closed-loop scheme.
At the beginning the best correction is computed as previously explained and sent to the TDM. After the settling time the residual wavefront ϕ_r is measured. This is used as the new target for the algorithm. Since the new correction must be added to the previous one, the boundaries are properly shifted in order to ensure that the total correction remains inside the allowed region. This iteration can be repeated as many times as needed. As will be discussed in subsequent sections, it allows an improvement in the actuation efficiency and the capability of tracking time-changing conditions.

5.5 Wavefront correction characterization

5.5.1 Zernike generation

For the characterization of the TDM we decided to use target wavefronts composed of single Zernike modes. In this way, as it will be shown in Section 5.5.2, we are able to derive quantitative estimates of the TDM performance. Since the generation of higher Zernike modes is limited by the spatial frequency of the actuator pattern, we restricted our study to the first 20 modes (Zernike polynomials with order up to 5, except piston, tilt and focus of first and second order).

Convergence The results shown are obtained in a closed-loop control configuration. In Fig.5.18 we show an example of the evolution of residual RMS as a function of the number of iterations. Each iteration allows a settling time of 10 s. After less than 10 iterations the resulting phase image is stable and corresponds to the best solution.

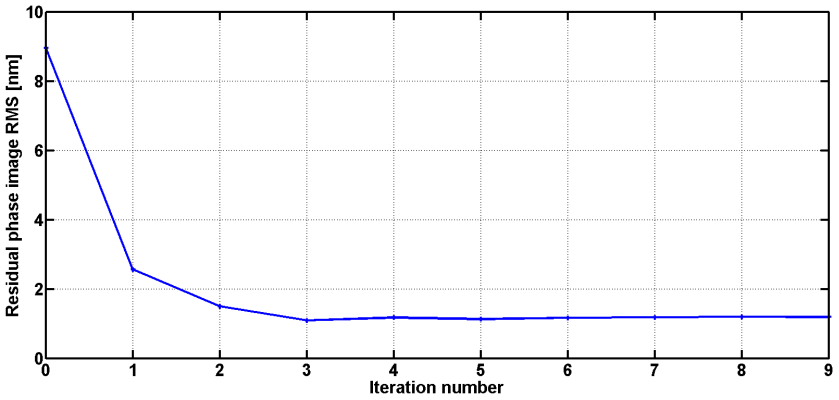

FIGURE 5.18: RMS of the residual image in a closed-loop control for the target mode Z_3^{-3} at 50 nm PtV (9 nm RMS) (First prototype). The first iteration corresponds to the residual RMS that may be obtained in an open-loop control.

Figure 5.19(b) shows an example of the Zernike mode Z_3^{-3} generated in this way by the first prototype. In figure 5.19 (c) we see the residual wavefront after TDM correction. This residual phase shape has a dominant spatial frequency of 0.5 mm^{-1} which is directly related to the spatial frequency of the actuator array. This effect can therefore be assimilated the actuator footprint.

In Fig.5.20 are examples of the Zernike modes generated by the second TDM prototype at 150 nm PtV. We can see that the more the Zernike index increases, the higher is the residual RMS and then the less accurate is the generation. The best reproduced Zernike for each order are the modes exhibiting the lowest spatial frequencies computed in Chapter 4.

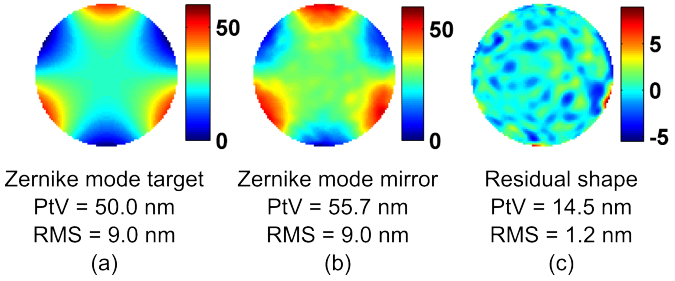

FIGURE 5.19: (a) Target Zernike mode. (b) Zernike mode Z_3^{-3} generated by theTDM over a pupil of 7 mm. An RoC of 350 m and a horizontal tilt of 5 μrad have been numerically subtracted. (c) The difference between the two modes is the residual phase image (colorscales are in nm).

Actuation range In order to determine the linear working range of actuation in terms of Zernike modes, the modes are generated in closed-loop within an amplitude range adapted to each prototype ability.

The generation of the modes of the second- and third-order demonstrate a linear working range of almost 20 nm RMS for the first prototype (see Fig.5.21a). The RMS value of the residual phase images is about few nm RMS, with a quasi constant value in the limits of the linear working range (see Fig.5.21b).

For the second prototype, a rule of thumb can be extracted from the experimental results: the linear range decreases by a factor 2 each time the order increases. The second order generation exhibits a linear range at least up to 160 nm RMS. The third order reproduction is linear up to 80 nm RMS. The linear range of the forth order is less than 40 nm RMS and for the fifth order it is about 20 nm RMS (see Fig.5.22). Again, the RMS value of the residual phase images is almost constant with a maximum of about 10 nm RMS within the linear dynamic range limits of each order (see Fig.5.23).

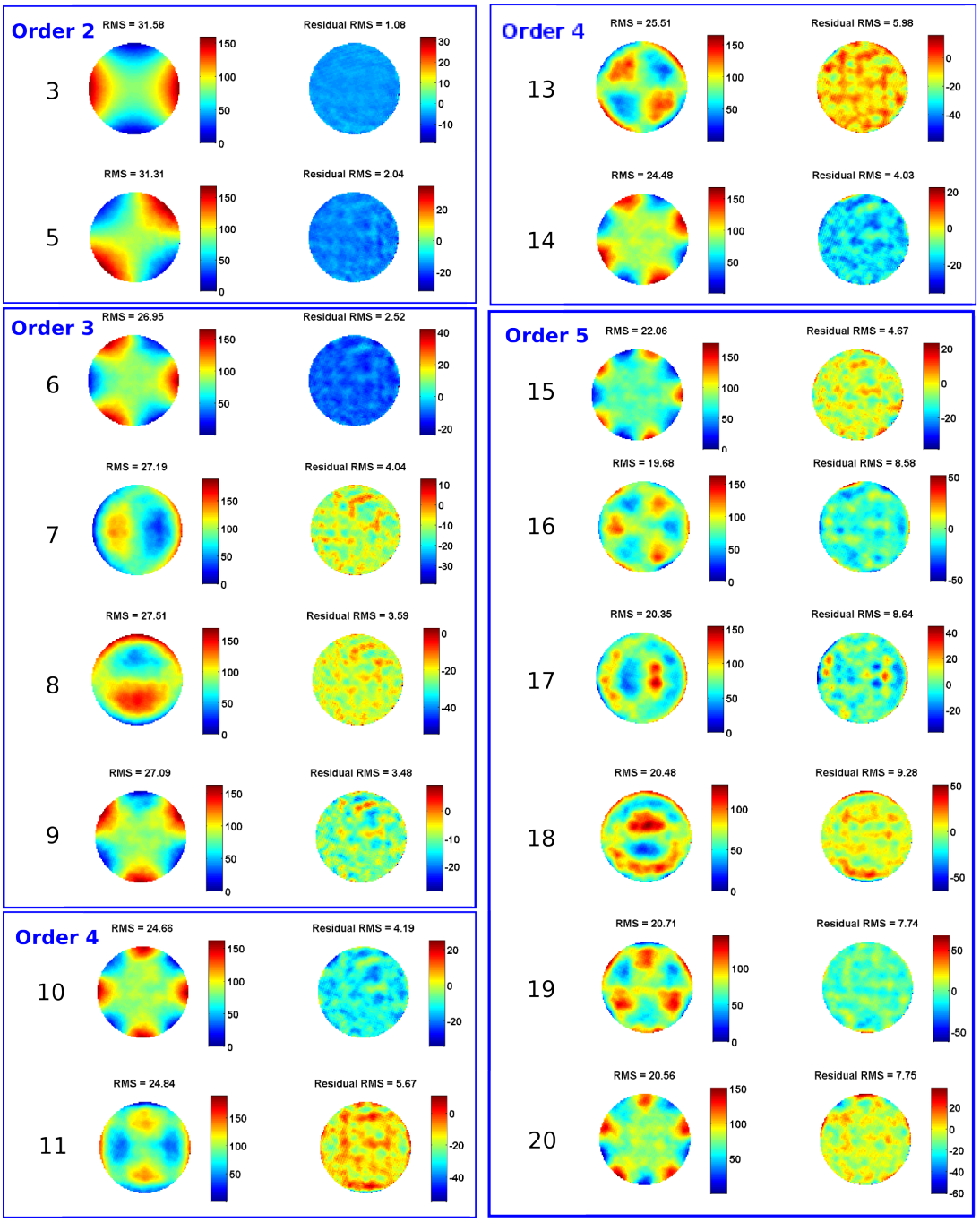

FIGURE 5.20: Experimental Zernike modes generated in a closed-loop control by the second prototype at 150 nm PtV. For each mode, the left picture is the phase deformation produced and the right picture is the residual phase shape. The frames are delimiting the orders.

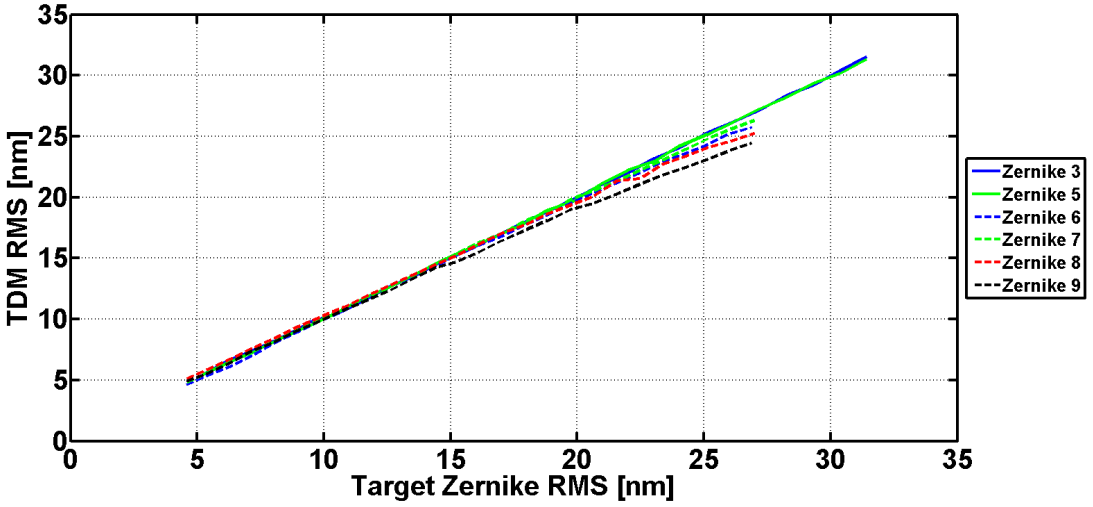

(A) First prototype: RMS value of the Zernike produced by the mirror for a full scan of the Zernike modes from the second- and third-order.

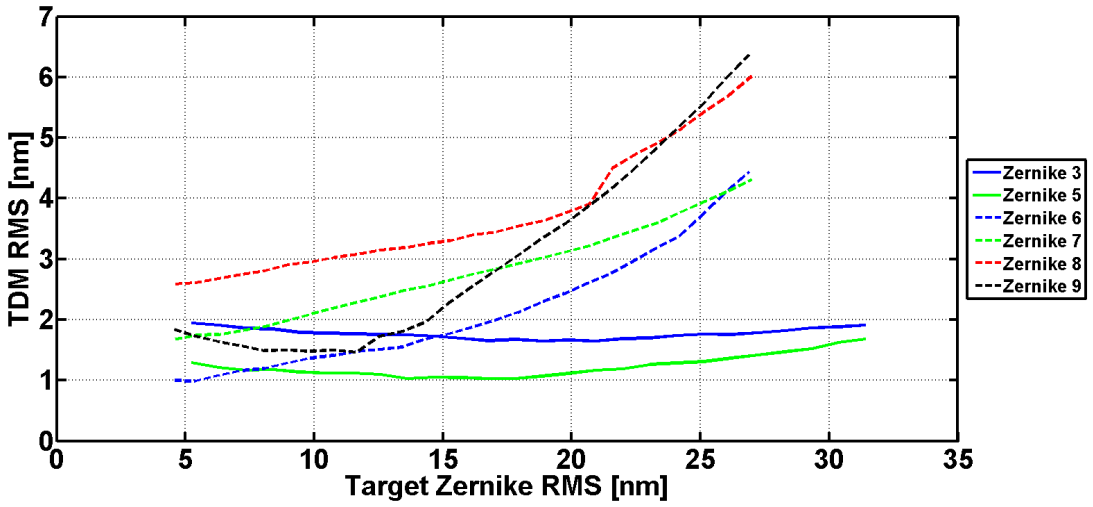

(B) First prototype: RMS value of the residual image for a full scan of the Zernike modes from the second- and third-order.

FIGURE 5.21: Scan results of the first prototype

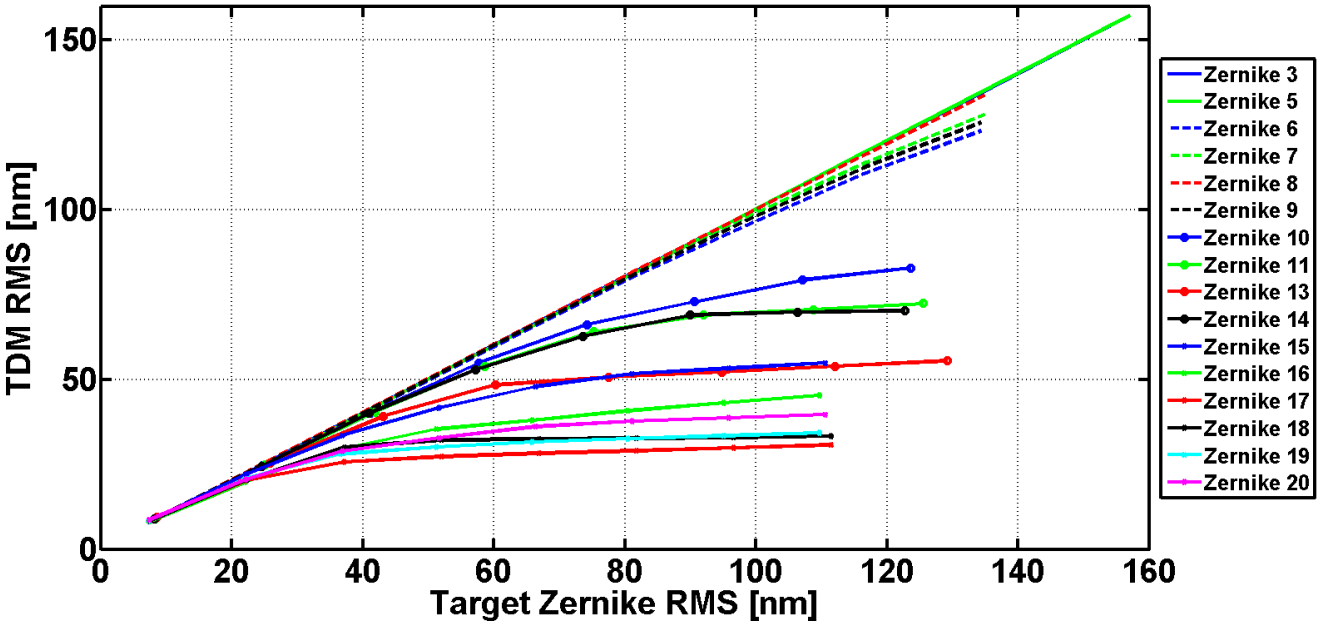

FIGURE 5.22: Second prototype: RMS value of the Zernike produced by the mirror for a full scan of the Zernike modes from the second- and third-order in the range of 50 to 800 nm PtV

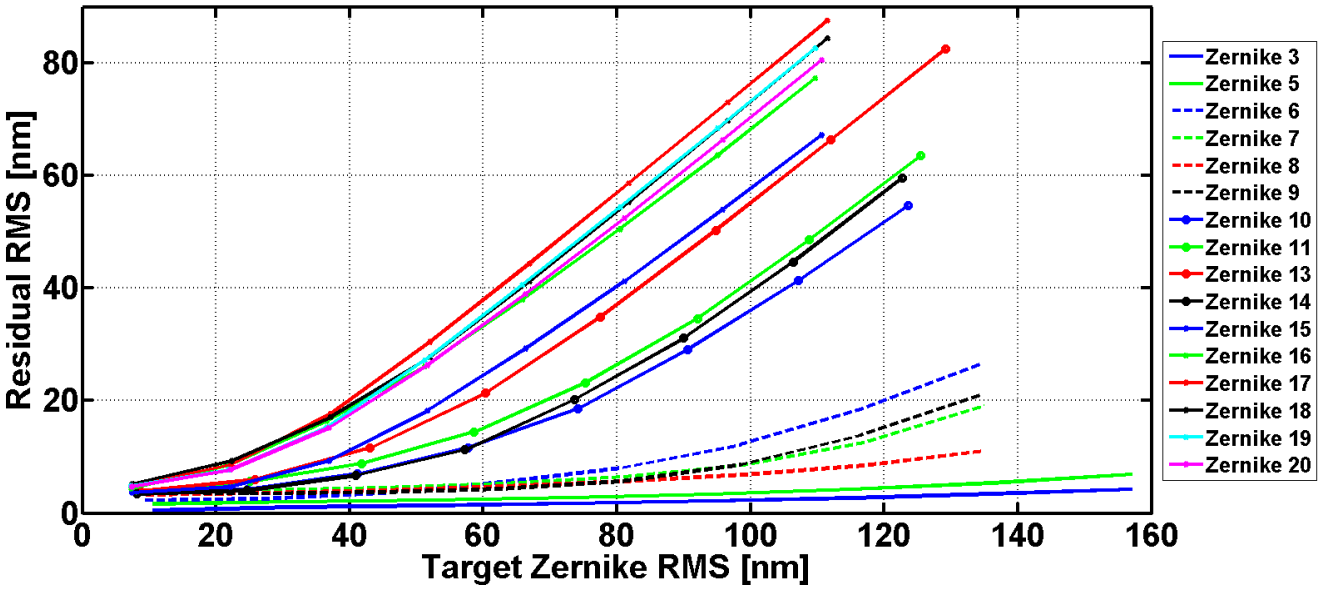

FIGURE 5.23: Second prototype: RMS value of the residual image for a full scan of the Zernike modes from the second- and third-order in the range of 50 to 800 nm PtV.

5.5.2 Efficiency and accuracy of the correction

We define two quantitative criteria that will help in evaluating the quality of the Zernike mode generated by the TDM and in determining what is the limiting factor for the correction. With the normalization chosen in Chapter 4, the RMS amplitude of the wavefront is equal to the sum of the coefficients from the projection onto the Zernike basis of N modes:

$$RMS_\phi = \sqrt{\sum_{i=1}^{N} \alpha_i^2} \tag{5.9}$$

In the following, we assume that we want to generate a target Zernike mode Z_t whose amplitude is α_t. After convergence in a closed-loop control, the resulting wavefront is $\phi_{TDM} = \sum_{i=1}^{N} \alpha_i^{TDM} Z_i$.

The *efficiency* E determines if the correction is limited by the dynamic range. To evaluate this first criterion, we compare the amplitude α_t^{TDM} of the reproduced mode to the amplitude α_t of the target mode.

$$E = 1 - \frac{|\alpha_t - \alpha_t^{TDM}|}{\alpha_t} \tag{5.10}$$

The closer to 1 this parameter, the greater the efficiency of the TDM to reproduce the target mode. A high efficiency indicates that the actuation is made within the dynamic range of the TDM.

The second criterion concerns the generation of unwanted Zernike modes by the TDM. This parameter is similar to the *purity* proposed in [24]. We define the *accuracy* A of the mode generation as:

$$A = \frac{\alpha_t^{TDM}}{\sqrt{\sum_{i=1}^{20} \left(\alpha_i^{TDM}\right)^2}} \tag{5.11}$$

The closer to 1 this parameter, the fewer unwanted modes generated by the TDM. It indicates that the mode coupling is relatively low: the Zernike mode can be generated independently of others. The experimental results obtained in closed-loop control are shown in figure 5.24 for Zernike modes up to 20 for Zernike target modes having a 10 nm RMS for the first prototype. For the second prototype, the results are shown at 25 nm RMS (see Fig.5.25), that is just up to the limit of linear range for the fifth order, and at 50 nm RMS (see Fig.5.26), that would be a desirable dynamic range for our application.

First prototype The accuracy is very high for all polynomials tested. The minimum value obtained is for the mode 18. We may therefore conclude that the spatial resolution

of the TDM is sufficient to correct up to the 20^{th} Zernike mode with minimal mode coupling. For modes below to the third order (modes 3 to 9), the efficiency is also close to 1 with a minimum of 98.5, at which point the actuation is limited by the actuator footprint. The efficiency is globally decreasing for the 4th and 5th order (modes 13 to 20). It reaches a minimum for the mode 18 at 46.6%. The reduced efficiency is attributed to the increasing number of saturated actuators, thereby confirming that for higher order Zernikes the TDM is limited by its dynamic range.

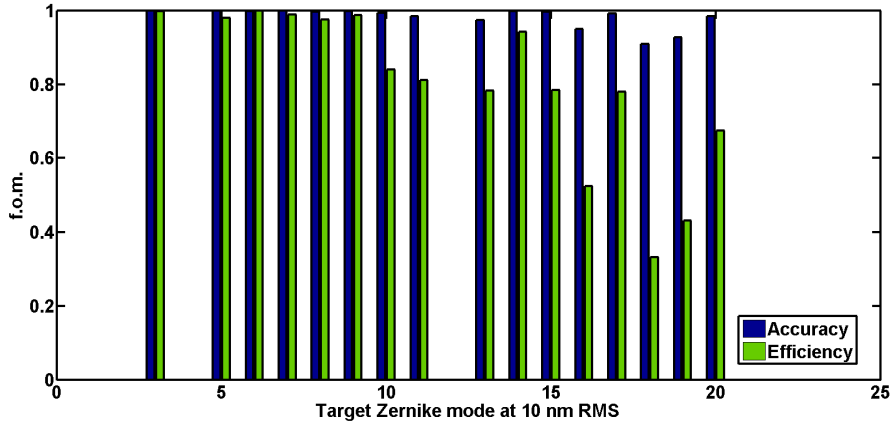

FIGURE 5.24: Characterization of the modes generated by the first prototype: for each mode the efficiency is given in the green bars (right portions of the bars) and the accuracy is given in the blue bars (left portions). All Zernike target modes have an RMS of 10 nm.

Second prototype We perform the same study with the second prototype. As expected, the efficiency is much better for the 4th and 5th order due to the actuation stroke larger by a factor 5. This is very clear at 25 nm RMS target, where the efficiency is higher than 80 % at the minimum. We observe a slight decrease in the accuracy of actuation, that might be attributed to the loss in homogeneity from the larger temperature cross-coupling between the actuators. At 50 nm RMS, both efficiency and accuracy are good for the 2nd and 3rd order, and acceptable for the 4th order, but the efficiency is greatly reduced for the 5th order, with a minimum at 47%. Therefore this prototype enables us to work with a good dynamic range if we limit the actuation to the 4 first Zernike orders. We now have to check what would be the equivalent matching improvement.

5.5.3 Mismatch correction

In terms of mode matching applications, the target wavefront corresponds to the initial mismatch to be corrected; the residual phase corresponds to the aberrations that will limit the best achievable matching. We want to determine how the correction produced

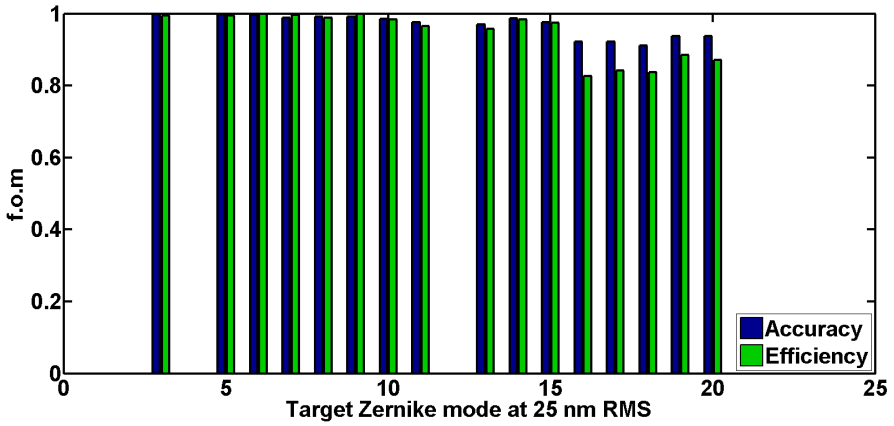

FIGURE 5.25: Characterization of the modes generated by the second prototype: for each mode the efficiency is given in the green bars (right portions of the bars) and the accuracy is given in the blue bars (left portions). All Zernike target modes have an RMS of 25 nm.

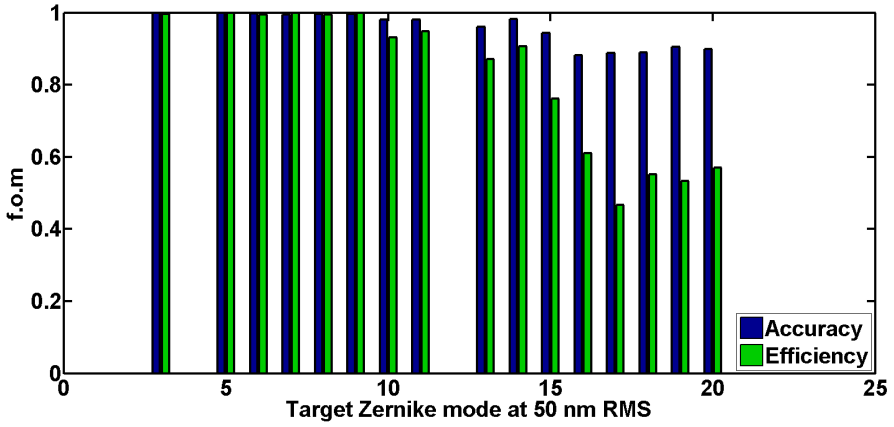

FIGURE 5.26: Characterization of the modes generated by the second prototype: for each mode the efficiency is given in the green bars (right portions of the bars) and the accuracy is given in the blue bars (left portions). All Zernike target modes have an RMS of 50 nm.

by the TDM can improve the matching. As performed in Chapter 4, the equivalent mismatch correction that depends on the amplitude and the composition of the residual can be computed by overlap calculation (see Eq. 4.32).

First prototype At almost 20 nm RMS, the 2nd and 3rd order modes are equivalent to a mismatching of around 3% for each mode. The RMS value of the residual image is between 1.2 nm and 4 nm RMS for the Zernike orders 2 and 3. From these results, we can infer that if we have a mismatch due to aberrations composed of the second- or third-order Zernike polynomials inside the tested range, the TDM is able to correct them to reach a match better than 99% (see Table 5.27).

— Extrapolated results of the TDM correction —			
Zernike		Matching	
order	mode	initial (%)	after correction (%)
2	3	96.10	99.99
	5	96.10	99.99
3	6	97.08	99.92
	7	97.21	99.93
	8	97.21	99.86
	9	97.08	99.83

FIGURE 5.27: Table of the correction of the mode matching by extrapolation of the first prototype experimental results.

Second prototype Around 50 nm RMS, the correction is within the specifications for Advanced Virgo for the order 2, 3 and 4 when the input amplitude deformation is about 50 nm RMS (see Table 5.28). For the 5th order, the extrapolated matching is below 99%. However, we have seen that the actuators are saturated . This confirms that the TDM performance will be limited by the dynamic range to reach the Advanced Virgo specifications.

Conclusion These experimental results show that the TDM is able to generate Zernike polynomials up to the mode 20^{th} and therefore to correct high order aberrations. The limiting factors are the power of actuation and the residual footprint: the power of actuation restricts the linear response range of the TDM while the residual footprint limits the precision of the mode reproduction. The first prototype has a small dynamic range and a low reliability. For the second prototype we can deduce by an overlap integral calculation that if we have a mismatching due to aberrations composed of the second, third or forth order Zernike polynomials introducing mismatch up to 10%, the TDM is able to correct them to reach a matching better than 99%. Furthermore, it will be able to correct the 5?th order aberrations at better than 99% if for 5% of initial mismatch. It means that in the limits of its dynamic range the TDM can correct these aberrations within the specifications for Advanced Virgo.

— Extrapolated results of the TDM correction —					
Zernike		Amplitude		Matching	
order	mode	PtV (nm)	RMS (nm)	initial (%)	after correction (%)
2	3	250	52	94.10	99.99
	5	250	52	94.03	99.97
3	6	250	45	96.64	99.96
	7	250	45	86.86	99.87
	8	250	45	86.86	99.90
	9	250	45	96.64	99.92
4	10	350	58	95.42	99.75
	11	250	42	91.57	99.66
	13	250	43	90.84	99.53
	14	350	57	95.49	99.77
5	15	350	52	96.76	99.34
	16	350	51	90.21	98.43
	17	350	52	80.60	94.96
	18	350	52	80.60	97.00
	19	350	51	90.21	97.96
	20	350	52	96.76	98.95

FIGURE 5.28: Table of the correction of the mode matching by extrapolation of the second prototype experimental results for an initial amplitude of Zernike about 50 nm RMS.

5.6 Possible improvements for the next prototype

5.6.1 Dynamic range and Homogeneity

The correction ability of the second prototype is mainly limited by the dynamic range. However, we already operated at maximum with a power higher than the maximum power rating recommended by the suppliers (0.1 W for 0.063 W of power rating). But, according to our estimation, the power coupling into the substrate is relatively low. Therefore a possible improvement would be to insert an interaction layer between the resistor array and the substrate that favor a better power coupling. Furthermore, at the maximum of actuation for the second prototype, the mirror coatings have been damaged. We suspect an interaction with the thermal paste combined with a too high

temperature. An additional interaction layer may protect the coating.
As seen in the thermal pictures of the resistors, the homogeneity is not perfect for the two prototypes. In the first one, the homogeneity defect comes from the shape of the resistor. In the second prototype, it comes also from the heat diffusion between the resistors through the solder lines and from the structure of the actuators, that are made of two resistors.
Based on these observations, we study the possibility to add a thermal conductive layer.

Copper homogeniser A solution based on a copper homogenizer is proposed. When put in contact with the resistor array of the second prototype, this device should be able to provide a better homogeneity at the substrate contact and minimizing the unwanted coupling between actuators. Some simulations have been performed with a copper layer, chosen for its high thermal conductivity ($\kappa = 401$ W.m^{-1}.K^{-1}): it appears that a large thickness is necessary to recover an homogeneous temperature distribution at the substrate level. It makes the requirements for this metallic piece very stringent.

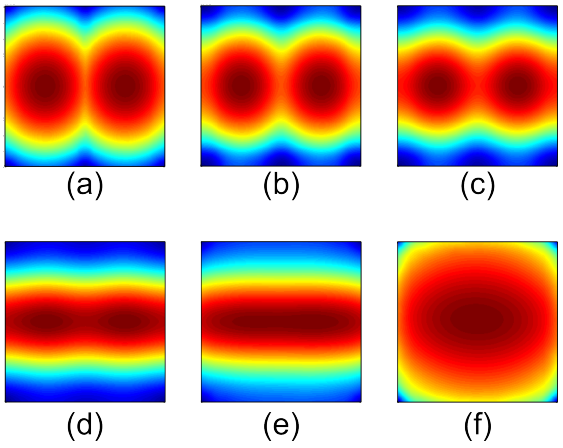

FIGURE 5.29: FEA simulations of the temperature distribution after a copper layer with different thicknesses (a) 10 μm (b) 50 μm (c) 100 μm (d) 300 μm (e) 500 μm (f) 1000 μm. The size of the square is 1 mm.

Some tests are performed with a copper *homogenizer* especially ordered: in a 0.5 mm thick copper layer, 61 squares of 1×1 mm^2 have been machined by laser ablation (see Fig.5.30). The square hold together at their corner. The ablation was made with a decreasing thickness along the copper layer high, so the space between the squares is 25 μm on the thinnest edge and 200 μm on the largest edge. However, the results are quite disappointing. The heat is diffusing by conduction through the copper array instead of to be coupled into the substrate. The spatial resolution is completely lost (see Fig.5.31), enlarging the influence functions and reducing the mean amplitude by almost a factor 4. The FWHM is increased by a factor 1.6. An explanation could be found in the probably too large thickness of the bridge between actuators. The diffusion of the heat inside

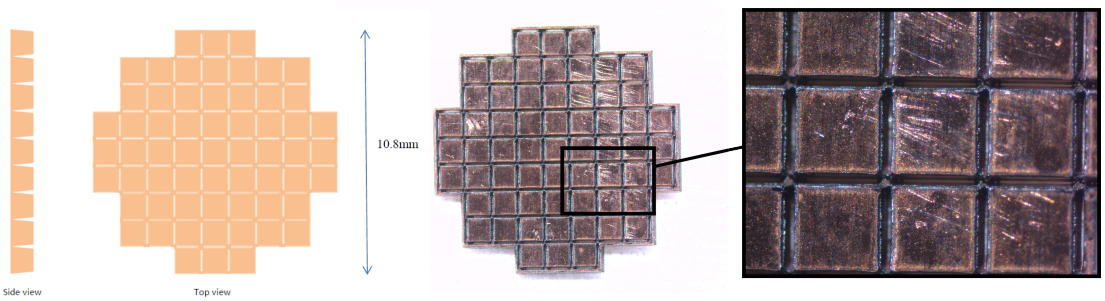

FIGURE 5.30: Homogeniser made of 61 copper squares hold together at their corners. According to the manufacturer, the space between the squares is 25 um on the thinnest edge and 200 um on the largest edge. The thickness of the homogenizer is 500 μm.

the homogenizer has to be studied (for example by observing the warm-up period) to improve the design.

A solution to avoid the bridge inter-actuators should be to directly put the copper pieces one by one in contact with the actuators. It is a complicated task and the danger is to create short-cuts if a piece moves out of its regular position. Furthermore, as the experimental results are already quite satisfying without an homogenizer, the priority should be the thermal contact between the resistor array and the substrate. An efficient, in-vacuum and protective solution should be found.

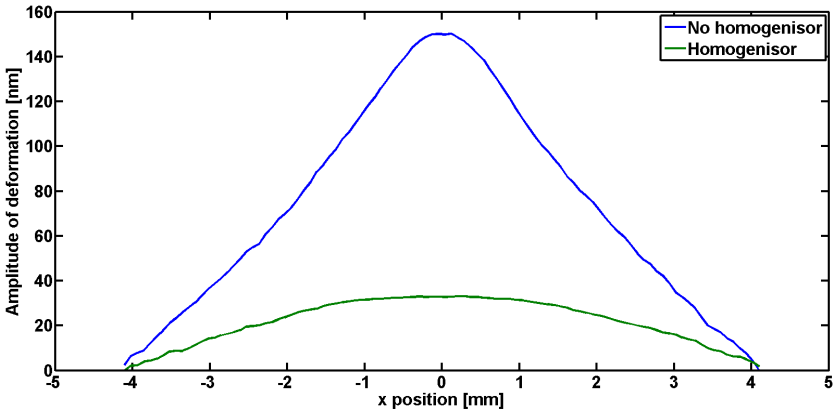

FIGURE 5.31: Actuation at 4000 PWM. The amplitude is slighlty lower than the previous calibration because we added more thermal intercation layers in order to ensure that there will be no short-cut between the copper layers and the resistors.

5.6.2 Density

It seems difficult to increase the density of actuators limited by the size of the resistors, mainly because it will be difficult to have smallest devices able to sustain this load of power. If needed an obvious solution is to increase the size of the beam. However, it means that some supplementary optics are required, so the aberrations will potentially

increase in the system.

In the next chapter, we will study the implementation of the TDM second prototypes in a matching correction system to prepare the experimental tests of Chapter 7.

Chapter 6

Analytical Control of the Beam Modal Content

We have experimentally demonstrated that the TDM is able to generate some common aberrations up to the order 5 of the Zernike polynomials. The analysis was performed in the plane of the TDM surface.

In this chapter, we explore the possibility to improve the input laser beam matching into a cavity by reducing the high order modes with the help of the TDM. It should be noted that some modes will be more or less harmful for different applications. This will lead to different requirements. Here we propose a general scheme for the mode reduction. A full description of the input beam is made through a decomposition in Hermite-Gaussian modes. The initial modal content of a beam is preserved along the propagation if no defect is encountered in the system. The propagation of the different modes is studied here to understand how and where to act to reduce a specific mode power. This analysis highlights the importance of the relative Gouy phase into the conception of a corrective system. A the end of the chapter, we propose some recommendations to perform a mode matching improvement by the TDMs based on the theoretical correction.

6.1 Propagation and correction of an aberrated beam

6.1.1 Hermite Gaussian beam

According to the solution of the paraxial wave equation, a laser beam is a combination of modes: a fundamental mode E_{00} that corresponds to an ideal Gaussian beam and some high order modes E_{mn} produced by the aberrations (see Appendix A). Any laser

beam can be decomposed in an unique way in an orthogonal basis. One can choose the basis into which to solve the paraxial wave equation [69] according to the geometry of the considered problem. In some cases, it could be useful to describe the modes resonant into a cavity with a basis that is taking into account the ellipticity of the modes (Ince-Gauss basis [70]). Here we consider the Hermite-Gaussian functions, as we are making no assumption on the defects of the cavity or the aberrations in the laser beam (axis-symmetric or non-axis-symmetric defects).
With $E(x, y, z)$ the electric complex field, we can write the aberrated beam in the Hermite-Gauss basis:

$$E(x, y, z) = a_{00} E_{00}(x, y, z) + \sum_{mn} a_{mn} E_{mn}(x, y, z) \tag{6.1}$$

$$E(x, y, z) = E_{00}(x, y, z)[a_{00} + \sum_{mn} a_{mn} \frac{1}{\sqrt{2^{m+n} m! n!}} H_m(\frac{\sqrt{2}x}{w(z)}) H_n(\frac{\sqrt{2}y}{w(z)}) e^{i(m+n)atan(\frac{z}{z_R})}] \tag{6.2}$$

with:

$$E_{00}(x, y, z) = \sqrt{\frac{2}{\pi}} \frac{1}{w(z)} e^{-ikz - i\frac{k}{2q(z)}(x^2+y^2) + iatan(\frac{z}{z_R})} \tag{6.3}$$

a_{00} is the coefficient of the fundamental mode TEM_{00} and a_{mn} are the complex coefficients of the high order modes, with

$$|a_{00}^2| + \sum_{mn} |a_{mn}^2| = 1 \tag{6.4}$$

We can clearly see from Eq.6.2 that the high order modes are adding a phase dependent term and an amplitude dependent term. Both terms need to be suppressed to recover an ideal Gaussian beam. A corrective device like a TDM is however able to act on the phase dependent term only. But we know that any phase modification along the propagation will affect the modal content and will therefore have an impact on the amplitude term as well. With two devices adequately positioned to act in different phase planes, a control of the modal content is possible as we will see straightaway.

6.1.2 Correction at the first order

6.1.2.1 Calculation

Let's now consider 2 planes of coordinates z_1 and z_2 along the beam propagation. In each plane, we assume we can act on the optical path length in the approximation of the small amplitudes. In order to simplify the problem, we will first consider an aberrated

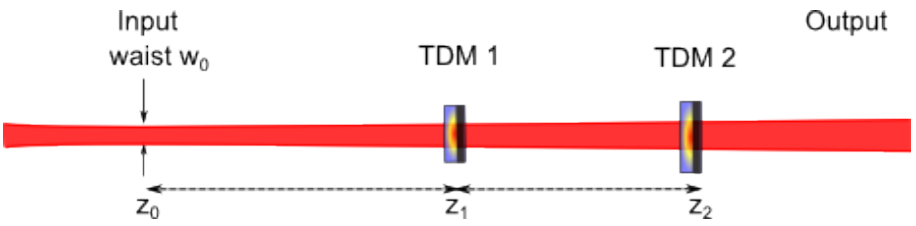

FIGURE 6.1: Principle of the computation based of a FFT simulation: a laser beam propagates from the waist plane and the phase is modified in the two planes TDM1 and TDM2 separated by the distance $z_2 - z_1$. A description of the simulation can be found in section 6.2.

beam with only one high order mode H_{mn}. We can rewrite Eq.6.1:

$$E(x, y, z_1) = E_{00}(x, y, z_1)[a_{00} + a'_{mn} H_{mn}(z_1) e^{\phi_{z_1}}] \tag{6.5}$$

with:

$$\begin{cases} \phi_{z_1} = (m+n) atan(\frac{z_1}{z_R}) \\ a'_{mn} = a_{mn} \frac{1}{\sqrt{2^{m+n} m! n!}} \\ H_{mn}(z_1) = H_m(\frac{\sqrt{2}x}{w(z_1)}) H_n(\frac{\sqrt{2}y}{w(z_1)}) \end{cases} \tag{6.6}$$

We can apply a phase correction in the plane z_1, that has the shape of the aberration to correct:

$$\phi_{correction} = b_1 H_{mn} \tag{6.7}$$

that leads at the first order to:

$$e^{i\phi_{correction}} \simeq 1 + i b_1 H_{mn} \tag{6.8}$$

with $b_1 \in \mathbb{R}$.

$$E_{corrected_1} = E(x, y, z_1) e^{i\phi_{correction}} \tag{6.9}$$

$$E_{corrected_1} \simeq E_{00}(x, y, z_1)[a_{00} + a'_{mn} H_{mn}(z_1) e^{i\phi_{z_1}} + i a_{00} b_1 H_{mn}(z_1) + o(H^2_{mn}(z_1)) + ...] \tag{6.10}$$

Here, and subsequently, we neglect the H^2_{mn} and upper terms. We then propagate the corrected field to the plane z_2:

$$E(x, y, z_2) = E_{00}(x, y, z_2)[a_{00} + a'_{mn} H_{mn}(z_2) e^{i(\phi_{z_1} + \phi_{z_2})} + i a_{00} b_1 H_{mn}(z_2) e^{i\phi_{z_2}}] \tag{6.11}$$

with ϕ_{z_2} the accumulated Gouy phase between the planes z_1 and z_2 with respect to the fundamental mode:

$$\phi_{z_2} = (m+n) atan(\frac{z_2}{z_R}) - \phi_{z_1} \tag{6.12}$$

We act again on the phase, this time in the plane z_2, and again neglect the terms from H_{mn}^2. We have at the first order:

$$E_{corrected_2} = E_{00}(x,y,z_2)[a_{00}+a'_{mn}H_{mn}(z_2)e^{i(\phi_{z_1}+\phi_{z_2})}+ia_{00}b_1H_{mn}(z_2)e^{i\phi_{z_2}}+ia_{00}b_2H_{mn}(z_2)] \tag{6.13}$$

From Eq.6.13, we can clearly see that it is possible to suppress the high order modes by choosing appropriately the phase correction in the 2 planes. The general solution is then:

$$a'_{mn}H_{mn}(z_2)e^{i(\phi_{z_1}+\phi_{z_2})} + ia_{00}b_1H_{mn}(z_2)e^{i\phi_{z_2}} + ia_{00}b_2H_{mn}(z_2) = 0 \tag{6.14}$$

The coefficient a_{mn} is a complex number, we obtain from Eq.6.14:

$$\begin{cases} \Re(a'_{mn})\cos(\phi_{z_1}+\phi_{z_2}) - \Im(a'_{mn})\sin(\phi_{z_1}+\phi_{z_2}) - a_{00}b_1\sin(\phi_{z_2}) = 0 \\ \Re(a'_{mn})\sin(\phi_{z_1}+\phi_{z_2}) + \Im(a'_{mn})\cos(\phi_{z_1}+\phi_{z_2}) + a_{00}b_1\cos(\phi_{z_2}) + a_{00}b_2 = 0 \end{cases} \tag{6.15}$$

defined only if $\phi_{z_2} \neq 0[\pi]$. We obtain the corrective phases:

$$\begin{cases} b_1 = \frac{\Re(a'_{mn})}{a_{00}}\frac{\cos(\phi_{z_1}+\phi_{z_2})}{\sin(\phi_{z_2})} - \frac{\Im(a'_{mn})}{a_{00}}\frac{\sin(\phi_{z_1}+\phi_{z_2})}{\sin(\phi_{z_2})} \\ b_2 = -\frac{\Re(a'_{mn})}{a_{00}}(\sin(\phi_{z_1}+\phi_{z_2}) + \frac{\cos(\phi_{z_1}+\phi_{z_2})}{\tan(\phi_{z_2})}) - \frac{\Im(a'_{mn})}{a_{00}}(\cos(\phi_{z_1}+\phi_{z_2}) - \frac{\sin(\phi_{z_1}+\phi_{z_2})}{\tan(\phi_{z_2})}) \end{cases} \tag{6.16}$$

6.1.2.2 Discussion of the results

In theory, as long as we stay in the small amplitudes approximation, we can completely suppress a given mode by acting on the phase into two separate planes. The approximation is valid when $b_{1,2} \ll 1$. It means $\| (a_{mn}) \| H_{mn} \ll a_{00}$, so we have to consider very low values of mismatching. The corrections that we will have to apply are:

$$b_{1,2}H_{mn} = \frac{2\pi}{\lambda}\delta s_{1,2} \tag{6.17}$$

with $\delta s_{1,2}$ the optical path difference produced by the TDMs. It is worthy of notice that the correction pattern of the mode we want to suppress is given by the spatial representation of the corresponding Hermite polynomial. We now have a direct information on the maximal spatial frequency we need to correct a given set of aberrations.

According to these results, ϕ_{z_2} has to be in the interval $]0\ ;\ \pi[\ +\ k\pi$, $k \in \mathbb{N}$. From the Eq.6.12, we can rewrite the accumulated phase of the fundamental mode between the

planes z_1 and z_2:

$$\phi_{00_{z_2}} = \frac{\phi_{z_2}}{m+n} \tag{6.18}$$

The configuration of the setup has then to be choose to have the Gouy phase of the fundamental mode different than π over the maximum order to suppress. For example, in the case of the modes until the 5th order, a fundamental Gouy phase range allowed is $]\ 0\ ;\ \frac{\pi}{5}[$.

6.1.3 Effect of the correction at the second order

6.1.3.1 General case

In the previous section, we limit our calculation to the first order. We now want to have an idea of the impact of the creation of the other modes. So let's rewrite the equations developed up to the second order. From the Eq.6.9, we have:

$$\begin{aligned} E_{corrected_1} \simeq E_{00}(x,y,z_1)[\, a_{00} + a'_{mn} H_{mn}(z_1) e^{i\phi_{z_1}}][1 + ib_1 H_{mn}(z_1) - ... \\ \frac{b_1^2}{2} H^2_{mn}(z_1))] \end{aligned} \tag{6.19}$$

$$\begin{aligned} E_{corrected_1} \simeq E_{00}(x,y,z_1)[\, a_{00} + a'_{mn} H_{mn}(z_1) e^{i\phi_{z_1}} + a_{00} b_1 H_{mn}(z_1) \\ + a_{mn} b'_1 H_{mn}(z_1)^2 e^{i\phi_{z_1}} - a_{00} \frac{b_1^2}{2} H^2_{mn}(z_1))] \end{aligned} \tag{6.20}$$

And then, after propagation and correction by the second TDM, the output field can be expressed by:

$$\begin{aligned} E_{corrected_2} = E_{00}(x,y,z_2)[a_{00} + H_{mn}(z_2)(a'_{mn} e^{i(\phi_{z_1}+\phi_{z_2})} + ia_{00} b_1 e^{i\phi_{z_2}} + ia_{00} b_2) \\ H^2_{mn}(z_2)(-a_{00}(\frac{b_2^2}{2} + b_1 b_2 e^{i\phi_{z_2}} + \frac{b_1^2}{2} e^{iX}) + ... \\ ia'_{mn} e^{i\phi_{z_1}} (b_1 e^{iX} + b_2 e^{i\phi_{z_2}}))] \end{aligned} \tag{6.21}$$

We retrieve the terms in H_{mn}, that are suppressed according to Eq.6.14, so it remains:

$$\begin{aligned} E_{corrected_2} = E_{00}(x,y,z_2)[a_{00} + H^2_{mn}(z_2)(-a_{00}(\frac{b_2^2}{2} + b_1 b_2 e^{i\phi_{z_2}} + \frac{b_1^2}{2} e^{iX}) \\ + ia'_{mn} e^{i\phi_{z_1}} (b_1 e^{iX} + b_2 e^{i\phi_{z_2}}))] \end{aligned} \tag{6.22}$$

The phase X depends on the high order Hermite-Gauss modes created by the correction and propagated through the system. To express it, we have to know the development of H_{mn}^2 in the Hermite-Gauss basis. According to the general formula [71] computing the product of the H_{mn} modes, it leads to have new modes in the corrected beam. Fortunately, Eq.6.22 shows that all these terms are of the second order. So, the main aberration is effectively corrected at the first order, and the residual aberration contains the modes predicted by [71].

6.1.3.2 Example of the modes m + n = 2

We compute the power of the Hermite-Gauss polynomials for the 6 first orders (see Table A.1 in AppendixA), and in particular we obtain:

- $m = 1, n = 1$

$$H_{11}^2 = H_{22} + 2H_{20} + 2H_{02} + 4H_{00} \tag{6.23}$$

  In this case, the mode H_{11} is completely suppressed at the second order. However, the other modes of $m + n = 2$, and the "harmonic" of the order 4 have been created.

- $m = 2, n = 0$

$$H_{20}^2 = H_{40} + 8H_{20} + 8H_{00} \tag{6.24}$$

  In this case, the mode H_{20} is only reduced. Again the harmonic of order 4 has been created.

6.1.3.3 Example of the mode H_{30}

In the same way the square of the mode H_{30} is:

$$H_{30}^2 = H_{60} + 18H_{40} + 72H_{20} + 48H_{00} \tag{6.25}$$

From this result, we can see that the square of any Hermite polynomial generates even modes at each order. This is confirmed by the equation given in the Appendix A:

$$H_i^2(x) = \sum_{k=0}^{i} k!\ 2^k \binom{i}{k}^2 H_{2i-2k}(x) \tag{6.26}$$

Moreover some power is always sent to the fundamental mode H_{00} for any mode square.

6.2 Simulations of the linear analytical model

To validate our analytical model and evaluate its limits, we implement a simple simulation: an aberrated beam is propagating through two TDMs on which we apply the corrections previously computed. We use a Matlab code based on the Fast Fourier Transforms [72] to propagate the beam. This allows to have an accurate information on the beam content and when the phase are added with the TDMs, to take into account all the mode content and being limited by the sampling accuracy. The simulation is made with an adaptive window [73]: the size of the window is adjusted to the beam size that varies with the divergence. This solution allows to work with a good description of the beam at each step of the propagation (see Fig.6.2). The TDMs are modeled by simple infinite phase plates perfectively transmissive: there is no additional phase due to the reflection, and no reflectivity/transmission coefficients. The corrections have a large spatial resolution (no actuator pattern) and there is no limit of actuation amplitude.

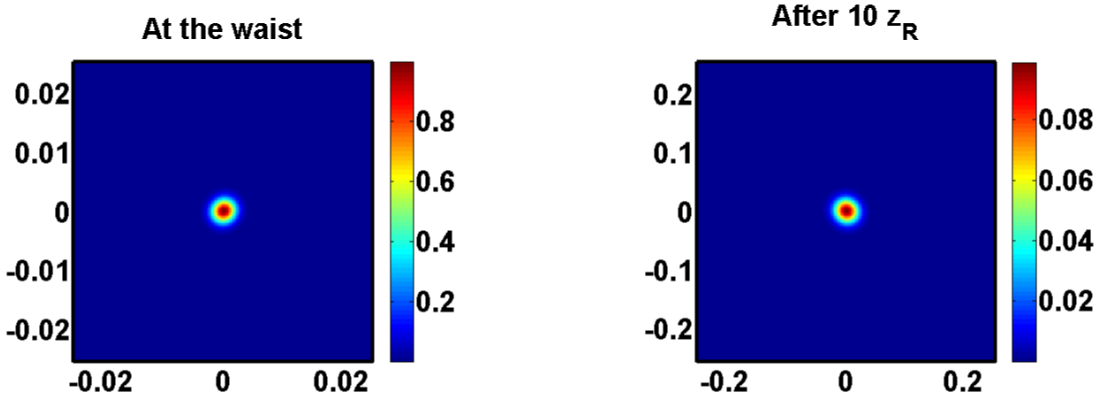

FIGURE 6.2: Example of the adaptive window along a propagation: the beam at the waist (left figure) and the beam after a propagation along 10 Rayleigh lengths (z_R) (right figure). The spatial coordinates are indicated on the axes in meters and the amplitude are normalized.

6.2.1 Correction efficiency

We test our model with a simulation based on the following configuration: the laser beam contains the fundamental mode H_{00} and a single high order mode H_{mn}. The initial mode composition is normalized with $\| a_{mn} \| = 10^{-3}$. Two phase plates representing the TDMs are separated by a phase $\phi_{z_2} = \frac{\pi}{4}$ for the mode H_{mn}. We assume that all modes are generated in the waist plane. On the first TDM, the mode H_{mn} has a phase $\phi_{z_1} = \frac{\pi}{4}$. The modal projection is made with the modes up to the order 15 (136 modes).

We develop the result analysis for 2 cases: the mode HG_{11} and the mode HG_{20}.

Mode HG11 Let's consider the mode H_{11} introducing a mismatch of 10^{-3}. If we have a look on the mode composition before the correction and after the correction (see Fig.6.4), we can see that the correction factor for the mode considered is: $\frac{10^{-3}}{10^{-8}} = 10^5$.

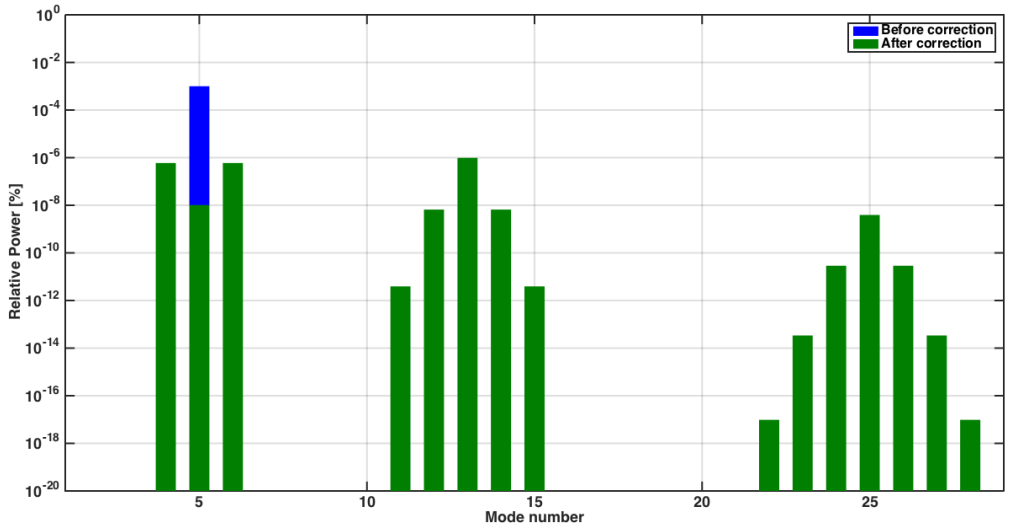

FIGURE 6.3: Normalized composition of the laser beam before and after the correction by the TDMs. The initial high order mode content is 10^{-3}.

We can clearly see on the same figure that other modes that were not present in the initial beam are also generated. The first interesting point is that the modes expected from the second order calculation (see previous paragraph) are the main important modes generated: we observe the modes H_{20} and H_{02}, as well as the mode H_{22}. The second interesting point is that the modes are only generated in the even orders. The mismatching after correction goes from 10^{-3} to 10^{-6}.

Mode HG20

We perform the same analysis for the mode HG_{20}. The mode composition after correction is different from the previous case: we retrieve the modes expected from the analytical computation. The correction for the mode goes from 10^{-3} to 3.5 10^{-6}, so a factor almost 300 of correction is performed.

6.2.2 Model linearity

In order to estimate the validity domain of our analytical model, we perform the correction of the beam composed of the fundamental mode E_{00} with a varying proportion of

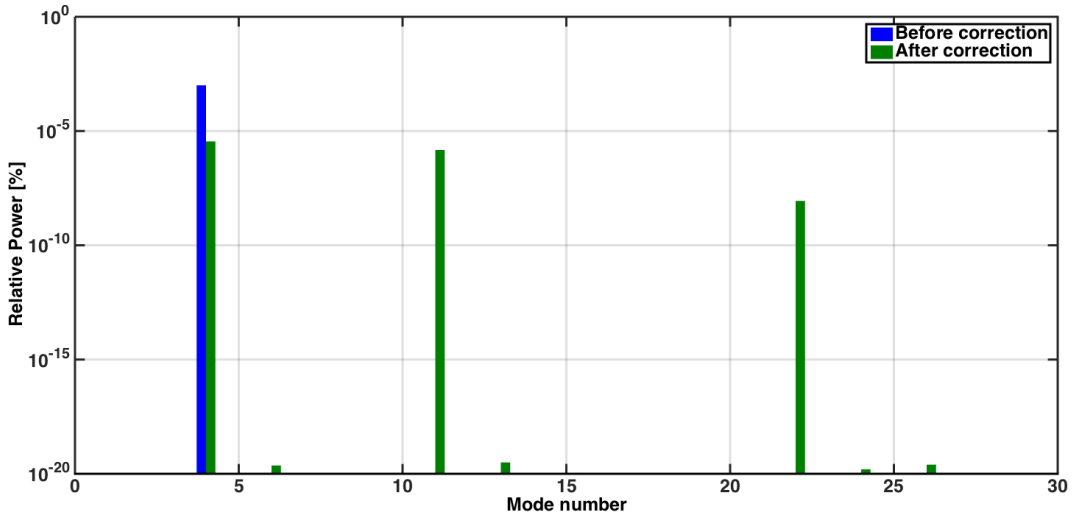

FIGURE 6.4: Normalized composition of the laser beam before and after the correction by the TDMs. The initial high order mode content is 10^{-3}.

the mode H_{20}. It is equivalent to different initial mismatches starting from 10^{-6} to 10^{-1}. We observe that the correction is very efficient when the initial mismatch is below 10^{-3}: the result is dominated by the numerical noise (see Fig.6.5). If the initial mismatch is smaller or equal to 10^{-2}, the mismatch is reduced by a factor 10 and we can say that it is still worth to perform the correction. The linear model is then valid until an initial mismatch of 10^{-3} and the correction is efficient for mismatch up to 10^{-1} when the phase is reasonable.

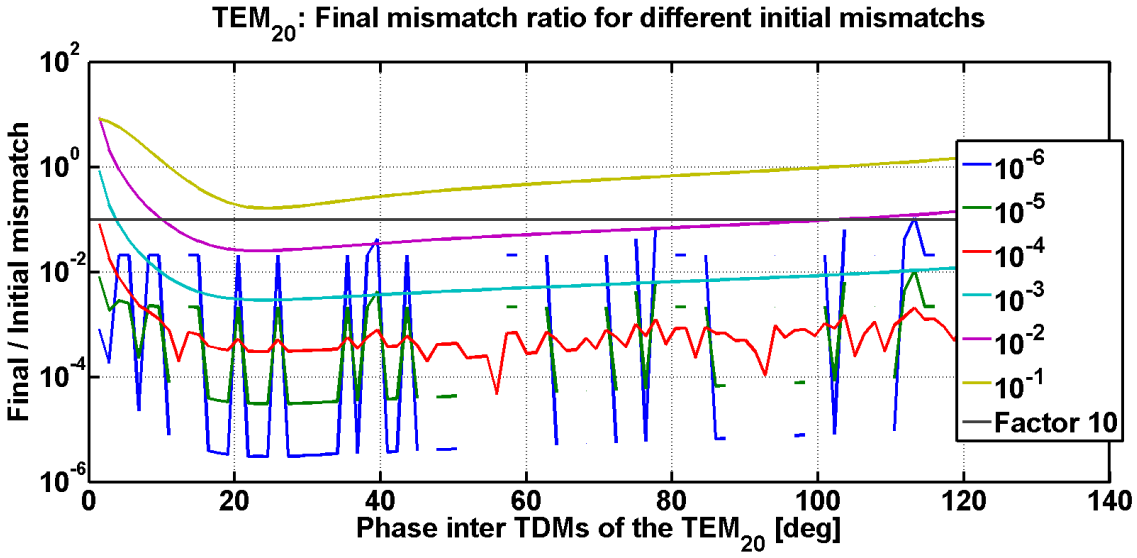

FIGURE 6.5: Correction efficiency of the mode HG_{20} as a function of the inter-TDMs phase for different initial mode content. The correction is perfectly performed up to an initial mismatch of 10^{-3}: we can see that the result is dominated by numerical noise.

6.2.3 Position of the TDMs: Inter-TDMs phase

We have seen that the amplitude of correction required from the TDMs is related to the complex amplitude of the mode composition, that is to the initial phase between the fundamental mode and the mode to correct, as well as to the phase between the two planes of correction (TDMs). According to Eq.6.16, there is no constraint on the initial phase to perform a correction: it will be possible to reduce the high order mode whatever will be the initial phase.

During the propagation from the waist to the positive infinite, the Gouy phase of the fundamental mode varies from 0 to $\frac{\pi}{2}$ (see Fig.6.6). If the high order modes are in phase with the fundamental mode at the waist, the Gouy phase of these modes ϕ_{z_2} with respect to the fundamental mode varies from 0 to $(m+n)\frac{\pi}{2}$.

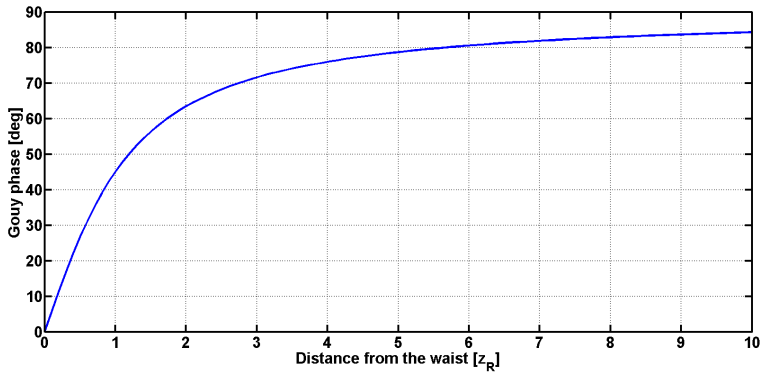

FIGURE 6.6: Gouy phase of the fundamental mode

As discussed before, no correction is possible for a mode when the TDMs are separated by $\phi_{z_2} = \pi$ for the mode to correct. With the simulation, we can illustrate that the correction diverges when the phase between the TDMs is equal to π (see Fig.6.7).

6.2.4 Successive correction of several modes

In order to test the correction of several modes, we propagate a beam with three modes at the input creating a mismatch of 6%. The initial beam contains 1.1% of HG_{11}, 1% of HG_{12} and 0.1% of HG_{13}. The correction is performed by applying successively the correction maps corresponding to the mode with the highest proportion (see Fig.6.8). For example, we start with the correction of the mode HG_{11}: it is reduced by a factor 400. Then the maps for the correction of the mode HG_{12} are applied and it is reduced by a factor 10. Finally, the mode HG_{13} is reduced by a factor 60. We observe some

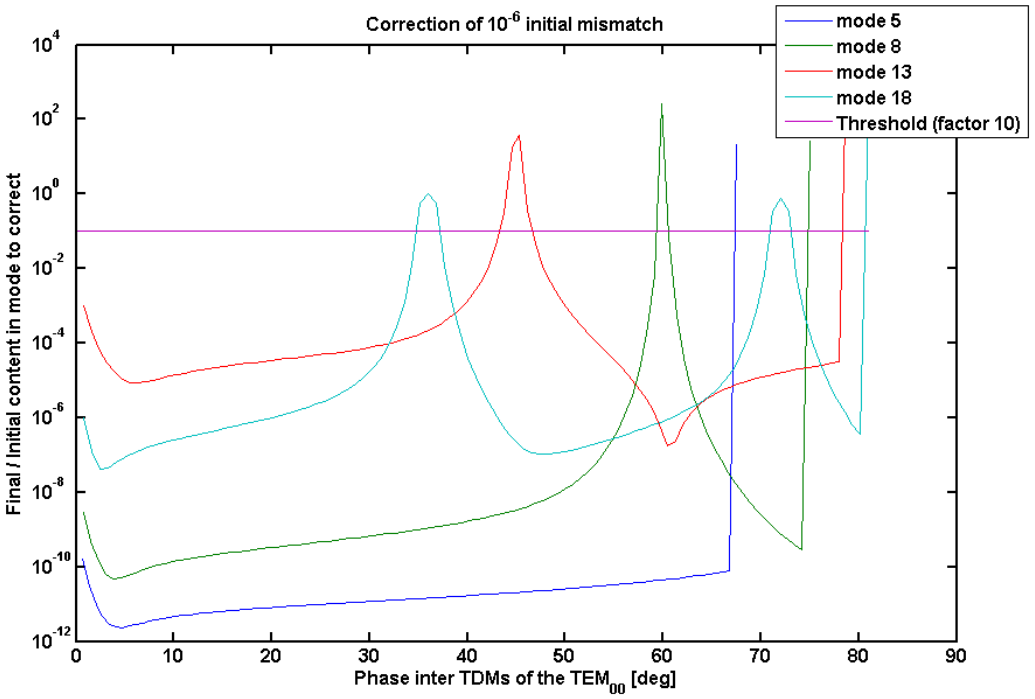

FIGURE 6.7: Correction efficiency of different modes as a function of the fundamental mode inter-TDMs phase. The correction is diverging for the values of $\pi/(m+n)$.

coupling between the modes, so the proportion of the first modes slightly increases again after several corrections. After three iterations the matching is increased up to more than 99% (see Fig.6.9).

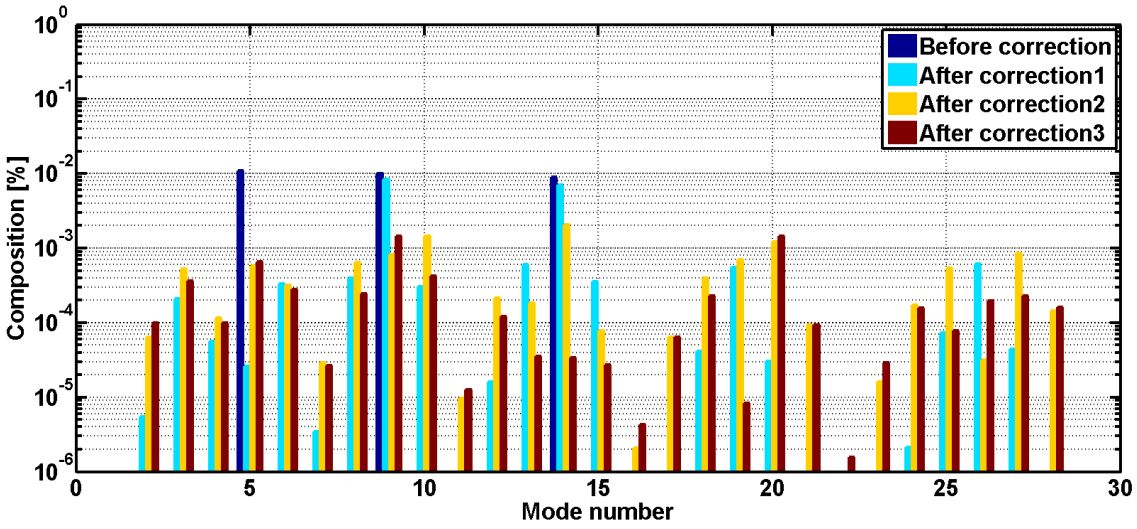

FIGURE 6.8: Successive compositions of the beam at the output of the setup at the beginning and after three successive corrections.

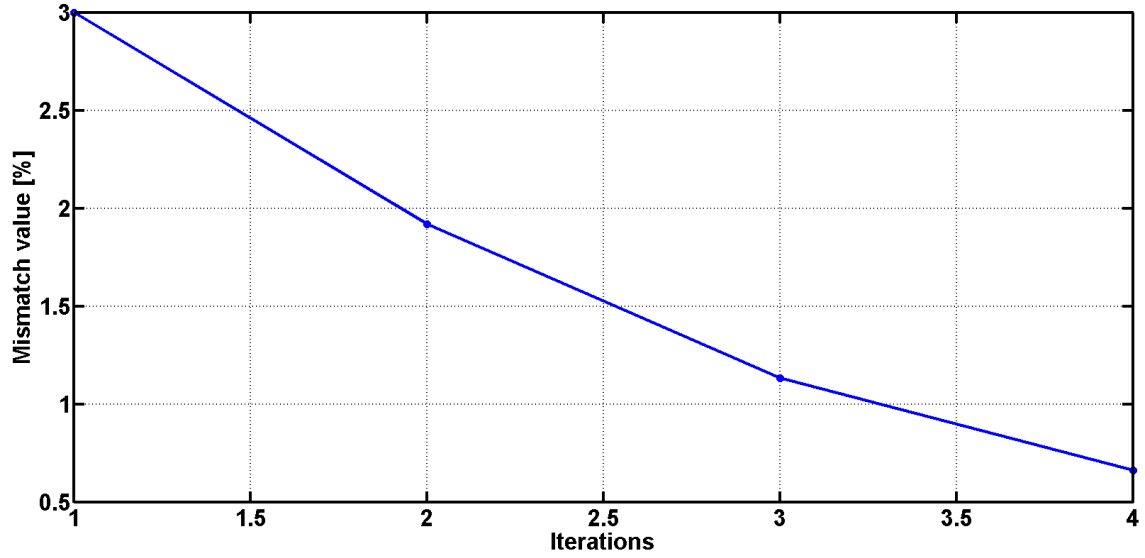

FIGURE 6.9: Reduction of the mismatching value by applying three successive corrections.

6.2.5 Physical constraints: towards a more realistic model

Strictly speaking, to perform the correction predicted by the previous computation a device able to provide spatially infinite and high amplitude diverging phase would be required. The TDM substrate defines a finite area that has large dimensions with respect to the beam waist. The TDM substrate is 2" diameter, so the effect of the mirror clipping will be very low. As said before, for the highest Hermite-Gauss mode we want to correct (TEM_{50}), the clipping has to be larger than $1.52\ \sqrt{5}\ w_0 \simeq 3.4\ w_0$ to control more than 99% of the power. With a mirror of 2" diameter, the beam is not clipped at all even for the mode TEM_{50}.
The actuation is made over the active area in the center. The present study is performed with the second prototype under the same conditions that have been tested in Chapter 5, so the active area is 10.2 mm diameter for a beam waist of 2.6 mm: it is large enough to control more than 99.9% of the beam power contained in the fundamental mode, but only 78.5% of the power in the mode TEM_{50}. However, the correction is not limited to the active area: the deformation produced by the edge actuators extends around thank to the thermal deformation properties of the substrate. With actuators having a HWHM of 2 mm, we would be able to control up to 88% of the power.

Unfortunately, the Hermite polynomials are impossible to reproduce with a TDM due to their diverging shape at the edges of the active area. For instance, the first polynomials $H_n(x)$ are represented in Fig.6.10. The sampling of the phase with the TDM actuators

will be another difference with respect to the ideal (unrealistic) case. A correction compatible with the physical constraints of the TDM has then to be find.

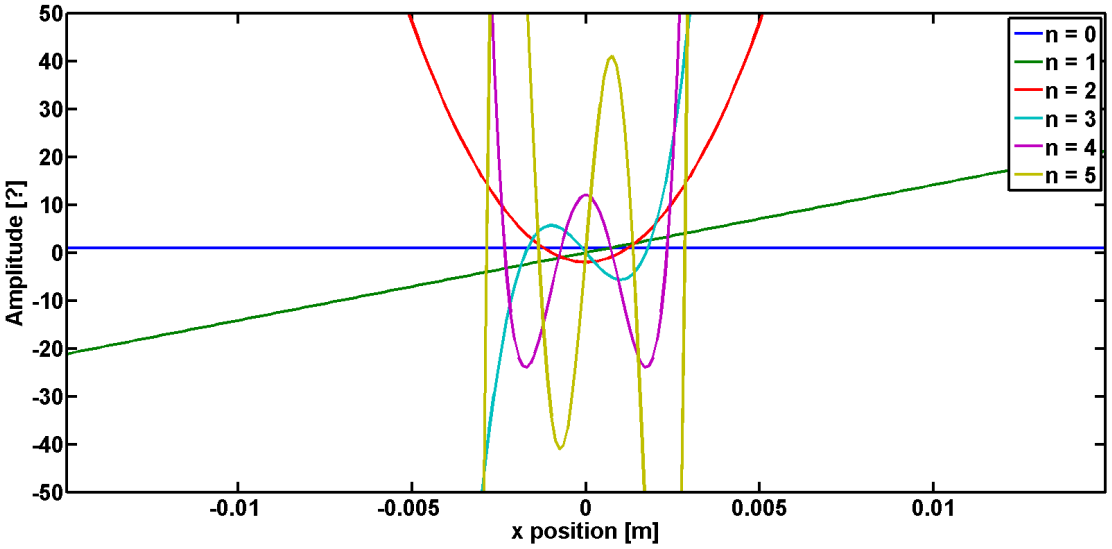

FIGURE 6.10: Section of the Hermite polynomials $H_n(\frac{\sqrt{2}x}{w_0})$ over the TDM substrate for a 2.6 mm waist. The active are is 5.1 mm radius.

6.3 Proposition of correction by the TDM

6.3.1 Identification of a set of correction maps

A simple solution is to weight the phase by the beam intensity, i.e. to apply the Hermite-Gauss maps instead of the Hermite polynomials.

We then choose to apply the HG_{mn} maps in the simulations.

$$Map_{mn} = HG_{mn} \tag{6.27}$$

Another solution have been proposed in [74] and in [29] for a pretty similar problem: the correction of the mirror maps inside a cavity. For the correction of degenerate modes inside a cavity (Hermite-Gauss or Laguerre-Gauss modes), correction maps have been proposed to apply with a thermal corrective device on the reflective coating of the cavity mirrors. The solution, found through the minimization of the error with the ideal non reflective maps, or with a more analytical computation, is to correct modes of the same order with the Hermite-Gauss maps weighted by the fundamental mode. And then to orthogonalize the maps. It is proposed to reduce the mean square value of the difference between the fundamental mode and the mode corrected by reflection on a mirror. The

maps proposed by [29] are found to be:

$$Map_{mn} = HG_{mn}HG_{00}* \tag{6.28}$$

However, we can say, anticipating the results of the next chapter, that we found experimentally that these last maps are less efficient to act on the modal content than the previous set.

6.3.2 Limits of the analytical model

We have demonstrated that it is possible to reduce a specific high order mode by choosing appropriate maps two TDMs can generate and by selecting a distance between them representing a Gouy phase shift for the high order mode.

To perform the correction predicted by the analytical model, we need to have a complete information on the setup: exact phase between modes at both planes, knowledge of the complex amplitude coefficient. This would be very complex to obtain experimentally. So an experimental strategy to act on the TDMs is still to be determined. A simple solution would be to apply the corrective pattern for the target mode, and to scan the amplitudes of correction on both TDMs, to find the minimum of mismatch. This is tested in the next chapter.

Chapter 7

Experimental Mode Matching Control

This chapter is dedicated to the experimental proof-of-principle of the mode matching improvement where we demonstrate that the high order mode content of the beam can be reduced with a combination of two TDMs.
Two setups have been successively implemented to obtain a control on the modal composition of the beam. After a description of the first experimental setup, we review some sensing methods that have been developed within the frame of the laser beam control. Then, the early tests conducted with the first setup are explained: they have demonstrated the possibility to correct the mismatch with the TDMs and the necessity to implement some design changes to improve the performance. The second setup is then described and some examples of matching control are shown.

7.1 Setup for the Mode Matching Control

The correction setup (see Fig.7.1) is based on two TDMs separated by a definite Gouy phase which we have demonstrated the importance in the previous chapter. On each TDM, the laser beam has the diameter required by design, that is 5.2 mm. Some telescopes ensure that both conditions are met on the TDMs. The laser beam is sent into a fixed cavity, while a sensing system (photodiodes and cameras) is measuring the matching. The laser is frequency locked on the cavity by the mean of a Pound-Drever-Hall control [75].

Triangular cavity The fixed cavity has a mode cleaner design: it is triangular that allows to have a separation of the reflection and the transmission of the cavity. When the

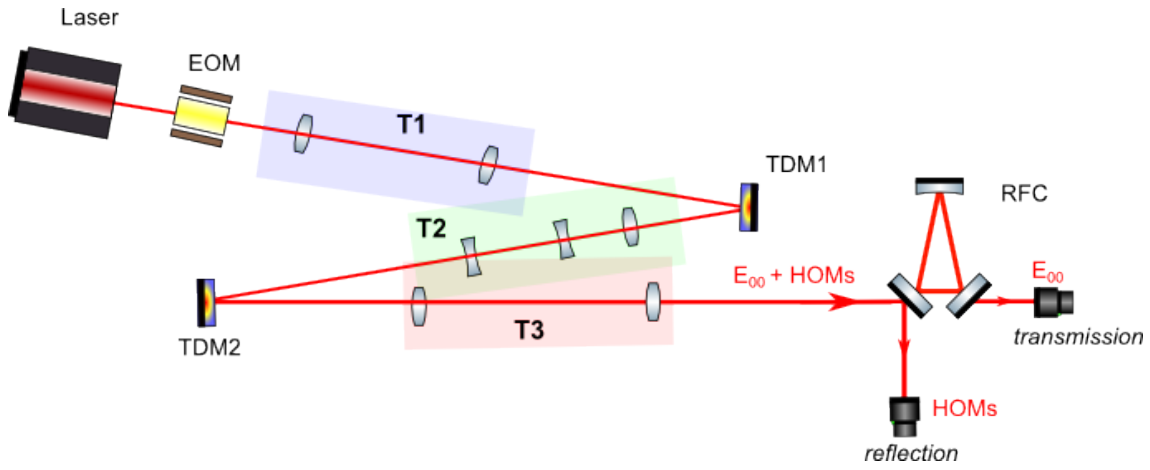

FIGURE 7.1: Scheme of a setup for the mode matching correction with two TDMs (TDM1 and TDM2) and three telescopes (T1, T2, T3).

laser is locked on the cavity, the fundamental mode is transmitted and the aberrations are rejected towards the perpendicular direction (see Fig.7.1). In a linear cavity, the modes of the same order $m + n = \alpha$ are resonating at the same frequency that is determined by the corresponding Gouy phase shift:

$$\phi_G(\alpha) = (\alpha + 1) \arctan\left(\frac{z}{z_R}\right) \tag{7.1}$$

In a triangular cavity, there is a removal of degeneracy due to the geometry and only the even modes of the same order α are superimposed at $\phi_G(\alpha)$ while the odd modes are resonating at $\phi_G(\alpha) + \pi$.

A scan of the cavity transmission provides the modal composition of the beam with an indetermination about the relative weight of the degenerated modes. Moreover, some modes are superimposed if the Gouy phase is the same multiple after several round-trips. The degeneracy in the determination of the modal content is effectively a limiting factor in our experiments (see Section 7.5).

7.2 First Mode Matching Setup description

A first setup has been built to control the matching of laser beam into the Reference Cavity (RFC) of Virgo. It is composed of three telescopes that are determined with a Matlab routine based on the ABCD matrices. The routine finds the telescope design that meets a set of objectives: length, Gouy phase and waist, for a given set of available lenses by an error minimization process. As for the characterization setup, the laser

— Telescope 1: Input - TDM1 —		
L_1	L_2	
0.04	0.1	
— Telescope 2: TDM1 - TDM2 —		
L_3	L_4	L_5
0.2	-0.1	-0.1
— Telescope 3: TDM2 - RFC —		
L_6	L_7	
0.1	-0.06	

FIGURE 7.2: First Mode Matching setup: telescopes features as determined by the Matlab routine. The focal lengths are given in meters.

beam is a pick-off from a Nd:YAG NPRO laser (λ = 1064 nm) with an input power of about 1 mW.

TDM prototypes The thermal contact is made with a layer of thermal paste between two layers of thermal tape. The substrate is a 2" HR mirror in fused silica. The two TDMs are switched on at half of the power: it corresponds to a RoC of 4.4 m.

Telescopes The first telescope enlarges the beam from the collimator after the fiber that brings the beam on the table (waist = 0.640 mm at 1.61 m from the output) to have a beam radius of 2.6 mm on the first TDM. The constraints for the second telescope (between TDM1 and TDM2) concern the beam size at the output, the Gouy phase that is carefully chosen, and the maximum length. By design, the second telescope gives a Gouy phase difference around 90 degrees for the fundamental mode between the TDMs and ensures to keep the beam radius at 2.6 mm on the second TDM. We now know that this Gouy phase value is not appropriate but the design of the setup was made earlier than the analytical computation presented in Chapter 6. The third telescope is used to match the beam into the cavity leading to have the main constraint on the beam size at the telescope output. It allows to reduce the beam waist to 0.286 mm at the input of the cavity. These last lenses are on translation stages to adjust more easily the matching. The lens values of the different telescopes are presented in Table 7.2 and the beam propagation is summarized in Fig.7.10.

Beam propagation The whole setup was simulated with Matlab (see Fig.7.3). Afterwards, the beam propagation has been checked via a software especially developed to design optical setups within the frame of Gravitational Wave Interferometers (Optcad). This allows to verify the configuration with thick lenses. The result is presented in Fig.7.4.

Fixed cavity The matching is studied into the RFC of Virgo. This cavity was used in Virgo/Virgo+ as a long term length reference. It has been reinstalled in Advanced Virgo for the same purpose. It is a 30 cm long triangular cavity [76] composed of two planes silica mirrors at the input and the output at 45 degrees and a silica concave mirror with a RoC of 0.5 m. The FSR of the cavity is about 472 kHz and the finesse for the p -polarization is higher than 900. The laser is frequency locked on the RFC cavity. The sidebands for the PDH lock are created at 8.35 MHz with the EOM at the input of the setup. The index of modulation is about 0.17: the sidebands power is 1.4 % of the total power and is the theoretical minimum power that could be reflected by the cavity.

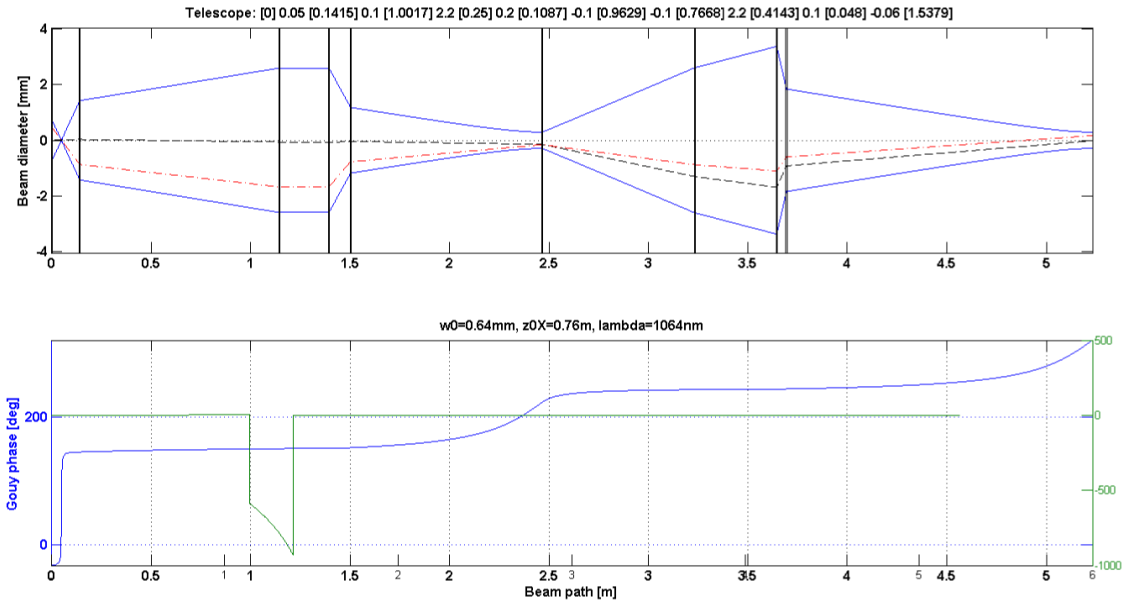

FIGURE 7.3: Optical configuration of the first Mode Matching Setup: (top) the three telescopes are presented with the lens values and the distances are given in the square brackets. (bottom) the Gouy phase (blue) and the curvature (green) variation along the propagation. Matlab presentation from H. Heitmann

Sensing We installed 2 cameras on the reflection path: a Near Field (NF) camera and a Far Field (FF) camera in the aim to implement a phase diversity sensing.

The whole setup is very sensitive to air fluctuations and turbulences. With the air conditioning system of the clean room, it was not possible to perform the test: the

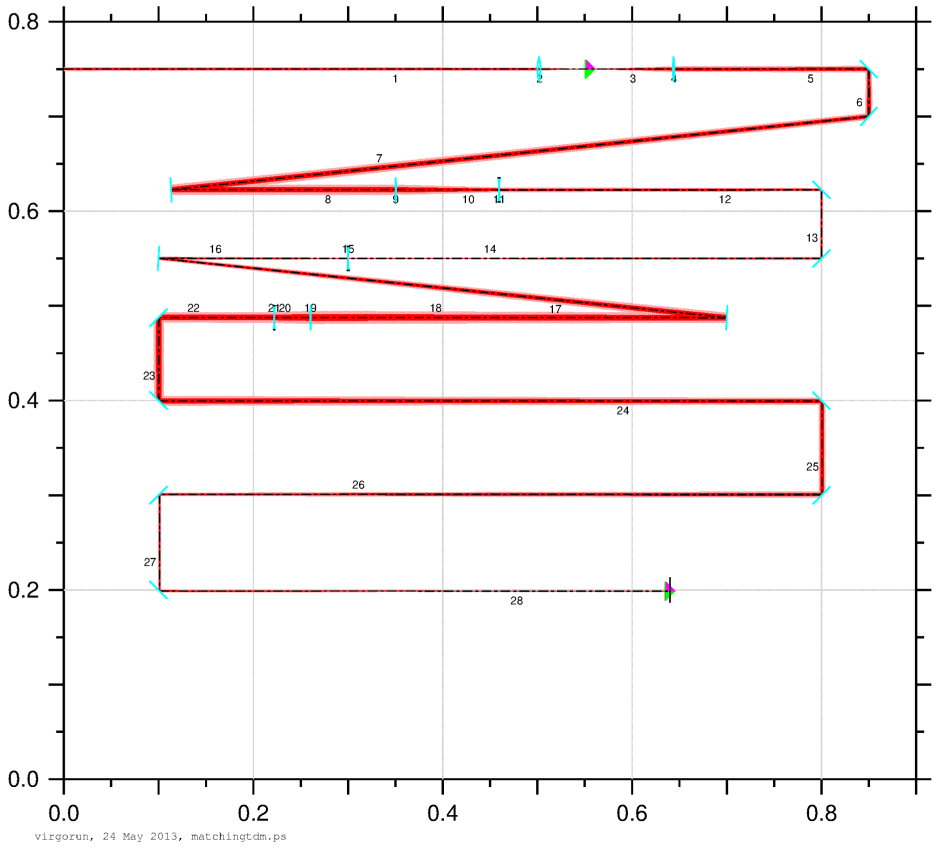

FIGURE 7.4: Optocad scheme to check the first Mode Matching setup design. The axis are in meters. The beam is represented by the red lines with a section proportional to the radius. The triangles represent the beam waists. The optical components are represented in blue.

beam fluctuations were greater than the correction provided by the TDMs. So thermal insulation covers have been added on the setup to protect it. We were able to observe a great reduction of the reflection signal fluctuations: the fluctuation amplitude descreases from 0.15 V to 0.005 V. The image was much more stable on the reflection cameras: it was possible to start the observation of the TDM effects on the matching.

7.3 Choice of the sensing

According to the formula of Hermite-Gauss modes (see Eq.6.2), the information of the modal composition is contained in the amplitude and the phase. Moreover the Gouy phase shift directly depends on the mode order. If we have access to the Gouy phase shift, we can try to observe the beam at different frequencies and retrieve the modal content.

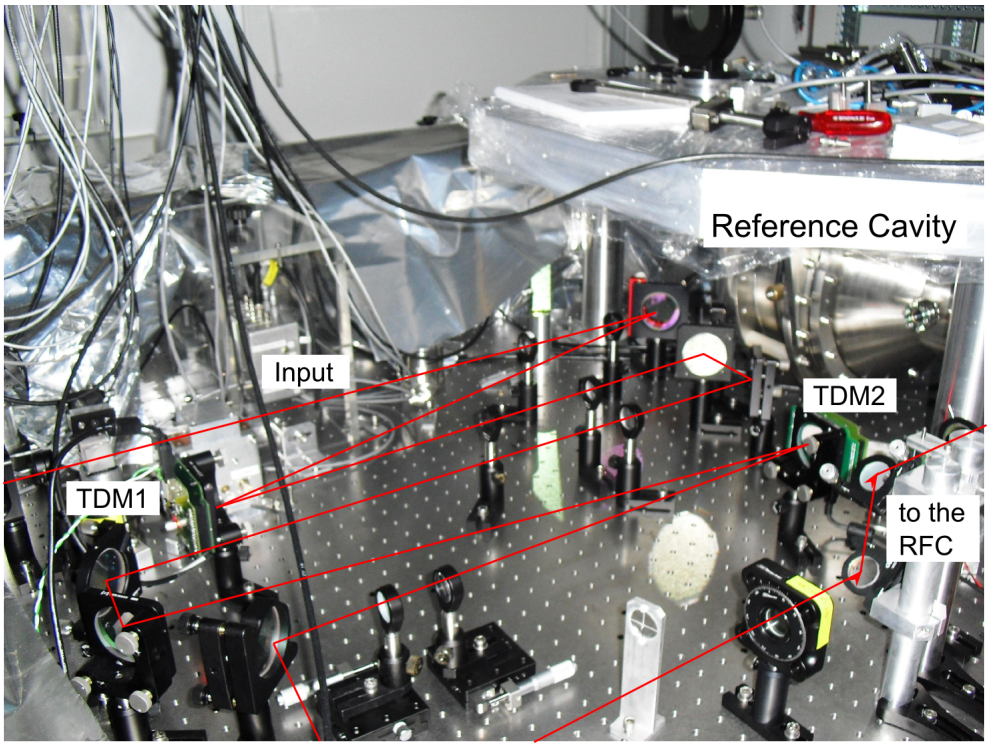

FIGURE 7.5: Photo of the first Mode Matching setup with the RFC. The beam propagation is represented by the red lines.

Spectra determination We can distinguish different sensing approaches, some of them are based on the spectral content of the beam:

- the spectral decomposition with the cavity itself: the cavity will act like as a spatial mode filter. We can recover the beam composition from a cavity scan. However, this implies to unlock the cavity. One might use a scanning Fabry-Perot cavity aside, but the modal composition can be different: one will have to assume that the basis is the same Hermite-Gauss basis. In both cases, an additional camera is helpful to identify the modes.
- with the heterodyne detection. Several methods are proposed to recover the modal composition at a given frequency that corresponds to the aberrations [31, 77] with the help of sidebands at the appropriate frequency (see Appendix A). Usually, one would need a complementary spatial information to identify the mode (modes of the same order at the same frequency)

We would like to use a method that allows to recover easily the modal content up to the order 5. So the methods based on the sidebands are probably not flexible enough, in the sense that we would need five sideband frequencies and a heavy material for the setup. The time constraint is quite low: we would have few seconds to compute the

mode content. Then a "blind" minimization algorithm could be considered. It is more flexible because it is not limited by the setup devices on the maximum mode content. We then start with this approach.

Phase diversity The *phase diversity* methods are based on the spatial composition of the modes: the principle is to observe the spatial content of a beam at different Gouy phases and to deduce the mode content via different minimization algorithms [78]. Several methods have been developed to recover the composition of a beam from two cameras at different Gouy phase planes.

Matching evaluation If it is not possible to recover the mode content, the matching can be evaluated through a simple figure of merit, based on the relative power variations in reflection or transmission. According to the energy conservation principle, the power P_i of the laser beam sent into the cavity is:

$$P_i = P_r + P_t + \mathcal{L} \tag{7.2}$$

with P_r the power reflected by the cavity, P_t the power transmitted by the cavity and $\mathcal{L}$ the losses from absorption and scattering.

If we neglect the losses, the matching is defined by the power transmitted by the cavity over the incident power:

$$Matching = \frac{P_t}{P_i} = \frac{P_i - P_r}{P_i} \tag{7.3}$$

This is the figure of merit we will experimentally use in the following, combined with cavity scans, that will be explained in the next paragraphs. The main inconvenient of this method, however, is that the matching is affected by simple misalignment or by a wrong beam waist position or value without the possibility to tell the difference with the high order mode content variation. This will be an impediment to go deeply into the setup analysis.

7.4 Results for the first matching setup

7.4.1 Stochastic parallel gradient descent algorithm

The first tests on the RFC cavity have been made with a minimum search algorithm [**?**] to control independently the 122 actuators of the TDMs. The error signal was the sum of the intensity on the 2 cameras (NF and FF) placed in reflection.

The principle of the algorithm is an adaptation of the stochastic parallel gradient descent algorithm:

1. The initial power P0 is read on the cameras.
2. Random values are sent to the TDMs to produce random maps of actuation and the power Pi is read on the cameras.
3. If Pi is inferior to P0, we go back to step 1: these maps are the new initial values and a new random try is made. P_0 is updated to P_i.
4. If Pi is superior to P0, the gradient is computed to produce new maps of actuation in the direction opposite to the gradient.
5. If the power Pi+1 is lower than P0, these maps are the new initial maps. Otherwise, we go back to P0 and try new random maps.

After one night, we obtained the curve in Fig.7.6. After calibration of the signal with the reflection photodiode and the power meter, the final mismatch corresponds to 2.3% for an initial mismatch of 14%. The slowness of the minimum search was an impediment to efficiently improve the algorithm and the setup. It was difficult to maintain the setup conditions unchanged for long periods of time due to thermal variations and mechanical drifts.

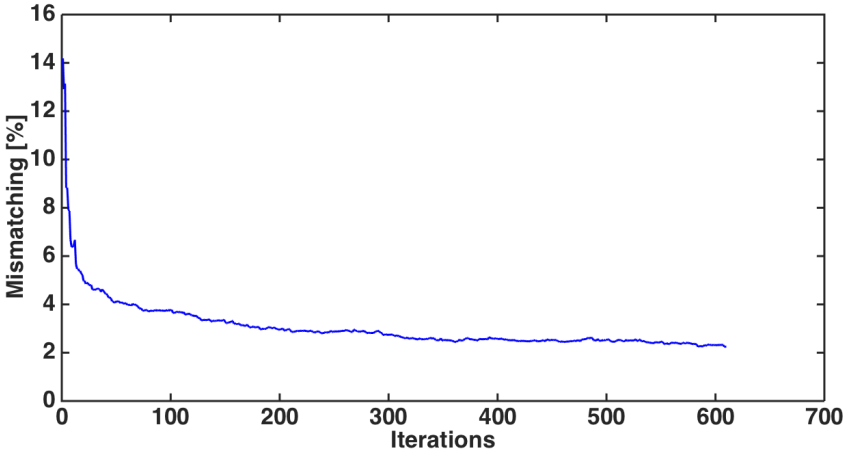

FIGURE 7.6: First Mode Matching setup: first tests with the SPGD algorithm and the RFC.

7.4.2 Golden search on gradient values

We applied an another algorithm that demonstrated to be faster in simulations. It computes the gradient of the actuation and then searches the minimum of mismatch along the gradient line with a golden search method [79].

Moreover, we decide to use a similar-Zernike polynomial basis to reduce the number of space search dimensions and to start with the correction of low spatial frequencies. At the time of these experiments, the computations about the analytical control of the modal control of the beam were not already performed. Here we use progressively the 4 first order Zernike modes. We compute the mismatch by observing the power reflected on the cavity. In Fig.7.7 is the convergence result. The reduction of the mismatch power is in theory limited by the sidebands, but we are limited at an higher mismatching value (over 2.5%) as for the stochastic algorithm.

In order to understand this limitation, we scan the cavity with a function generator at 10 mHz and 200 mV (triangular function) on the laser temperature. The results of the scan are presented in Fig.7.8 where the modes are identified with the camera in transmission of the cavity. For each mode, the top image is before correction and the down image is with the correction. We can clearly see the effect of the TDMs that are reducing the low spatial frequency modes.

However, the correction is saturated without cancelling completely the first modes whatever algorithm is implemented. For example, even after several attempts, we were not able to correct the focus very efficiently and it was dominating the mismatch. We infer that it is due to the fact that the TDMs are separated by a Gouy phase of 90 degrees after performing the analytical computation in Chapter 6. Moreover, the high finesse of the cavity does not make easy the mode management.

7.5 Second Matching Setup

The design of the second setup has been realized after the computations of Chapter 6. Therefore, the Gouy phase has been chosen to be 20 degrees in agreement with our computations. An additional TDM, called TDM0, is placed at the entrance of the setup (see Fig.7.12). It allows to play in a controlled way with the initial modal content of the beam. As for the previous setup, three telescopes are designed. The first telescope is here used to reach the good diameter on the TDM1. The details on the second setup configuration are presented in Table 7.9 and Fig.7.10.

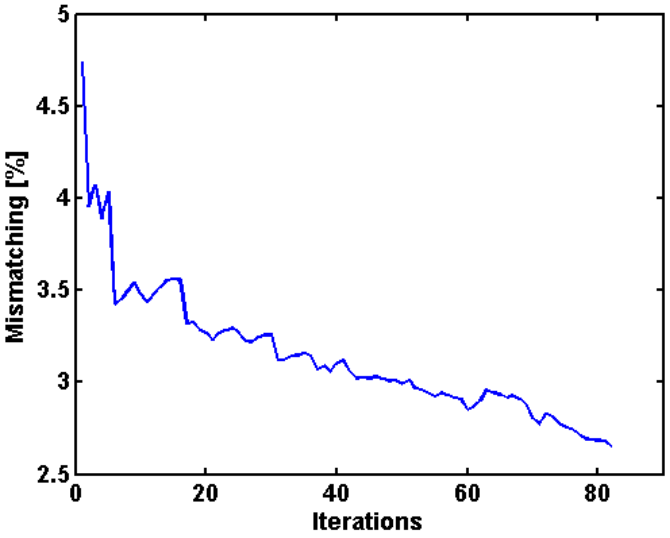

FIGURE 7.7: First Mode Matching setup: first tests with the Golden search algorithm and the Zernike maps with the RFC. The matching is increased by 2% in 80 iterations.

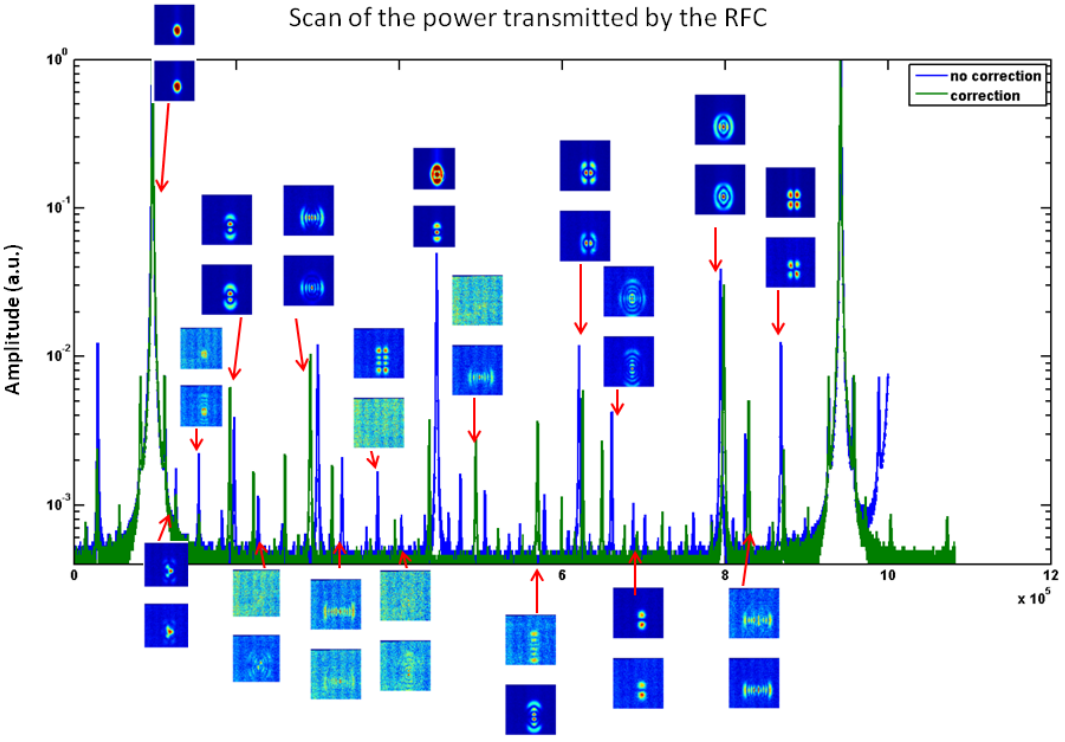

FIGURE 7.8: First Mode Matching setup: scan of the RFC before and after the correction by the TDMs. The modes are identified thanks to the images from the camera in transmission of the cavity. For each mode, the corresponding pictures are indicated by a red arrow: the top picture is the mode before correction and the bottom picture is the mode after correction.

— Telescope 1: TDM0 - TDM1 —	
L_1	L_2
0.2	0.125

— Telescope 2: TDM1 - TDM2 —		
L_3	L_4	L_5
0.3	-0.1	-0.1

— Telescope 3: TDM2 - OMC —	
L_6	L_7
0.25	0.3

FIGURE 7.9: Second Mode Matching setup: Telescopes features as determined by the Matlab routine. The focal lengths are given in meters.

The cavity is the Output Mode Cleaner (OMC) cavity of Virgo/Virgo+, the RFC being not available any more. The OMC cavity is a monolitic cavity made of Fused Silica. The input faces of the crystal are flat whereas the end face has a RoC of 0.3 m. It has a finesse of 50 and a FSR of 2 GHz (optical path of 7.5 cm). The input waist required is 140 μm [80].

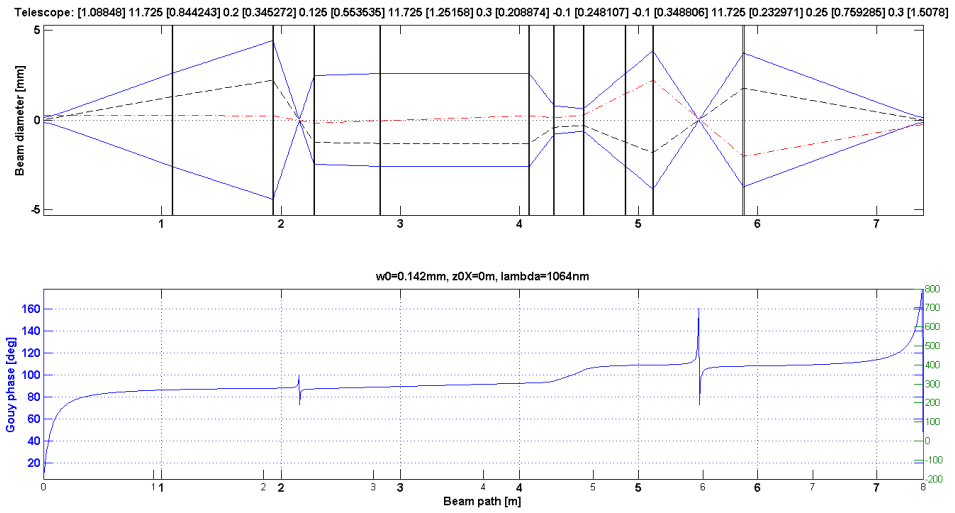

FIGURE 7.10: Optical configuration of the Second Mode Matching setup: (top) the three telescopes are presented with the lens values and the distances in the square brackets. (bottom) the Gouy phase (blue) variation along the propagation. Matlab presentation from H. Heitmann

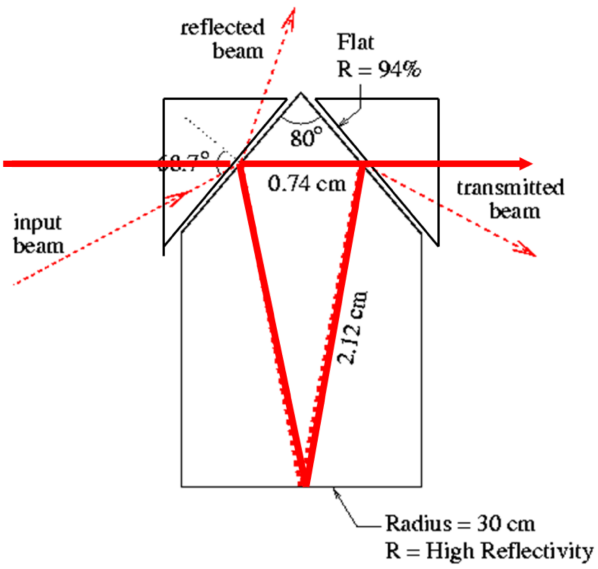

FIGURE 7.11: Scheme of the OMC with the main geometrical features of this monolithic cavity.

Sensing The reflected power read by a photodiode indicates the power changes to estimate the mismatch. A scan of the cavity transmission indicates the beam composition with a photodiode and a camera in transmission completes the information by displaying the modes. Therefore, there is no information about the mode degeneracy: we can not separate the relative content in modes resonating at the same frequency in the cavity.

7.5.1 Increase of the high order mode content

7.5.1.1 Map set to control the modes

In order to apply the analytical HG_{corr} maps with the TDMs, the interaction matrix M of one TDM is computed from the simulated influence functions. Thanks to the well known formula:

$$Map_{tdm} = M^{-1} HG_{corr} \tag{7.4}$$

we obtain the relative value of actuation for each actuator of the TDM. This result is presented in Fig.7.13. First we apply some of the maps with the TDM0 to increase the power of a particular mode.

7.5.1.2 Increase of the astigmatism

The HG_{11} map is applied with an amplitude maximum of 0.1 W delivered by resistor. The actuation limit is set at 0.15 W. The mismatch increases. By scanning the OMC

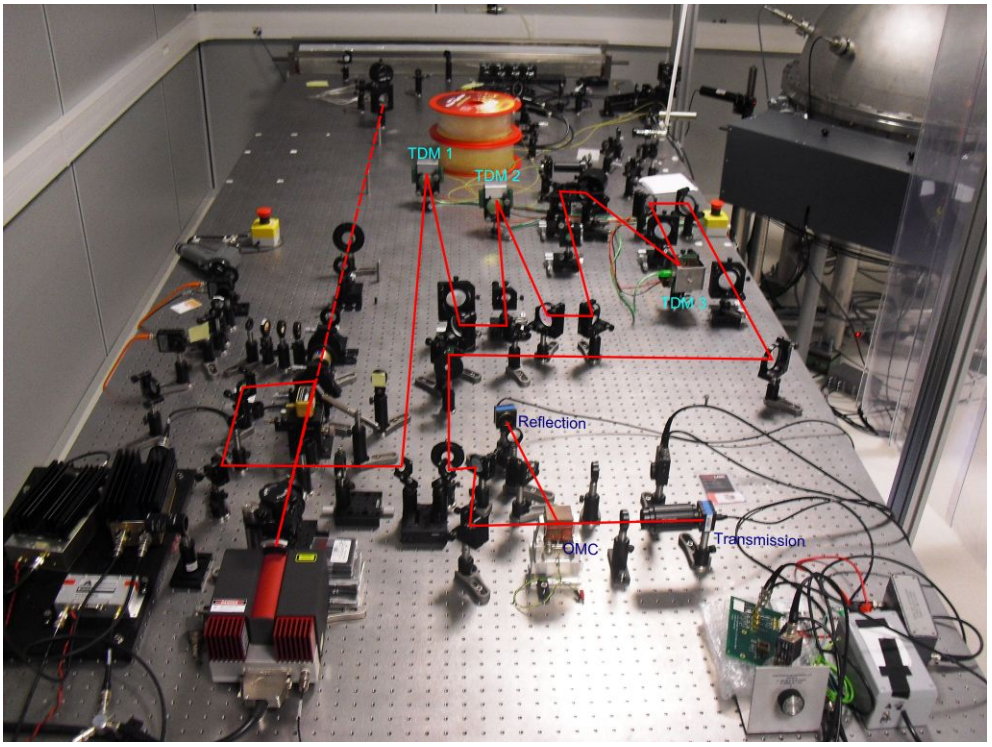

FIGURE 7.12: Second Mode Matching setup: photo of the installation at the CALVA platform (Orsay) with the OMC cavity.

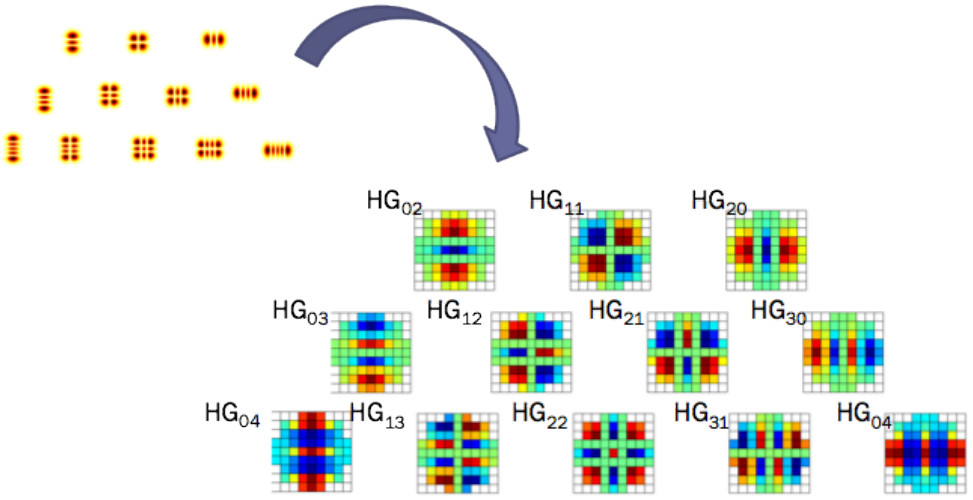

FIGURE 7.13: Correction maps Map_{tdm} defined from the Hermite-Gauss modes and projected on the TDM actuator basis thanks to the theoretical influence functions.

cavity we check the increase of the HG11 amplitude (see Fig.7.14). The mode content of the HG_{11} was increased by a factor 10. The tilt was manually corrected after the actuation by adjusting the tip/tilt mirror in front of the cavity. We observe an increase of the focus and some high order modes as well but they were not corrected manually.

7.5.1.3 Increase of the mode HG_{30}

The HG_{30} map is applied on the TDM0 with an amplitude of 70 mW per resistor. The mode content of the HG_{30} increases by a factor 2.5 (see Fig.7.14). Again, the tilt is manually corrected after actuation. Some other modes increase as well but for these modes are different than for the HG_{11} case.

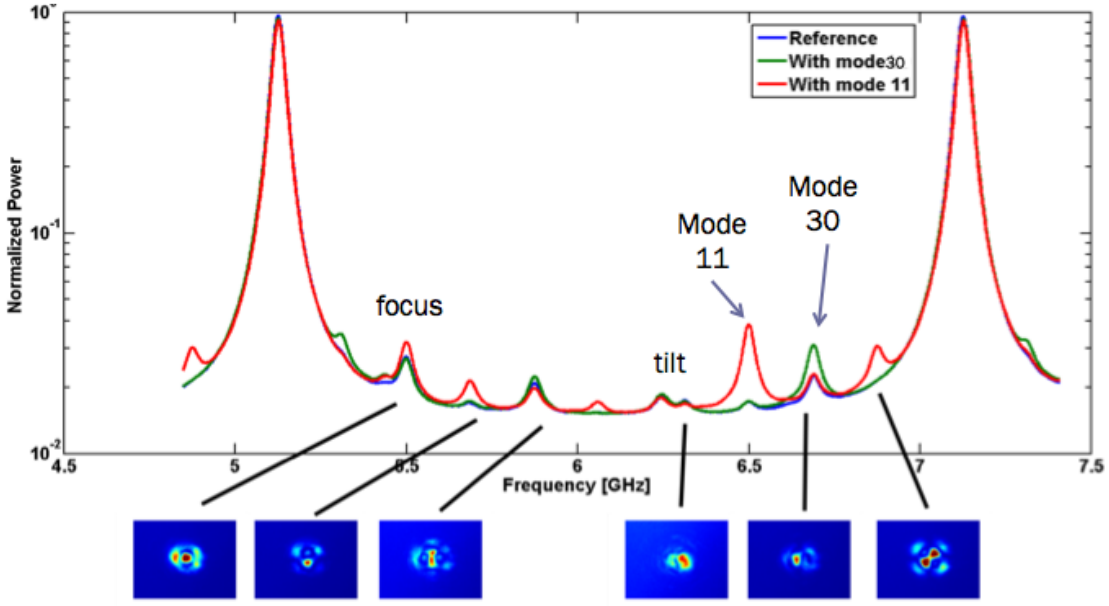

FIGURE 7.14: Scans of the OMC transmission before (reference) and after the application of the maps on the TDM0. Both scans have been renormalized to have an equal integral content and the maximum of the transmission was adjusted with the matching value when the OMC was locked.

7.5.2 Reduction of the high order modes

With the same set of maps, we now want to reduce these modes with the TDM1 and TDM2. The amplitude of the actuation is found by scanning the amplitudes of the maps on both TDMs to minimize the power reflected by the cavity.

7.5.2.1 Control of the mode HG_{11}

In Fig.7.15, we can observe that the mode HG_{11} is reduced by a factor 3. There is also a slight coupling to some other modes, mainly to the defocus, tilt and the mode HG_{30}. This leads to the stop of the algorithm at a pseudo minimum: the correction is found optimal otherwise the tilt and the focus will continue to increase. We are therefore limited by the coupling to the low order modes.

7.5.2.2 Control of the mode HG_{30}

In Fig.7.16, we can observe that the mode HG_{11} is reduced by a factor 1.9. There is also a slight coupling to some other modes, mainly to the defocus and to the tilt.

7.6 Results discussion

We have been able to show experimentally that our system of combined TDMs is able to improve the matching into a simple cavity. This was the first proof-of principle that the modal content of the beam can be controlled by TDMs. We have shown that some modes can be successively increased and reduced by applying the corresponding actuation maps.

However, the correction is mainly limited by the coupling to the other high order modes as a side effect. The TDMs are mainly introducing tilt and focus that have to be taken under control to have the possibility to improve the correction. For this purpose, we need a system of alignment to control the tip/tilt and a matching telescope to continuously adjust the focus. Further investigation will continue to study the addition of an automatic alignment and focus system.

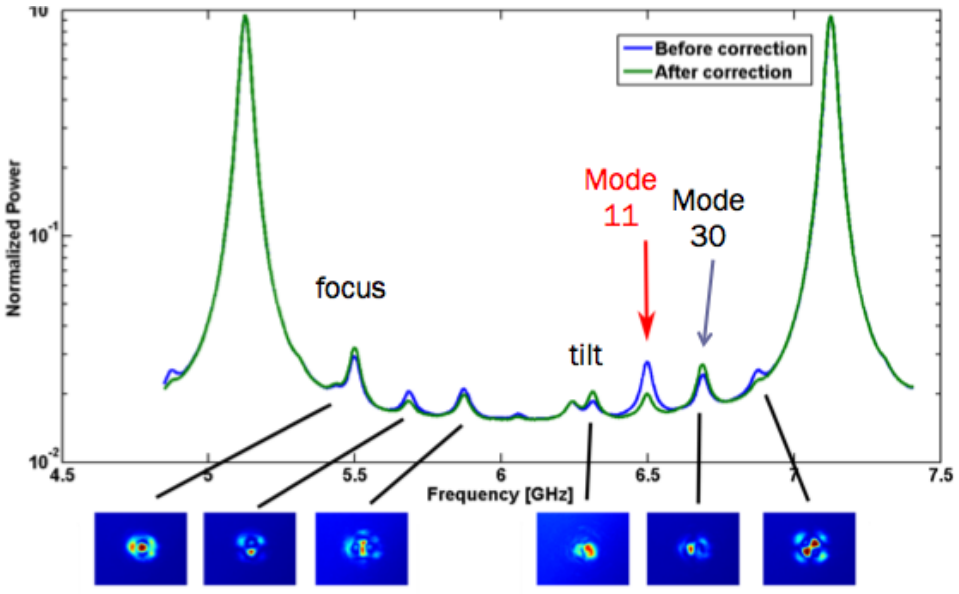

FIGURE 7.15: Scans of the OMC transmission before (reference) and after the application of the maps on the TDM1 and TDM2. The content in the mode HG_{11} is reduced by a factor 3.

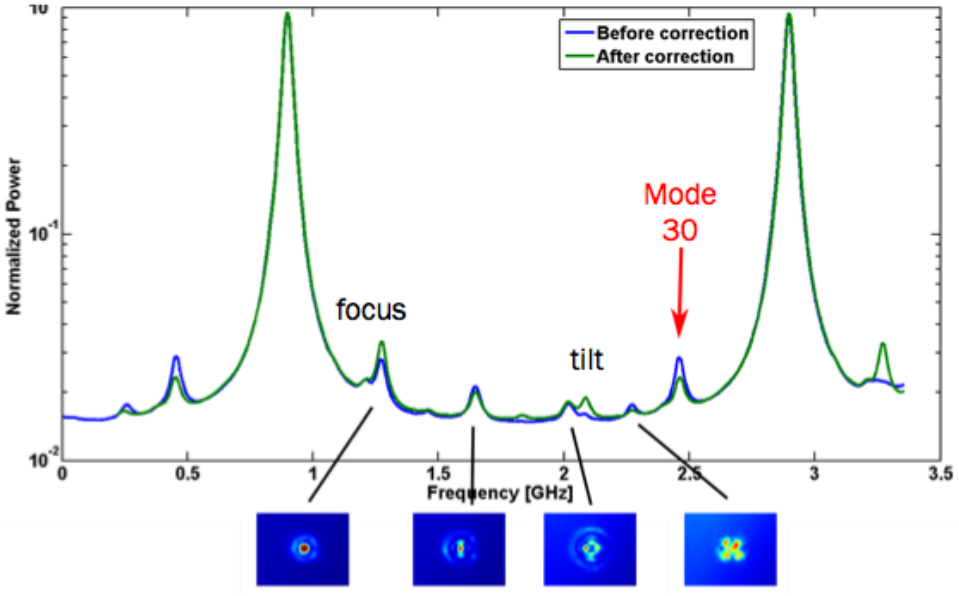

FIGURE 7.16: Scans of the OMC transmission before (reference) and after the application of the maps on the TDM1 and TDM2. The content in the mode HG_{30} is reduced by a factor 1.9.

Conclusion

We have demonstrated that the Thermally Deformable Mirror (TDM) is a promising device, especially designed for the control and improvement of the matching of a laser beam into resonant cavities within the environment of the Advanced gravitational wave interferometers, notably at the input of the interferometer.

We have first established the spatial response of the substrate to an input power field that leads to the definition of the substrate transfer function. This can be approximated by a series of two spatial filters: a band-pass filter around the fundamental frequency u_0, that depends on the thermal conductivity, and a low-pass filter of second-order: the high spatial frequencies are attenuated in $1/\mathrm{u}^2$ with the cut-off frequency that depends on the substrate thickness. However, we have seen that at high frequencies the influence of the thickness on the substrate response is negligible. The analysis also allowed to estimate that the thermal conductivity of the substrate will be determinant for the resulting shape of the temperature field inside the substrate. Afterwards, we performed accurate simulations with a finite element analysis tool to determine the exact shape of the temperature field inside the substrate for different inputs, materials and thicknesses. We found that the shape is enlarged by the radiation at the barrel of the substrate and confirmed that the thickness is poorly influencing the response. We studied various substrates and demonstrated that the Fused Silica is a good trade-off that gives a large actuation but also a small temperature increase.

After establishing the influence function of a single actuator, we studied the full TDM with 61 actuators. To produce the adequate correction, that minimizes the difference with the input wavefront, the power delivered by the actuators can be found through the inversion of the matrix that contains all influence functions. For a given influence function, the quality of the correction mainly depends on the gap between the actuators. Controlling the Zernike modes up to order 5 requires that this gap is lower than 0.5 mm. We then demonstrated by simulation that built TDMs should be able to reach the specifications on matching.

Afterwards, the prototypes have been experimentally characterized by observing the phase variations on a probe beam in the conjugate plane of the TDMs. We checked the linearity of the response with the input power, the response time and the linear superposition. We implemented a control loop for the Zernike polynomials generation based on a least square algorithm. The experimental results shown that the TDM is able to generate Zernike polynomials up to the order 5. The dynamic range is the main limiting factor to reproduce the highest modes with the correct amplitude while the mode coupling is very low and the residual footprint limits the precision of the mode reproduction. We deduced that if the mismatch is due to aberrations lower than the 5^{th} order at the level of 5 %, the TDM is able to correct it to reach a matching better than 99%.

As a TDM is only able to modify the beam wavefront, a couple of devices placed at different Gouy phases is therefore necessary. With a simple analysis, we demonstrated that a correction with Hermite-shape maps is possible, suppressing a high order mode in a first approximation and that the position of the TDMs have to be carefully chosen. The linearity of the model and the successive correction of several modes have been discussed.

Finally, we experimentally tested the mode matching correction, in particular with a setup with 3 TDMs: one to have the possibility to generate known aberrations in the system and two to correct the matching into a fixed triangular cavity. We have been able to demonstrate that a TDM is able to generate a Hermite-Gauss mode from a specific map of actuation. With a minimization algorithm on the power reflected by the cavity, some Hermite-Gauss modes have also been reduced, leading to demonstrate the possibility to control the matching with the TDMs. The study was limited by the coupling of the modes to the alignment and the curvature of the beam.

The TDMs have then demonstrated, by simulations and experiments, their ability to correct optical aberrations and to provide mode matching improvement in an adequate system. They will hopefully be helpful devices in the correction of matching for Advanced gravitational interferometers in any place where the systems are sensitive to mismatch losses, like at the injection, the detection or in squeezing systems.

The next step toward the completion of the study with these prototypes should be to pursue the implementation of an automatic alignment and focus control, to reduce the mode coupling into these fundamental modes. Then, an iterative method of mode reduction may be tested and a systematic analysis of mode reduction efficiency may be performed. Afterwards, one can focus on the sensing improvement to have a direct access to the modal decomposition of the beam, without unlocking the system.

Furthermore, several improvements are necessary to deliver a device ready for an implementation on Advanced detectors. Going deeply with the simulations, in particular with the heat conduction in the mounts, would allow to precise the final design. The thermal contact should be improved to increase the power coupling into the substrate and thereby increase the dynamic range. A challenging task will be to build a vacuum compatible prototype. Then, a new characterization of the device may be performed to detect any difference with the in air measurements. Afterwards, the TDM should be tested on a suspended bench to control the noise compatibility. In the end, it will be possible to implement a complete adaptive optics system in Advanced detectors after an appropriate error signal will have been found.

Appendix A

Gaussian modes and Resonant cavities

A.1 Fundamental Gaussian mode

We will derive the Gaussian-spherical solution of the paraxial wave equation following the simple method proposed by Born and Wolf using the complex point source derivation. The wavelength is λ. In free space, the electromagnetic waves are propagating according to the *Paraxial wave equation*:

$$\left[\nabla^2 + k^2\right] \tilde{E}(x, y, z) = 0 \tag{A.1}$$

We assume that the wave is propagating in the z direction, so the field will depends on $\exp(-jkz)$. This $\exp(-jkz)$ has a spatial variation of one λ in the z direction. We can separate the transverse variation of the field x, y and the longitudinal variation z. The transverse variation depends on the longitudinal position z, so we can rewrite:

$$\tilde{E}(x, y, z) \simeq \tilde{u}(x, y, z) e^{-jkz} \tag{A.2}$$

The paraxial wave equation becomes:

$$\frac{\partial^2 \tilde{u}}{\partial x^2} + \frac{\partial^2 \tilde{u}}{\partial y^2} + \frac{\partial^2 \tilde{u}}{\partial z^2} - 2jk\frac{\partial \tilde{u}}{\partial z} = 0 \tag{A.3}$$

The *paraxial approximation* expresses the fact that the transverse variations due to the z dependence are slow compare the the other dependences. That is:

$$\left|\frac{\partial^2\tilde{u}}{\partial z^2}\right| \ll \left|\frac{\partial^2\tilde{u}}{\partial x^2}\right| or \left|\frac{\partial^2\tilde{u}}{\partial y^2}\right| or \left|2k\frac{\partial\tilde{u}}{\partial z}\right| \tag{A.4}$$

The paraxial wave equation is the:

$$\nabla_t^2\tilde{u}(\mathbf{s},z) - 2jk\frac{\partial\tilde{u}(\mathbf{s},z)}{\partial z} = 0 \tag{A.5}$$

where $\mathbf{s}$ denotes the spatial coordinates (x,y) or (r,θ) and t refers to the transverse plane.

One exact solution of the wave equation (Eq. A.1) is the uniform spherical wave emerging from a point source r_0 expressed by:

$$\tilde{E}(r,r_0) = \frac{\exp[-jk\rho(r,r_0)]}{\rho(r,r_0)} \tag{A.6}$$

The distance $\rho(r,r_0)$ from the point $(s_0),z0$ to the observation point $(s),z$:

$$\rho(r,r_0) = \sqrt{(x-x_0)^2+(y-y_0)^2+(z-z_0)^2} \tag{A.7}$$

that can be approximated by:

$$\rho(r,r_0) = z - z_0 + \frac{(x-x_0)^2+(y-y_0)^2}{2(z-z_0)} + ... \tag{A.8}$$

So the wave equation is equivalent to (= *paraxial-spherical wave*, exact analytical solution of the paraxial wave equation):

$$\tilde{E}(r,r_0) = \frac{1}{z-z_0}\exp\left[-jk(z-z_0) - jk\frac{(x-x_0)^2+(y-y_0)^2}{2(z-z_0)}\right] \tag{A.9}$$

Let's consider a complex point source instead of a real one. The real point sources implies to have an infinite transverse description of the field, that is to have an infinite energy. We can retrieve a physical description with the complex number as demonstrated here.

We replace the quantity z_0 by the complex quantity $z_0 - \tilde{q}_0$. We introduce the complex radius of curvature $\tilde{q} = z - (z_0 - \tilde{q}_0)$. The real radius of curvature $R(z) = R_0 + z - z_0$. The equation is then:

$$\tilde{E}(x,y,z) = \frac{1}{\tilde{q}(z)}\exp\left[-jk\tilde{q}(z) - jk\frac{(x-x_0)^2+(y-y_0)^2}{2\tilde{q}(z)}\right] \tag{A.10}$$

To retrieve the standard notation in laser beams, we write:

$$\frac{1}{\tilde{q}(z)} = \frac{1}{R(z)} - \frac{\lambda}{\pi w^2(z)} \tag{A.11}$$

Then:

$$\tilde{E}(x,y,z) = \frac{1}{\tilde{q}(z)} \exp\left[-jk\tilde{q}(z) - jk\frac{(x-x_0)^2 + (y-y_0)^2}{2\tilde{q}(z)}\right] \tag{A.12}$$

A.1.1 Fundamental mode

We can now write the main characteristics of the fundamental mode. From Eq. A.12, we see that the transverse spatial distribution has a minimum in z_0 that is the *waist* w_0 of the beam:

$$w(z) = w_0\sqrt{1 + (\frac{z}{z_R})^2} \qquad z_R = \frac{\pi w_0^2}{\lambda} \tag{A.13}$$

$$R(z) = z\left[1 + \left(\frac{z_R}{z}\right)^2\right] \tag{A.14}$$

z_R is the *Rayleigh* distance. From Eq. A.12, we recognize the term of amplitude:

$$\tilde{E}(x,y,,z) = E_0\frac{w_0}{w(z)}\exp(-\frac{r^2}{w^2(z)}) \tag{A.15}$$

the term of the longitudinal phase:

$$\exp(-j(kz - atan(\frac{z}{z_0}))) \tag{A.16}$$

and the term of the transverse phase:

$$\exp(-j\frac{kr^2}{2R(z)}) \tag{A.17}$$

We also can separate the longitudinal phase of the beam, that is called the *Gouy phase*:

$$\phi_g = atan(\frac{z}{z_R}) \tag{A.18}$$

This term is an additional phase shift that depends on the mode that is propagating.

A.2 High order Hermite-Gauss modes

We can decompose the beam in the basis of the Hermite-Gauss polynomials (Cartesian coordinates). The solution of the equation in the cylindrical coordinates is the Laguerre-Gauss mode basis.
For the mode mn, the general equation is then:

$$E_{mn}(x,y,z) = \sqrt{\frac{2}{\pi}}\frac{1}{w(z)}\frac{1}{\sqrt{2^{m+n}m!n!}}H_m(\frac{\sqrt{2}x}{w(z)})H_n(\frac{\sqrt{2}y}{w(z)})e^{-i\left(\frac{k}{2q(z)}(x^2+y^2)+\left(kz-(m+n+1)atan(\frac{z}{z_R})\right)\right)} \tag{A.19}$$

The Gouy phase term is then:

$$\phi_g = (m+n+1)atan(\frac{z}{z_R}) \tag{A.20}$$

The Hermite polynomials are defined by:

$$H_0(x) = 1 \tag{A.21}$$

$$H_1(x) = 2x \tag{A.22}$$

$$H_{j+1}(x) = 2xH_j(x) - 2jH_{j-1}(x) \tag{A.23}$$

Some of the modes are represented in Fig. A.1.

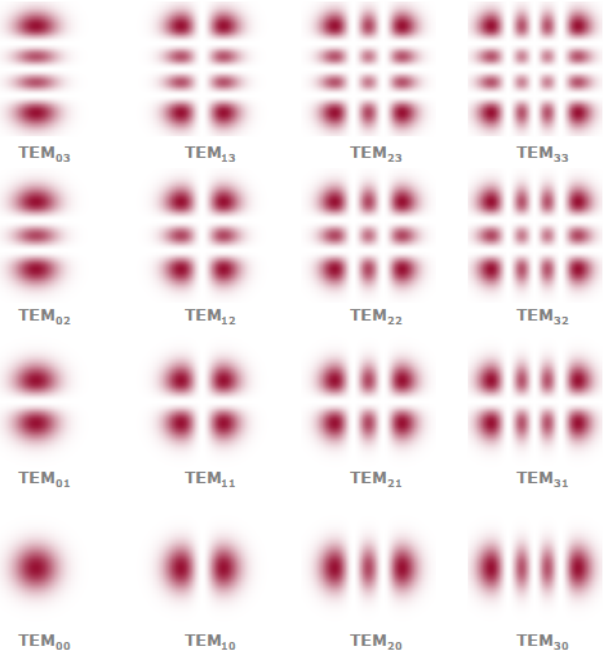

FIGURE A.1: Spatial representation of the Hermite-Gauss modes

A.2.1 Times table of the first Hermite-Gauss polynomials (Physicist)

When we developed the correction with the TDMs in Chapter 6, we need to compute the product of the Hermite-Gauss modes. The formula is given in [71]. The product of two Hermite polynomials $H_i(x)$ and $H_j(x)$ is:

$$H_i(x)H_j(x) = \sum_{k=0}^{\min(i,j)} k!\, 2^k \binom{i}{k}\binom{j}{k} H_{i+j-2k}(x) \tag{A.24}$$

In Table A.1 is the computation up to the 6^{th} order.

mode m	mode n	Result
H_1	H_1	$= H_2 + 2H_0$
H_1	H_2	$= H_3 + 4H_1$
H_1	H_3	$= H_4 + 6H_2$
H_1	H_4	$= H_5 + 8H_3$
H_1	H_5	$= H_6 + 10H_4$
H_2	H_2	$= H_4 + 8H_2 + 8H_0$
H_2	H_3	$= H_5 + 12H_3 + 24H_1$
H_2	H_4	$= H_6 + 16H_4 + 48H_2$
H_3	H_3	$= H_6 + 18H_4 + 72H_2 + 48H_0$

TABLE A.1: Table of the Hermite product

A.3 Coupling of aberrations with a cavity and high order modes

A.3.1 Mode Matching

A stable cavity is characterized by a set of eigen spatial (TEM) modes.

We extend the definition given in [31]: "Proper [*matching*] between an input laser beam and a optical cavity means exactly this: that the laser beam couples completely to the fundamental (longitudinal) spatial mode of the cavity and not at all to the higher-order (off-axis) spatial modes."

The term *alignment* is here used for angular orientation and transverse displacement: a beam is properly aligned with respect to a cavity when the propagation axis corresponds to the optical axis of the cavity and when the beam waist position and waist size correspond to the waist of the cavity.

The misalignment of a beam with a cavity will produce coupling into the high order modes. This is extensively described in [31] for a two mirror cavity, that has six degrees

of freedom concerning the misalignment: x and y tips, x and y tilts and the waist size and the waist position. In the following we recall the main results of this paper that can be extended to a three mirrors (or Mode Cleaner) cavity.

The input beam is the fundamental modes $\psi = AU_0$ with a small amount of the different misalignments. At the waist, we have:

$$E_0(x) = \left(\frac{2}{\pi w_0^2}\right)^{1/4} \; e^{-\left(\frac{x}{w_0}\right)^2} \tag{A.25}$$

$$E_1(x) = \left(\frac{2}{\pi w_0^2}\right)^{1/4} \; \left(\frac{2x}{w_0}\right) \; e^{-\left(\frac{x}{w_0}\right)^2} \tag{A.26}$$

A.3.2 Tip and Tilt

The tips and tilts are more easily described with the Cartesian coordinates. The coupling with the Hermite-Gauss modes is described. The study of the x direction is only performed, since the equations are the equivalent in the y direction. The results are approximated at the first order.

Tip The input beam is translated by a:

$$\psi(x) = AU_0(x-a) \tag{A.27}$$

$$\psi(x) = A\frac{2}{\pi w_0^2}\exp\left[-\frac{(x-a)^2}{w_0^2}\right] \tag{A.28}$$

$$\psi(x) \simeq A\frac{2}{\pi w_0^2}\left(1 + 2a\frac{x}{w_0^2}\right) e^{-\left(\frac{x}{w_0}\right)^2} \tag{A.29}$$

$$\psi(x) \simeq A\left(E_0(x) + \frac{a}{w_0}E_1(x)\right) \tag{A.30}$$

Tilt If the beam misaligned by the optical axis, the phase of the beam becomes:

$$\psi(x) = \frac{2\pi}{\lambda}x\sin(\alpha) \simeq \frac{2\pi}{\lambda}x\alpha \tag{A.31}$$

Then

$$\psi(x) = A\left(\frac{2}{\pi w_0^2}\right)^{1/4} \; e^{-\left(\frac{x}{w_0}\right)^2} \; e^{i\frac{2\pi}{\lambda}x\alpha} \tag{A.32}$$

$$\psi(x) \simeq A\left(\frac{2}{\pi w_0^2}\right)^{1/4} \; e^{-\left(\frac{x}{w_0}\right)^2} \; \left(1 + i\frac{2\pi}{\lambda}x\alpha\right) \tag{A.33}$$

$$\psi(x) \simeq A\left(\frac{2}{\pi w_0^2}\right)^{1/4} \; \left(E_0(x) + i\frac{\pi}{\lambda}w_0\alpha E_1(x)\right) \tag{A.34}$$

A.3.3 Position and size of the waist

The position and size of the waist is axisymmetric, so the Laguerre-Gauss description is more appropriate.

We have, for the fundamental and the first modes:

$$V_0(r) = \sqrt{\frac{2}{\pi}}\frac{1}{w_0}\ e^{-\frac{r^2}{w_0^2}} \tag{A.35}$$

$$V_1(r) = \sqrt{\frac{2}{\pi}}\frac{1}{w_0}\left(1-2\frac{r^2}{w_0^2}\right)e^{-\frac{r^2}{w_0^2}} \tag{A.36}$$

Waist size If the waist size is $w_0' = w_0(1+\epsilon)$, we have:

$$\psi(r) = A\sqrt{\frac{2}{\pi}}\frac{(1+\epsilon)}{w_0}\ e^{-\frac{r^2(1+\epsilon)^2}{w_0^2}} \tag{A.37}$$

$$\psi(r) \simeq A\sqrt{\frac{2}{\pi}}\frac{(1+\epsilon)}{w_0}\ e^{-2\epsilon\frac{r^2}{w_0^2}}\ e^{-\frac{r^2}{w_0^2}} \tag{A.38}$$

$$\psi(r) \simeq A\sqrt{\frac{2}{\pi}}\frac{(1+\epsilon)}{w_0}\ (1-2\epsilon\frac{r^2}{w_0^2})\ e^{-\frac{r^2}{w_0^2}} \tag{A.39}$$

$$\psi(r) \simeq A\sqrt{\frac{2}{\pi}}\frac{1}{w_0}\ (1-2\epsilon\frac{r^2}{w_0^2}+\epsilon)\ e^{-\frac{r^2}{w_0^2}} \tag{A.40}$$

$$\psi(r) \simeq AV_0(r) + A\epsilon V_1(r) \tag{A.41}$$

Waist position We have to consider the spatial variation of the modes

$$V_0(r,z) = \sqrt{\frac{2}{\pi}}\frac{1}{w(z)}\ e^{-r^2\left(\frac{1}{w(z)^2}+i\frac{\pi}{\lambda R(z)}\right)} \tag{A.42}$$

$$V_1(r) = \sqrt{\frac{2}{\pi}}\frac{1}{w(z)}\left(1-2\frac{r^2}{w(z)^2}\right)e^{-r^2\left(\frac{1}{w(z)^2}+i\frac{\pi}{\lambda R(z)}\right)} \tag{A.43}$$

Now the beam position is shifted with respect to the cavity and we obtain:

$$\psi(r,z) \simeq A\left(V_0 + i\frac{\lambda b}{2\pi w_0^2}\epsilon V_1\right) \tag{A.44}$$

Appendix B

Zernike polynomials

The spatial representation of the Zernike polynomials Z_n^m is given in the figure below with, for each mode, the ANSI index j under the polynomial.

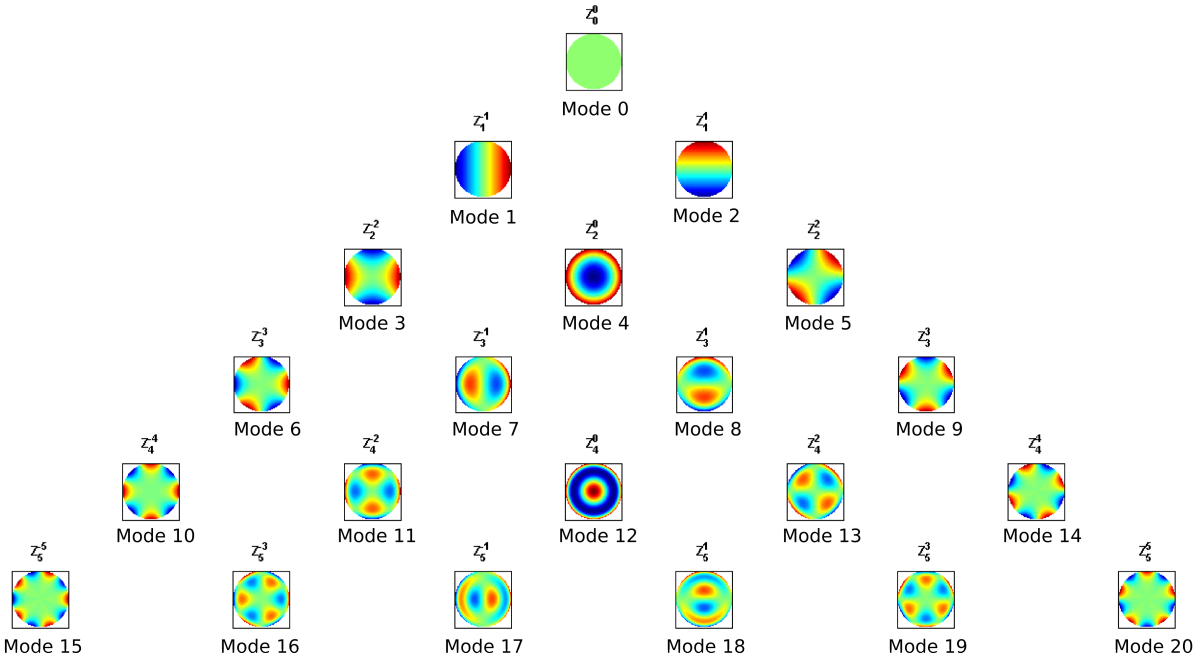

Appendix C

Datasheets

C.1 First prototype

We warmly thank Stevenage Circuits (Stevenage Circuits Ldt., Stevenage, UK) for their cordial work and assistance in the construction of the resistor circuit array for the first prototype.

C.2 Second prototype

The drivers for the second prototype have been designed and realized by Adam Kutynia and the Smart Instruments company that we would like to warmly thank for their hard work and enthusiasm.

Resistors of the second prototype The resistors circuit boards for the second prototype have been made by the European Circuit Company that we thank for their collaboration. Two types of resistors have been mounted on the boards: from Panasonic (ERJ-2RKF1001X) and Vishay (CRCW0402). They have been both chosen for their ability to support high temperatures and for their size. Here are summarized their main characteristics as provided by the suppliers.

	P - ERJ2R	V - 0402
Resistance [Ω]	1000 (±0.5%)	1000 (±0.5%)
Power rating [1] at 70deg [W]	0.063	0.063
Limiting Element Voltage [V]	50	50
Max. Overload Voltage [V]	100	> 75
Weight [mg]	0.8	0.65

TABLE C.1: Characteristic of the resistors. [1] The power dissipation on the resistor generates a temperature rise against the local ambient, depending on the heat flow support of the printed-circuit board (thermal resistance). The rated dissipation applies only if the permitted film temperature of 155 deg is not exceeded.

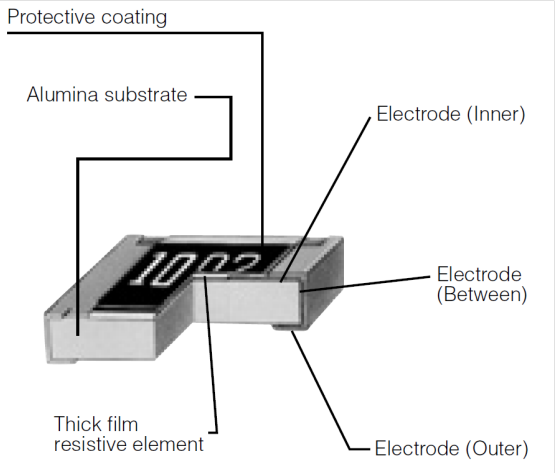

FIGURE C.1: Scheme of a resistor from the Panasonic Company.

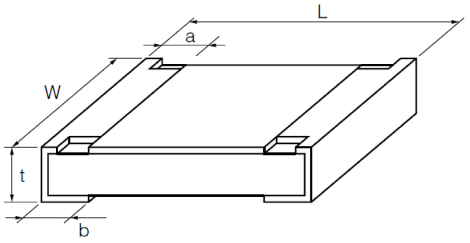

(A)

Length	P - ERJ2R [mm]	V - 0402 [mm]
L	1.00 (± 0.05)	1.00 (± 0.05)
w	0.50 (± 0.05)	0.50 (± 0.05)
a	0.20 (± 0.10)	0.20 (± 0.10)
b	0.25 (± 0.05)	0.25 (± 0.05)
t	0.35 (± 0.05)	0.35 (± 0.05)

(B)

FIGURE C.2: Dimensions of the resistor from the Panasonic Company (A) Scheme of the resistor with dimension labelling (B) Table of the dimension figures.

Appendix D

Abbreviations

D.1 List of Acronyms

GW Gravitational Wave

BNS Binary Neutron Star

SQL Standard Quantum Limit

PWM Pulse Width Modulation

TDM Thermally Deformable Mirror

RMS Root Mean Square

LSQ Least Square Algorithm

DAC Digital Analog Converter

AR Anti Reflective

HR High Reflective

RoC Radius of Curvature

CP Compensating Plate

ITM Input Test Mass

ETM End Test Mass

IMC Input Mode Cleaner

OMC Output Mode Cleaner

MMT Mode Matching Telescope

RH Ring Heater

CHRoCC Central Heating Radius of Curvature Correction

ZnSe Zinc Selenite

CHRAC Central Heating for Aberration Correction

FF Far Field

NF Near Field

OPD Optical Path Difference

OPL Optical Path Length

FEA Finite Element Analysis

HWHM Half Width Half Maximum

FWHM Full Width at Half Maximum

FS Fused Silica

SMD Surface Mount Device

CW Continious Wave

TT Transverse Traceless

PR Power Recycling

SR Signal Recycling

RC Recycling Cavity

TEM Transverse Electromagnetic Mode

HOM High Order Modes

TCS Thermal Compensation System

VSR Virgo Science Run

RF Radio-Frequency

RFC Reference Cavity

List of Figures

List of Tables

Bibliography

[1] Albert Einstein. The foundation of the general theory of relativity. *The Principle of Relativity. Dover Books on Physics. June 1, 1952. 240 pages. 0486600815, p. 109-164*, 1:109–164, 1952.

[2] David G Blair. *The detection of gravitational waves*. Cambridge university press, 2005.

[3] Peter R Saulson. *Fundamentals of interferometric gravitational wave detectors*, volume 7. World Scientific, 1994.

[4] J Aasi, J Abadie, BP Abbott, R Abbott, TD Abbott, M Abernathy, T Accadia, F Acernese, C Adams, T Adams, et al. Prospects for localization of gravitational wave transients by the advanced ligo and advanced virgo observatories. *arXiv preprint arXiv:1304.0670*, 2013.

[5] Joseph Weber. *Gravitational radiation experiments*. Springer, 1970.

[6] A. A. Michelson and E. W. Morley. On the Relative Motion of the Earth and the Luminiferous Ether. *American Journal of Science*, 34:333–345, 1887.

[7] Max Born and Emil Wolf. *Principles of Optics: Electromagnetic Theory of Propagation, Interference and Diffraction of Light*. Cambridge University Press, 7th edition, October 1999. ISBN 0521642221. URL http://www.amazon.com/exec/obidos/redirect?tag=citeulike07-20&path=ASIN/0521642221.

[8] Matthew Pitkin, Stuart Reid, Sheila Rowan, and James Hough. Gravitational wave detection by interferometry (ground and space). *Living Reviews in Relativity*, 14(5), 2011. doi: 10.12942/lrr-2011-5. URL http://www.livingreviews.org/lrr-2011-5.

[9] G. Vajente. Interferometer configurations. *VESF School on Advanced Gravitational Wave Detectors*, 2012.

[10] The Virgo Collaboration. Advanced virgo technical design report. *Virgo collaboration internal document*, 2012.

[11] B Canuel, R Day, E Genin, P La Penna, and J Marque. Wavefront aberration compensation with a thermally deformable mirror. *Classical and Quantum Gravity*, 29(8):085012, 2012. URL http://stacks.iop.org/0264-9381/29/i=8/a=085012.

[12] P. Hello and J.Y. Vinet. Analytical models of thermal aberrations in massive mirrors heated by high power laser beams. *J. Phys. France*, 51(12):1267–1282, 1990.

[13] P. Hello and J.Y. Vinet. Analytical models of transient thermoelastic deformations of mirrors heated by high power cw laser beams. *J. Phys. France*, 51(12):2243–2261, 1990.

[14] Ryan Christopher Lawrence. *Active wavefront correction in laser interferometric gravitational wave detectors*. PhD thesis, Massachusetts Institute of Technology, 2003.

[15] AA Andrade, T Catunda, I Bodnar, J Mura, and ML Baesso. Thermal lens determination of the temperature coefficient of optical path length in optical materials. *Review of scientific instruments*, 74(1):877–880, 2003.

[16] Jean-Yves Vinet. On special optical modes and thermal issues in advanced gravitational wave interferometric detectors. *Living Reviews in Relativity*, 12(5), 2009. doi: 10.12942/lrr-2009-5. URL http://www.livingreviews.org/lrr-2009-5.

[17] M. Prijatelj et al. The output mode cleaner of geo600. *LIGO Document*, pages P1100124–v1.

[18] Holger Wittel, Harald Lück, Christoph Affeldt, Katherine L Dooley, Hartmut Grote, Jonathan R Leong, Mirko Prijatelj, Emil Schreiber, Jacob Slutsky, K Strain, et al. Thermal correction of astigmatism in the gravitational wave observatory geo 600. *Classical and Quantum Gravity*, 31(6):065008, 2014.

[19] E. Tournefier. Advanced virgo output mode cleaner: Specifications. *VIRGO Document*, pages VIR–NOT–071A–08.

[20] R. Gouaty et al. Advanced virgo output mode cleaner: Revisions of the specifications. *VIRGO Document*, pages VIR–0020A–11.

[21] ET Science team. Einstein gravitational wave telescope - conceptual study.

[22] P.F. Cohadon et al. E. Calloni. A proposal for the development and implementation of a vacuum squeezed light source in advanced virgo. *Virgo week presentation*, pages VIR – 0280A–14, 2014.

[23] Enrique J. Fernandez, Laurent Vabre, Boris Hermann, Angelika Unterhuber, Boris Povazay, and Wolfgang Drexler. Adaptive optics with a magnetic deformable mirror:

applications in the human eye. *Opt. Express*, 14(20):8900–8917, Oct 2006. doi: 10.1364/OE.14.008900. URL http://www.opticsexpress.org/abstract.cfm?URI=oe-14-20-8900.

[24] Eugenie Dalimier and Chris Dainty. Comparative analysis of deformable mirrors for ocular adaptive optics. *Opt. Express*, 13(11):4275–4285, May 2005. doi: 10.1364/OPEX.13.004275. URL http://www.opticsexpress.org/abstract.cfm?URI=oe-13-11-4275.

[25] Michael Shaw, Simon Hall, Steven Knox, Richard Stevens, and Carl Paterson. Characterization of deformable mirrors for spherical aberration correction in optical sectioning microscopy. *Opt. Express*, 18(7):6900–6913, Mar 2010. doi: 10.1364/OE.18.006900. URL http://www.opticsexpress.org/abstract.cfm?URI=oe-18-7-6900.

[26] Shin Oya, Aurelien Bouvier, Olivier Guyon, Makoto Watanabe, Yutaka Hayano, Hideki Takami, Masanori Iye, Masayuki Hattori, Yoshihiko Saito, Meguru Itoh, Stephen Colley, Matthew Dinkins, Michael Eldred, and Taras Golota. Performance of the deformable mirror for subaru lgsao, 2006. URL http://dx.doi.org/10.1117/12.670773.

[27] Frédéric Druon, Gilles Chériaux, Jérôme Faure, John Nees, Marc Nantel, Anatoly Maksimchuk, Gérard Mourou, Jean Christophe Chanteloup, and Gleb Vdovin. Wave-front correction of femtosecond terawatt lasers by deformable mirrors. *Opt. Lett.*, 23(13):1043–1045, Jul 1998. doi: 10.1364/OL.23.001043. URL http://ol.osa.org/abstract.cfm?URI=ol-23-13-1043.

[28] Supriyo Sinha, Justin D. Mansell, and Robert L. Byer. Deformable mirrors for high-power lasers, 2002. URL http://dx.doi.org/10.1117/12.454728.

[29] G. Vajente. In situ correction of mirror surface to reduce round-trip losses in fabry perot cavities. *Appl. Opt.*, 53(7):1459–1465, Mar 2014. doi: 10.1364/AO.53.001459. URL http://ao.osa.org/abstract.cfm?URI=ao-53-7-1459.

[30] M. Rakhmanov. Dynamics of laser interferometric gravitational wave detectors, 2000.

[31] Dana Z. Anderson. Alignment of resonant optical cavities. *Appl. Opt.*, 23(17):2944–2949, Sep 1984. doi: 10.1364/AO.23.002944. URL http://ao.osa.org/abstract.cfm?URI=ao-23-17-2944.

[32] K. Aoshima, N. Funabashi, K. Machida, Yasuyoshi Miyamoto, K. Kuga, N. Shimidzu, and F. Sato. An ultra-high definition spatial light modulation device driven by spin-polarized electrons, Oct 2009. ISSN 0197-2618.

[33] Alfredo Dubra, John S. Massa, and Carl Paterson. Hysteresis compensation in pzt bimorph mirrors: Preisach's classical and non-linear models, 2005. URL http://dx.doi.org/10.1117/12.669384.

[34] G. Vdovin M. Loktev, O. Soloviev. Adaptive optics guide. *OKO Technologies*, ISBN: 90-8559-164-3:35–26, 2008.

[35] Gleb V. Vdovin, Nicolas Kugler, and Martin Schacht. Membrane deformable mirrors under cw laser load, 1999. URL http://dx.doi.org/10.1117/12.363601.

[36] Göran B. Scharmer, Peter Dettori A, Mats G. Löfdahl A, and Mark Sh. Adaptive optics system for the new swedish solar telescope, 2002.

[37] Reiner Volkmer, Oskar von der Luehe, Franz Kneer, Juergen Staude, Axel Hofmann, Wolfgang Schmidt, Michal Sobotka, Dirk Soltau, Eberhardt Wiehr, Axel Wittmann, and Thomas Berkefeld. Gregor: the new 1.5m solar telescope on tenerife, 2003. URL http://dx.doi.org/10.1117/12.471367.

[38] W. Winkler, K. Danzmann, A. Rüdiger, and R. Schilling. Heating by optical absorption and the performance of interferometric gravitational-wave detectors. *Phys. Rev. A*, 44:7022–7036, Dec 1991. doi: 10.1103/PhysRevA.44.7022. URL http://link.aps.org/doi/10.1103/PhysRevA.44.7022.

[39] H. Luck, K. O. Muller, P. Aufmuth, and K. Danzmann. Correction of wavefront distortions by means of thermally adaptive optics. *Optics Communications*, 175(4-6): 275–287, March 2000. URL http://www.sciencedirect.com/science/article/B6TVF-3YRVGNF-3/2/7e3749c33630d8ba78e82b93ebcad87a.

[40] P. Hello. Compensation for thermal effects in mirrors of gravitational wave interferometers. *Eur. Phys. J. D*, (15):373–383, 2001.

[41] Ryan Lawrence, Michael Zucker, Peter Fritschel, Phil Marfuta, and David Shoemaker. Adaptive thermal compensation of test masses in advanced ligo. *Classical and Quantum Gravity*, 19(7):1803, 2002. URL http://stacks.iop.org/0264-9381/19/i=7/a=377.

[42] Jérôme Degallaix, Chunnong Zhao, Li Ju, and David Blair. Thermal lensing compensation for aigo high optical power test facility. *Classical and Quantum Gravity*, 21(5):S903, 2004. URL http://stacks.iop.org/0264-9381/21/i=5/a=079.

[43] H Lück, A Freise, S Goßler, S Hild, K Kawabe, and K Danzmann. Thermal correction of the radii of curvature of mirrors for geo 600. *Classical and Quantum Gravity*, 21(5):S985, 2004. URL http://stacks.iop.org/0264-9381/21/i=5/a=090.

[44] Ryan Lawrence, David Ottaway, Michael Zucker, and Peter Fritschel. Active correction of thermal lensing through external radiative thermal actuation. *Opt. Lett.*, 29(22):2635–2637, Nov 2004. doi: 10.1364/OL.29.002635. URL http://ol.osa.org/abstract.cfm?URI=ol-29-22-2635.

[45] V Quetschke, J Gleason, M Rakhmanov, J Lee, L Zhang, KY Franzen, C Leidel, G Mueller, R Amin, DB Tanner, and DH Reitze. Adaptive control of laser modal properties. *Optics letters*, 31(2):217 – 219, January 2006. ISSN 0146-9592. doi: 10.1364/ol.31.000217. URL http://europepmc.org/abstract/MED/16441035.

[46] Muzammil A Arain, Volker Quetschke, Joseph Gleason, Luke F Williams, Malik Rakhmanov, Jinho Lee, Rachel J Cruz, Guido Mueller, D B Tanner, and David H Reitze. Adaptive beam shaping by controlled thermal lensing in optical elements. *Appl Opt*, 46(12):2153–65, 2007. ISSN 0003-6935. URL http://www.biomedsearch.com/nih/Adaptive-beam-shaping-by-controlled/17415383.html.

[47] R. Day et al. Central heating radius of curvature correction (chrocc) for use in large scale gravitational wave interferometers. *Classical and Quantum Gravity*, 30 (5):055017, 2013. URL http://stacks.iop.org/0264-9381/30/i=5/a=055017.

[48] E. Calloni, J. T. Baker, F. Barone, R. DeRosa, L. Di Fiore, L. Milano, and S.R. Restaino. Adaptive optics approach for prefiltering of geometrical fluctuations of the input laser beam of an interferometric gravitational waves detector. *Review of Scientific Instruments*, 74(4):2570–2574, Apr 2003. ISSN 0034-6748. doi: 10.1063/1.1537043.

[49] S. Avino. Adaptive optics techniques for gravitational wave interferometers. *PhD thesis, Universita degli studi di Napoli Federico II*, 2006.

[50] Muzammil A. Arain, William Z. Korth, Luke F. Williams, Rodica M. Martin, Guido Mueller, D. B. Tanner, and David H. Reitze. Adaptive control of modal properties of optical beams using photothermal effects. *Opt. Express*, 18(3):2767–2781, Feb 2010. doi: 10.1364/OE.18.002767. URL http://www.opticsexpress.org/abstract.cfm?URI=oe-18-3-2767.

[51] Valeria Malvezzi for TCS Team. Adv tcs ring heater update, 2012.

[52] Canuel B, Day R, Genin E, Paoletti F, and Nocera F. High power input optics r and d for advanced virgo. *Final Report Virgo Collaboration Internal Document*, (VIR-0296A-10), 2010.

[53] RA Day, G Vajente, M Kasprzack, and J Marque. Reduction of higher order mode generation in large scale gravitational wave interferometers by central heating residual aberration correction. *Physical Review D*, 87(8):082003, 2013.

[54] Euan Morrison, Brian J. Meers, David I. Robertson, and Henry Ward. Automatic alignment of optical interferometers. *Appl. Opt.*, 33(22):5041–5049, Aug 1994. doi: 10.1364/AO.33.005041. URL http://ao.osa.org/abstract.cfm?URI=ao-33-22-5041.

[55] Zhanwei Liu, Paul Fulda, Muzammil A. Arain, Luke Williams, Guido Mueller, D. B. Tanner, and D. H. Reitze. Feedback control of optical beam spatial profiles using thermal lensing. *Appl. Opt.*, 52(26):6452–6457, Sep 2013. doi: 10.1364/AO.52.006452. URL http://ao.osa.org/abstract.cfm?URI=ao-52-26-6452.

[56] P. Hello. Modele physique et simulation de l'antenne interferometrique gravitationnelle virgo, 1990.

[57] M Abramovich and IA Stegun. Handbook of mathematical functions. *Graphs and Mathematical Tables (National Bureau of Standards Applied Mathematics, Washington, 1964)*, 1965.

[58] Cyril Petit. *Etude de la commande optimale en OA et OAMC, validation numerique et experimentale*. PhD thesis, Universite Paris 13, 2006.

[59] Enrique Fernandez and Pablo Artal. Membrane deformable mirror for adaptive optics: performance limits in visual optics. *Optics express*, 11(9):1056–1069, 2003.

[60] Carl Paterson, Ian Munro, and J Dainty. A low cost adaptive optics system using a membrane mirror. *Optics Express*, 6(9):175–185, 2000.

[61] Robert K Tyson and Dale M Byrne. The effect of wavefront sensor characteristics and spatiotemporal coupling on the correcting capability of a deformable mirror. In *1980 Technical Symposium East*, pages 21–25. International Society for Optics and Photonics, 1980.

[62] James E Harvey and Gary M Callahan. Wavefront error compensation capabilities of multi-actuator deformable mirrors. In *1978 Technical Symposium East*, pages 50–57. International Society for Optics and Photonics, 1978.

[63] Javier Alda and Glenn D Boreman. Zernike-based matrix model of deformable mirrors: optimization of aperture size. *Applied optics*, 32(13):2431–2438, 1993.

[64] Sven Verpoort and Ulrich Wittrock. Actuator patterns for unimorph and bimorph deformable mirrors. *Applied Optics*, 49(31):G37–G46, 2010.

[65] Robert J. Noll. Zernike polynomials and atmospheric turbulence. *J. Opt. Soc. Am.*, 66(3):207–211, Mar 1976. doi: 10.1364/JOSA.66.000207. URL http://www.opticsinfobase.org/abstract.cfm?URI=josa-66-3-207.

[66] Sabrina Velghe, Jérôme Primot, Nicolas Guérineau, Mathieu Cohen, and Benoit Wattellier. Wave-front reconstruction from multidirectional phase derivatives generated by multilateral shearing interferometers. *Optics letters*, 30(3):245–247, 2005.

[67] M. Parisis. Mitigation of laser beam perturbations in the virgo and advanced-virgo gravitational waves detectors, 2011.

[68] Thomas F Coleman and Yuying Li. A reflective newton method for minimizing a quadratic function subject to bounds on some of the variables. *SIAM Journal on Optimization*, 6(4):1040–1058, 1996.

[69] Anthony E Siegman. *Lasers. Mill Valley.* University Science Books, 1986.

[70] Miguel A Bandres, Julio C Gutiérrez-Vega, et al. Ince-gaussian modes of the paraxial wave equation and stable resonators. *JOSA A*, 21(5):873–880, 2004.

[71] L. Carlitz. The product of several hermite or laguerre polynomials. *Monatshefte für Mathematik*, 66:393–396, 1962. URL http://eudml.org/doc/177184.

[72] Richard A. Day. A new fft code: Fog, fast fourier transform optical simulation of gravitational wave interferometers. *Presentation at the AGWDW*, 2012. URL https://dcc.ligo.org/public/0092/G1200629/001/DAY_GWADW2012.pdf.

[73] P Hello and J Y Vinet. Simulation of beam propagation in off-axis optical systems. *Journal of Optics*, 27(6):265, 1996. URL http://stacks.iop.org/0150-536X/27/i=6/a=005.

[74] G. Vajente and R. A. Day. Adaptive optics sensing and control technique to optimize the resonance of the laguerre-gauss 33 mode in fabry-perot cavities. *Phys. Rev. D*, 87:122005, Jun 2013. doi: 10.1103/PhysRevD.87.122005. URL http://link.aps.org/doi/10.1103/PhysRevD.87.122005.

[75] Eric D Black. An introduction to pound–drever–hall laser frequency stabilization. *American Journal of Physics*, 69(1):79–87, 2001.

[76] J. Marque P. Benoit B. Canuel, E. Genin. Reference cavity characterization. Technical report.

[77] Guido Mueller, Qi ze Shu, Rana Adhikari, D. B. Tanner, David Reitze, Daniel Sigg, Nergis Mavalvala, and Jordan Camp. Determination and optimization of mode matching into optical cavities by heterodyne detection. *Opt. Lett.*, 25(4):266–268,

Feb 2000. doi: 10.1364/OL.25.000266. URL http://ol.osa.org/abstract.cfm?URI=ol-25-4-266.

[78] James R Fienup. Phase retrieval algorithms: a comparison. *Applied optics*, 21(15): 2758–2769, 1982.

[79] William H Press, Saul A Teukolsky, William T Vetterling, and Brian P Flannery. Numerical recipes in c+. 2002.

[80] Laurent Derome. *Le système de détection de l'expérience Virgo dédiée à la recherche d'ondes gravitationnelles*. PhD thesis, 1999.